FERRITIN-BASED NANOPLATFORMS FOR DRUG DELIVERY AND PHOTODYNAMIC THERAPY AGAINST CANCER

by

WEI TANG

(Under the Direction of Jin Xie)

ABSTRACT

Ferritin (FRT) is a major iron storage protein found in humans and most living organisms. Each FRT is composed of 24 subunits, which self-assemble to form a cage-like nanostructure. The surface of FRT nanocage can be easily modified for tumor targeting and/or imaging. The interior of FRT can be loaded with different therapeutics. For example, we have used RGD-modified FRTs (RFRTs) to selectively deliver doxorubicin to tumors. The doxorubicin-loaded RFRTs showed improved tumor uptake, enhanced treatment efficacy, and reduced cardiotoxicity compared to free doxorubicin. The FRT nanocages can also be loaded with photosensitizers to facilitate photodynamic therapy (PDT). By choosing different targeting ligands, PDT can target different components in a tumor. For instance, folic acid-conjugated and $ZnF_{16}Pc$-loaded FRTs can efficiently kill cancer cells in tumors. $ZnF_{16}Pc$-loaded RFRTs, on the other hand, target tumor endothelium, and the impact is highly dependent on irradiation doses: at high irradiation doses, the enabled PDT causes vasculature collapse and blockage, leading to tissue ischemia; at low irradiation doses, PDT causes temporally enhanced vasculature permeability, which is beneficial to delivery of nanoparticles to tumors. More recently, we conjugated an anti-fibroblast activation protein (anti-FAP) scFv to $ZnF_{16}Pc$-loaded FRTs and

investigated the enabled PDT. The treatment efficiently killed cancer associated fibroblasts (CAFs) but left most cancer cells unharmed. Yet, efficient tumor growth suppression and extended survival was observed. We've also developed a technology called red blood cell-facilitate PDT (RBC-PDT). In the RBC-PDT, we tether a large amount of photosensitizer-loaded FRTs to erythrocytes, which are natural O_2 transporters. Because photosensitizers are located within an O_2 rich zone on RBC membrane, they can efficiently produce $^1O_2$ even when the overall oxygen level is low, for instance, in hypoxic tumor areas. This leads to efficient tumor therapy and represents a novel PDT approach. In summary, FRT-based drug delivery is a safe and efficient technology that holds great potential in clinical translation.

INDEX WORDS: Ferritin, Cancer Treatment, Drug Delivery, Photodynamic Therapy, Photoimmunotherapy, RGD Peptide, Folic Acid Ligand, Single Chain Fragment Variable, Red Blood Cell, Tumor Endothelium, Tumor Hypoxia, Cancer-Associated Fibroblasts, Fibroblast Activation Protein, $CD8^+$ T Cells.

FERRITIN-BASED NANOPLATFORMS FOR DRUG DELIVERY AND PHOTODYNAMIC THERAPY AGAINST CANCER

by

WEI TANG

B.S., University of Science and Technology of China, 2011

A Dissertation Submitted to the Graduate Faculty of The University of Georgia in Partial Fulfillment of the Requirements for the Degree

DOCTOR OF PHILOSOPHY

ATHENS, GEORGIA

2016

FERRITIN-BASED NANOPLATFORMS FOR DRUG DELIVERY AND PHOTODYNAMIC THERAPY AGAINST CANCER

by

WEI TANG

Major Professor:	Jin Xie
Committee:	Jason Locklin
	Sergiy Minko

Electronic Version Approved:

Suzanne Barbour
Dean of the Graduate School
The University of Georgia
December 2016

ACKNOWLEDGEMENTS

I would like to thank all people who have provided me with support and help during my Ph.D. study. First and foremost, I would like to thank my advisor, Prof. Jin Xie. His guidance, inspiration, passion, and patience have led me to manage my research projects and conduct experiments like a scientist. Thanks him for being so kind and supportive to me all the time.

Thanks all members in the Xie research group: Dr. Zipeng Zhen, Dr. Hongmin Chen, Dr. Trever Todd, Taku Cowger, Bryan Zhang, Shiyi Zhou, Jeff Wang, Dr. Anil Kumar, Daye Lee, and Benjamin Cline. It has been great to work as a team with you guys and to support each other. I really learned a lot from each of you. I would like to especially thank Dr. Zipeng Zhen, who taught me all the biological operations and techniques, gave me constructive advices, and provided me the greatest help in my experiments.

Thanks my committee members: Professor Jason Locklin, Professor Sergiy Minko, and Professor Marcus Lay. Your scientific guidance and suggestions have been helped me a lot to accomplish this dissertation.

Thanks our collaborators: Dr. Xiaoyuan Chen from NIH, Professor Zibo Li from UNC Chapel Hill, Professor Gang Liu from Xiamen University, and Professor Qun Zhao and Professor Lianchun Wang from UGA. Your efforts and help laid the ground of much work in this dissertation.

Thanks the department staff: Kristie Huff, Lauren Hutchison, Lauren Bowman, and Kistie Manders. You are always available whenever I need help.

Thanks my friends here at Athens, GA. Your help and accompaniments have made my life easier and full of joy during the past five years. And also thanks my old friends in China and United States: Tang Tang, Fang Xu, Shishi Jiang, Shiliang Zhou, Dingli Wang, Yujun Zhou, Minzhi Deng, Xi Peng, Jianjun He, and Youlong Zhu. I know you will always be there whenever I need you. Your accompaniments in my vacations and the ACS meetings have made my life more colorful.

Finally, I would like to thank my mom and dad for providing me the everlasting love and encouragement. You always give me the strongest support and help me to keep in positive and optimistic when I got stuck in research. Thanks my grandpa and grandma for believing in me and being proud of me all the time. Thanks my fiance, Yijie Chen, who has always been on my side. All the love, faith, care, help, and patience you have given to me are extremely important. I could not have accomplished my dissertation work without your support.

TABLE OF CONTENTS

LIST OF TABLES

Page

LIST OF FIGURES

Page

CHAPTER 1

FERRITIN-BASED NANOPLATFORMS FOR BIONANOTECHNOLOGY

1.1 Introduction

Nanoscaled biomolecules such as nucleic acids, carbohydrates, proteins, peptides, and lipids, play an important role during the course of life evolution. In recent years, naturally occurring nanostructures in biology have become a source of inspiration for new nanotechnological designs and are developed for bionantechnological applications in medicine, materials science, and civil engineering.[1-4] In particular, protein-based nanocages, such as ferritins, heat shock proteins (Hsp), DNA-binding proteins from starved cells (Dps), and the cowpea chlorotic mottle virus (CCMV), are being widely investigated since they are monodisperse, robust, well-defined, and amenable to functionalities. Their surfaces allow for a convenient functionalization, and their interior cavities are ideal biotemplates for inorganic nanoparticle synthesis and drug loading.[5-7]

Ferritin is ubiquitous in nature and has been intensively studied in bionantechnological applications. Nearly 3000 published patents mention applications of ferritin in nanotechnology, 100 of which specifically focus on bionantechnology.[8] In this review, we summarized recent progress in applications of ferritin-based nanoplatforms in bionantechnology, such as biomedicine, biosensors, and bioassays.

1.2 Ferritin Protein: Structure and Function

Ferritin is a major iron storage protein that can be found in most living organisms, including humans.[9] It was first isolated from horse spleen in 1937 by Czech biologist Vilem Laufberger.[10] However, it was not until 1991 that the crystal structure of ferritin was elucidated.[11] Since then, ferritin has been well characterized. The properties of ferritins in animals, bacteria, and plants have been the topic of many reviews and of a full issue of *Biochimica Biophysica Acta* (*1800, 8,* **2010**).

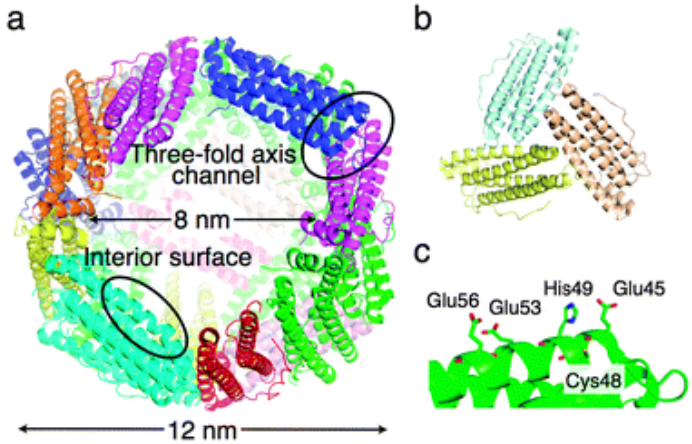

Figure 1.1 Ferritin Structure. (a) Whole structure of apoferritin, (b) The three-fold axis channel, and (c) Metal accumulation center.[12]

Ferritin is a 450 kDa hollow nanocage, which is capable of accommodating up to 4500 iron atoms. It is composed of 24 subunits, which self-assemble to a roughly rhombic dodecahedron shape (space group F432) with inner and outer diameters of ~ 8 and ~12 nm, respectively.[13] Two genetically and functionally distinct ferritin subunits exist: heavy chain ferritin (H-ferritin) and light chain ferritin (L-ferritin).[14,15] In humans, the two subunits share around 55% of the amino acid sequence and have molecule weights of about 21 KDa and 19 KDa, respectively.[14,15] H-ferritin mainly functionalizes as the catalytic ferroxidase center,[16-18] while L-ferritin mainly serves as the iron nucleation site in the protein cavity.[16,19] The ratio of the

subunits differs among organisms, reflecting different functions in different tissues: fast iron metabolism or long-term iron storage. For example, in humans, H-ferritin predominates in the heart, whereas L-ferritin predominates in the liver.[20] In addition, the ratio can be altered in inflammation and other pathological conditions.

Each ferritin subunit is composed of a four-helix bundle and a fifth short helix at the C terminus.[11] In its assembled form, there are a large number of salt bridges and hydrogen bonds formed between subunits, possessing ferritin with unique physical and chemical properties, such as high stability in high temperatures (> 80 ℃) and in various denaturants (e.g., urea or guanidinium chloride).[21] On the surface of the ferritin shell, there are eight hydrophilic funnel-like channels at the three-fold axis and six hydrophobic channels at the four-fold axis. Both channels have a diameter of approximately 0.4 nm.[22] It has been proposed that iron entry occurs through the three-axis channels in nature, with guidance from the electrostatic field gradient.[23,24] Similar transportation mechanisms apply to the entry of other metal species, such as ferrioxamine B.[9] Despite the rigidness under physiological environments, ferritin nanocages can be broken into subunits when the pH drops to 2. When the pH returns to neutral, these subunits can be reassembled to an almost intact cage structure.[25] During this reversible, pH-mediated disassemble-reassemble process, nanoparticles, bulk solution, and dissolved molecules can be entrapped in the interior. This provides an alternative strategy to encapsulate materials into the ferritin cavity, especially for materials that could not pass the channels on the protein shell.

Ferritin can also be easily modified to integrate functionalities onto the surface, either genetically or chemically. Peptides, antibody fragments, dye molecules, and quencher molecules have been successfully conjugated onto the ferritin surface by chemical methods. Moreover, motifs can be precisely introduced into the ferritin shell via genetic modification of the ferritin

sequence. The functional protein surface in combination with the nanoparticles encapsulated in the cavity, make ferritin a powerful platform for a wide range of bionanotechnology applications.

1.3 The Ferritin Protein Shell as a Multivalent Scaffold

1.3.1 Chemically

Several chemical methods can be used for selective modification of certain amino acids (**Figure 1.2**). The reactive groups such as amine, carboxyl, and thiol, are the most targeted. Wetz and Crichton reported that in apoferritin, 1.0 ± 0.1 cysteine residues, 4.4 ± 0.4 lysine residues, and 11.0 ± 0.4 carboxyl groups per subunit can be modified, while the corresponding values for native ferritin are 3 ± 0.3 lysine residues and 7.1 ± 0.7 carboxyl groups per subunit.[26] They also demonstrated that apoferritin with all 11 carboxyl groups blocked with glycineamide failed to reassemble to a cage-like structure and lost the catalytic properties of the protein. In contrast, the modification of one cysteine residue per subunit, of 3 or 4 lysine residues per subunit, or of 7 carboxyl groups per subunit has no effect on the catalytic activity of apoferritin.[26] These functional groups have been employed to chemically attached tumor targeting ligand, dyes, quencher molecules, polymerization initiators, and polyethylene glycol (PEG) molecules.[27-29]

The Wang research group has evaluated the reactivity and accessibility of the lysine residues of horse spleen apoferritin by matrix-assisted laserdesorption/ionization time-of-flight (MALDI-TOF) mass spectrometry in combination of trypsin/V8 digestion.[30,31] The conventional N-hydroxysuccinimde (NHS)-mediated amidation reaction was employed for chemical modification of the lysine group. For small reagents, up to four alkyne moieties could be conjugated to each subunit, and the reactive lysine residues was identified to be K97, K83, K104, K67, and K143. Larger reagents like 5-carboxyfluorescein NHS (FL-NHS) ester react only with

K97, K83, and K143, but not K104 and K67. The fluorescence signal analysis indicated that only one FL-NHS per apoferritins subunit could be conjugated, which may due to the relatively higher steric hindrance from FL. The click-reaction between alkyne-functionalized ferritin and an azide-bearing coumarin-derivative showed good consistence with the conclusion, with about one coumarin-triazole per ferritin subunit in the final product.[31] The Wang group also functionalized the protein shell with bromo-isobutyl NHS ester. The resulting derivatized ferritin could be used as a macro-initiator for atom transfer radical polymerization (ATRP) reaction.[31] Emrick and coworkers expanded this method to preparation of ferritin-polymer conjugates. They grafted poly(methacryloyloxyethyl phosphorylcholine) (polyMPC) and poly(PEG methacrylate) (polyPEGMA) chains onto the ferritin nanocages by ATRP, in which the molecular weight of the polymer grafts was controlled by the monomer-to-initiator feed ratio (**Figure 1.3**).[32] The resultant ferritin-polymer conjugates showed a suppressed inclusion into diblock copolymer films comparing to native ferritin, suggesting the polymer coating could mask the ferritin nanocages from antibody recognition. In addition, the Boker group developed a hydrogel consisting of ferritin-poly(N -isopropyl acrylamide) (ferritin-PNIPAAm) conjugates by ATRP in water at low temperatures, which allows the formation of thermoresponsive nanocapsules for controlled drug release.[33] Besides, we have used the NHS-mediated amidation reaction for dye labelling and biotinylation of the ferritin nanocages.[34-36]

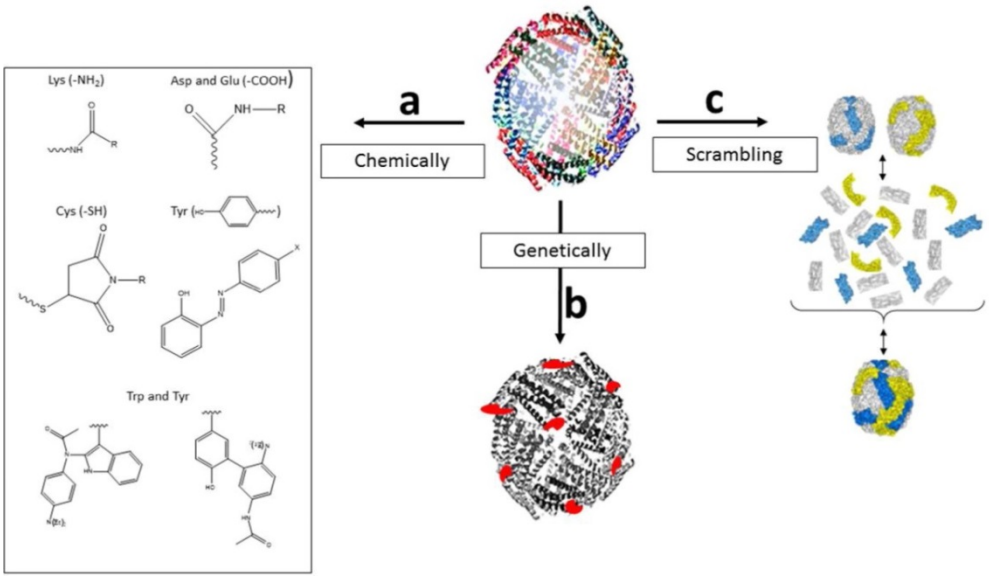

Figure 1.2 Surface Modification of Ferritin. Ferritin can be modified via chemistry (a) or using genetic (b) modification. Ferritins having different modifications can also be easily combined because of the reversible disassembly/reassembly process (c). This also allows for the preparation of more complex and multifunctional bionanoparticles.[1]

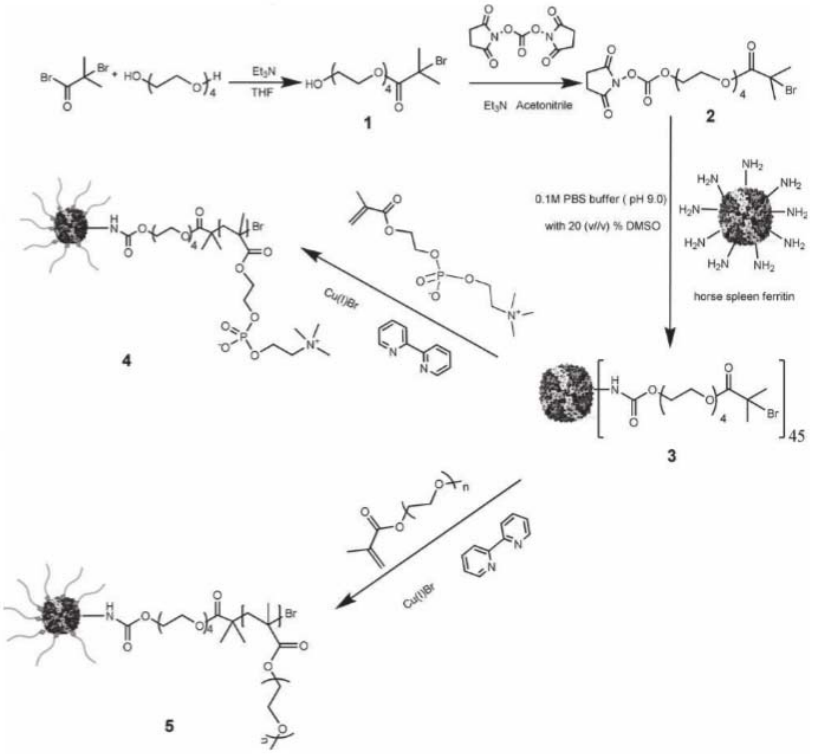

Figure 1.3 "Grafting-from" Chemistry on Ferritin by ATRP.[32]

The carboxyl moieties on the ferritin surface could also be activated by carbodiimide. The Mann group has derivateized the ferritin shell with long alkyl chains and successfully developed organic-soluble "hydrophobic ferritin".[37,38] After carbodiimide activation of the surface carboxyl groups, ferritin could be efficiently conjugated with long chain (C_9, C_{12}, C_{14}) primary alkyl amines in water/THF, water/methanol, or water/ethanol mixtures (1:1 V/V). In the case of C_9-ferritin, there was an estimation of around 400 covalently bound nonylamine molecules per ferritin nanocages. These hydrophobic ferritins could be extracted into dichloromethane, ethyl acetate and toluene from THF/water mixtures by adding of small amounts of NaCl, and could be back-extracted into water by adding of a large amount of water. TEM images demonstrated intact, non-aggregated protein macromolecules in the organic solvents. The transfer/back-transfer could be monitored by the color changes of the phase containing the orang-brown ferritin nanoparticles.

In other studies, the thiol groups exposed on the ferritin surface have been activated with maleimide groups. For example, the Ceci group [39] used an NHS-PEG-MAL linker to conjugate anti-Chondroitin Sulphate Proteoglycan 4 (CSPG4) monoclonal antibodies (mAbs) onto the ferritin surface. The resulting ferritin nanocages specifically bind to a $CSPG4^+$ melanoma cell line for selective drug delivery. In an earlier study, the Nagayama group investigated the site-specific reactivities of cysteine 52 (C52, located on the inner ferritin surface) and cysteine 130 (C130, located at the 3-fold channels of the shell) in horse L-apoferritin.[40] They found that 7-fluoro-4-sulfamoyl-2,1,3-benzoxadiazole (ABD-F) selectively reacted with C52, while p-chloromercuribenzoic acid (PCMB) reacted only with C130. N-(9-acridinyl) maleimide (NAM), and 4-male-imido-2,2,6,6-tetramethylpiperidine-N-oxyl (NEM-TEMPO) reacted with both C52 and C130.

1.3.2 Genetically

Ferritins can also be conveniently functionalized with ultimate precision via genetic engineering. Targeting moieties, such as RGD peptide,[28] anti-melanocyte stimulating hormone peptide,[41] and extracellular domain of myelin oligodendrocyte glycoprotein (MOG),[42] have been fused at the N-terminal, uniformly and precisely presenting 24 targeting domains on each ferritin subunit. Recently, Lee et al. simultaneously displayed four functional peptides on the ferritin surface by N-terminal cloning: an enzymatically cleaved peptide (ECP) to release siRNA, a cationic peptide (CAP) to capture siRNA, a tumor cell penetrating peptide (CPP), and a tumor cell targeting peptide (CTP).[43] Alternatively, peptides can be fused with ferritin subunit at the C-terminal. For example, Han et al. added SIINFEKL or ISQAVHAAHAEINEAGR peptide to the C-terminus of ferritin for the development of dendritic cell-based vaccines.[44] In addition, the N-terminus and C-terminus can be simultaneously modified for dual functionalities. Recently, Kim et al. developed double chambered ferritin nanocages by loading the tumor-targeting proapoptotic peptide $CGKRK(KLAKLAK)_2$ onto the N-terminal and green fluorescent protein (GFP) onto the C-terminal.[45]

1.3.3 Scrambling

The pH-dependent disassembly and reassembly of ferritin nanocages provides a facile and unique method to construct hybrid ferritin. For example, Lin et al. used this method to prepare hybrid ferritins that presenting both RGD4C, a tumor targeting ligand, and Cy5.5, a near-infrared dye (**Figure 1.4**).[28] In brief, they prepared two sets of H-ferritins. One group was chemically coupled with Cy5.5, and the other was genetically modified with RGD4C peptide. Both the Cy5.5 conjugation and the RGD4C peptide introduction were carefully controlled to achieve one functional molecule per ferritin subunit. Next, these two types of ferritins were mixed and broken

down into discrete subunits in an acidic environment (pH = 2). Then, the pH was adjusted back to 7.4 to reconstitute the ferritin subunits into hybrid nanostructures. The composition of the hybrid ferritin could be tuned by adjusting the initial ratios between RGD4C and Cy5.5 presenting ferritin, which was confirmed by the size exclusion chromatography analysis. Lin et. al. also used this method to prepare hybrid ferritin with Cy5.5-*Gly-Pro-Leu-Gly-Val-Arg-Gly* and black hole quencher-3 (BHQ-3) for active tumor imaging.[27] This work will be discussed in details in Section 1.5.2.

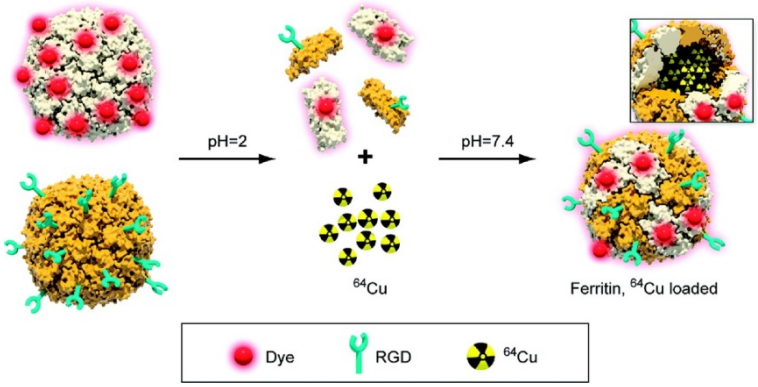

Figure 1.4 Chimeric Ferritin Nanocages. Schematic illustration of the process of triple-loading. First, RGD4C and Cy5.5 were introduced onto the surfaces of two sets of ferritins, via genetic and chemical means. These two ferritins were then mixed and broken down into subunits at pH = 2 and incubated with $^{64}CuCl_2$ to achieve radiolabeling. The pH was then adjusted back to 7.4 to facilitate the reformation of nanostructures. The reconstituted chimeric ferritin nanocages have both RGD4C and Cy5.5 on their surfaces and ^{64}Cu loaded in their cavities.[28]

1.4 The Ferritin Protein Core as a Mineralization Template

In nature, the iron oxide mineralization process can be summarized by a series of reactions:

$$P + 2Fe^{2+} \rightarrow P[Fe_2]^{4+}$$

$$P[Fe_2]^{4+} + O_2 \rightarrow P[Fe_2O_2]^{4+}$$

$$P[Fe_2O_2]^{4+} \rightarrow P[Fe_2^{6+}O_2^{2-}]^{4+}$$

$$P[Fe_2^{6+}O_2^{2-}]^{4+} + H_2O \rightarrow P[Fe_2O]^{4+} + H_2O_2$$

$$P[Fe_2O]^{4+} + H_2O \rightarrow P + 2Fe(O)OH + 2H^+$$

In the above reactions, "P" stands for a vacant ferroxidase site. Ferritin recognizes and binds two Fe^{2+} ions in the ferroxidase center, where Fe^{2+} is oxidized to Fe^{3+} by oxygen molecules.[46] The oxidized Fe^{3+} ions transfer to the central cavity and bind to the nucleation sites for mineralization.[47] The negatively charged pores at the three-fold axis on the protein shell allow the entry and exit of cations during mineralization and demineralization.[23,24] These channels can also work as a pathway for a variety of metal ions. The ferritin nanocages allow chemical synthesis to happen in size-confined reactors with homogenous atomic composition and render the synthesized cores water-solublility and biocompatibility. Bulky molecules, on the other hand, can be incorporated into the cavity via the pH-dependent disassembly/reassembly process for further biomineralization (**Figure 1.5**). Benefiting from the channels on the protein surface and the reversible disassembly/reassembly property of the protein nanostructure, a wide range of non-physiological metals and metal complexes has been encapsulated into ferritin nanocages (**Table 1**) for different applications. The inclusion approaches of these functional systems will be discussed in this section.

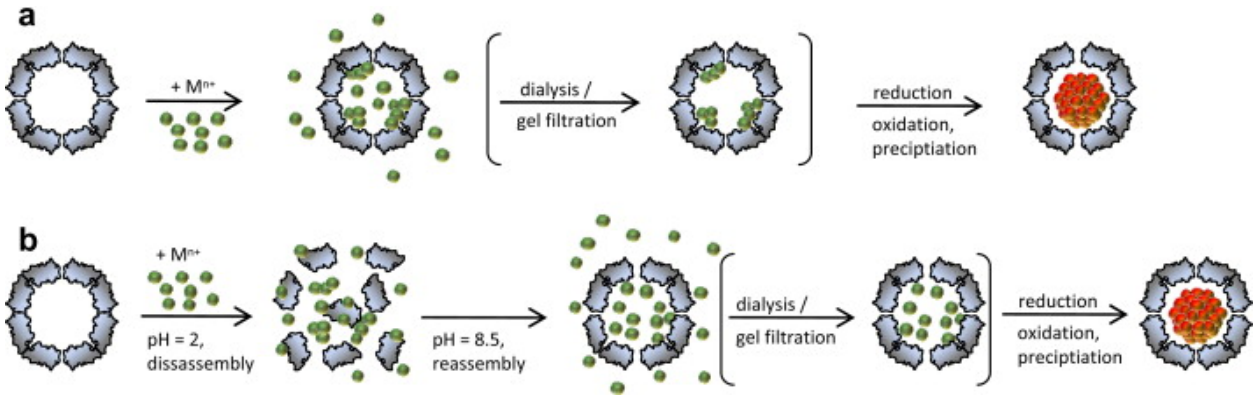

Figure 1.5 Ferritin for the Template Synthesis of Inorganic Nanoparticles. (a) Ferritin as nanoreactor. (b) Synthesis of nanoparticles by the disassembly/reassembly route. Removal of excess salt by dialysis or gel filtration is optional as the ferritin cavity provides for some reactions a specific reaction environment over the surrounding.[48]

Metal nanoparticles or metal alloy nanoparticles are widely exploited for their applications in catalysis, magnetism, and *in vivo* diagnosis. In general, metals inside the ferritin template are obtained by incubation of apoferritins with metal cations or metal complex ions, followed by reduction with $NaBH_4$. For example, Pd(0) nanoclusters were in situ synthesized in the apoferrtin by Ueno et al. for the catalytic hydrogenation of olefins in aqueous medium.[49] The successfully in situ synthesis of Pd nanoclusters was demonstrated by FPLC, TEM, and native SDS-PAGE analyses. Similarly, Pd/Au alloy nanoparticles or Au@Pd core-shell nanoparticles were prepared by a co-reduction or sequential reduction in the ferritin cavity (**Figure 1.6**), achieving an improved catalytic reactivity of olefin hydrogenation compared to Pd(0) nanoparticles in the cage.[50] Silver nanoparticles could also be prepared by incubation with $AgNO_3$, followed by the reduction with $NaBH_4$.[51] The excess silver ions were removed before adding reduction agent. The size of the Ag nanoparticles can be tuned by adjusting the initial amount of Ag^+ ions. For instance, the initial Ag^+-to-ferritin molar ratio of 500:1 and 5000:1 yielded the Ag nanoparticles at 1 nm and 4 nm, respectively. The HRTEM images indicated that some of the synthesized Ag nanoparticles were single domain fcc crystals. An alternative way for Ag nanoparticle preparation was to design chimeric ferritin cages with specific silver-binding peptides, which work as templates to reduce silver ions to metallic silver. Kramer et al. inserted an Asn-Pro-Ser-Ser-Leu-Phe-Arg-Tyr-Leu-Pro-Ser-Asp (AG4) peptide to the C-terminal of the L-ferritin and expressed the protein in *E.Coli*.[6] The resulting chimeric ferritins (10 mg/mL) were incubated with silver nitrate solution (0.4 nM) at 37 ˚C for 3 h in either 50 mM phosphate buffer (pH = 7.5) or 50 mM Tris-Cl buffer(pH = 8.0), yielding monocrystalline pure silver particles with an average diameter of 5 nm in the protein cavities.

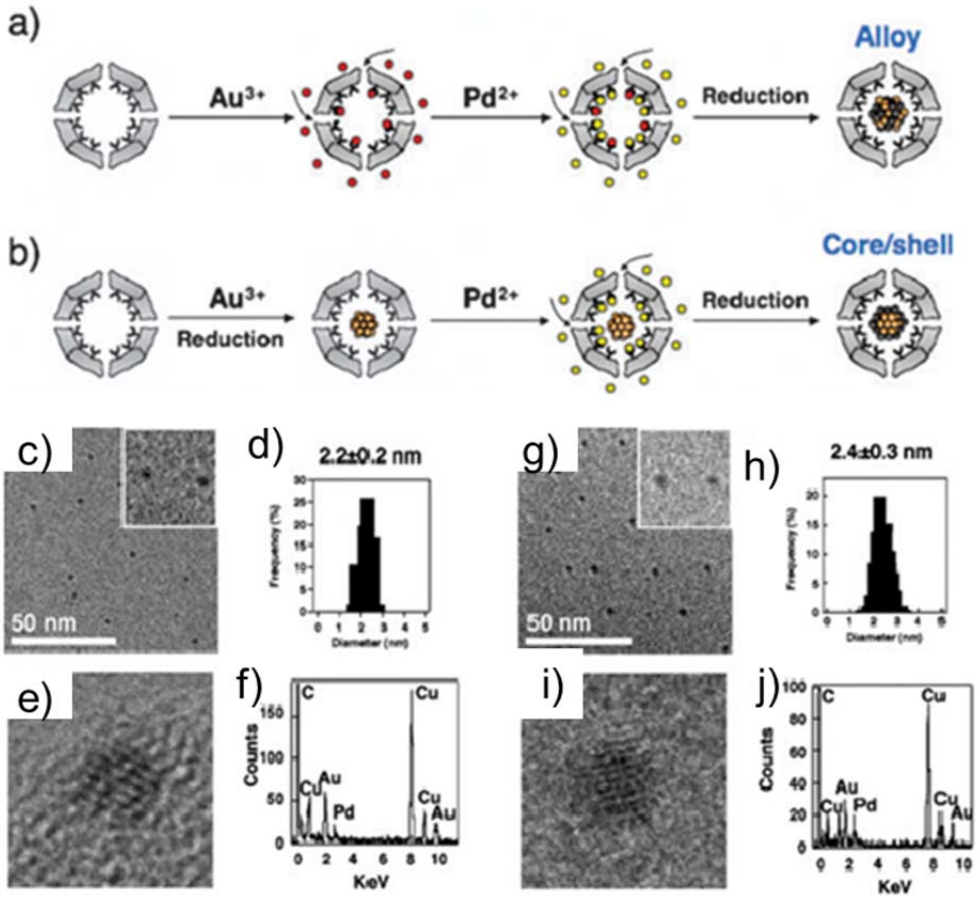

Figure 1.6 Au/Pd Bimetallic Nanoparticles in Apo-Ferritin. (a)-(b) Schematic of synthesis of Au/Pd alloy (a) and Au@Pd (b) in apoferritin. Au^{3+}, Au^{0}, Pd^{2+} and Pd^{0} atoms are colored red, orange, yellow and brown, respectively. (c)-(j) TEM, DLS, HRTEM, EDX characterization of Au/Pd alloy (c-f) and Au@Pd (g-j).[50]

Metal oxides are also of special interests due to their useful properties, such as magnetic or luminescence. Typically, they were synthesized by incubation of ferritin with metal ions, followed by oxidization with air or H_2O_2. The Douglas group used this method to fabricate ferritin iron oxide nano-composite magnetic resonance contrast agents.[52] In brief, $(NH_4)_2FeSO_4 \cdot 6H_2O$ (iron source) and H_2O_2 (oxidant) were continuously and slowly added to ferritin solution at pH 8.5 and 65 ˚C under a N_2 atmosphere. The amount of iron atom and the size of the iron oxide nanoparticles inside the ferritin nanocages were determined by the initial amount of $(NH_4)_2FeSO_4 \cdot 6H_2O$. Ferrtin encapsulated with 1000, 3000, or 5000 Fe atoms per cage

was obtained, corresponding to a size of 3.6 ± 0.7, 5.1 ± 0.9, or 5.9 ± 0.9 nm. Although the nanoparticle could not be unambiguously identified as maghemite (γ-Fe_2O_3) or magnetite (Fe_3O_4), an obvious size dependent T_2-shortening effect was observed in the MRI phantom tests. Manganese oxide cores were obtained by incubating $MnCl_2$ solution at pH 8.0 - 9.2 with air or H_2O_2 as oxidant, yielding crystalline γ-MnOOH, α-MnOOH, Mn_3O_4, or their mixtures.[53-57]

Ferritin-metal salt complexes, which represent an important type of ferritin mineralization, can be prepared by incubation of the metal ions and the anions with ferritin solutions. Mann and co-workers successfully prepared $CaCO_3$, $BaCO_3$, and $SrCO_3$ nanoparticles inside the ferritin cavity, with water-soluble polyelectrolytes added to prevent the cation precipitation.[58] The nanoparticles were carefully characterized by TEM and DLS, showing an average size of 5.1 – 5.4 nm. Another example is the synthesis of Prussian Blue particles inside the ferritin cavity. The pH-dependent disassembly/reassembly strategy was employed by Dominguez-Vera et al. to encapsulate bulky ionic complexes inside the ferritin cavity (**Figure 1.7**).[59] The ferritin nanocages were first dissociated into 24 subunits at pH 2.0 in the presence of the hexacyanoferrate(III) ions to be trapped. After reconstitution and extensive dialysis at pH 8.5, the resulting ferritin-hexacyanoferrate(III) nanocages were reacted with Fe(II) to form the Prussian Blue complexes inside the ferritin cavity. TEM and EDX analyses indicated discrete spherical particles with iron presenting. The UV-vis and IR spectrum showed the feature charge-transfer band of the C-N stretching mode in the Fe(II)-CN-Fe(III) fragment, suggesting successful preparation of ferritin-Prussian Blue nanocomposite.

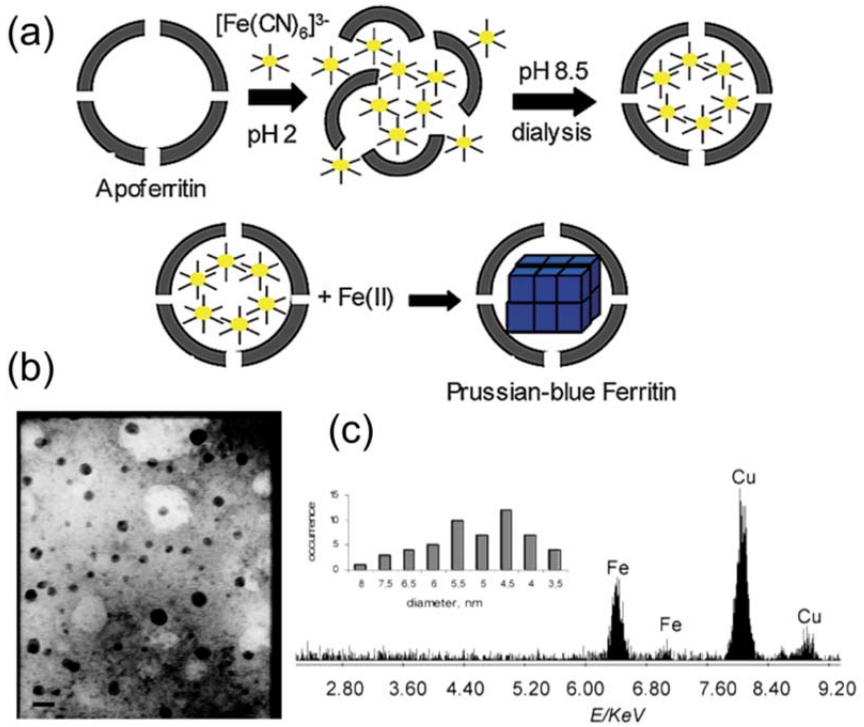

Figure 1.7 Prussian Blue-Ferritin Nanoparticles. (a) Schematic Representation of the pH-Induced Dissociation−Re-formation Process of Apoferritin in the Presence of Hexacyanoferrate(III) and the Subsequent Reaction with Iron(II) Giving Rise to Prussian Blue (PB) Complex within the Apoferritin Cavity. (b) TEM image of PB nanoparticles (scale bar 10 nm). (c) Particle size distribution for PB nanoparticles formed inside the apoferritin cavity and EDXA spectrum of the nanoparticles showing the presence of iron corresponding to PB. Copper peaks are due to the sample grid.[59]

In addition, ferritins can also work as nanoreactors for semiconductor nanoparticles. These size-confined semiconductor nanoparticles are promising materials for quantum dots and fluorescence labelling. Although the reaction between the oppositely charged ions (e.g. Cd^{2+} and S^{2-}) is very quick and often induces unintended aggregation, Yamashita et al. successfully synthesized CdSe nanoparticles by using a slow reaction system.[60] In the reaction, $Cd(NH_3)_4^{2+}$ was used as a stable Cd source and selenourea was used for continuous and slow release of Se^{2-} ions. XPS analysis confirmed the core composition of Cd and Se. XRD on heat-annealed (500 ˚C) samples suggested the core structure was predominantly the cubic phase. TEM and DLS indicated a narrow size distribution and an average size of 6 nm of the CdSe nanoparticles. Later,

the same group optimized the experimental conditions of the slow reaction system. The highest core formation ratio (CFR) of 75 % was achieved under the following conditions: 5 mM of pH 9.5 ammonia water, deoxygenation by N_2 gas bubbling.[61] A similar synthesis approach of ferritn-CdSe was reported by Xing et al, in which ethylenediaminetetraacetic acid disodium salt (EDTA) was added to stabilize Cd^{2+} and NaHSe was used for Se^{2-} supply.[62] In addition, this slow chemical reaction protocol was successfully applied to other semiconductor nanoparticles, such as ZnSe, CdS, CuS, and PbS.[63-66]

Table 1.1 Materials Synthesized Inside Ferritin[a]

Core composition	reactants	Particle-forming chemical	Metals/ferritin[b]	Ref
		Metals		
Ag	$AgNO_3$	$NaBH_4$	380	51,67
Ag	$AgNO_3$	AG4 peptide (-Asn-Pro-Ser-Ser-leu-Phe-Arg-Tyr-Leu-Pro-Ser-Asp-)		6
Ag/Au	$AgNO_3$/ $HAuCl_4$	$NaBH_4$		68
Au	Au NPs	Gold binding peptide: MHGKTQATSGTIQS/reassembly		69
Au	$HAuCl_4$	$NaBH_4$ or 3-(Nmorpholino)propanesulfonic acid (MOPS)		70
Au	$HAuCl_4$	(1) $NaBH_4$; (2) ascorbic acid		71
Au/Pd alloy, Au@Pd	$KAuCl_4$/$KPdCl_4$	$NaBH_4$		50
Co	Co^{2+}	$NaBH_4$		72
CoPt	$Co(NO_3)_2$•$6H_2O$/ K_2PtCl_4	$NaBH_4$		53
Cu	$CuSO_4$	$NaBH_4$	225 - 2000	73,74
FePt	$(NH_4)_2Fe(SO_4)_2$/ K_2PtCl_4	$NaBH_4$		53
Ni	Ni^{2+}	$NaBH_4$		72
Pd	K_2PdCl_4	$NaBH_4$	~ 500	49,75
Pt	K_2PtCl_4	$NaBH_4$	250 - 1000	76,77
		Metal Oxide-Derivations		
Cd_2O_3	$Cd(NO_3)_3$•$6H_2O$	EDTA	1700	78
CeO_2	$CeCl_3$•$7H_2O$	air		79
CoOOH	Co^{2+}	H_2O_2	2250	57,80
CrOOH	$(NH_4)_2Cr(SO_4)_2$	CO_2	4500	81
Cu(0)-FeOOH	$CuSO_4$•$5H_2O$/$(NH_4)_2Fe(SO_4)_2$	Sodium citrate or potassium sodium tartrate/UV	2000 Cu/ 1000 Fe	82
EuOOH	Eu^{3+}-citrate	O_2/light	1000	83
FeOOH	$(NH_4)_2Fe(SO_4)_2$	air	~ 4500	84,85

FeOOH	Fe^{3+}-citrate	O_2/light	1000	83
α-Fe_2O_3	$(NH_4)_2Fe(SO_4)_2$	sodium oxalate, 97 ℃	1000	86
γ-Fe_2O_3	$(NH_4)_2Fe(SO_4)_2$	H_2O_2, 65℃	2000 - 5000	53,87
Fe_3O_4	$(NH_4)_2Fe(SO_4)_2$	H_2O_2	3000	52
Fe_3O_4	$(NH_4)_2Fe(SO_4)_2$	air, 600 ℃	3000	84
Fe_3O_4-γ-Fe_2O_3	$(NH_4)_2Fe(SO_4)_2$	Me_3NO, N_2, pH= 8.6, 65℃	3150	86
MnOOH	$MnCl_2$	Air	3000	54-57
Mn_3O_4	$MnCl_2$	H_2O_2	1000	53
NiOOH	Ni^{2+}	CO_2; Na_2CO_3	8000	81
$TiO(OH)_2$	Ti^{4+}-citrate	O_2/light	1000	83
UOOH	$UO_2(OAc)_2$	air	800	56
		Salts		
$Cd_3(PO_4)_2$	$CdCl_2$/PBS			88
$Cd_3(PO_4)_2$	$Cd(NO_3)_2$/PBS			89
$LuPO_4$	$LuCl_3$/PBS		500	90
$PbPO_4$	$Pb(NO_3)_3$/PBS			88,89
UPO_4	$U(OAc)_2$/PBS			91
$Zn_3(PO_4)_2$	$Zn(NO_3)_2$/PBS			88
$Fe_3(PO_4)_2$	$FeSO_4$ or $FeCl_2$/H_3PO_4	air	~ 2000	92
$Fe_3(AsO_4)_2$	$FeSO_4$ or $FeCl_2$/H_3AsO_4	air	~ 2000	92
$Fe(MoO_2)$	$FeSO_4$ or $FeCl_2$/H_2MoO_2	air	~ 2000	92
$Fe_3(VO_4)_2$	$FeSO_4$ or $FeCl_2$/H_3VO_4	air	~ 2000	92
$BaCO_3$	$BaCl_2$/Na_2CO_3	PMMA-mediated	~ 1600	58
$CaCO_3$	$CaCl_2$/Na_2CO_3	PMMA-mediated	~ 1600	58
$SrCO_3$	$SrCl_2$/Na_2CO_3	PMMA-mediated	~ 1600	58
CuFe Prussian Blue	$CuSO_4$/$[Fe(CN)_6]^{3-}$	urea		74
Prussian Blue	$[Fe(CN)_6]^{3-}$/Fe^{2+}			59
		Semiconductors		
Au_2S	$KAuCl_4$/thiourea		3000	93
CdS	$Cd(OAc)_2$/Na_2S		275	66
CdS	$Cd(OAc)_2$/thioacetic acid	ammonia solution		94
CdSe	$CdCl_2$/NaHSe	EDTA		62
CdSe	$CdCl_2$/selenourea	ammonia solution	1000	60
CuS	$Cu(OAc)_2$/thioacetic acid			64
FeS	$(NH_4)_2Fe(SO_4)_2$/ Na_2S	(1) air	3000	95
FeS	(1) $Fe(NO_3)_3$; (2) H_2S		3000	96
PbS	$Pb(OAc)_2 \cdot 3H_2O$/Na_2S	dithioglycerol (DTG)		97
ZnSe	$Zn(OAc)_2$/selenourea	ammonium acetate	1500	65

[a] Table updated and modified from ref 1. [b] The value represents the maxim number of metals/ferritin reported in the literature.

Ferritin nanocages, with homogeneity in size and versatility to encapsulate functionalities, are ideal building blocks for the fabrication of two-dimensional arrays of protein cage-templated nanoparticles by bottom-up approach. After elimination of the protein moiety, the well-ordered two-dimensional crystalline nanoparticle arrays can be widely applied in areas such as nanoelectronics. Two major approaches have been employed to make two-dimensional ferritin arrays. One approach employs the electrostatical interactions between the protein cages and the substrate. For example, Yamashita et al. modified a specific area of the Si substrate with 3-Aminopropyl-triethoxysilane (APTES) pattern to make it positively charged. The ferritin exterior surface was negatively charged with a neutral pH, which could potentially be attracted by the APTES coating and be placed on the substrate one by one (**Figure 1.8**).[98] The other approach utilizes specific peptides filtered by phage display techniques, which can selectively bind to specific substrates. Kase et al. introduced a carboneous biding peptide (D-Y-F-S-S-P-Y-E-Q-L-F) on the ferritin surface. The recombinant ferritin was demonstrated not only to selectively adhere to carboneous materials on the substrate, but also to attract other recombinant ferritin through hydrophobic interactions.[99]

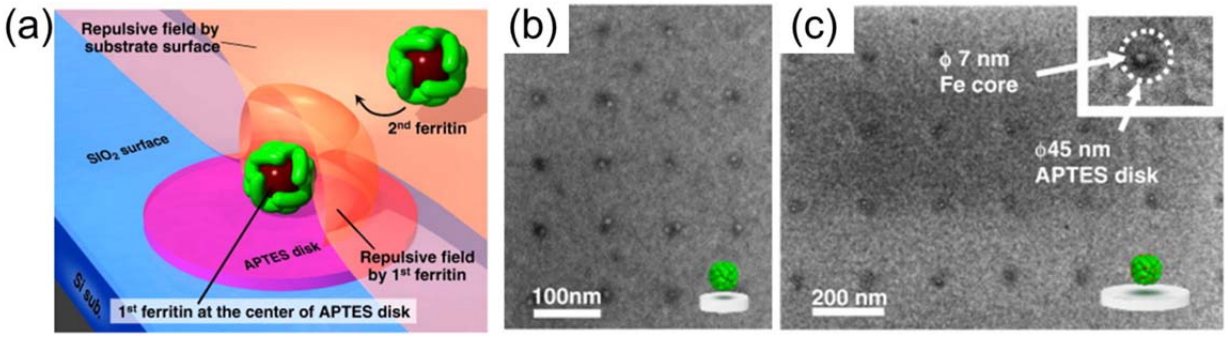

Figure 1.8 2D Ferritin Arrays. (a) A schematic drawing for single ferritin adsorption onto APTES disk. The second ferritin approaching the APTES disk is blocked by the repulsive field of the substrate surface and the first ferritin, which is located at the center of the disk. (b)&(c) SEM image of single ferritin placement. (b) Fer8S on 15 nm APTES disk. (c) Mutant ferritin on 45 nm APTES disk. Each APTES disk has one ferritin with Fe core.[98]

1.5 Application in Bionanotechnology

1.5.1 Tumor targeting

The first identified ferritin receptor was the murine T-cell Immunoglobulin and Mucin domain-2 (TIM-2),[100] which is overexpressed on splenic B cell and oligodendrocyts and shows specific affinity with H-ferritin but not L-ferritin.[100,101] After binding to TIM-2 on the cell surface, the H-ferritin is capable of being internalized into endosomes and lysosomes.[100] It was not until 2010 that a human ferritin receptor, transferrin receptor 1(TfR1), was identified by the Seaman Group through expression cloning.[102] Same to the TIM-2, the TfR1 has specific affinity to H-ferritin and the H-ferrtin-TfR1 complex can be internalized.[102] The TfR1 targeting strategy has been extensively investigated in tumor imaging and therapy. The Yan group has successfully developed a magnetoferritin nanoparticle for tumor visualization (**Figure 1.9**).[103] They examined the interactions between TfR1 and H-ferritin in more than 474 clinical tissue specimens and found that H-ferritin specifically interacts with nine types of tumor tissues, including breast, lung, liver, prostate, ovarian, cervical, colon, and thymus cancer tissues, but not binds to non-tumor tissues. The magnetoferritin nanoparticles have intrinsic peroxidase-like activity. They showed a blue color when reacting with 3,3',5,5'-Tetramethylbenzidine (TMB) or produced brown precipitate with 3,3'-Diaminobenzidine (DAB). Therefore, the magnetoferrtin can be used for visualizing tumors among healthy tissues. Recently, an L-ferritin receptor was identified—Scavenger Receptor Class A, Member 5 (SCARA-5), which is found in retina and macrophage.[104]

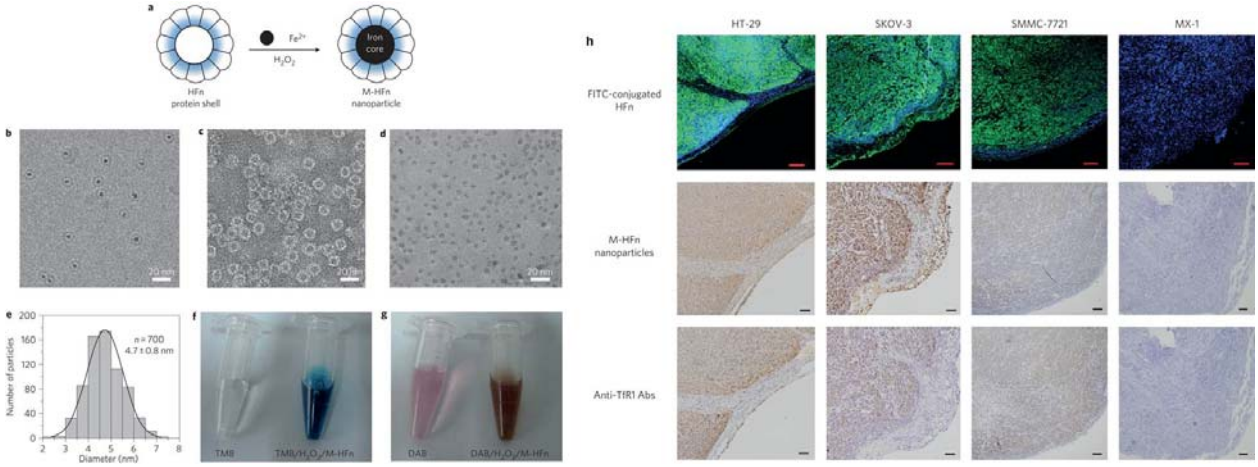

Figure 1.9 Tumor Targeting of H-Ferritin. (a) Schematic showing the preparation of magnetoferritin (M-HFn) nanoparticles and their structure. (b) CryoTEM image of M-HFn nanoparticles. (c)&(d) TEM images of HFn protein shells (c) and iron oxide cores (d). HFn protein shells were negatively stained with uranyl acetate for TEM observations and iron oxide cores in HFn were unstained. (e) Size distribution of iron oxide cores, with a median diameter of 4.7 ± 0.8 nm. (f)&(g) Characterization of peroxidase activity of M-HFn nanoparticles. M-HFn catalysed the oxidation of peroxidase substrates TMB (f) and DAB (g) in the presence of H_2O_2 to give a coloured product. (h) FITC-conjugated HFn-based fluorescence staining (top row), M-HFn nanoparticle-based peroxidase staining (middle row) and anti-TfR1 Abs-based immunohistochemical staining (bottom row) of paraffin-embedded HT-29 colon cancer, SKOV-3 ovarian cancer, SMMC-7721 liver cancer and MX-1 breast cancer xenograft tumours. TfR1-positive xenograft tumours showed strong positive staining for FITC-conjugated HFn (green fluorescence), M-HFn nanoparticles (brown) and anti-TfR1 Abs (brown), whereas TfR1-negative xenograft tumours showed no staining for FITC-conjugated HFn, M-HFn nanoparticles and anti-TfR1 Abs (scale bars, 100 μm). Abs, antibodies.[103]

In addition to the natural targeting of ferritin towards cancer cells, many research groups have modified the surface of the ferritin nanocages with a variety of targeting motifs, such as peptides, antibodies, antibody fragments, and targeting ligands to selectively navigate the nanocages to specific cancer cells. For example, our group has genetically fused an RGD4C peptide on the ferritin surfaces,[34,35] which specifically interacts with integrin $\alpha_v\beta_3$ that overexpressed by tumor endothelium cells and many types of cancer cells. We have chemically conjugated folic acid ligands on the ferritin surfaces.[105] The folic acid receptor is overexpressed in about 40% of human cancers and is able to mediate endocytosis of folic acid conjugated

tumors.[106] Besides, the α-melanocyte stimulating hormone (α-MSH) peptide was also expressed on the ferritin surfaces to target the receptors that overexpressed by melanoma cells.[107]

1.5.2 *In vivo* imaging

Ferritin can serve as a mineralization reactor for metals and metal complexes, and the protein shell can be engineered with probe molecules either chemically or genetically. All these features make ferritin an ideal platform for *in vivo* imaging. In particular, ferritin-based nanoplatforms have extensive applications in magnetic resonance imaging (MRI), optical imaging, positron emission tomography (PET) imaging, and photoacoustic imaging (PAI).

MRI is a powerful diagnostic technique with deep penetration, high sensitivity and resolution. A single crystal magnetite core (Fe_3O_4) was synthesized in the H-ferritin core, showing an r_2 relaxivity of 224 $mM^{-1}s^{-1}$.[108] When tested *in vivo* in MDA-MB-231 tumor bearing mice, the nanoparticles induced significant T_2 signal drop attributed to the TfR1-mediated tumor accumulation. T_1 contrast agents have also been produced using ferritin cavities as nanoreactors. Gd nanoparticles, with an average size of 5 nm, have been produced inside ferritins, showing a 10 or 70 times higher of the longitudinal or transverse relaxivity than clinically approved paramagnetic Gd-chelates.[109] Mn-based contrast agents have been prepared by partial reduction/dissolution of β-MnOOH inside the ferritin cavities, containing up to 300–400 Mn(II) ions per ferritin and exhibiting an r1 relaxivity of 4000 - 7000 $mM^{-1}s^{-1}$.[110]

Optical imaging, on the other hand, is mostly achieved by surface modification of the ferritin nanocages. We have chemically conjugated a near-infrared dye, IRDye800, onto the ferritins to monitor the *in vivo* migration of ferritin nanocages with a Maestro imaging system.[34,35] Very recently, Kim et. al. genetically fused green fluorescent protein (GFP) onto the C-terminal of ferritins to monitor the nanoparticle uptake by MDA-MB-231 cells.[45] Besides, Lin

et. al. developed a hybrid ferritin system as activatable probes for tumor imaging (**Figure 1.10**).[27] Specifically, they prepared a hybrid ferritin presenting both Cy5.5-tagged peptide (Cy5.5-Gly-Pro-Leu-Gly-Val-Arg-Gly-Cys) and black hole quencher-3 (BHQ-3) by the pH-dependent disassembly/reassembly strategy. The Gly-Pro-Leu-Gly-Val-Arg (PLGVR) is a known substrate for multiple types of matrix metalloproteinases (MMPs) and the BHQ-3 is a widely untilized quencher of Cy5.5. The hybrid ferritin was in a quenched state when both dyes and quenchers were presenting on the protein surface. However, when the probes were exposed to an MMP-rich environment, the PLGVR substrate would be cut off to release Cy5.5, resulting in restored fluorescence activity.[27]

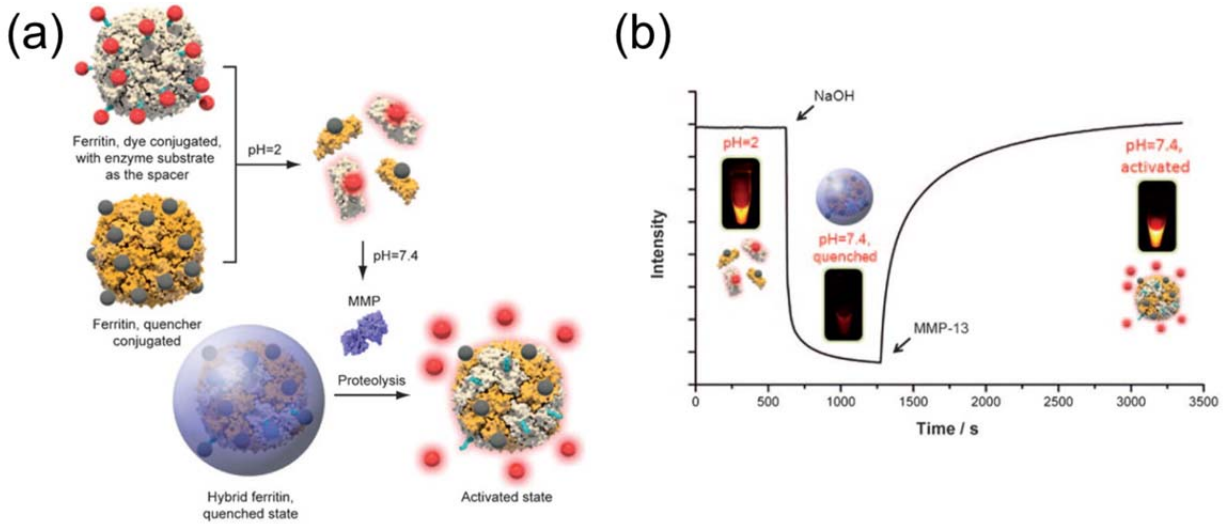

Figure 1.10 Ferritin Cage-Based Activatable Probes. (a) Schematic of the probe formation. (b) Fluorescence intensity change of hybrid ferritin (Cy5.5/BHQ-3 ratio =1:1) during the course of disassembly, reassembly, and activation.[27]

PET has been widely applied in clinical due to its non-invasive, sensitive, and quantitative properties.[111] PAI has high contrast and spatial resolution, holding great potential for animal or human organ imaging, especially for blood vessels.[112,113] Recently, Wang et. al. developed copper sulfide-ferritin nanocages for PET/PAI dual modality tumor imaging.[114]

Integration of PAI and PET offers high sensitivity and fine spatial resolution. The CuS–ferritin nanocages had higher tumor accumulation than free copper and exhibited superior improvements in real-time *in vivo* PAI and PET imaging of entire tumors. They have also used the CuS–Ferritin nanocages for photothermal therapy (PTT), which will be discussed in Section 1.5.5.

1.5.3 Drug delivery

The excellent biocompatibility, high stability, unique nanostructure, and facile surface modification make ferritins ideal nanoplatforms for drug delivery. Platinum anticancer drugs encapsulation was first reported by Yang et al. in 2007.[115] They encapsulated cisplatin (CDDP) and carboplatin (CBDCA) into H-ferritins in separate studies by both the pH-dependent disassembly/reassembly strategy and the diffusion strategy, yielding 15 platinum drug molecules per ferritin cage. Later, Falvo et al. coupled the cisplatin encapsulated ferritin with a monoclonal antibody (mAb)—Ep1, which specifically bind to the melanoma antigen CSPG4.[39] The resulting HFt-Pt-Ep1 showed enhanced efficacy of antiblastic therapy, especially for melanoma, which is totally refractory to chemotherapy in advanced stages. Non-metal containing drugs, although bearing limited interactions with the protein cages, have also been successfully loaded into the ferritin cavities. We developed a Cu-assisted method to improve the loading of doxorubicin.[34] RGD4C peptide was introduced onto ferritin surfaces (RFRTs) for tumor-targeting delivery. The doxorubicin can be loaded into the RFRTs (D-RFRTs) at a ratio as high as 73.49 wt%. And the loaded-DOX was slowly released from the RFRTs within 10 h in PBS at 37 ˚C. After FRT encapsulation, the DOX showed longer circulation half-lives, higher tumor accumulation, enhanced treatment efficacy, and less cardiotoxicity when tested on U87MG tumor model (**Figure 1.11**).[34] In addition, the Yan group loaded DOX into H-ferritin cages via the disassembly/reassembly strategy.[116] High loading efficiency was also achieved, with 33 DOX

molecules per ferritin cage. The H-ferritin-DOX complex specifically bounded to tumor cells via the overexpressed TfR1. It showed more than 10 times higher tumor accumulation than free DOX and significantly inhibited tumor growth after one single dose injection.[116]

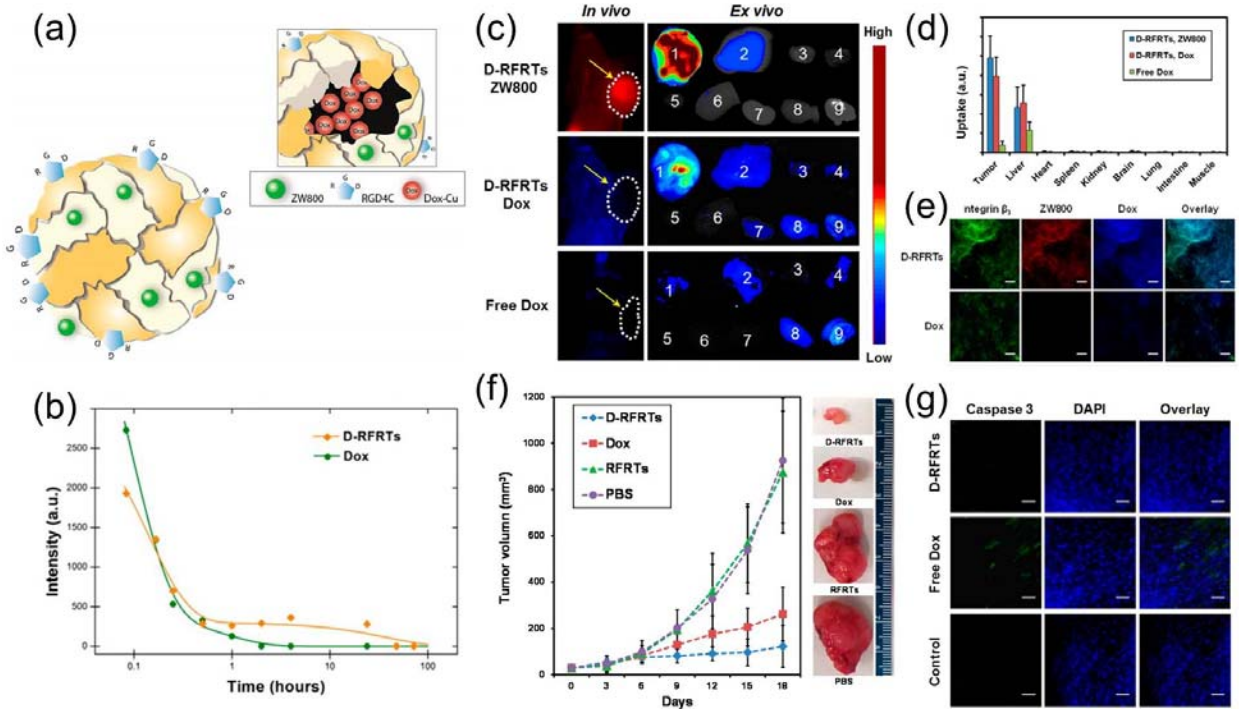

Figure 1.11 RGD-Modified Apoferritin Nanoparticles for Efficient Drug Delivery. (a) Schematic illustration of D-RFRTs. DOX was precomplexed with Cu, and then encapsulated into RFRTs. (b) Plasma DOX concentrations at different time points after iv injection of D-RFRTs or free DOX into healthy nude mice. (c) *In vivo* and *ex vivo* imaging results of U87MG tumor-bearing mice injected with ZW800-labeled D-RFRTs and free Dox. For *ex vivo* studies, the organs were arranged in the following order: 1, tumor; 2, liver; 3, lung; 4, muscle; 5, heart; 6, spleen; 7, kidneys; 8, brain; 9, intestine. (d) Column histograms of fluorescence activities in different organs obtained from the *ex vivo* imaging data. (e) Immunohistology results from tumor sections. Green, Cy5.5; red, ZW800; blue, Dox. Scale bar, 50 μm. (f) Therapy studies performed on U87MG tumor-bearing nude mice (n = 5/group). On day 18, significant difference in tumor growth was found between D-RFRT treated mice and those treated with PBS, RFRTs and free DOX ($P < 0.05$). Eighteen days after the onset of the treatment, a TGI rate of 89.6% was observed for D-RFRTs, in comparison to that of 74.0% for free DOX. (g) Immunofluorescence staining of caspase-3 for myocardium from D-RFRTs, free Dox and PBS treated mice. Blue, DAPI; green, caspase-3. Scale bar: 50 μm.[34]

Ferritin nanocages have been used for miRNA or siRNA delivery. As discussed in Section 1.3.2, Lee et. al. have recently developed a genetic variant of H-ferritin to mediated the targeted delivery and internalization of siRNA on the ferritin surface[43]. When tested in red fluorescent protein (RFP)-expression tumors cells, the functional H-ferritins significantly suppressed the RFP expression by delivery of siRNA with complementary sequence to RFP mRNA.[43]

Ferritin nanocages have also been used for delivery of radioisotopes for cancer treatment since they can reduce the toxicity and immune response from the heavy metals. For example, Lutetium-177 and Yttrium-90 had been incorporate in ferritin nanocages in the formation of phosphate salts, with a loading ratio of 500 lutetium or yttrium ions per ferritin, for radioimmunotherapy against cancer.[90,117] Uranium-235 had also been encapsulated in ferritin cages at a loading rate of 800 U atoms per ferritin for uranium neutron-capture therapy.[91]

1.5.4 Photodynamic therapy

Photodynamic therapy (PDT) is currently under intensive preclinical and clinical investigations for the treatment of many types of diseases, including cancer, age-related macular degeneration (AMD), localized infection, and non-malignant skin conditions.[118] PDT requires photosensitizers, light, and oxygen to active. When irradiated with light at specific wavelength, the photosensitizers can transfer energy to nearby oxygen, produce cytotoxic reactive oxygen species (ROSs) such as $^1O_2$, and kill cancer cells. However, most photosensitizers are hydrophobic and do not provide conjugation friendly functional groups, which are major barriers for selective delivery of photosensitizers to tumors. Ferritins can serve as safe and efficient photosensitizer carriers due to their excellent biocompatibility and facile surface modification.

Table 1.2 Ferritin Nanoplatforms for Cancer Theranostic

Core composition	Loading efficiency (per ferritin)	Surface modification	Targeting strategy	Application	Ref
Gd-HPDO3A	8-10 molecules			MRI	119
Gd (III)	1700 Gd			MRI	78
β-MnOOH	3000–4000 Mn atoms			MRI	110
Fe_3O_4	~ 4000 Fe atoms	α-melanocyte-stimulating hormone peptide (α-MSH) /PEG/Rhodamine	melanoma	MRI/ Optical imaging	107
Fe_3O_4 or Gd-DTPA		Cy5.5	H-ferritin-TfR1 interaction	MRI/ Optical imaing	108
		Cy5.5- PLGVR/BHQ-3		Optical imaging	27
^{64}Cu		Cy5.5/RGD4C	RGD-integrin $\alpha_v\beta_3$	PET/ Optical imaging	28
$^{64}CuS/CuS$				PAI/PET/PTT	114
IR820	17.32 wt%			PAI/Optical Imaging/PTT	120
Cisplatin	50 molecules	mAb Ep1	$CSPG4^+$ melanoma	Chemotherapy	39
Cisplatin	15 molecules			Chemotherapy	115
Carboplatin	15 molecules			Chemotherapy	117
Doxorubicin	up to 73 wt%	RGD4C peptide	RGD-integrin $\alpha_v\beta_3$	Chemotherapy	34
Doxorubicin	33 molecules		H-ferritin-TfR1 interaction	Chemotherapy	116
		$CGKRK(KLAKLAK)_2$/ GFP	tumor-targeting peptide	induce apoptosis/ Optical imaging	45
		tumor cell targeting peptide (CTP)/ cell penetrating peptide(CPP)/ cationic peptide (CAP)/ enzymatically cleaved peptide (ECP)	tumor targeting peptide	siRNA delivery	43
$ZnF_{16}Pc$	up to 60 wt%	RGD4C peptide	RGD-integrin $\alpha_v\beta_3$	PDT	35
$ZnF_{16}Pc$	up to 60 wt%	folic acid	folic acid receptor	PDT	105
$ZnF_{16}Pc$	up to 60 wt%	red blood cell	tumor hypoxia	PDT	36
^{235}U	800 U atoms			neutron-capture therapy	91
$^{89}YPO_4$	500 Y atoms			radioimmunotherapy	117
$^{177}LuPO_4$	500 Lu atoms	biotin molecules		radioimmunoimaging/ radioimmunotherapy	90

We used $ZnF_{16}Pc$ as the photosensitizer for our ferritin nanoplatform-based PDT studies.[35,105] $ZnF_{16}Pc$ has a high potent, with a quantum yield of 0.85 in tetrahydrofuran (THF) solution. It has a maximum excitation wavelength of 671 nm. Although rather hydrophobic, it is able to be loaded into ferritins with a loading rate as high as 60 wt %, which means 1.5 mg $ZnF_{16}Pc$ can be loaded into 1 mg ferritin. The resulting P@FRTs showed excellent colloidal stability in PBS.[35] By conjugating the P@FRT nanocages with different targeting ligands, PDT can target different components in a tumor. For example, we used folic acid conjugated P@FRTs (P@FRT-FAs) for cancer cell-targeted PDT. An excellent cell targeting specificity and internalization of the P@FRT-FAs was observed *in vitro*. Moreover, the P@FA-FRT-mediated PDT treatment effectively suppressed tumor growth and lung metastasis.[105] The $ZnF_{16}Pc$-loaded RFRTs (P@RFRTs), on the other hand, can be used for tumor endothelium-targeted PDT (**Figure 1.12**). It selectively accumulated at tumors (tumor-to-normal tissue ratio of 26.82 ± 4.07 at 24 h), showing excellent overlap with tumor vessels. When combining with a relatively high irradiation fluence (300 mW/cm^2, 15 min), the P@RFRT-mediated PDT significantly suppressed tumor growth and induced intensive apoptosis in the treated tumors. Skin toxicity, which is a most critical issue of PDT, was also evaluated by caspase 3 staining. No obvious apoptosis was found in the skin tissues that exposed to ambient light. In addition, H&E staining suggested no abnormalities in normal organ tissues, confirming minimal off-target damage of this treatment.[35]

1.5.5 Photothermal therapy

Photothermal therapy (PTT) also requires light to active. It employs photothermal agents to convert light energy into heat for killing cancer cells. Similar to photosensitizers, most photothermal agents show low biocompatibility and poor pharmacokinetics, which adversely affect their clinical applications.[121,122] Huang et al. developed a near-infrared dye IR820-loaded

ferritin for PAI/fluorescence dual-modal imaging-guided PTT.[120] Two excitation wavelengths were applied: 550 nm for high quantum yield fluorescence imaging, while 808 nm for PAI and efficient PTT. The cancer theranostic ability was carefully investigated both *in vitro* and *in vivo*. 100% tumor elimination plus no tumor recurrence and no systematic toxicity, were achieved when a laser was applied (808 nm, 0.5 W/cm^2, 10 min), [120] The CuS-ferritin nanocages reported by Wang et al., which has been discussed as PAI/PET dual-modality imaging probe in Section 1.3.2, can also be used for PTT. Full tumor elimination was observed when CuS-ferritins were intravenously injected and a low irradiation dose (808 nm, 0.8 W/cm^2, 5 min) was applied.[114]

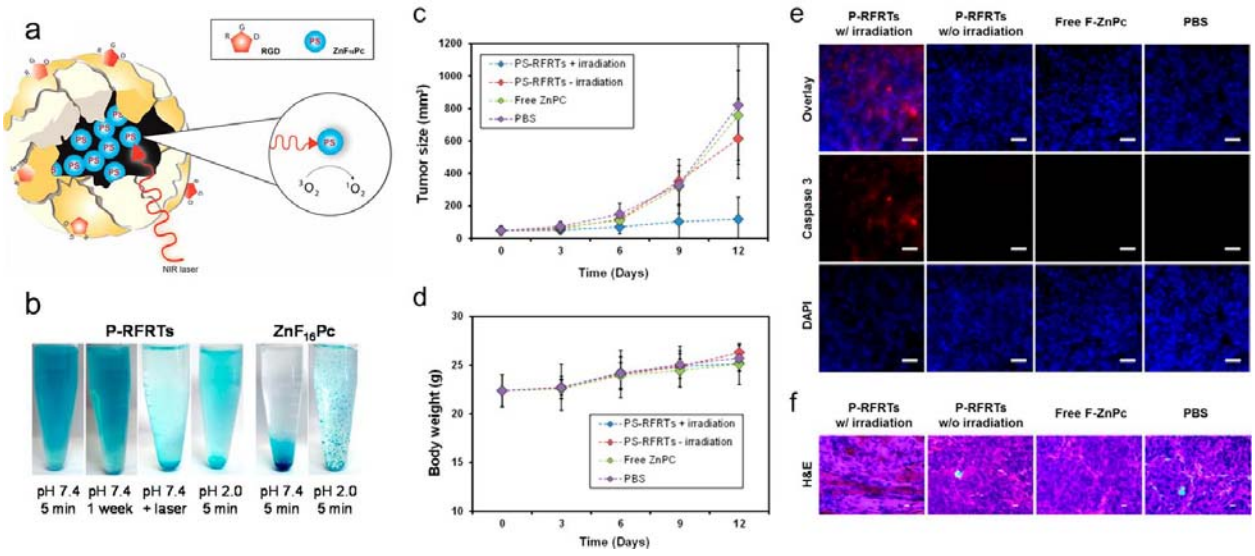

Figure 1.12 Ferritin Nanocages to Selectively Deliver Photosensitizers for Efficient PDT. (a) Schematic illustration of the formation and working mechanism of P-RFRTs. (b) Photographs of P-RFRTs and free ZnF16Pc in PBS under different conditions. (c) Tumor growth curve. Significant tumor suppression was found in the P-RFRTs, with irradiation group ($P < 0.05$). On day 12, a TIR of 83.64 ± 2.52% was found. (d) Weight growth curve. No significant weight drop was found with animals injected with P-RFRTs, with or without irradiation. (e) Caspase 3 staining with tumor tissues. High level of apoptosis was found in tumors from the P-RFRTs, with irradiation group but not in the other control groups. Red, caspase 3 (Cy5, ex/em = 650/670 nm); blue, DAPI. Scale bars, 50 μm. (f) H&E staining with tumor tissues. Densely packed neoplastic cells were found in the controls. In the treatment group, markedly disturbed tumor architecture was observed. Scale bars, 10 μm.[35]

1.5.6 Vaccines

Recently, ferritin nanocages are being used for vaccine development and antigen delivery due to their non-immunogenicity. The Nabel group developed self-assembling influenza nanoparticle vaccines by using ferritins as the scaffolds, which improved the potency and breadth of influenza virus immunity.[123] In brief, they genetically fused a viral haemagglutinin (HA) to each ferritin subunit. Adjacent HAs at the three-fold axils spontaneously assembled to a trimeric viral spike on ferritin surface (**Figure 1.13**). Compare to the traditional influenza vaccines, immunization with this ferritin-based influenza vaccine elicited more than tenfold higher HA inhibition antibody titers.[123] In addition, the Kang group used ferritin nanocages as a versatile antigen delivery platform for dendritic cell (DC)-based vaccine development.[44] They fused two ovalbumin peptides (OT1: SIINFEKL; OT-2: ISQAVHAAHAEINEAGR) onto the surfaces of separate ferritins, and effectively delivered the antigenic peptides to DCs. The delivered OT-1 successfully induced antigen-specific $CD8^+$ T cell proliferation and differentiation, inducing selective killing of antigen-specific target cells. OT-2, on the other hand, induced effective proliferation and differentiation of $CD4^+$ T cells both *in vitro* and *in vivo*.[44]

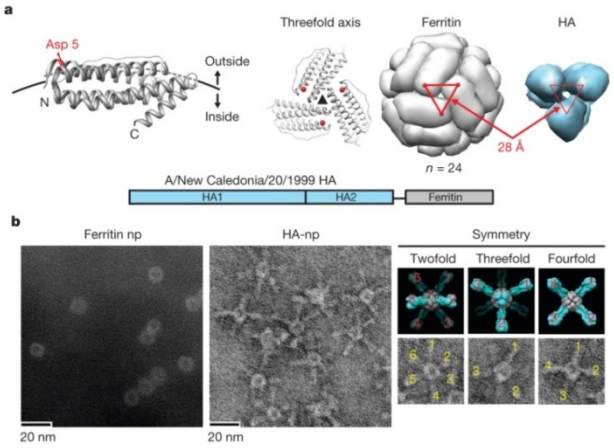

Figure 1.13 Molecular Design and Characterization of Ferritin Nanoparticles Displaying Influenza Virus HA.[123]

1.5.7 Bioassays/biosensors

The ferritin nanocages can also be used for the development of highly sensitive bioassays for molecular diagnosis. Liu et al. loaded a fluorescence marker (fluorescein anion) and an electrochemical markers (hexacyanoferrate(III)) into biotinylated ferritins in separate studies.[124] The biotin-functionalized and marker-loaded ferritins were used for signal amplification in sandwich immunoassays, showing detection limits of 0.06 (0.39 pM) and 0.08 ng mL^{-1} (0.52 pM) IgG in the fluorescence immunoassay and the electrochemical immunoassay, respectively (**Figure 1.14**).[124] Later, a carbon nanocapsule with lead phosphate-loaded ferritin had been developed for electrochemical immunoassays of human phosphorylated p53 at serine 15 (phosphor-$p53^{15}$), a potential biomarker of gamma-radiation exposure.[125] The linear range was from 0.02 to 20 ng /mL, and the detection limit was 0.01 ng /mL, which was 30-fold lower than that of the ELISA measurement.

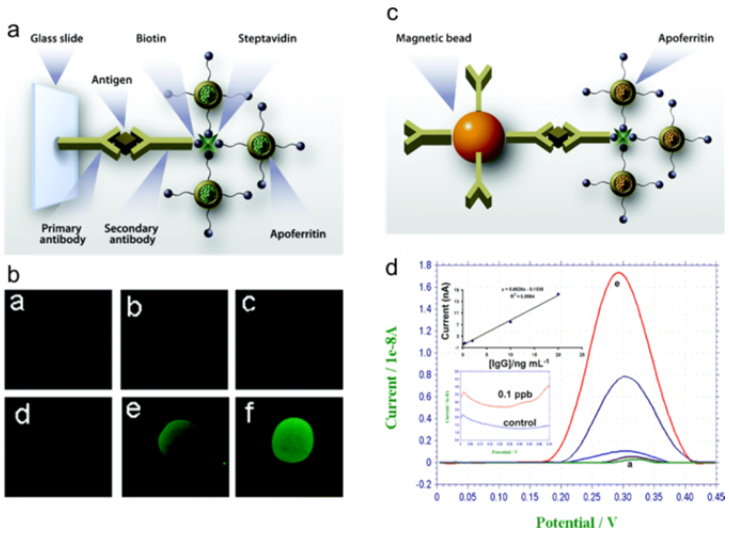

Figure 1.14 Versatile Apoferritin Nanoparticle Labels for Assay of Protein. (a) Fluorescence microscopy immunoassay. (b) Fluorescence microscopy images of immunoassay with the increasing concentration of the IgG (a-f: 0, 0.1, 1, 5, 10, 20 ng/mL). (c) Magnetic beads and electrochemical sandwich immunoassay. (d) Typical square wave voltammograms of electrochemical immunoassay with increasing concentration of the IgG.[124]

1.6 Conclusions and Prospects

The unique nanostructure of ferritin makes it a promising nanoplatform for bionanotechnology applications, especially biomedicine. When compared with artificial nanomaterials, ferritin holds a number of advantages including excellent biocompatibility, long circulation half-lives, and facile surface modification. In addition, the hollow cavity in apoferritins can be loaded with multiple functionalities, such as imaging probes and anticancer drugs. All these features suggest great potential for the clinical translation of ferritin-based nanoplatforms.

In the next few chapters, we will discuss different ferritin nanoplatforms we have developed for drug delivery and photodynamic therapy. By surface modification of ferritins with different tumor targeting ligand, we can deliver anti-cancer drugs or photosensitizers to different tumor components, achieving significant tumor growth inhibition with minimal side effects. In Chapter 2, we used RGD4C-modified ferritins (RFRTs) to selectively deliver doxorubicin to tumor endothelium cells and cancer cells. The doxorubicin-loaded RFRTs showed improved tumor uptake, enhanced treatment efficacy, and reduced cardiotoxicity compared to free doxorubicin. In Chapter 3 and Chapter 4, we modified the ferritins with folic acid ligands and RGD4C peptide to deliver photosensitizers to cancer cells and tumor vasculature cells, respectively. In Chapter 5, we used RFRTs to site-specifically deliver photosensitizers to tumor vasculature cells, but carefully controlled the PDT stimulus on tumor vessels. Enhanced EPR effect was achieved, which greatly improved the tumor accumulation and treatment efficacy of nanoparticle drugs. In Chapter 6, we developed a red blood cell-facilitate PDT (RBC-PDT) technology, in which photosensitizer-loaded ferrtitins were conjugated onto RBCs. Even in hypoxic tumor regions, there are O_2 molecules released from RBCs to the surroundings, producing an oxygen-rich zone close to the RBC surface. The photosensitizers can benefit from

the oxygen flow and the long circulation of RBCs to continuously produce $^1O_2$, even in hypoxic regions. In Chapter 7, we modified ferritins with anti-fibroblast activation protein single-chain fragment variables (scFvs) to specifically deliver photosensitizers to cancer associated fibroblasts (CAFs). The PDT treatment effectively killed CAFs, increased the frequency and infiltration of $CD8^+$ T cells in tumors, leading to efficient tumor suppression and significantly extended survival.

References

(1) Jutz, G.; van Rijn, P.; Santos Miranda, B.; Boker, A. *Chemical Reviews* **2015**, *115*, 1653.
(2) Mashaghi, S.; Jadidi, T.; Koenderink, G.; Mashaghi, A. *International Journal of Molecular Sciences* **2013**, *14*, 4242.
(3) Lee, L. A.; Wang, Q. *Nanomedicine: Nanotechnology, Biology, and Medicine* **2006**, *2*, 137.
(4) Doll, T. A.; Raman, S.; Dey, R.; Burkhard, P. *Journal of the Royal Society, Interface* **2013**, *10*, 20120740.
(5) Maham, A.; Tang, Z.; Wu, H.; Wang, J.; Lin, Y. *Small* **2009**, *5*, 1706.
(6) Kramer, R. M.; Li, C.; Carter, D. C.; Stone, M. O.; Naik, R. R. *Journal of the American Chemical Society* **2004**, *126*, 13282.
(7) McMillan, R. A.; Paavola, C. D.; Howard, J.; Chan, S. L.; Zaluzec, N. J.; Trent, J. D. *Nature Materials* **2002**, *1*, 247.
(8) He, D.; Marles-Wright, J. *New Biotechnology* **2015**, *32*, 651.
(9) Munro, H. N.; Linder, M. C. *Physiological Reviews* **1978**, *58*, 317.
(10) Laufberger, V. *Bulletin de la Société de Chimie Biologique* **1937**, *19*, 1575.
(11) Lawson, D. M.; Artymiuk, P. J.; Yewdall, S. J.; Smith, J. M.; Livingstone, J. C.; Treffry, A.; Luzzago, A.; Levi, S.; Arosio, P.; Cesareni, G.; et al. *Nature* **1991**, *349*, 541.
(12) Sanghamitra, N. J. M.; Ueno, T. *Chemical Communications* **2013**, *49*, 4114.
(13) Banyard, S. H.; Stammers, D. K.; Harrison, P. M. *Nature* **1978**, *271*, 282.
(14) Boyd, D.; Vecoli, C.; Belcher, D. M.; Jain, S. K.; Drysdale, J. W. *The Journal of Biological Chemistry* **1985**, *260*, 11755.
(15) Jain, S. K.; Barrett, K. J.; Boyd, D.; Favreau, M. F.; Crampton, J.; Drysdale, J. W. *The Journal of Biological Chemistry* **1985**, *260*, 11762.
(16) Wade, V. J.; Levi, S.; Arosio, P.; Treffry, A.; Harrison, P. M.; Mann, S. *Journal of Molecular Biology* **1991**, *221*, 1443.
(17) Levi, S.; Luzzago, A.; Cesareni, G.; Cozzi, A.; Franceschinelli, F.; Albertini, A.; Arosio, P. *The Journal of Biological Chemistry* **1988**, *263*, 18086.
(18) Cozzi, A.; Corsi, B.; Levi, S.; Santambrogio, P.; Albertini, A.; Arosio, P. *The Journal of Biological Chemistry* **2000**, *275*, 25122.
(19) Levi, S.; Corsi, B.; Rovida, E.; Cozzi, A.; Santambrogio, P.; Albertini, A.; Arosio, P. *The Journal of Biological Chemistry* **1994**, *269*, 30334.
(20) Theil, E. C. *Annual Review of Biochemistry* **1987**, *56*, 289.
(21) Fan, K. L.; Gao, L. Z.; Yan, X. Y. *Wires Nanomedicine and Nanobitechnology* **2013**, *5*, 287.
(22) Takahashi, T.; Kuyucak, S. *Biophysical Journal* **2003**, *84*, 2256.
(23) Crichton, R. R.; Declercq, J. P. *Biochimica et Biophysica Acta* **2010**, *1800*, 706.
(24) Watt, R. K.; Hilton, R. J.; Graff, D. M. *Biochimica et Biophysica Acta* **2010**, *1800*, 745.
(25) Webb, B.; Frame, J.; Zhao, Z.; Lee, M. L.; Watt, G. D. *Archives of Biochemistry and Biophysics* **1994**, *309*, 178.
(26) Wetz, K.; Crichton, R. R. *European Journal of Biochemistry* **1976**, *61*, 545.
(27) Lin, X.; Xie, J.; Zhu, L.; Lee, S.; Niu, G.; Ma, Y.; Kim, K.; Chen, X. *Angewandte Chemie* **2011**, *50*, 1569.
(28) Lin, X.; Xie, J.; Niu, G.; Zhang, F.; Gao, H.; Yang, M.; Quan, Q.; Aronova, M. A.; Zhang, G.; Lee, S.; Leapman, R.; Chen, X. *Nano Letters* **2011**, *11*, 814.

(29) Kumashiro, Y.; Ikezoe, Y.; Tamada, K.; Hara, M. *The Journal of Physical Chemistry. B* **2008**, *112*, 8291.
(30) Zeng, Q.; Reuther, R.; Oxsher, J.; Wang, Q. *Bioorganic Chemistry* **2008**, *36*, 255.
(31) Zeng, Q.; Li, T.; Cash, B.; Li, S.; Xie, F.; Wang, Q. *Chemical communications* **2007**, 1453.
(32) Hu, Y.; Samanta, D.; Parelkar, S. S.; Hong, S. W.; Wang, Q.; Russell, T. P.; Emrick, T. *Advanced Functional Materials* **2010**, *20*, 3603.
(33) Mougin, N. C.; van Rijn, P.; Park, H.; Müller, A. H. E.; Böker, A. *Advanced Functional Materials* **2011**, *21*, 2470.
(34) Zhen, Z.; Tang, W.; Chen, H.; Lin, X.; Todd, T.; Wang, G.; Cowger, T.; Chen, X.; Xie, J. *ACS Nano* **2013**, *7*, 4830.
(35) Zhen, Z.; Tang, W.; Guo, C.; Chen, H.; Lin, X.; Liu, G.; Fei, B.; Chen, X.; Xu, B.; Xie, J. *ACS Nano* **2013**, *7*, 6988.
(36) Tang, W.; Zhen, Z.; Wang, M.; Wang, H.; Chuang, Y.-J.; Zhang, W.; Wang, G. D.; Todd, T.; Cowger, T.; Chen, H.; Liu, L.; Li, Z.; Xie, J. *Advanced Functional Materials* **2016**, *26*, 1757.
(37) Wong, K. K. W.; Colfen, H.; Whilton, N. T.; Douglas, T.; Mann, S. *Journal of Inorganic Biochemistry* **1999**, *76*, 187.
(38) Wong, K. K. W.; Whilton, N. T.; Colfen, H.; Douglas, T.; Mann, S. *Chemical Communications* **1998**, 1621.
(39) Falvo, E.; Tremante, E.; Fraioli, R.; Leonetti, C.; Zamparelli, C.; Boffi, A.; Morea, V.; Ceci, P.; Giacomini, P. *Nanoscale* **2013**, *5*, 12278.
(40) Takeda, S.; Yamaki, M.; Ebina, S.; Nagayama, K. *Journal of Biochemistry* **1995**, *117*, 267.
(41) Fantechi, E.; Innocenti, C.; Zanardelli, M.; Fittipaldi, M.; Falvo, E.; Carbo, M.; Shullani, V.; Di Cesare Mannelli, L.; Ghelardini, C.; Ferretti, A. M.; Ponti, A.; Sangregorio, C.; Ceci, P. *ACS Nano* **2014**, *8*, 4705.
(42) Lee, J. H.; Seo, H. S.; Song, J. A.; Kwon, K. C.; Lee, E. J.; Kim, H. J.; Lee, E. B.; Cha, Y. J.; Lee, J. *ACS Nano* **2013**, *7*, 10879.
(43) Lee, E. J.; Lee, S. J.; Kang, Y.-S.; Ryu, J. H.; Kwon, K. C.; Jo, E.; Yhee, J. Y.; Kwon, I. C.; Kim, K.; Lee, J. *Advanced Functional Materials* **2015**, *25*, 1279.
(44) Han, J.-A.; Kang, Y. J.; Shin, C.; Ra, J.-S.; Shin, H.-H.; Hong, S. Y.; Do, Y.; Kang, S. *Nanomedicine: Nanotechnology, Biology and Medicine* **2014**, *10*, 561.
(45) Kim, S.; Kim, G. S.; Seo, J.; Gowri Rangaswamy, G.; So, I.-S.; Park, R.-W.; Lee, B.-H.; Kim, I.-S. *Biomacromolecules* **2016**, *17*, 12.
(46) Lawson, D. M.; Treffry, A.; Artymiuk, P. J.; Harrison, P. M.; Yewdall, S. J.; Luzzago, A.; Cesareni, G.; Levi, S.; Arosio, P. *FEBS Letters* **1989**, *254*, 207.
(47) Santambrogio, P.; Levi, S.; Cozzi, A.; Corsi, B.; Arosio, P. *The Biochemical Journal* **1996**, *314 (Pt 1)*, 139.
(48) Jutz, G.; Böker, A. *Polymer* **2011**, *52*, 211.
(49) Ueno, T.; Suzuki, M.; Goto, T.; Matsumoto, T.; Nagayama, K.; Watanabe, Y. *Angewandte Chemie* **2004**, *43*, 2527.
(50) Suzuki, M.; Abe, M.; Ueno, T.; Abe, S.; Goto, T.; Toda, Y.; Akita, T.; Yamada, Y.; Watanabe, Y. *Chemical Communications* **2009**, 4871.
(51) Dominguez-Vera, J. M.; Galvez, N.; Sanchez, P.; Mota, A. J.; Trasobares, S.; Hernandez, J. C.; Calvino, J. J. *European Journal of Inorganic Chemistry* **2007**, 4823.

(52) Uchida, M.; Terashima, M.; Cunningham, C. H.; Suzuki, Y.; Willits, D. A.; Willis, A. F.; Yang, P. C.; Tsao, P. S.; McConnell, M. V.; Young, M. J.; Douglas, T. *Magnetic Resonance in Medicine* **2008**, *60*, 1073.
(53) Jolley, C. C.; Uchida, M.; Reichhardt, C.; Harrington, R.; Kang, S.; Klem, M. T.; Parise, J. B.; Douglas, T. *Chemistry of Materials* **2010**, *22*, 4612.
(54) Kálmán, F. K.; Geninatti-Crich, S.; Aime, S. *Angewandte Chemie International Edition* **2010**, *49*, 612.
(55) Meldrum, F. C.; Douglas, T.; Levi, S.; Arosio, P.; Mann, S. *Journal of Inorganic Biochemistry* **1995**, *58*, 59.
(56) Meldrum, F. C.; Wade, V. J.; Nimmo, D. L.; Heywood, B. R.; Mann, S. *Nature* **1991**, *349*, 684.
(57) Zhang, B.; Harb, J. N.; Davis, R. C.; Kim, J. W.; Chu, S. H.; Choi, S.; Miller, T.; Watt, G. D. *Inorganic Chemistry* **2005**, *44*, 3738.
(58) Li, M.; Viravaidya, C.; Mann, S. *Small* **2007**, *3*, 1477.
(59) Dominguez-Vera, J. M.; Colacio, E. *Inorganic Chemistry* **2003**, *42*, 6983.
(60) Yamashita, I.; Hayashi, J.; Hara, M. *Chemistry Letters* **2004**, *33*, 1158.
(61) Iwahori, K.; Morioka, T.; Yamashita, I. *Physica Status Solidi a-Applications and Materials Science* **2006**, *203*, 2658.
(62) Xing, R.; Wang, X.; Yan, L.; Zhang, C.; Yang, Z.; Wang, X.; Guo, Z. *Dalton Transactions* **2009**, 1710.
(63) Hennequin, B.; Turyanska, L.; Ben, T.; Beltran, A. M.; Molina, S. I.; Li, M.; Mann, S.; Patane, A.; Thomas, N. R. *Advanced Materials* **2008**, *20*, 3592.
(64) Iwahori, K.; Takagi, R.; Kishimoto, N.; Yamashita, I. *Materials Letters* **2011**, *65*, 3245.
(65) Iwahori, K.; Yoshizawa, K.; Muraoka, M.; Yamashita, I. *Inorganic Chemistry* **2005**, *44*, 6393.
(66) Wong, K. K. W.; Mann, S. *Advanced Materials* **1996**, *8*, 928.
(67) Kasyutich, O.; Ilari, A.; Fiorillo, A.; Tatchev, D.; Hoell, A.; Ceci, P. *Journal of the American Chemical Society* **2010**, *132*, 3621.
(68) Shin, Y.; Dohnalkova, A.; Lin, Y. *The Journal of Physical Chemistry C* **2010**, *114*, 5985.
(69) Zheng, B.; Yamashita, I.; Uenuma, M.; Iwahori, K.; Kobayashi, M.; Uraoka, Y. *Nanotechnology* **2010**, *21*, 045305.
(70) Zhang, L.; Swift, J.; Butts, C. A.; Yerubandi, V.; Dmochowski, I. J. *Journal of Inorganic Biochemistry* **2007**, *101*, 1719.
(71) Fan, R.; Chew, S. W.; Cheong, V. V.; Orner, B. P. *Small* **2010**, *6*, 1483.
(72) Galvez, N.; Sanchez, P.; Dominguez-Vera, J. M.; Soriano-Portillo, A.; Clemente-Leon, M.; Coronado, E. *Journal of Materials Chemistry* **2006**, *16*, 2757.
(73) Ceolin, M.; Galvez, N.; Sanchez, P.; Fernandez, B.; Dominguez-Vera, J. M. *European Journal of Inorganic Chemistry* **2008**, 795.
(74) Galvez, N.; Sanchez, P.; Dominguez-Vera, J. M. *Dalton Transactions* **2005**, 2492.
(75) Clemente-Leon, M.; Coronado, E.; Soriano-Portillo, A.; Galvez, N.; Dominguez-Vera, J. M. *Journal of Materials Chemistry* **2007**, *17*, 49.
(76) Zhang, L.; Laug, L.; Munchgesang, W.; Pippel, E.; Gosele, U.; Brandsch, M.; Knez, M. *Nano Letters* **2010**, *10*, 219.
(77) Deng, Q. Y.; Yang, B.; Wang, J. F.; Whiteley, C. G.; Wang, X. N. *Biotechnology Letters* **2009**, *31*, 1505.

(78) Sanchez, P.; Valero, E.; Galvez, N.; Dominguez-Vera, J. M.; Marinone, M.; Poletti, G.; Corti, M.; Lascialfari, A. *Dalton Transactions* **2009**, 800.
(79) Okuda, M.; Suzumoto, Y.; Yamashita, I. *Crystal Growth & Design* **2011**, *11*, 2540.
(80) Douglas, T.; Stark, V. T. *Inorganic Chemistry* **2000**, *39*, 1828.
(81) Okuda, M.; Iwahori, K.; Yamashita, I.; Yoshimura, H. *Biotechnology and Bioengineering* **2003**, *84*, 187.
(82) Ensign, D.; Young, M.; Douglas, T. *Inorganic Chemistry* **2004**, *43*, 3441.
(83) Klem, M. T.; Mosolf, J.; Young, M.; Douglas, T. *Inorganic Chemistry* **2008**, *47*, 2237.
(84) Meldrum, F. C.; Heywood, B. R.; Mann, S. *Science* **1992**, *257*, 522.
(85) Honarmand Ebrahimi, K.; Hagedoorn, P. L.; Jongejan, J. A.; Hagen, W. R. *Journal of Biological Inorganic Chemistry* **2009**, *14*, 1265.
(86) Wong, K. K. W.; Douglas, T.; Gider, S.; Awschalom, D. D.; Mann, S. *Chemistry of Materials* **1998**, *10*, 279.
(87) Parker, M. J.; Allen, M. A.; Ramsay, B.; Klem, M. T.; Young, M.; Douglas, T. *Chemistry of Materials* **2008**, *20*, 1541.
(88) Liu, G.; Wu, H.; Dohnalkova, A.; Lin, Y. *Analytical Chemistry* **2007**, *79*, 5614.
(89) Liu, G.; Wu, H.; Wang, J.; Lin, Y. *Small* **2006**, *2*, 1139.
(90) Wu, H.; Engelhard, M. H.; Wang, J.; Fisher, D. R.; Lin, Y. *Journal of Materials Chemistry* **2008**, *18*, 1779.
(91) Hainfeld, J. F. *Proceedings of the National Academy of Sciences of the United States of America* **1992**, *89*, 11064.
(92) Polanams, J.; Ray, A. D.; Watt, R. K. *Inorganic Chemistry* **2005**, *44*, 3203.
(93) Yoshizawa, K.; Iwahori, K.; Sugimoto, K.; Yamashita, I. *Chemistry Letters* **2006**, *35*, 1192.
(94) Naito, M.; Iwahori, K.; Miura, A.; Yamane, M.; Yamashita, I. *Angewandte Chemie* **2010**, *49*, 7006.
(95) Douglas, T.; Dickson, D. P. E.; Betteridge, S.; Charnock, J.; Garner, C. D.; Mann, S. *Science* **1995**, *269*, 54.
(96) St. Pierre, T. G.; Chua-anusorn, W.; Sipos, P.; Kron, I.; Webb, J. *Inorganic Chemistry* **1993**, *32*, 4480.
(97) Hennequin, B.; Turyanska, L.; Ben, T.; Beltrán, A. M.; Molina, S. I.; Li, M.; Mann, S.; Patanè, A.; Thomas, N. R. *Advanced Materials* **2008**, *20*, 3592.
(98) Yamashita, I.; Iwahori, K.; Kumagai, S. *Biochimica Et Biophysica Acta-General Subjects* **2010**, *1800*, 846.
(99) Kase, D.; Kulp, J. L., 3rd; Yudasaka, M.; Evans, J. S.; Iijima, S.; Shiba, K. *Langmuir* **2004**, *20*, 8939.
(100) Chen, T. T.; Li, L.; Chung, D. H.; Allen, C. D.; Torti, S. V.; Torti, F. M.; Cyster, J. G.; Chen, C. Y.; Brodsky, F. M.; Niemi, E. C.; Nakamura, M. C.; Seaman, W. E.; Daws, M. R. *The Journal of Experimental Medicine* **2005**, *202*, 955.
(101) Todorich, B.; Zhang, X.; Slagle-Webb, B.; Seaman, W. E.; Connor, J. R. *Journal of neurochemistry* **2008**, *107*, 1495.
(102) Li, L.; Fang, C. J.; Ryan, J. C.; Niemi, E. C.; Lebron, J. A.; Bjorkman, P. J.; Arase, H.; Torti, F. M.; Torti, S. V.; Nakamura, M. C.; Seaman, W. E. *Proceedings of the National Academy of Sciences of the United States of America* **2010**, *107*, 3505.
(103) Fan, K. L.; Cao, C. Q.; Pan, Y. X.; Lu, D.; Yang, D. L.; Feng, J.; Song, L. N.; Liang, M. M.; Yan, X. Y. *Nature Nanotechnology* **2012**, *7*, 459.

(104) Li, J. Y.; Paragas, N.; Ned, R. M.; Qiu, A.; Viltard, M.; Leete, T.; Drexler, I. R.; Chen, X.; Sanna-Cherchi, S.; Mohammed, F.; Williams, D.; Lin, C. S.; Schmidt-Ott, K. M.; Andrews, N. C.; Barasch, J. *Developmental cell* **2009**, *16*, 35.
(105) Zhen, Z.; Tang, W.; Zhang, W.; Xie, J. *Nanoscale* **2015**, *7*, 10330.
(106) Low, P. S.; Kularatne, S. A. *Current opinion in Chemical Biology* **2009**, *13*, 256.
(107) Vannucci, L.; Falvo, E.; Fornara, M.; Di Micco, P.; Benada, O.; Krizan, J.; Svoboda, J.; Hulikova-Capkova, K.; Morea, V.; Boffi, A.; Ceci, P. *International Journal of Nanomedicine* **2012**, *7*, 1489.
(108) Cao, C.; Wang, X.; Cai, Y.; Sun, L.; Tian, L.; Wu, H.; He, X.; Lei, H.; Liu, W.; Chen, G.; Zhu, R.; Pan, Y. *Advanced Materials* **2014**, *26*, 2566.
(109) Sanchez, P.; Valero, E.; Galvez, N.; Dominguez-Vera, J. M.; Marinone, M.; Poletti, G.; Corti, M.; Lascialfari, A. *Dalton Transactions* **2009**, 800.
(110) Kalman, F. K.; Geninatti-Crich, S.; Aime, S. *Angewandte Chemie* **2010**, *49*, 612.
(111) Hu, H.; Huang, P.; Weiss, O. J.; Yan, X.; Yue, X.; Zhang, M. G.; Tang, Y.; Nie, L.; Ma, Y.; Niu, G.; Wu, K.; Chen, X. *Biomaterials* **2014**, *35*, 9868.
(112) Song, J.; Yang, X.; Jacobson, O.; Huang, P.; Sun, X.; Lin, L.; Yan, X.; Niu, G.; Ma, Q.; Chen, X. *Advanced Materials* **2015**, *27*, 4805.
(113) Huang, P.; Lin, J.; Li, W.; Rong, P.; Wang, Z.; Wang, S.; Wang, X.; Sun, X.; Aronova, M.; Niu, G.; Leapman, R. D.; Nie, Z.; Chen, X. *Angewandte Chemie* **2013**, *125*, 14208.
(114) Wang, Z.; Huang, P.; Jacobson, O.; Wang, Z.; Liu, Y.; Lin, L.; Lin, J.; Lu, N.; Zhang, H.; Tian, R.; Niu, G.; Liu, G.; Chen, X. *ACS Nano* **2016**, *10*, 3453.
(115) Yang, Z.; Wang, X.; Diao, H.; Zhang, J.; Li, H.; Sun, H.; Guo, Z. *Chemical Communications* **2007**, 3453.
(116) Liang, M.; Fan, K.; Zhou, M.; Duan, D.; Zheng, J.; Yang, D.; Feng, J.; Yan, X. *Proceedings of the National Academy of Sciences of the United States of America* **2014**, *111*, 14900.
(117) Wu, H.; Wang, J.; Wang, Z.; Fisher, D. R.; Lin, Y. *Journal of Nanoscience and Nanotechnology* **2008**, *8*, 2316.
(118) Brown, S. B.; Brown, E. A.; Walker, I. *The Lancet. Oncology* **2004**, *5*, 497.
(119) Aime, S.; Frullano, L.; Geninatti Crich, S. *Angewandte Chemie* **2002**, *41*, 1017.
(120) Huang, P.; Rong, P.; Jin, A.; Yan, X.; Zhang, M. G.; Lin, J.; Hu, H.; Wang, Z.; Yue, X.; Li, W.; Niu, G.; Zeng, W.; Wang, W.; Zhou, K.; Chen, X. *Advanced Materials* **2014**, *26*, 6401.
(121) Fernandez-Fernandez, A.; Manchanda, R.; Lei, T.; Carvajal, D. A.; Tang, Y.; Kazmi, S. Z.; McGoron, A. J. *Molecular Imaging* **2012**, *11*, 99.
(122) Zha, Z.; Deng, Z.; Li, Y.; Li, C.; Wang, J.; Wang, S.; Qu, E.; Dai, Z. *Nanoscale* **2013**, *5*, 4462.
(123) Kanekiyo, M.; Wei, C. J.; Yassine, H. M.; McTamney, P. M.; Boyington, J. C.; Whittle, J. R.; Rao, S. S.; Kong, W. P.; Wang, L.; Nabel, G. J. *Nature* **2013**, *499*, 102.
(124) Liu, G.; Wang, J.; Wu, H.; Lin, Y. *Analytical Chemistry* **2006**, *78*, 7417.
(125) Chen, A.; Bao, Y.; Ge, X.; Shin, Y.; Du, D.; Lin, Y. *RSC Advances* **2012**, *2*, 11029.

CHAPTER 2

RGD-MODIFIED APOFERRITIN NANOPARTICLES FOR EFFICIENT DRUG DELIVERY TO TUMORS

2.1 Introduction

The apoferritins (FRTs) is a cage-like structure self-assembled with 24 subunits. It has an external and an internal diameter of 12 and 8 nm, respectively.[1] In the acidic environment (pH = 2.0), the nanocage breaks into subunits.[1] Interestingly, such a process is reversible. As the pH return to neutral, these subunits reconstitute into an almost intact cage-like structure.[2] With a hollow cavity, the apoferritins can serve as size-confined nanoreactors to grow metallic nanoparticles.[3-5] On the other hand, many functionalities, such as Gd-DO3A[6] and cisplatin,[7] can be encapsulated into FRTs, either by diffusion or by the pH-disassembly strategy.[2] Moreover, the surface of the ferritin can be easily modified either genetically or chemically. In particular, Uchida et al. introduced Cys-Asp-Cys-Arg-Gly-Asp-Cys-Phe-Cys (RGD4C), an RGD derivative, onto the FRT surface.[8] RGD is a three-amino-acid sequence with high affinity toward integrin $\alpha_v\beta_3$, which is a tumor angiogenesis biomarker overexpressed on tumor endothelial cells and many types of tumor cells.[9-12]

During the past decade, ferritins have been extensively investigated as drug carriers due to their excellent biocompatibility, non-immunogenicity, unique nanostructure, and facile surface modification. In this study, we developed a Cu-assisted method for efficient loading of Dox to RGD4C-modified apoferritins (RFRTs). This is the first *in vivo* study on utilizing surface

modified FRT nanocages as a drug carrier for doxorubicin (Dox)-based chemotherapy (**Figure 2.1a**). It has been demonstrated by positron emission tomography (PET) and near-infrared fluorescence imaging studies that these RFRTs can efficiently target to tumors through RGD–integrin interaction and the enhanced permeability and retention (EPR) effect.[2] When studied on U87MG subcutaneous tumor models, these Dox-loaded ferritin nanocages showed a longer circulation half-life, higher tumor uptake, better tumor growth inhibition, and less cardiotoxicity than free doxorubicin. Such a technology might be extended to load a broad range of therapeutics and holds great potential in clinical translation.

2.2 Results and Discussion[a]

2.2.1 Preparation and characterization of D-RFRTs

We used human heavy-chain FRTs/RFRTs throughout the study. The expression, production, and purification of FRTs/RFRTs were reported previously.[2] Sodium dodecyl sulfate–polyacrylamide gel electrophoresis (SDS-PAGE) studies found bands at ~22 and ~28 kDa for FRT and RFRT products, correlating well with the molecular weights of their subunits. The yields were 2.5 mg/100 mL cell culture for FRTs and 0.5 mg/100 mL for RFRTs, respectively. Dynamic light scattering (DLS) found a larger size for RFRTs (18.7 nm) than that for FRTs (8.2 nm). This size increase has been attributed to the imparted RGD4C sequence on the FRT surface.

Free Dox shows a relatively low loading rate with either FRTs or RFRTs. To facilitate the loading, we investigated using Cu(II), Mn(II), Zn(II) and Fe(III), all of which are known to be able to form a complex with Dox,[13,14] as a helper agent. Briefly, we incubated Dox–metal complexes with FRT/RFRT nanoparticles. Unloaded drug was removed by passing through a

[a] Zipeng Zhen, Wei Tang, Hongmin Chen, Xin Lin, Trever Todd, Geoffrey Wang, Taku Cowger, Xiaoyuan Chen, and Jin Xie**ACS Nano* **2013**, *7*, 4830–4837. Reprinted here with permission of publisher.

NAP-5 column. The use of Mn(II) and Zn(II) led to a very low FRT/RFRT yield. When Cu(II) or Fe(III) were used, on the other hand, we observed a significantly improved Dox loading, with Cu(II) being the more efficient one. For RFRTs, precomplexation with Cu increased Dox loading rate to 73.49 wt %, in comparison to that of 14.14 wt % for free Dox. Disassembling RFRT nanocages was found to be associated with a low production yield and the approach was not used. It is noted that preincubating RFRTs with Cu(II) can significantly block the drug loading (down to 8.28 wt %). Our previous studies with ^{64}Cu showed that free copper was mainly loaded into the cavity of RFRTs, possibly by association with the interior metal binding sites. The fact that free Cu(II) can block the Dox–Cu loading indicates that the complex competes for the same binding sites at the interiors of nanocages. Therefore, it is deduced that for empty RFRTs, the drug is mostly encapsulated into the nanocages rather than loaded on the surface.

A gel-filtration chromatography study was performed to evaluate the size change over the drug loading. For RFRTs, we found a single peak at 27.37 min (**Figure 2.1b**). This peak was shown on the spectrum of Dox-loaded RFRTs (D-RFRTs) at the same position (27.40 min), indicating that for the majority of the product, the size remained unchanged. This supports the hypothesis that Dox–Cu was encapsulated into the interiors of RFRTs, otherwise a decrease in retention time would have been observed. Notably, a small peak at 15.53 min was found on the spectrum of D-RFRTs. This is attributed to a small portion of particle clustering that was formed during the drug loading, which, according to chromatogram integration, accounts for only 3.53% of the overall product. This result correlates well with the atomic force microscopy (AFM) observation, which found a slightly increased degree of particle clustering after drug loading, albeit an overall comparable size (18.32 ± 4.09 nm for RFRTs and 19.72 ± 2.28 nm for D-RFRTs). Dynamic light scattering (DLS) analysis showed that the size of D-RFRTs was 21.03

nm, which is comparable to that of RFRTs. D-RFRTs were very stable in PBS and showed no precipitation for weeks when kept at a concentration lower than 0.5 mg/mL.

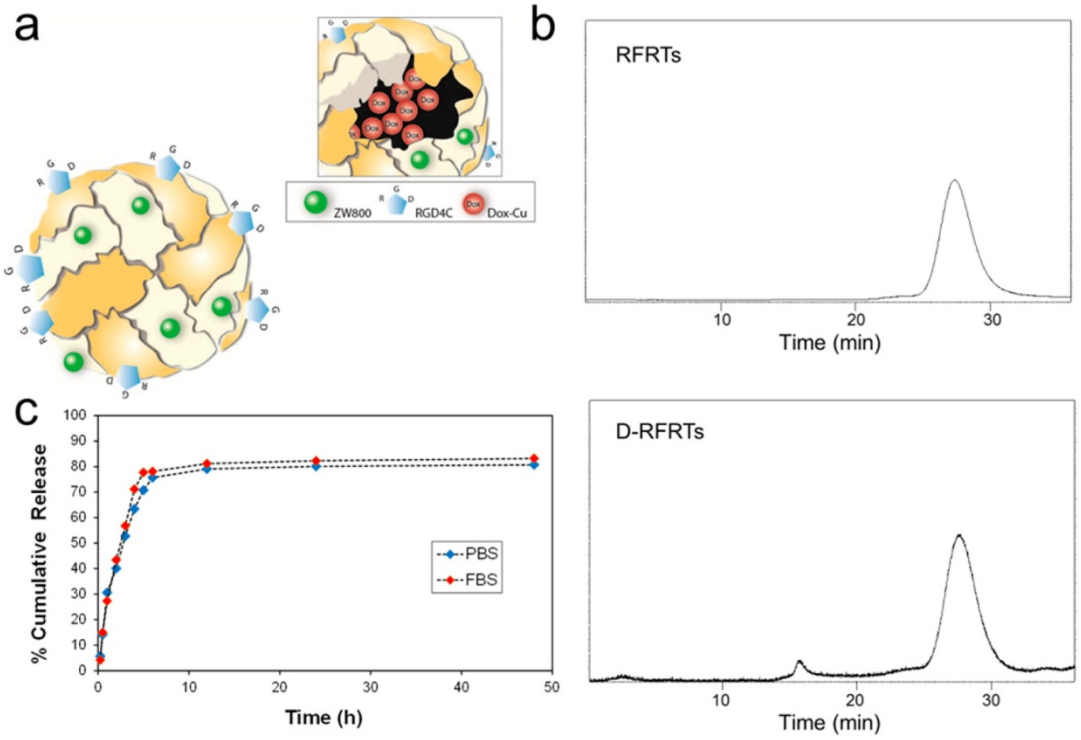

Figure 2.1 Doxorubicin-Loaded and RGD Peptide-Modified Ferritins (D-RFRTs). (a) Schematic illustration of D-RFRTs. Dox was precomplexed with Cu, and then encapsulated into RFRTs. (b) Gel-filtration chromatography analysis of RFRTs and D-RFRTs. The same peak at around 27.4 min was observed for both RFRTs and D-RFRTs. (c) Cumulative drug release curves of D-RFRTs in PBS (pH 7.4) and FBS.

The release of Dox from D-RFRTs was studied in PBS at 37 °C. Unlike Cu(II) that remains bound to the interiors of nanocages,[2] Dox was found to be gradually released from the nanocarriers (**Figure 2.1c**). We also studied drug release in fetal bovine serum (FBS). It is well-known that Cu-based complexes are susceptible to transchelation in the serum for its association with serum proteins.[2,15] If Dox–Cu was immobilized onto the surface of RFRTs, incubation in

the serum would result in a dramatically accelerated drug release compared to PBS. The results, however, showed an overall comparable release rate (**Figure 2.1c**).

2.2.2 *In vitro* studies

We next studied the selectivity of D-RFRTs against integrin $\alpha_v\beta_3$ (**Figure 2.2a**). We incubated D-RFRTs with U87MG cells, a human glioblastoma cell line which overexpresses integrin $\alpha_v\beta_3$ on the surface.[9,16,17] To facilitate the tracking, we labeled the RFRTs with ZW800, a near-infrared dye molecule (ex/em: 780/800 nm).[18] D-RFRTs efficiently bound with U87MG cells and internalized (**Figure 2.2a**). Co-incubation with free c(RGDyK) (20×) significantly inhibited the uptake, indicating that the targeting was mainly mediated by RGD-integrin interaction. While at early time points, both RFRTs (ZW800) and Dox were distributed in the cytoplasm, Dox was found predominantly in the nuclei at late time points. This is because Dox was gradually released from the nanocarriers and diffused into the nuclei, where it intercalated with DNA to induce cell death.[19] MTT assays were performed with D-RFRTs against U87MG cells, which found a concentration-dependent cytotoxicity (**Figure 2.2b**). It is worth mentioning that no significant toxicity was observed with Cu(II)-loaded RFRTs (**Figure 2.2b**). This is not surprising because the toxicity of Cu(II) usually occurs when it is in a free form.[20] As observed in our previous studies, Cu(II) remained bound to RFRT interiors[2] and hence, would not cause extra cytotoxicity.

2.2.3 *In vivo* studies

We intravenously (iv) injected D-RFRTs and free Dox (5 mg Dox/kg) into normal mice, and studied the circulation half-lives of D-RFRTs and free Dox by analyzing the Dox contents in the blood at different time points (**Figure 2.2c**). Free Dox showed a quick washout from the circulation and a short half-life of 6.5 min, which is similar to our previous observations.[19] For D-RFRTs, we observed a biphasic plasma concentration profile with a second phase $t_{1/2}$ of 27 h

(**Figure 2.2c**, simulation performed with software WinNonlin). As mentioned above, Cu-based complexes are easily subjected to transchelation in the blood.[15] Such a significantly extended half-life again supports the hypothesis that Dox was mostly located at the interiors of the nanocages.

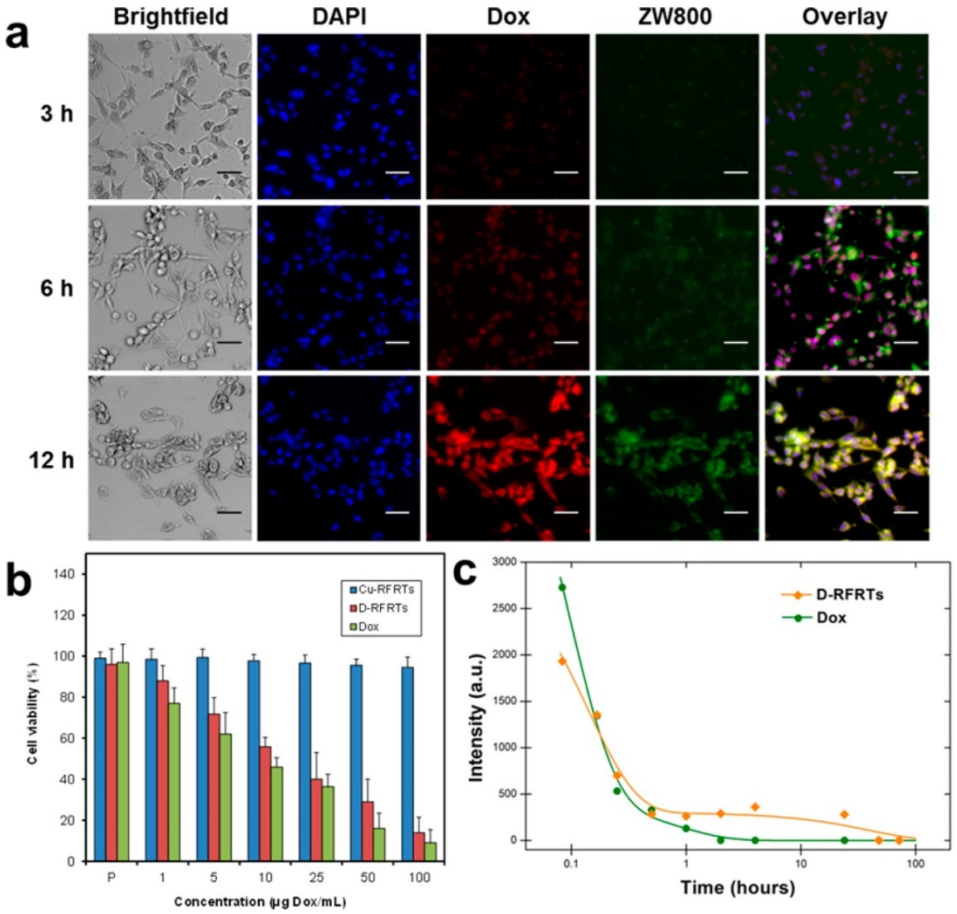

Figure 2.2 *In Vitro* Studies. (a) Time dependent uptake of ZW800-labeled D-RFRTs by U87MG cells. Blue, DAPI; red, Dox; green, ZW800. Scale bar, 50 μm. (b) Viability assay results of U87MG cells with D-RFRTs, free Dox, and Cu-bearing RFRTs. (c) Plasma Dox concentrations at different time points after iv injection of D-RFRTs or free Dox into healthy nude mice.

We then used NIRF imaging to study the tumor selectivity of D-RFRTs in a subcutaneous U87MG tumor model. ZW800-labeled D-RFRTs (5 mg Dox/kg) were iv injected and images were taken at selected time points on a Maestro II system. Results from 24 h are

shown in **Figure 2.3a**. Strong activities from ZW800 were observed in the tumor areas with a tumor-to-normal-tissue ratio of 55. Immediately after the imaging at 24 h, the animals were sacrificed. The tumors as well as major organs were harvested, placed on a sheet of black paper, and subjected to an *ex vivo* imaging study (**Figure 2.3a**). We found that the activities in the tumor were two times higher than those in the liver, and the accumulation in other organs was low (**Figure 2.3b**).

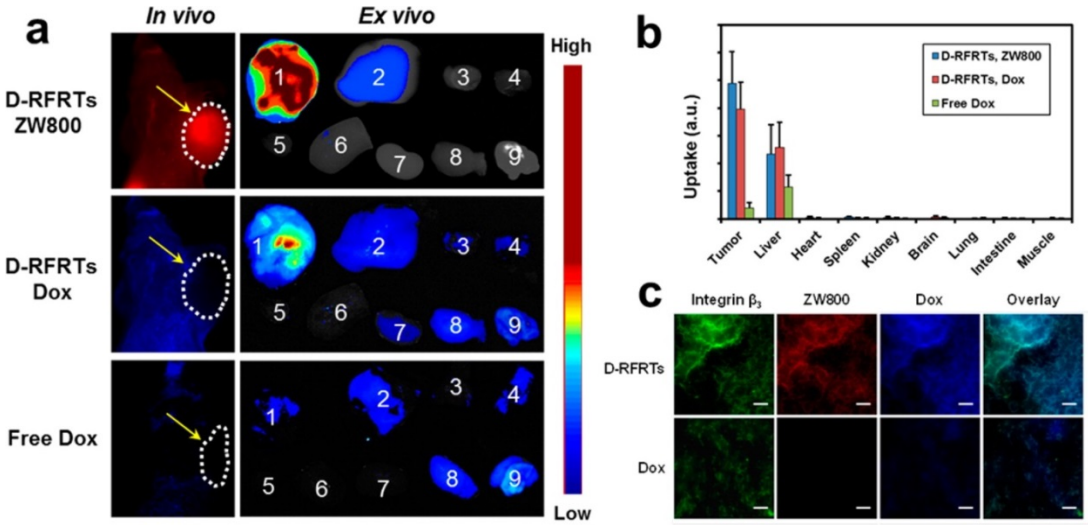

Figure 2.3 *In Vivo* Studies. (a) *In vivo* and *ex vivo* imaging results of U87MG tumor-bearing mice injected with ZW800-labeled D-RFRTs and free Dox. For *ex vivo* studies, the organs were arranged in the following order: 1, tumor; 2, liver; 3, lung; 4, muscle; 5, heart; 6, spleen; 7, kidneys; 8, brain; 9, intestine. (b) Column histograms of fluorescence activities in different organs obtained from the *ex vivo* imaging data. (c) Immunohistology results from tumor sections. Good overlap was found between RFRTs (ZW800) and positive integrin β_3 staining, indicating that the targeting was mainly mediated by RGD-integrin interaction. Dox, on the other hand, displayed a diffusive distribution pattern, suggesting the release of Dox from the carriers. Green, Cy5.5; red, ZW800; blue, Dox. Scale bar, 50 μm.

We also studied the distribution of Dox (ex/em: 480/570 nm). Unlike the observation with ZW800, we found a low tumor-to-normal-tissue contrast from *in vivo* imaging (0.11, **Figure 2.3a**). This was attributed to the strong tissue auto-fluorescence from the animal

skin as the excitation/emission of Dox lies in the visible spectrum window. Indeed, *ex vivo* Dox imaging exhibited a biodistribution pattern that was similar to the ZW800 results (**Figure 2.3a**). As a comparison, free Dox at the same dose was injected in a control group. In that case, both *in vivo* and *ex vivo* imaging found a much lower tumor uptake (**Figure 2.3a, b**).

Histology studies were performed with the tumor tissues (**Figure 2.3c**). Good correlation was observed between RFRT (ZW800) and anti-integrin β_3 staining (Cy5), suggesting that the targeting was mainly mediated by RGD-integrin interaction. Notably, most of the nanocarriers remained within the blood vessels, likely caused by association with integrins expressed on endothelial cells. On the other hand, Dox showed a more disseminated distribution pattern as many of the activities were found outside of the vessels. It indicates that Dox was released from the nanocages and diffused into the interstitial space and tumor cells.

2.2.4 Therapy studies

A therapeutic study was performed in U87MG subcutaneous tumor models. Briefly, D-RFRTs (5 mg Dox/kg) were iv injected every three days for two weeks (n = 5). In the control groups, PBS, RFRTs, and free Dox at the same dose were injected (n = 5). Eighteen days after the start of the treatment, D-RFRT group showed a tumor volume of 122.02 ± 80.35 mm^3, compared to that of 924.34 ± 269.57 mm^3 for the PBS group and 874.97 ± 253.6 mm^3 for the RFRT group (**Figure 2.4**). This represents a tumor growth inhibition (TGI) rate of 89.6%, which is significantly higher than that of 74.0% for free Dox (P< 0.05). No significant weight loss was observed with the D-RFRT treated mice.

Cardiotoxicity has been one major limiting factor in Dox-based therapy.[21] To study this, we performed caspase-3 staining on the heart tissues from both Dox and D-RFRT treated mice (**Figure 2.5a**). A much lower level of positive staining was observed with the D-RFRT group,

indicating mitigated toxicity by using RFRTs as a drug carrier. Similarly, H&E staining found necrosis in the tumors treated with D-RFRT, but no obvious pathological abnormalities such as hemorrhage, edema, lymphocyte infiltration and necrosis in major organs including the heart (**Figure 2.5b**).

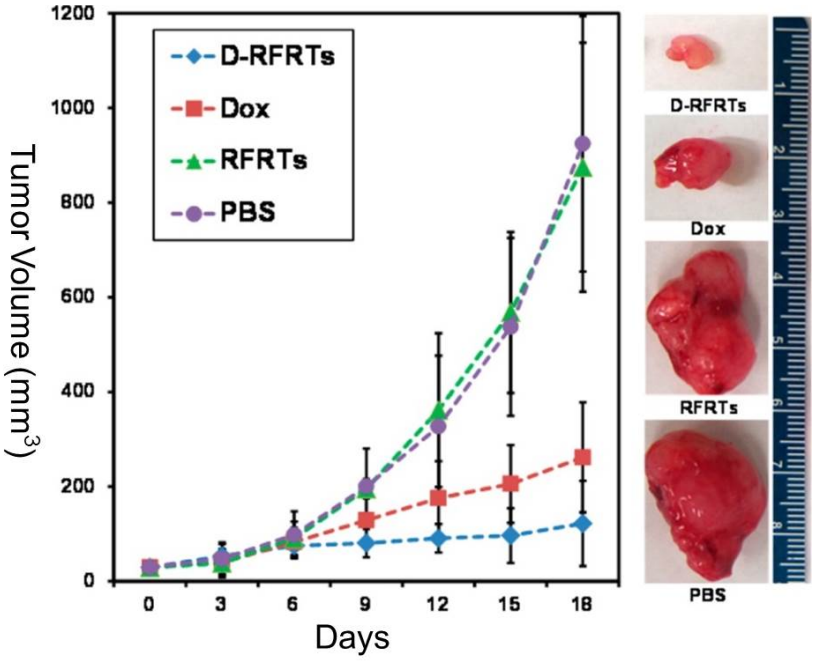

Figure 2.4 Therapy Studies Performed on U87MG Tumor-Bearing Nude Mice. On day 18, significant difference in tumor growth was found between D-RFRT treated mice and those treated with PBS, RFRTs and free Dox ($P < 0.05$). Eighteen days after the onset of the treatment, a TGI rate of 89.6% was observed for D-RFRTs, in comparison to that of 74.0% for free Dox ($n = 5$/group).

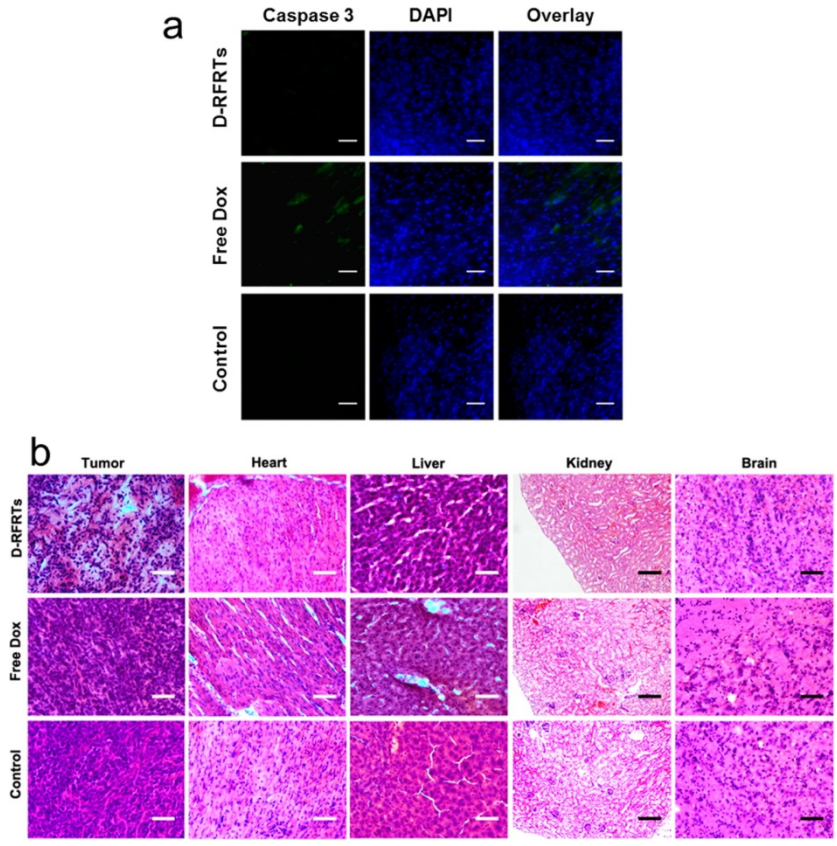

Figure 2.5 Histological Analyses on Major Organs. (a) Immunofluorescence staining of caspase-3 for myocardium from D-RFRTs, free Dox and PBS treated mice. Blue, DAPI; green, caspase-3. Scale bar: 50 μm. (b) H&E staining results from tumors and major organs. More necrosis was found in the tumors from the D-RFRT group than that from the Dox group. No obvious pathological abnormality was found in other normal tissues for D-RFRT treated mice. Scale bar, 50 μm.

2.3 Conclusions[b]

We showed that precomplexation with Cu(II) can significantly improve the loading of Dox onto RFRT nanocages. Such a metal-assisted Dox loading has been observed previously with liposome-based nanocarriers,[22,23] though with a different mechanism. Gel-filtration chromatography found an overall unchanged nanoparticle size, suggesting that the drug was mostly internalized into the cavity of the particles. This was supported by the observations made

[b] Zipeng Zhen, Wei Tang, Hongmin Chen, Xin Lin, Trever Todd, Geoffrey Wang, Taku Cowger, Xiaoyuan Chen, and Jin Xie**ACS Nano* **2013**, *7*, 4830–4837. Reprinted here with permission of publisher.

in the drug release and circulation half-life studies, which found no sign of copper transchelation when exposing D-RFRTs to serum proteins. Also, it was found that the loading of Dox–Cu can be efficiently blocked by free Cu(II), which is known to be encapsulated into the interiors of RFRTs. There are both threefold and fourfold symmetric channels present on FRT surface.[24] The threefold channel is hydrophilic and usually serves as a pathway to transfer metal cations in and out of the protein cage, with a potential gradient directing toward the cavity of the nanocages.[24] The fourfold channel, on the other hand, has a potential gradient in the opposite direction, and is believed to be used to expel species from the cavity.[24] The fact that the internalization of Dox–Cu can be blocked by free Cu(II) suggests that the complex is taken up through a similar mechanism as free metal cations do. It is postulated that complexation with Cu(II) provides a driving force that facilitates the internalization of the drug through the threefold channel, which is otherwise not accessible by Dox.

We observed significantly improved pharmacokinetics of Dox by using RFRTs as a drug carrier. These include an extended circulation half-life, reduced cardiotoxicity, and much higher tumor uptake. Immunostaining results confirmed the role of RGD–integrin interaction in the tumor selectivity. In addition to this specific interaction, we believe that the EPR effect has also played a role. It is noted that the gel-filtration chromatography study found a small portion (less than 4%) of particle clustering in D-RFRTs. The stability, cellular uptake, *in vivo* imaging, and therapy study results, however, found no significant impact of the clustering on tumor targeting and drug delivery.

The surface engineering and drug loading techniques developed in the current study can be extended to construct other FRT-based nanoplatforms. For instance, different targeting motifs (α-melanocyte stimulating hormone, bombesin, folic acid, just to name a few), or combinations

of motifs, can be introduced onto FRTs to allow delivery to a different target.[25] It was reported recently that many cancer cell lines express transferrin receptor 1 (TfR1) to which FRTs can be bound,[26] suggesting the possibility of using parent FRTs as a drug carrier. It is worth noting that the relatively low carrier extravasation rate observed in the current study is due to the association of RFRTs with integrin $\alpha_v\beta_3$ expressed on tumor endothelial cells. For a ligand whose target is on tumor cells instead of tumor vasculature, we expect to see a much higher extravasation rate. In addition to Dox, it is expected that other metal-drug complexes can be loaded *via* a similar route.

In summary, we showed that Dox can be efficiently encapsulated into RFRT nanocages by using Cu(II) as a helper agent. The drug-loaded RFRTs kept integrin selectivity, which was confirmed by both *in vitro* and *in vivo* imaging. Therapeutic studies on a subcutaneous U87MG tumor model found improved tumor suppression and reduced cardiotoxicity. Overall, FRT-based drug delivery is a safe and efficient technology and holds great potential in clinical translation.

Materials and Methods

Expression and Purification of RFRTs and FRTs. The protocol is similar to the one reported previously.[2] In brief, PCR was used to amplify FRTs/RFRTs from cDNA using respective primers to introduce NcoI and XhoI restriction sites flanking the normal start and stop codons. The double digested PCR product was ligated into NcoI/XhoI digested plasmid pRSF with T4 DNA ligase and the ligation mixture was used to transform competent cells of *Escherichia coli* XL1-Blue by standard procedures. The resulting pRSF/FRT (or RFRT) plasmids were screened by appropriate restriction digests, verified by DNA sequencing, and then used to transform the expression strain *E. Coli* BL21(DE3). For expression, a 1 L LB-kanamycin (50 μg/mL) culture of *E. Coli* BL21(DE3)/RFRT was grown at 37 °C until an OD600 of 0.8 was reached. For induction, 1 mM IPTG was added to the culture and the culture was heated at 37 °C for 4 h. After sonication, the cell lysate was centrifuged at 10 400 rpm (12 930*g*) for 30 min to remove cell debris. The supernatant was heated at 60 °C for 10 min and centrifuged at 13 000 rpm for 30 min to remove the precipitates. 2-Mercaptoethanol (10 mM) was added to stabilize the product. The raw product was purified by HPLC using a Superose 6 size exclusion column. The concentration of FRTs/RFRTs was determined by Bradford protein assay. The purified FRTs/RFRTs were stored at −80 °C. Gel-filtration study was also performed on a Superose 6 column using PBS as the mobile phase.

Dox Loading. For Dox loading, Dox (1 mg/mL) was first incubated with Cu(II) (1 mM) at room temperature for 20 min. The mixture was added into a RFRT solution (250 μg/mL) and incubated at room temperature for 120 min. The products were run through a NAP-50 column to remove free Dox and Cu(II). The loaded Dox was quantified at pH 2.0 using a fluorescence spectrometer (F-7000, Hitachi) by comparing to a standard curve. The Dox loading rate in weight percent (Dox/ferritin weight percent), was computed.

Labeling RFRTs/D-RFRTs with ZW800. For labeling, 5 μL ZW800-NHS was added into 1 mL of D-RFRTs solution at 100:1 molar ratio. The mixture was incubated at 4 °C for 30 min and purified by a NAP-50 column. ZW800 was quantified by a UV–vis spectrometer by comparing to a standard curve.

Drug Release. Dox release from D-RFRTs was studied with a slide-A-lyzer dialysis device (10K MWCO, Pierce). In detail, 0.5 mL of D-RFRTs was loaded onto the device and the device was immersed in 15 mL of PBS (pH 7.4 and pH 5.0). At selective time points, 0.5 mL of releasing medium was taken from the tube and replaced with 0.5 mL of fresh medium. The Dox concentrations in the sample solutions were measured by fluorescence spectrometry by comparing to a standard curve. Experiments were performed in triplicate. Drug release in FBS and a DTT solution was studied similarly.

Cellular Uptake and Viability Assays. U87MG human glioblastoma cells were cultured in MEM supplemented with 2 mmol/L L-glutamine, 1.5 g/L sodium bicarbonate, 0.1 mmol/L nonessential amino acids, 1.0 mmol/L sodium pyruvate, and 10% fetal bovine serum at 37 °C in a humidified atmosphere with 5% CO_2. For cellular uptake, 10^5 U87MG cells were seeded onto each well of a 4-chamber slide (Lab-Tek) one day prior to the studies. For cellular imaging, D-RFRTs were added into the chambers to reach a final concentration of 20 μg RFRT/mL. In the control groups, free c(RGDyK) at a 20× molar concentration was added 1 h prior to the addition of ZW800 labeled D-RFRTs. At selective time points, the incubation was stopped and the cells

were rinsed 5 times with PBS (pH 7.4) and fixed with 75% ethanol at 4 °C. The slides were mounted with DAPI containing mounting medium (Vector, Inc.) and imaged under an Olympus X71 fluorescence microscope. The cell viability was assessed by MTT assays using a gradient of D-RFRTs (Dox concentrations of 1, 5, 10, 25, 50, and 100 μg/mL). For controls, free Dox and Cu(II)-bearing RFRTs were studied.

Animal Models. Animal studies were performed according to a protocol approved by the Institutional Animal Care and Use Committee (IACUC) of University of Georgia. The U87MG tumor models were generated by subcutaneously injecting 5×10^6 cells in 100 μL of PBS into the right shoulders of 4–6 week old athymic nude mice (Harlan).

Circulation Half-Lives. To determine the circulation half-lives, D-RFRTs and Dox (5 mg Dox/kg) were iv injected into healthy nude mice. At selected time points, 2–10 μL of blood was collected from the tail vein and dissolved in heparin solution (1000 U/mL in PBS). The Dox was extracted by acidified 2-propanol, and the content was detected on a microplate reader by comparing to a standard curve. The results were plotted as the Dox level against time. The circulation half-lives were evaluated by fitting the results into a two-phase decay model.

***In Vivo* Imaging Studies.** The imaging studies started when tumors reached a size between 200 and 500 mm^3. D-RFRTs and Dox at the same Dox dose (10 mg/kg) were injected into U87MG bearing mice ($n = 3$). Images were taken on a Maestro II imaging system (PerkinElmer) at 1, 4, and 24 h post injection (p.i.) time points. After the 24 h scan, all the mice were sacrificed. Tumors as well as major organs were harvested, weighed, and subjected for *ex vivo* imaging. The images were unmixed by the vendor provided software. ROIs were circled around the organs, and the optical intensities (in total scaled counts/s) were read by the Maestro software. After the imaging, the tumors were snap-frozen in O.C.T. (Tissue-Tek) and stocked in a −80 °C freezer. The tumors were sectioned into 10 μm slices and subjected to integrin β_3 staining.

Therapy Studies. For therapy studies, 20 U87MG tumor bearing mice were randomly divided into 4 groups and iv injected with D-RFRTs (5 mg Dox/kg), free Dox (5 mg Dox/kg), RFRTs and PBS every three days for 2 weeks ($n = 5$, initial average tumor size was 29.45 mm^3). The tumor size and body weight were inspected every three days. The tumor size was calculated with the formula: tumor volume = length × $(\text{width})^2/2$. Measured values were presented as mean ± SD. The one-tailed Student's *t* test was used for comparison among groups, with *P*-values of 0.05 or less representing statistical significance. After therapy, major organs as well as tumors were collected and snap-frozen in O.C.T. at −80 °C. These tissues were sectioned into 10 μm slices for Caspase 3 and H&E staining. The anti-caspase 3 antibody (Abcam) detects only the cleaved p17 fragment, but not the precursor form.

References

(1) MaHam, A.; Tang, Z.; Wu, H.; Wang, J.; Lin, Y. *Small* **2009**, *5*, 1706.
(2) Lin, X.; Xie, J.; Niu, G.; Zhang, F.; Gao, H.; Yang, M.; Quan, Q.; Aronova, M. A.; Zhang, G.; Lee, S.; Leaprnan, R.; Chen, X. *Nano Letters* **2011**, *11*, 814.
(3) Douglas, T.; Stark, V. T. *Inorganic Chemistry* **2000**, *39*, 1828.
(4) Sun, C.; Yang, H.; Yuan, Y.; Tian, X.; Wang, L.; Guo, Y.; Xu, L.; Lei, J.; Gao, N.; Anderson, G. J.; Liang, X.-J.; Chen, C.; Zhao, Y.; Nie, G. *Journal of the American Chemical Society* **2011**, *133*, 8617.
(5) Wong, K. K. W.; Mann, S. *Advanced Materials* **1996**, *8*, 928.
(6) Crich, S. G.; Bussolati, B.; Tei, L.; Grange, C.; Esposito, G.; Lanzardo, S.; Camussi, G.; Aime, S. *Cancer Research* **2006**, *66*, 9196.
(7) Yang, Z.; Wang, X.; Diao, H.; Zhang, J.; Li, H.; Sun, H.; Guo, Z. *Chemical Communications* **2007**, 3453.
(8) Uchida, M.; Flenniken, M. L.; Allen, M.; Willits, D. A.; Crowley, B. E.; Brumfield, S.; Willis, A. F.; Jackiw, L.; Jutila, M.; Young, M. J.; Douglas, T. *Journal of the American Chemical Society* **2006**, *128*, 16626.
(9) Cai, W. B.; Shin, D. W.; Chen, K.; Gheysens, O.; Cao, Q. Z.; Wang, S. X.; Gambhir, S. S.; Chen, X. Y. *Nano Letters* **2006**, *6*, 669.
(10) Chen, K.; Chen, X. *Theranostics* **2011**, *1*, 189.
(11) Millard, M.; Odde, S.; Neamati, N. *Theranostics* **2011**, *1*, 154.
(12) Ye, Y.; Chen, X. *Theranostics* **2011**, *1*, 102.
(13) Feng, M.; Yang, Y. L.; He, P. G.; Fang, Y. Z. *Spectrochimica Acta Part a-Molecular and Biomolecular Spectroscopy* **2000**, *56*, 581.
(14) May, P. M.; Williams, G. K.; Williams, D. R. *Inorganica Chimica Acta-Bioinorganic Chemistry* **1980**, *46*, 221.
(15) Shokeen, M.; Anderson, C. J. *Accounts of Chemical Research* **2009**, *42*, 832.
(16) Chen, K.; Xie, J.; Xu, H.; Behera, D.; Michalski, M. H.; Biswal, S.; Wang, A.; Chen, X. *Biomaterials* **2009**, *30*, 6912.
(17) Li, Z.-B.; Wu, Z.; Chen, K.; Chin, F. T.; Chen, X. *Bioconjugate Chemistry* **2007**, *18*, 1987.
(18) Choi, H. S.; Nasr, K.; Alyabyev, S.; Feith, D.; Lee, J. H.; Kim, S. H.; Ashitate, Y.; Hyun, H.; Patonay, G.; Strekowski, L.; Henary, M.; Frangioni, J. V. *Angewandte Chemie-International Edition* **2011**, *50*, 6258.
(19) Quan, Q.; Xie, J.; Gao, H.; Yang, M.; Zhang, F.; Liu, G.; Lin, X.; Wang, A.; Eden, H. S.; Lee, S.; Zhang, G.; Chen, X. *Molecular Pharmaceutics* **2011**, *8*, 1669.
(20) Brewer, G. J. *Clinical Neurophysiology* **2010**, *121*, 459.
(21) Lefrak, E. A.; Pitha, J.; Rosenheim, S.; Gottlieb, J. A. *Cancer* **1973**, *32*, 302.
(22) Abraham, S. A.; McKenzie, C.; Masin, D.; Ng, R.; Harasym, T. O.; Mayer, L. D.; Bally, M. B. *Clinical Cancer Research* **2004**, *10*, 728.
(23) Kheirolomoom, A.; Mahakian, L. M.; Lai, C.-Y.; Lindfors, H. A.; Seo, J. W.; Paoli, E. E.; Watson, K. D.; Haynam, E. M.; Ingham, E. S.; Xing, L.; Cheng, R. H.; Borowsky, A. D.; Cardiff, R. D.; Ferrara, K. W. *Molecular Pharmaceutics* **2010**, *7*, 1948.
(24) Takahashi, T.; Kuyucak, S. *Biophysical Journal* **2003**, *84*, 2256.
(25) Lee, S.; Xie, J.; Chen, X. *Chemical Reviews* **2010**, *110*, 3087.

(26) Fan, K.; Cao, C.; Pan, Y.; Lu, D.; Yang, D.; Feng, J.; Song, L.; Liang, M.; Yan, X. *Nature Nanotechnology* **2012**, *7*, 459.

CHAPTER 3

FOLIC ACID CONJUGATED FERRITINS AS PHOTOSENSITIZER CARRIERS FOR PHOTODYNAMIC THERAPY

3.1 Introduction

Photodynamic therapy (PDT) is an emerging treatment modality which is under intensive preclinical and clinical investigations for the treatment of many types of diseases, including cancer, age-related macular degeneration (AMD), localized infection, and non-malignant skin conditions.[1] PDT requires photosensitizers, light, and oxygen to active. The photosensitizers are usually inactive in the dark. When irradiated with light at specific wavelength, the photosensitizers can transfer energy to nearby oxygen, produce cytotoxic reactive oxygen species (ROSs) such as $^1O_2$, and kill cancer cells. Ideally, this treatment can be confined to the areas of irradiation, inducing little systematic toxicity. In clinical, however, PDT is often associated with side effects, particularly to the skin and eyes.[2,3] Patients with PDT treatment have to stay away from sunlight or even room light for up to two months to avoid phototoxicity.[4] This situation is because that conventional photosensitizers have poor tumor-to-normal tissue selectivity.[5,6] To enhance tumor accumulation, the photosensitizers can be site-specifically delivered by coupling with tumor targeting ligands, such as folic acid. The folic acid receptor, is found to be overexpressed in about 40% human cancers and is able to mediate endocytosis of folic acid conjugated cargos.[7-9] However, most photosensitizers are hydrophobic and do not provide conjugation-friendly functional groups.

Ferritins are ideal drug carriers due to their unique nanostructure and facile surface modification. We have demonstrated that $ZnF_{16}Pc$, a near-infrared (NIR) photosensitizer, can be loaded into ferritin cavities at extremely high efficiency (up to 60 wt%).[10] In the present study, we loaded $ZnF_{16}Pc$ into folic acid-conjugated ferritins (P@FA-FRTs), and investigated the feasibility of the engineering ferritins for cancer cell targeting PDT. The P@FA-FRTs could efficiently home to and retain in 4T1 cells, which was attributed to folic acid receptor-mediated internalization. When tested *in vivo*, the PDT treatment caused efficient tumor growth suppression and cancer metastasis inhibition, without inducing detectable side effects.

3.2 Results and Discussion[c]

3.2.1 Cell targeting of P@FA-FRTs

We used human heavy chain ferritins throughout the whole study. The expression, production, and purification of ferritins have been reported by us before.[11] In our previous studies, we have successfully conjugated peptides[12] and dyes[13] to the surface of ferritins. A similar conjugation chemistry was used to achieve the coupling of folic acid to ferritins.[14] The folic acid coupled ferritins can still efficiently load $ZnF_{16}Pc$, yielding P@FA-FRTs.[15] Although it is possible to achieve formulations of even higher $ZnF_{16}Pc$ loading rates,[10] we used a 40 wt% formulation for the present study. This is based on the consideration that further increasing the loading rate may lead to compromised particle colloidal stability and/or cause self-quenching. The same loading rate was used for studies with RGD modified ferritins in our previous studies.[10]

Targeting specificity and internalization were investigated *in vitro* with 4T1 cells, which is folic acid receptor positive.[16,17] To facilitate the tracking of ferritins, P@FA-FRTs were

[c] Zipeng Zhen, Wei Tang, Weizhong Zhang, and Jin Xie* *Nanoscle* **2015**, *7*, 10330-10333. Reprinted here with permission of publisher.

labelled with IRDye800 (ex/em: 780/800 nm). For comparison, $ZnF_{16}Pc$ loaded parental ferritins were also investigated. Compared to ferritins, P@FA-FRTs display a much higher uptake by 4T1 cells (**Figure 3.1a**). Fluorescence microscopy found strong fluorescence signals evenly distributed in the cell plasma (**Figure 3.1a**). The uptake was attributed to folic acid receptor mediated endocytosis, which was observed previously with other types of nanoparticles that were coupled with folic acid.[18-20]

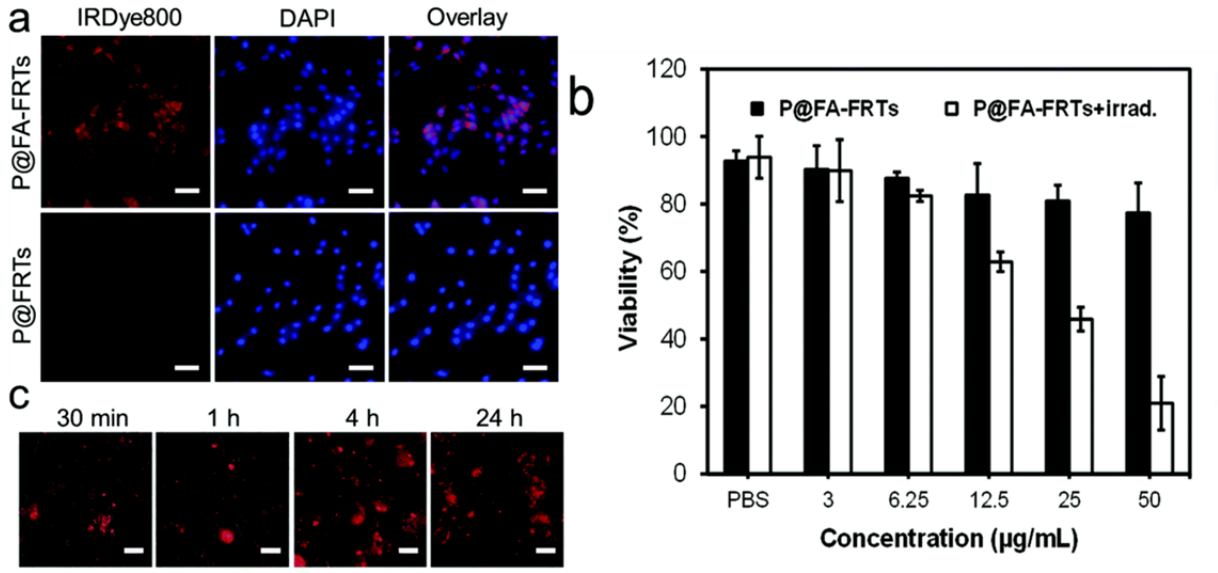

Figure 3.1 Cell Uptake and Phototoxicity of P@FA-FRTs. (a) Cell uptake studies. P@FA-FRTs (IRDye800 labeled) were efficiently internalized by 4T1 cells while parental ferritins were not. Red, IRDye800; blue, DAPI. Scale bars, 50 μm. (b) MTT cell viability assay results. Concentration dependent cell death was observed with P@FA-FRT-mediated PDT. Light irradiation: 671 nm, 100 mW/cm^2 for 200 s. (c) EthD-1 cell assay results. When extending the incubation time, there was an increased level of cell death, marked as red fluorescence. Red, EthD-1 (ex/em = 528/617 nm). Scale bars, 50 μm.

3.2.2 *In vitro* PDT

We investigated cell toxicity by both the 3-(4,5-dimethylthiazol-2-yl)-2,5-diphenyltetrazolium bromide (MTT) assay and the ethidium homodimer-1 assay (EthD-1, a.k.a. dead assay). In the dark, P@FA-FRTs induced little toxicity to cells; but when the incubation was followed by 671

nm irradiation (100 mW/cm^2, 200 seconds), extensive cell death was observed (**Figure 3.1b**). The toxicity is dependent on the incubation time and P@FA-FRT concentration. When the incubation time was fixed at 24 h, the cell survival was inversely correlated to the drug dose, showing viability values of 89.85 ± 9.22, 82.37 ± 1.66, 62.83 ± 2.90, 45.84 ± 3.55, and 20.91 ± 7.96% at $ZnF_{16}Pc$ concentrations of 3, 6.25, 12.5, 25, and 50 μg/mL, respectively (**Figure 3.1b**). Meanwhile, when the $ZnF_{16}Pc$ concentration was maintained (50 μg/mL), there was clearly an increased level of cell death when the incubation time was extended (**Figure 3.1c**).

3.2.3 *In vivo* immunogenicity

The *in vivo* studies were performed in 4T1 tumor bearing BALB/c mice. This is different from our previous investigations, where immunodeficient mice were used for tumor model establishment.[10] One of the concerns with the change, however, is that our ferritins are of human origin. Hence, the injected ferritin formulations are potentially immunogenic and may cause immune response that is detrimental or even lethal to the host. Hence, before the therapy studies, we conducted a safety study with normal BALB/c mice. Specifically, we injected large doses of ferritins, either intraperitoneally (i.p., 50 mg/kg) or intravenously (i.v., 15 mg/kg), to normal BALB/c mice and observed the animals for 2 weeks (**Figure 3.2**). Except for a seemingly minor weight loss in the first 24 h, there was no significant weight change in the observation period (**Figure 3.2**). In addition, there was no sign of severe acute inflammation or other abnormalities, suggesting good tolerance of the host to ferritins. This is not unexpected because human and mouse ferritins share a great deal of similarity. In particular, there is a 93% similarity in amino acids sequence between human and mouse heavy chain ferritins.[21]

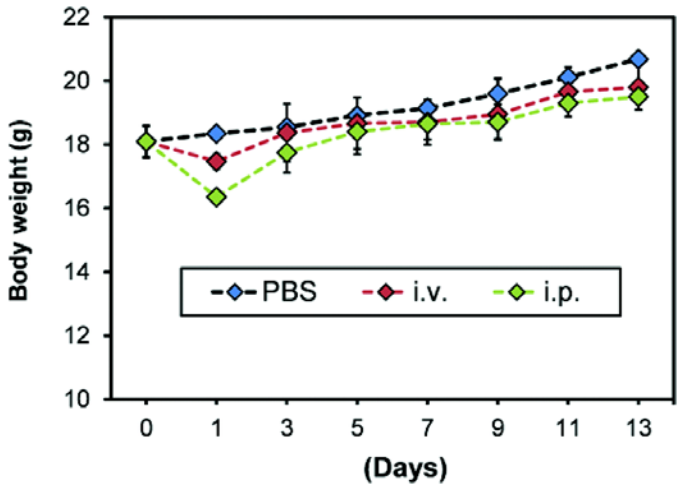

Figure 3.2 Body Weight Curves. Compared to the control group, the animals receiving either i.p. or i.v. injection of ferritins (50 mg/kg for i.p. injection and 15 mg/kg for i.v. injection) showed no significant weight loss except for a seemingly minor weight drop on day 1.

3.2.4 *In vivo* tumor targeting

We set out to study the targeting specificity of P@FA-FRTs in 4T1 tumor bearing animals. Specifically, IRDye800 labelled P@FA-FRTs were i.v. injected (5 mg/kg); fluorescence images were acquired at different time points on a Maestro II imaging system using a NIR filter (750 to 940 nm). The tumor areas were shaven to minimize interference by hairs. For control, $ZnF_{16}Pc$-loaded FRTs (P@FRTs, 40 wt% loading rate, IRDye800 labelled) were administered and evaluated. For P@FRTs, the nanoparticles were concentrated in the tumors at early time points (**Figure 3.3a**), but were gradually cleared from the area. At 24 h, only weak signals were retained in tumors (**Figure 3.3a**). For P@FA-FRTs, on the other hand, there was a much higher level of the fluorescence signal retained in tumors at 4 h or even 24 h. The difference in the tumor retention was attributed to the difference in the tumor uptake mechanism. For P@FRTs, the tumor accumulation was mainly mediated by the enhanced permeability and retention (EPR) effect. Without specific binding, however, the particles over time may re-enter the circulation or be cleared away by the lymphatic system. For P@FA-FRTs, on the other hand, many of the

particles are tethered to the cancer cell surface or are even internalized by interaction with the folic acid receptor, resulting in longer tumor retention. According to the region of interest (ROI) analysis, the tumor uptake of P@FA-FRTs at 24 h was 8.31 ± 1.54 times higher than that of P@FRTs (**Figure 3.3b**). Notably, fluorescence activities may slowly drop after particle endocytosis due to dye degradation in the acidic endosome/lysosome environments. Hence, the actual difference in tumor uptake of the particles may be even more significant. The difference in tumor uptake was also confirmed by post mortal histology studies (**Figure 3.3c**). Relative to P@FRTs, a high tumor uptake was observed with P@FR-FRTs. Most signals were found to be outside of the tumor vasculatures (stained by anti-CD31 antibody, labelled with phycoerythrin) and were distributed randomly, suggesting the contribution of the EPR effect to the tumor uptake.

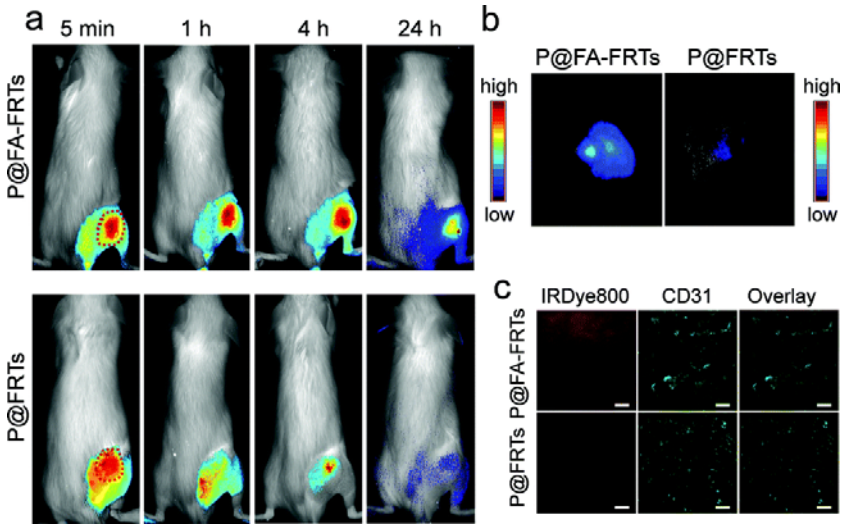

Figure 3.3 Tumor Targeting of P@FA-FRTs. (a) *In vivo* tumour targeting, investigated with 4T1 tumour-bearing BALB/c mice. Compared with parental ferritins, P@FA-FRTs were more efficiently accumulated in tumours, especially for late time points. (b) *Ex vivo* imaging to compare tumour uptake between P@FA-FRTs and P@FRTs. (c) Immunofluorescence staining results. Scale bars: 100 μm.

3.2.5 Therapy studies

We also investigated tumor treatment efficacy with P@FA-FRTs. The same 4T1 tumor models were used for the studies. Specifically, we i.v. injected P@FA-FRTs (1.5 mg $ZnF_{16}Pc$ kg^{-1}, 40 wt%) to the mice and irradiated the tumors at 24 h with a 671 nm laser over a 1 cm diameter beam (300 mW/cm^2, 15 minutes, $n = 5$). The control animals received PBS only, or P@FA-FRTs without photoirradiation. The tumor growth was monitored over a span of 2 weeks. While P@FA-FRTs alone induced no impact to tumor growth, P@FA-FRTs plus photoirradiation led to significant tumor growth suppression (**Figure 3.4 a & b**). Relative to the control animals, the tumor growth inhibition (TGI) rate of the treatment group was 82.65% on day 14 (**Figure 3.4 a**). Meanwhile, the treatment did not adversely affect the body weight of the animals (**Figure 3.4 c**). In fact, there was even a slight increase in the body weight of the treatment group on day 14.

To further assess the PDT treatment, we performed H&E staining on tumor and normal tissue samples. These include the lung, which is a common metastasis site for breast cancer. In particular, previous studies with 4T1 rodent models frequently found metastasis to the lung.[22] Indeed, in the two control groups, we observed multiple metastasis sites in the lung, manifesting pathological changes such as thickened alveolar membranes, bleeding, and inflammation (**Figure 3.4 d**). In the treatment group, on the other hand, there was no sign of metastasis in the lung as well as other normal tissues. The exact reason behind the suppressed metastasis is unknown. It is postulated, however, that an anti-tumor immune response stimulated by PDT may have contributed. Unlike chemotherapy and radiotherapy, PDT is an immunostimulatory treatment modality. Previous studies have observed that in addition to cellular and vascular effects, PDT induced immune response can also benefit tumor

management.[23,24] More detailed investigation into the anti-tumor immune response will be performed in future studies.

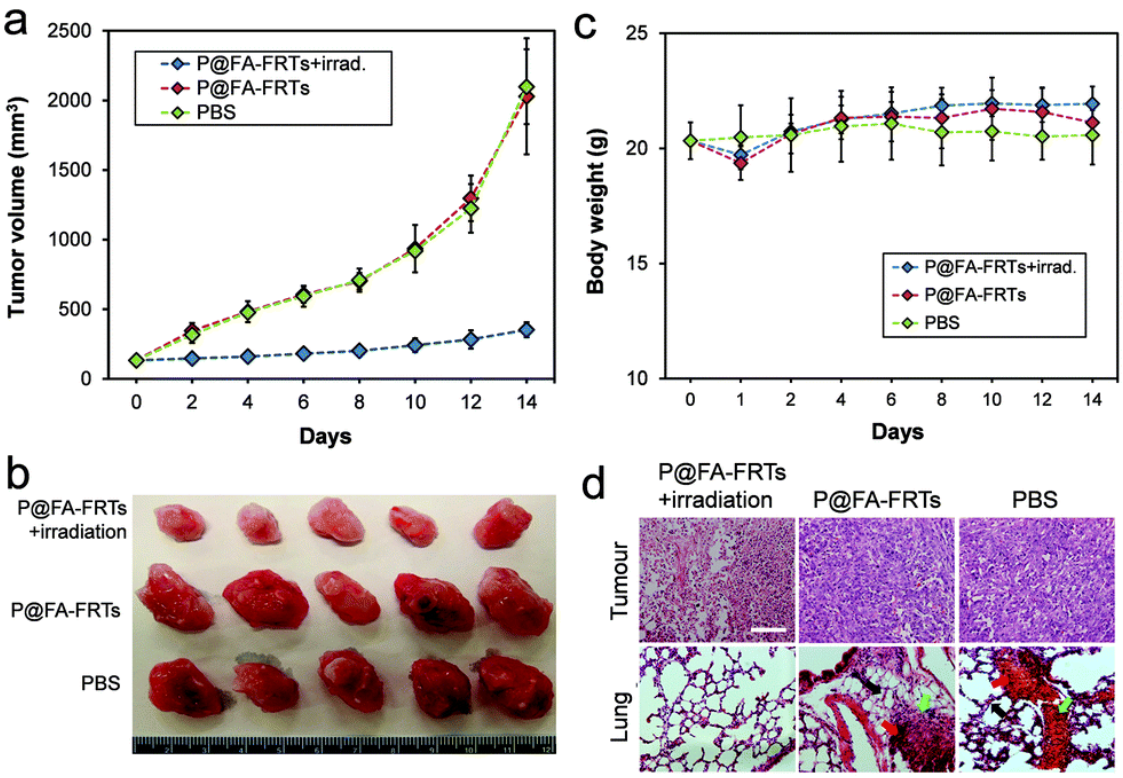

Figure 3.4 Therapy Studies. (a) Tumour growth curves. Significant tumour suppression was observed in animals treated with P@FA-FRT-mediated PDT. Compared to the control group, a tumour growth suppression rate of 82.65 ± 4.11% was observed on day 14. (b) Photographs of dissected tumours from (a). (c) Body weight curves. No significant weight loss was observed for the treatment group. (d) H&E staining with tumour (upper) and lung (lower) samples. Significant necrosis was observed in tumours treated with P@FA-FRT-mediated PDT. In addition, while the control groups showed signs of metastasis in the lung (*e.g.* thickened alveolar membranes [black arrows], bleeding [red arrows], and inflammation sites [green arrows]), there was no sign of lung metastasis for PDT treated animals. Scale bars, 100 μm.

3.3 Conclusions[d]

Overall, we have shown that folic acid can be coupled to ferritins that are loaded with photosensitizers like $ZnF_{16}Pc$. The resulting nanoconjugates after systematic injection can efficiently hone in on tumors. With photoirradiation, the treatment caused efficient tumor growth suppression while minimally affecting normal tissues. More interestingly, it was observed that PDT treatment helped suppress tumor metastasis to the lung, which is likely attributed to a PDT-stimulated anti-tumor response. These observations confirm ferritin as a safe and powerful nanoplatform for efficient delivery of photosensitizers.

[d] Zipeng Zhen, Wei Tang, Weizhong Zhang, and Jin Xie* *Nanoscle* **2015**, *7*, 10330-10333. Reprinted here with permission of publisher.

Materials and Methods

Cell culture: 4T1 (murine breast cancer) cell line was from ATCC, and grown in RMPI 1640 medium supplemented with 10% fetal bovine serum (FBS) and 100 U/mL penicillin and 1% streptomycin (MediaTech, USA). For cell culture, 4T1 cells were incubated at 37 °C in 5% CO_2.

Ferritin purification, folic acid coupling and $ZnF_{16}Pc$ loading: The protocols for producing ferritins and loading $ZnF_{16}Pc$ onto them are similar to what were published by us previously.[10] The photosensitizer loading was achieved by adding $ZnF_{16}Pc$ in DMSO into a FRT/FA-FRT solution in 0.01 M PBS (pH 7.4). After that, the mixture was incubated at room temperature for 45 min. The raw products were subjected to purification by going through a NAP-5 column to remove the unloaded $ZnF_{16}Pc$. The $ZnF_{16}Pc$ content was determined spectroscopically by comparing with a standard absorbance curve of $ZnF_{16}Pc$. The FRT/FA-FRT concentration was determined by Bradford protein assay. The loading rate was computed and expressed in weight percent (wt%). Coupling folic acid to ferritins was conducted following a published protein conjugation protocol with minor changes.[14] Typically, 5 mg of folic acid, 50 mg of 1-ethyl-3-(3-dimethylaminopropyl) carbodiimide hydrochloride (EDAC), and 50 mg of N-hydroxysuccinimide (NHS) were dissolved in 50 mL of a bicarbonate buffer (50 mM $NaHCO_3$, pH 6) at room temperature (25 °C). A 10 mL aqueous solution (0.5 mg/mL) was subsequently added, and the mixture gently agitated for 2 h at room temperature. The raw product was purified by dialysis (MWCO = 100k) against PBS (pH 7.4) at 4 °C. The PBS was replenished every 12 hours, for at least 4 times. The purified FA-FRTs were concentrated using a centrifugal filter unit (Millipore, 100k). Bradford protein assay was used to determine the concentration of FA-FRTs.

For IRDye800 labelling, ferritins or FA-FRTs were incubated with IRDye800-NHS for 30 min at room temperature and then purified through a NAP-5 column. A starting molar ratio of 2:1 between the dye and the protein nanocage was used. The coupling efficiency was assessed spectroscopically by comparing with a predetermined IRDye800 absorbance standard curve (780 nm). It was determined that the final conjugates have on average one IRDye800 per ferritin particle.

Animal models: All the animal studies were performed following a protocol approved by the Institutional Animal Care and Use Committee (IACUC) of the University of Georgia. For bio-safety evaluation, a total of 18 normal BALB/c mice were used. The animals were randomly divided into 3 groups, with 6 mice per group. Ferritins were administered either intraperitoneally (i.p.) at 50 mg/kg or intravenously (i.v.) at 15 mg/kg to two groups of the animals. A third group was monitored for controls. The animals were observed daily and their body weights were monitored for two weeks. 4T1 tumor models were established by subcutaneous injection of ~10^6 4T1 cancer cells to the hind limbs of 4-5 week BALB/c mic. The imaging or therapy studies were conducted 1 week after the inoculation when the tumors reached a size of ~100 mm^3.

***In vivo* tumor targeting:** For tumor targeting, IRDye800-labeled P@FA-FRTs (0.75 mg $ZnF_{16}Pc$/kg) were i.v. injected to 4T1 tumor bearing animals (average tumor size ~77.78 ± 11.84 mm^3, n = 5). Whole-body fluorescence images were acquired on a Maestro II imaging system (PerkinElmer) using an NIR emission filter (750 – 940 nm) up to 24 h post injection. The fluorescence images were unmixed by the vendor provided software. ROIs were circled around tumor areas, and the average optical intensities (in total scaled counts/cm^2/s) were recorded and

compared. After the 24 h imaging, the animals were euthanized. The tumors as well as major organs were harvested for histology studies.

***In vivo* therapy studies:** The therapy studies were also performed in 4T1 tumor models. For the treatment group, the animals were i.v. injected with P@FA-FRTs (1.5 mg $ZnF_{16}Pc$/kg). The tumors were irradiated at 24 h by a 671 nm laser (300 mW/cm^2, over a ~1 cm diameter beam) for 15 min. The two control groups received (1) P@FA-FRTs without irradiation, and (2) PBS only. Tumor sizes were measured every other day by a calliper and computed following the formula: size (mm^3) = length (mm) × width (mm)^2/2.

Immunofluorescence staining: The cryogenic slides with 8 μm thickness were fixed with cold acetone for 30 min and washed by running water for 5 min. Subsequently, phycoerythrin-labeled anti-CD31 antibody (ab25644) was incubated with the slides at 4 °C overnight. After gently rinsing with PBS, the slides were mounted. The images were acquired on an Olympus IX71 microscope.

Hematoxylin and eosin staining: H&E staining was performed according to a protocol provided by the vendor (BBC Biochemical). Briefly, 6 μm paraffin-embedded slides were prepared. After treated with 100% xylene for 3 times (3 min each time), the slides were hydrated with a gradient concentrations of alcohol (100, 95, and 70%), each for 3 min. The hematoxylin staining was then performed for 3 min, and the slides were washed with running water for 3 min. The eosin staining was performed for 1 min. The slides were washed, dehydrated, treated with xylene, and then mounted with Canada balsam. The images were acquired on a Nikon Eclipse 90i microscope.

Statistical methods: Quantitative data were expressed as mean ± s.e.m. A two-tailed Student's t-test was used for statistically comparing the treatment group and the control group. $P < 0.05$ was considered statistically significant.

References

(1) Brown, S. B.; Brown, E. A.; Walker, I. *The Lancet. Oncology* **2004**, *5*, 497.
(2) Corti, M. A. M.; Mainetti, C. *Photomedicine and Laser Surgery* **2010**, *28*, 697.
(3) Taub, A. F.; Garretson, C. B. *Journal of Drugs in Dermatology* **2011**, *10*, 1049.
(4) Allison, R. R.; Downie, G. H.; Cuenca, R.; Hu, X.-H.; Childs, C. J. H.; Sibata, C. H. *Photodiagnosis and Photodynamic Therapy* **2004**, *1*, 27.
(5) Triesscheijn, M.; Baas, P.; Schellens, J. H. M.; Stewart, F. A. *Oncologist* **2006**, *11*, 1034.
(6) Vrouenraets, M. B.; Visser, G. W. M.; Snow, G. B.; van Dongen, G. *Anticancer Research* **2003**, *23*, 505.
(7) Gabizon, A.; Shmeeda, H.; Horowitz, A. T.; Zalipsky, S. *Advanced Drug Delivery Reviews* **2004**, *56*, 1177.
(8) Low, P. S.; Kularatne, S. A. *Current Opinion in Chemical Biology* **2009**, *13*, 256.
(9) Parker, N.; Turk, M. J.; Westrick, E.; Lewis, J. D.; Low, P. S.; Leamon, C. P. *Analytical Biochemistry* **2005**, *338*, 284.
(10) Zhen, Z.; Tang, W.; Guo, C.; Chen, H.; Lin, X.; Liu, G.; Fei, B.; Chen, X.; Xu, B.; Xie, J. *ACS Nano* **2013**, *7*, 6988.
(11) Zhen, Z.; Tang, W.; Chen, H.; Lin, X.; Todd, T.; Wang, G.; Cowger, T.; Chen, X.; Xie, J. *ACS Nano* **2013**, *7*, 4830.
(12) Lin, X.; Xie, J.; Zhu, L.; Lee, S.; Niu, G.; Ma, Y.; Kim, K.; Chen, X. *Angewandte Chemie-International Edition* **2011**, *50*, 1569.
(13) Lin, X.; Xie, J.; Niu, G.; Zhang, F.; Gao, H.; Yang, M.; Quan, Q.; Aronova, M. A.; Zhang, G.; Lee, S.; Leaprnan, R.; Chen, X. *Nano Letters* **2011**, *11*, 814.
(14) Ren, Y.; Wong, S. M.; Lim, L.-Y. *Bioconjugate Chemistry* **2007**, *18*, 836.
(15) Garcia, A. M.; Alarcon, E.; Munoz, M.; Scaiano, J. C.; Maria Edwards, A.; Lissi, E. *Photochemical & Photobiological Sciences* **2011**, *10*, 507.
(16) Gao, Z.-G.; Tian, L.; Hu, J.; Park, I.-S.; Bae, Y. H. *Journal of Controlled Release* **2011**, *152*, 84.
(17) Reddy, J. A.; Xu, L. C.; Parker, N.; Vetzel, M.; Leamon, C. P. *Journal of Nuclear Medicine* **2004**, *45*, 857.
(18) Chen, H.; Li, S.; Li, B.; Ren, X.; Li, S.; Mahounga, D. M.; Cui, S.; Gu, Y.; Achilefu, S. *Nanoscale* **2012**, *4*, 6050.
(19) Luo, Z.; Ding, X.; Hu, Y.; Wu, S.; Xiang, Y.; Zeng, Y.; Zhang, B.; Yan, H.; Zhang, H.; Zhu, L.; Liu, J.; Li, J.; Cai, K.; Zhao, Y. *ACS Nano* **2013**, *7*, 10271.
(20) Stella, B.; Arpicco, S.; Peracchia, M. T.; Desmaele, D.; Hoebeke, J.; Renoir, M.; D'Angelo, J.; Cattel, L.; Couvreur, P. *Journal of Pharmaceutical Sciences* **2000**, *89*, 1452.
(21) Torti, S. V.; Kwak, E. L.; Miller, S. C.; Miller, L. L.; Ringold, G. M.; Myambo, K. B.; Young, A. P.; Torti, F. M. *Journal of Biological Chemistry* **1988**, *263*, 12638.
(22) Li, Y.; Jin, M.; Shao, S.; Huang, W.; Yang, F.; Chen, W.; Zhang, S.; Xia, G.; Gao, Z. *BMC Cancer* **2014**, *14*.
(23) Blank, M.; Lavie, G.; Mandel, M.; Keisari, Y. *Oncology Research* **2000**, *12*, 409.
(24) deVree, W. J. A.; Essers, M. C.; Koster, J. F.; Sluiter, W. *Cancer Research* **1997**, *57*, 2555.

CHAPTER 4

FERRITIN NANOCAGES TO ENCAPSULATE AND DELIVER PHOTOSENSITIZERS FOR EFFICIENT PHOTODYNAMIC THERAPY AGAINST CANCER

4.1 Introduction

Photodynamic therapy (PDT) is an emerging treatment modality that has shown promise for many types of disease, including cancer.[1,2] It is known that there are three main mechanisms by which PDT mediates tumor destruction: directly kill tumor cells by the induction of necrosis and/or apoptosis, damage the tumor-associated vessels to induce tumor ischemia, and activate immune responses against tumor cells.[3,4] These three mechanisms influence each other. However, the relative importance of each for the overall tumor response is unclear.[3,4]. In the previous chapter, we have demonstrated that cancer cell-targeted PDT with folic acid-conjugated ferritin can effectively inhibit tumor growth. Tumor vasculature-targeted PDT, which site-specifically delivers photosensitizers to tumor vessels, can be an alternative effective strategy for tumor-targeted PDT treatment.

Ferritin is a powerful platform that can be functionalized with different targeting ligands. We have demonstrated that RGD4C-modified ferritins (RFRTs) can specifically deliver doxorubicin to tumor endothelium cells via the RGD-integrin $\alpha_v\beta_3$ interactions.[5] In the current study, we employed the RFRTs to site-specifically deliver $ZnF_{16}Pc$ molecules (P-RFRTs). When tested on U87MG subcutaneous tumor models, P-RFRTs showed a high tumor accumulation rate (tumor-to-normal tissue ratio of 26.82 ± 4.07 at 24 h), a good tumor inhibition rate (83.64% on

day 12), as well as minimal toxicity to the skin and other major organs. This technology can be extended to deliver other metal-containing photosensitizers and holds great potential in clinical translation.

4.2 Results[e]

4.2.1 Preparation and characterization of P-RFRTs

The drug loading was achieved by adding $ZnF_{16}Pc$ in DMSO into a RFRT solution in 0.01 M PBS (pH 7.4) and, after that, incubating at room temperature for 45 min. The raw products were subjected to purification through a NAP-5 column to remove the unloaded $ZnF_{16}Pc$. The starting concentrations of $ZnF_{16}Pc$ and RFRT were tuned, and the loading capacity was investigated. We found that 1 mg of RFRTs can load up to 1.5 mg of $ZnF_{16}Pc$, yielding a loading rate as high as 60 wt %. For stability considerations, however, we used a formulation with a loading rate of 41.2 wt % for the current investigations. The sizes of the nanoparticles were studied by atomic force microscopy (AFM) analysis (**Figure 4.1 c & d**). We found overall comparable sizes before and after the $ZnF_{16}Pc$ loading (18.3 ± 4.1 nm for RFRTs and 18.6 ± 2.6 nm for P-RFRTs).

Despite the heavy loading, the resulting P-RFRTs are highly stable in PBS. A photograph of P-RFRTs in PBS is shown in **Figure 4.1b**. The solution was stable for more than a week without visible precipitation. In comparison, free $ZnF_{16}Pc$ at the same concentration quickly precipitated out due to its poor solubility. We also investigated the stability of P-RFRTs at pH = 2. Within 10 min, a large amount of blue precipitation had formed at the bottom of the vial (**Figure 4.1b**). It is known that FRT nanocages are disassembled at pH 2.0. This pH-induced

[e] Zipeng Zhen, Wei Tang, Cunlan Guo, Hongmin Chen, Xin Lin, Gang Liu, Baowei Fei, Xiaoyuan Chen, Binqian Xu, and Jin Xie**ACS Nano* **2013**, *7*, 6988–6996. Reprinted here with permission of publisher.

unloading suggests that the cargo was mostly internalized into hollow cores of the nanocages and was released upon particle decomposition.

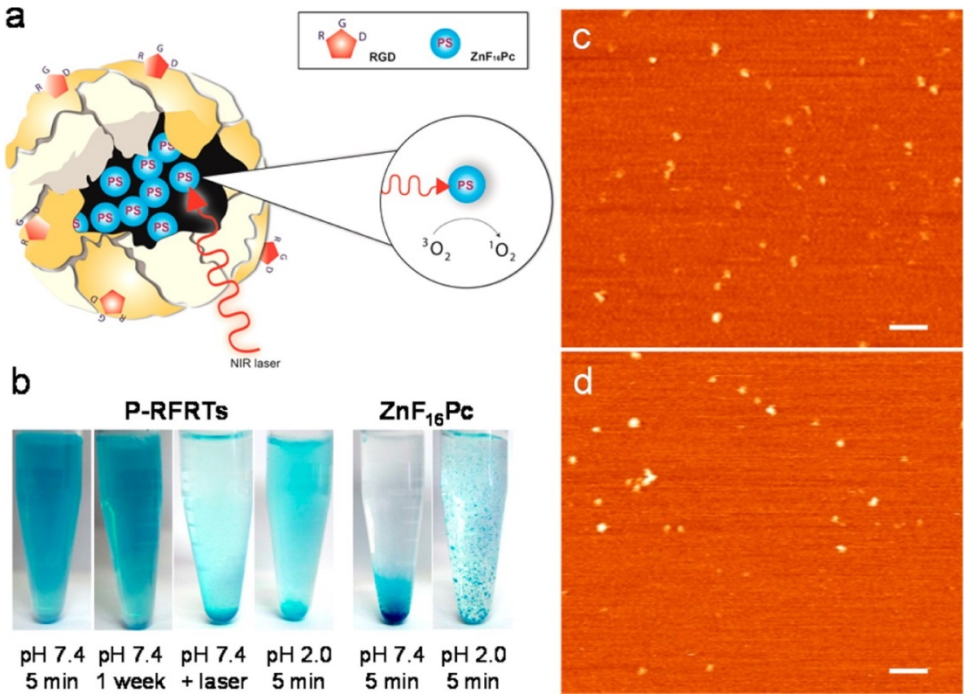

Figure 4.1 $ZnF_{16}Pc$-Loaded and RGD Peptide-Modified Ferritins (P-RFRTs). (a) Schematic illustration of the formation and working mechanism of P-RFRTs. (b) Photographs of P-RFRTs and free $ZnF_{16}Pc$ in PBS under different conditions. AFM images of (c) RFRTs and (d) P-RFRTs. Scale bars, 100 nm.

The generation of $^1O_2$ was studied using a singlet oxygen sensor green (SOSG) reagent (Invitrogen). SOSG is essentially a dye that is fluorescently quenched in its intact form but, upon activation in response to $^1O_2$, produces an increase of fluorescence signals at 525 nm. We incubated P-RFRTs at different concentrations with the SOSG reagent and irradiated the samples with a 671 nm laser. The relative increase of readings at 525 nm was recorded 1 min later. As a comparison, $ZnF_{16}Pc$ was dispersed in PBS containing 1% tween and subjected to the analyses at the same conditions. We found no significant difference between the results from the two groups, suggesting that $ZnF_{16}Pc$ is not quenched in the nanocarriers. We also examined the post-

irradiated P-RFRTs under AFM. Instead of finding ~20 nm nanoparticles, we observed clusters of debris across the scope. The particle destruction was attributed to the $^1O_2$ generated during the irradiation. This agrees with the above observation that $ZnF_{16}Pc$ was unloaded upon particle decomposition.

4.2.2 *In vitro* targeting and PDT

We then studied if the drug loading had affected the particles' ability to interact with integrin $\alpha_v\beta_3$. To facilitate the tracking of particles, P-RFRTs were labeled with ZW800, a near-infrared dye molecule (ex/em = 780/800 nm).[6] The coupling ratio was controlled so that on average one ZW800 was coupled to one RFRT. The *in vitro* studies were performed with U87MG human glioblastoma cells, which are known to express a high level of integrin $\alpha_v\beta_3$.[7] As shown in **Figure 4.2a**, P-RFRTs demonstrated time-dependent internalization by U87MG cells. This internalization was blocked when free c(RGDyK) (30×, relative to protein concentration; it is noted that there are 24 RGD4C moieties on the surface of each RFRT nanoparticle) was coincubated (**Figure 4.2a**). The results suggest that, despite the heavy loading, P-RFRTs kept the targeting specificity toward integrin $\alpha_v\beta_3$.

The particles' phototoxicity was also studied with U87MG cells. Briefly, we incubated cells with P-RFRTs in the dark and at different time points and irradiated them with a 671 nm laser (0.1 W/cm^2, 200 s). The cell viability was studied 120 min post-irradiation by ethidium homodimer-1 staining (Invitrogen), which marked dead cells (**Figure 4.2b**). Increased red fluorescence was found to be correlated with elevated incubation time and was suppressed when free c(RGDyK) (30×) was coincubated. On the other hand, if no laser was applied, the red fluorescence remained at a background level. Similar observations were made from MTT assays, where we found a marginal drop in cell viability when there was no light irradiation and

concentration-dependent cell death when there was. These observations suggest that cytotoxicity only occurs when both $ZnF_{16}Pc$ and light are present, which is the hallmark of PDT-induced phototoxicity.

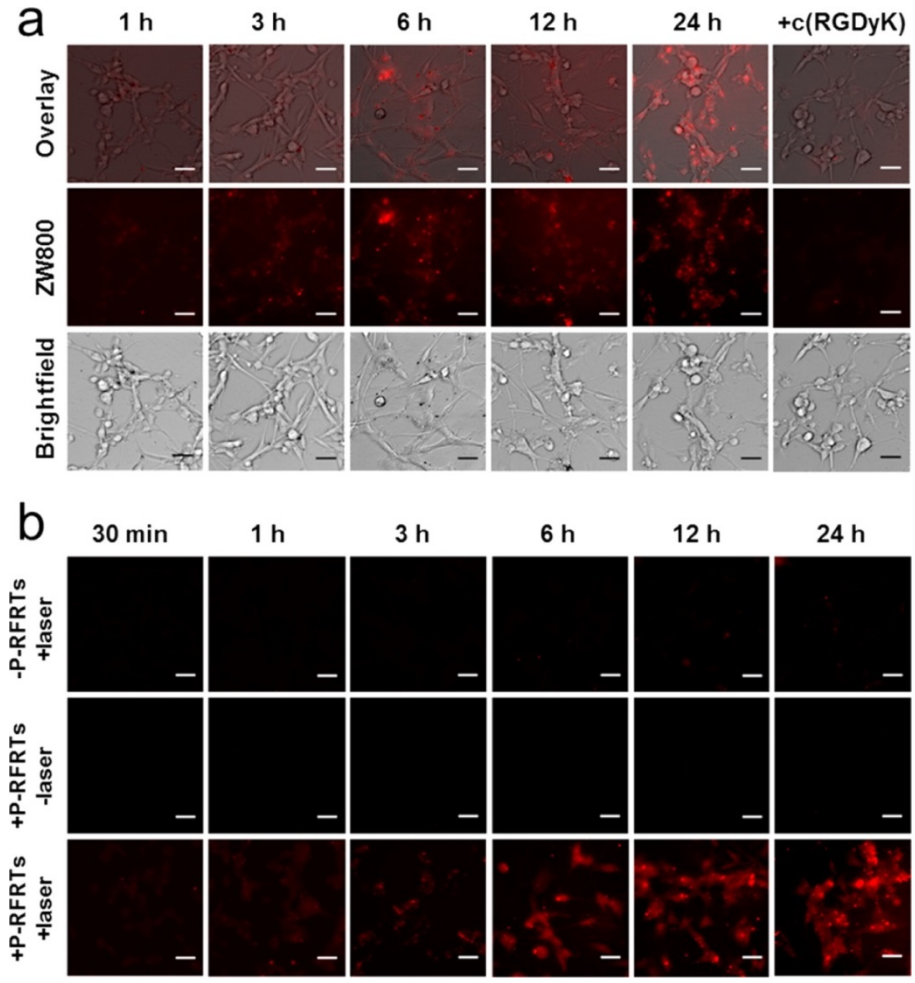

Figure 4.2 Cell Uptake and Phototoxicity of P-RFRTs. (a) Uptake of P-RFRTs (50 μg $ZnF_{16}Pc$/mL) by U87MG cells at different time points. The uptake can be efficiently inhibited if c(RGDyK) (30×) was coincubated. The P-RFRTs were labeled with ZW800 (ex/em = 780/800 nm). Scale bars, 50 μm. (b) Cell viability studies with P-RFRTs on U87MG cells. Elevated cytotoxicity (red fluorescence) was found with increased incubation time in the presence of light irradiation (671 nm, 0.1 W/cm^2 for 200 s). Without irradiation, no significant cell death was found. Red, ethidium homodimer-1 (ex/em = 528/617 nm), which stains dead cells. Scale bars, 50 μm.

4.2.3 *In vivo* imaging

We then studied the tumor selectivity of P-RFRT in subcutaneous (s.c.) U87MG tumor models. We injected ZW800-labeled P-RFRTs (5 mg RFRTs/kg) intravenously (i.v.) and acquired fluorescence images on a Maestro scanner using an "orange" filter (640 to 820 nm) at different time points. Tumor-to-normal tissue (T/N) ratios were evaluated to be 3.82 ± 0.56, 14.47 ± 1.69, and 26.82 ± 4.07 at 1, 4, and 24 h time points, suggesting good tumor accumulation (**Figure 4.3a**). When c(RGDyK) (30×) was injected prior to the P-RFRT injection, the tumor uptake was significantly diminished. This confirms that tumor accumulation was mainly mediated by RGD–integrin interaction. Post-mortem *ex vivo* imaging was performed with tumors and other major organs (**Figure 4.3a**). In addition to accumulation in the tumors, we also found a high level of fluorescence activity in the liver, which is common for a nanoparticle-based drug formulation. The uptake in other organs was much lower. We also examined the particle distribution in tumors by immunofluorescence staining using an anti-integrin β_3 antibody (**Figure 4.3b**). As expected, positive β_3 staining was found on both tumor vasculature and tumor cells.[8,9] The ZW800 signals overlapped well with the positive β_3 staining, confirming that the tumor retention was mainly caused by RGD–integrin interactions.

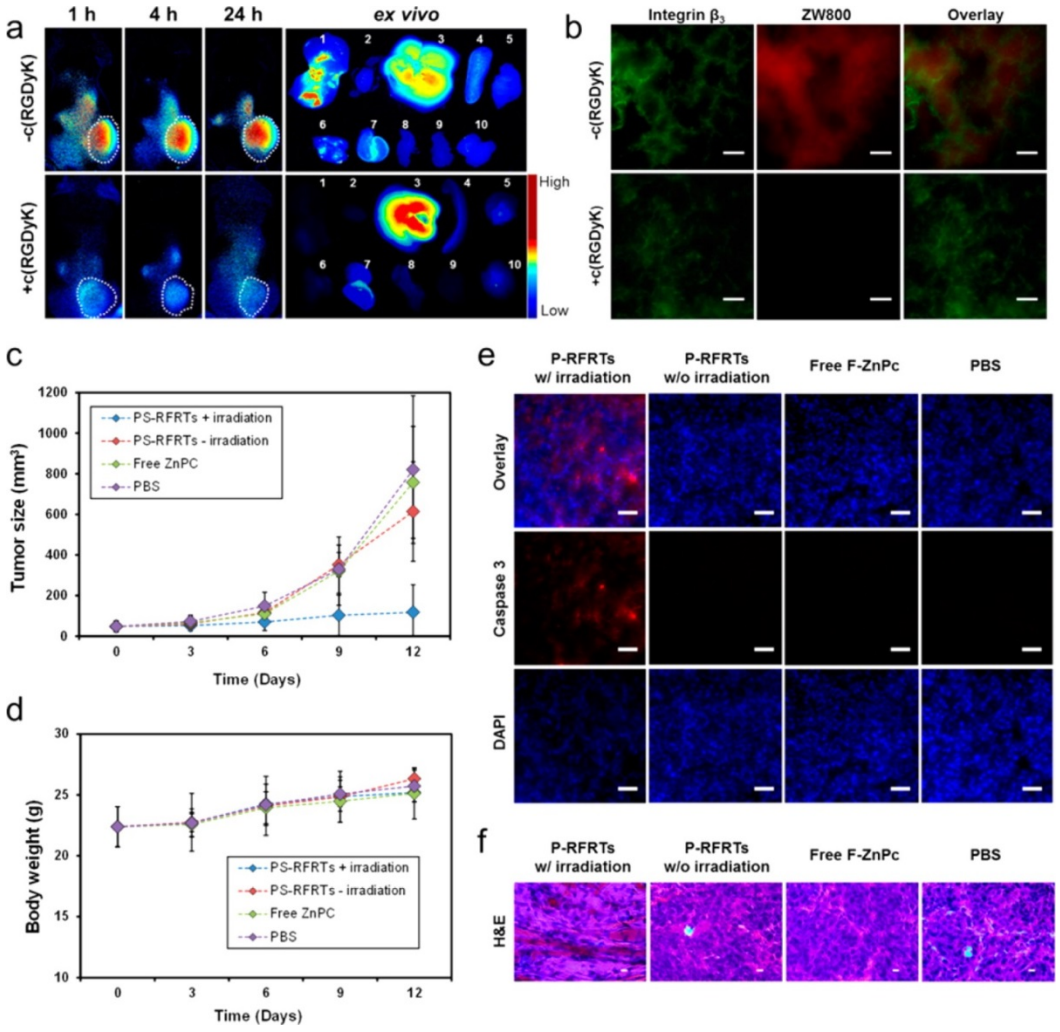

Figure 4.3 *In Vivo* Imaging and Therapy Studies. (a) *In vivo* and *ex vivo* fluorescence imaging results. P-RFRTs were i.v. injected, and images were taken at 1, 4, and 24 h. In the control group, c(RGDyK) (30×) was injected to block the tumor homing. The organs were arranged in the following order: (1) tumor; (2) heart; (3) liver; (4) spleen; (5) skin; (6) lung; (7) kidneys; (8) intestine; (9) muscle; (10) brain. (b) Immunofluorescence microscopic imaging results. Integrin β_3 is upregulated on both tumor vasculature and tumor cells. The distribution of P-RFRTs (ZW800, ex/em = 780/800 nm) was well correlated with the positive integrin β_3 staining (Cy5, ex/em = 650/670 nm), indicating that the tumor homing was mostly mediated by RGD–integrin interactions. In the control group, where c(RGDyK) was preinjected, minimal ZW800 signals were found in tumors. Scale bars, 50 μm. (c) Tumor growth curve. The animals were divided into four groups. Significant tumor suppression was found in the P-RFRTs, with irradiation group ($P < 0.05$). On day 12, a TIR of 83.64 ± 2.52% was found. (d) Weight growth curve. No significant weight drop was found with animals injected with P-RFRTs, with or without irradiation. (e) Caspase 3 staining with tumor tissues. Scale bars, 50 μm. (f) H&E staining with tumor tissues. Scale bars, 10 μm.

4.2.4 Therapy studies

We then evaluated the treatment efficacy of P-RFRTs on a s.c. U87MG tumor model. We i.v. injected P-RFRTs (1.5 mg $ZnF_{16}Pc$/kg) into the animals and illuminated (671 nm) the tumor surface over a 1 cm diameter beam spot (0.3 W/cm^2, 15 min) 24 h after the injection (n = 5). The three control groups are (1) P-RFRTs (1.5 mg $ZnF_{16}Pc$/kg, without irradiation); (2) free $ZnF_{16}Pc$ (1.5 mg $ZnF_{16}Pc$/kg, with irradiation); (3) PBS (without irradiation). Tumor growth was similar in all the control groups but was significantly suppressed in the treatment group (**Figure 4.3c**). On day 12, we observed an average tumor inhibition rate (TIR) of 83.64% from the treatment group and found no impact on animals' body weights (**Figure 4.3d**).

After therapy, we sacrificed the mice and dissected the tumors for histology studies. The apoptosis level in the tumors was examined by caspase 3 staining. We found positive staining with the samples from the treatment group but not with those from the controls (**Figure 4.3e**). Also, H&E staining demonstrates densely packed neoplastic cells in the controls but markedly disturbed tumor architecture in the treatment group (**Figure 4.3f**). These observations agree with the therapy results. To evaluate the size effects, we also performed caspase 3 staining with the skin and H&E staining with other normal organ tissues (*e.g.*, the skin, heart, liver, spleen, lung, kidneys, intestine, muscle, and brain). No abnormalities were observed (**Figure 4.4 a & b**), confirming that P-RFRT has minimal off-target damage.

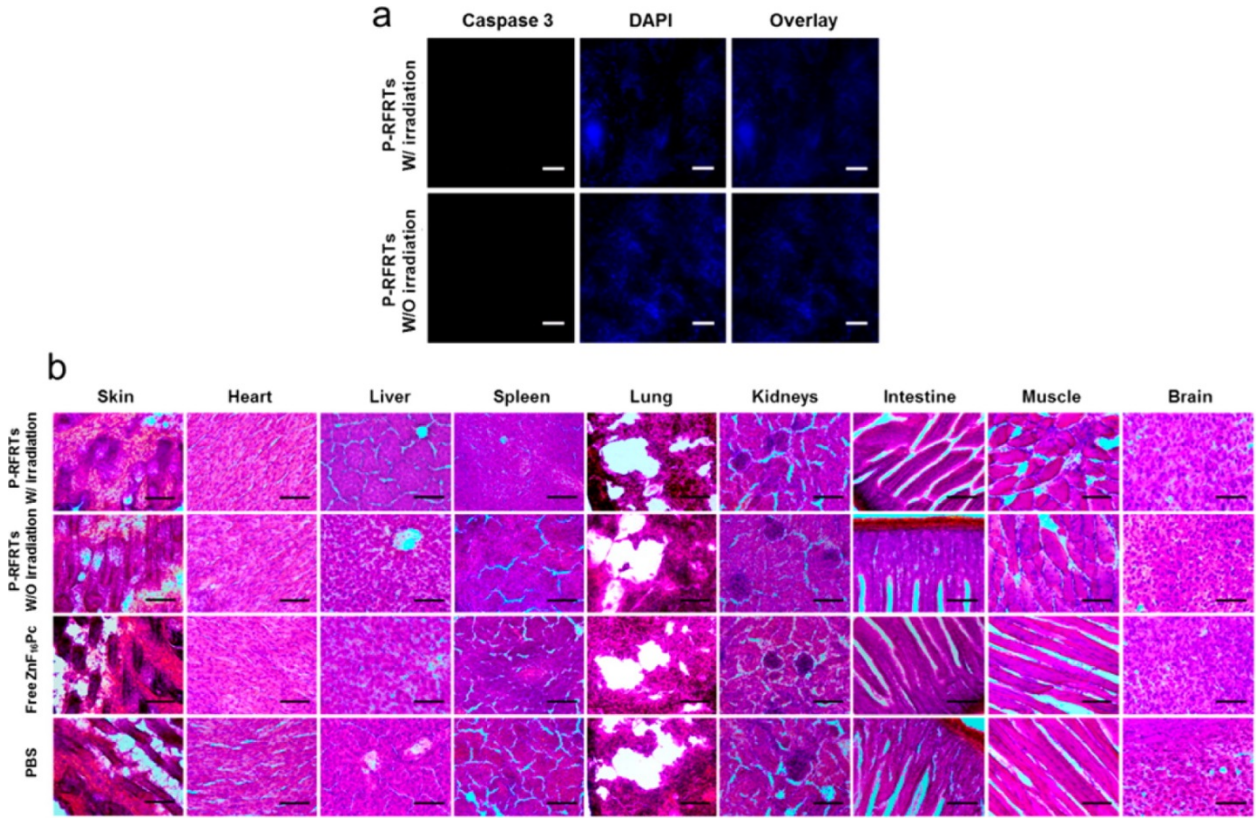

Figure 4.4 Histological Analyses on Major Organs. (a) Caspase 3 staining with the skin tissues from animals treated with P-RFRTs. No obvious apoptosis was found, either with or without light irradiation. Red, caspase 3 (Cy5, ex/em = 650/670 nm); blue, DAPI. Scale bars, 50 μm. (b) H&E staining with normal tissues. No abnormalities were observed. Scale bar, 100 μm.

4.3 Discussion[f]

$ZnF_{16}Pc$ is a ZnPc analogue with a good $^1O_2$ quantum yield[10,11] but poor water solubility (**Figure 4.1c**).[12] As shown in the therapy studies (**Figure 4.3c**), $ZnF_{16}Pc$ is not a satisfactory PS. As a matter of fact, poor stability is a problem shared by many PSs, most of which are porphyrin-like hydrophobic compounds.[13] These PSs are easily aggregated in the blood, causing self-quenching and poor pharmacokinetics.[14] There have been efforts to develop polymer-[15-17] and liposome-based[11,18] nanoparticle carriers for the delivery of PSs like ZnPc[15] or $ZnF_{16}Pc$.[19] These

[f] Zipeng Zhen, Wei Tang, Cunlan Guo, Hongmin Chen, Xin Lin, Gang Liu, Baowei Fei, Xiaoyuan Chen, Binqian Xu, and Jin Xie**ACS Nano* **2013**, *7*, 6988–6996. Reprinted here with permission of publisher.

approaches, however, are usually associated with a loading rate that is typically less than 10 wt %[20] and an overall particle size that is around or above 100 nm.[21] On the other hand, using protein nanocages as a PS vehicle has seldom been exploited and, to the best of our knowledge, has never been investigated *in vivo*. We showed in the current study that, despite the heavy loading, the size of P-RFRTs remains below 20 nm. This is much smaller than conventional nanoparticle–PS conjugates.[20] Both the high loading rate and the small overall size contributed to the good pharmacokinetics observed.

Although the possibility of surface docking cannot be excluded, several observations seem to support the idea that $ZnF_{16}Pc$ is mostly loaded into the interiors of the RFRT nanocages: First, the nanoparticle size was almost unchanged after the $ZnF_{16}Pc$ loading, as shown by AFM. Second, $ZnF_{16}Pc$ is unloaded by the decomposition of the nanocarriers, either by reducing the pH or by inducing PDT. Third, P-RFRTs kept the targeting specificity against integrin $\alpha_v\beta_3$. This was confirmed by both *in vitro* and *in vivo* imaging studies. Fourth, preincubating RFRTs with Cu(II) can significantly suppress the loading of $ZnF_{16}Pc$ (from 60 to 25 wt %). This indicates that most $ZnF_{16}Pc$ is competing for the same binding sites as Cu(II). The latter, according to our previous studies, is mainly encapsulated into the interiors of RFRTs.[7] However, the exact mechanism behind the heavy loading is still unclear at this stage. It is known that there are both three-fold and four-fold symmetric channels present on the FRT surface.[22] The three-fold channel, with a potential gradient directing toward the cavity of the nanocages, serves as a pathway to transfer metal cations into the protein cages. The four-fold channel, on the other hand, has a potential gradient in the opposite direction and is believed to be used to expel species from the cavity.[22] The fact that Cu can suppress the $ZnF_{16}Pc$ uptake suggests that $ZnF_{16}Pc$ is internalized *via* the three-fold channel as Cu does. However, the three-fold channel on intact

FRTs has a size of 3–4 Å,[22,23] which is considered to be small compared to the bulky $ZnF_{16}Pc$. It is possible that the exposure to $ZnF_{16}Pc$ or DMSO (a trace amount of DMSO may have been introduced during the drug loading) leads to an enlarged channel size that facilitates the uptake. It is also plausible that the planar structure of $ZnF_{16}Pc$ makes it relatively easy to penetrate the protein shell. Further investigations are needed to fully elucidate the mechanism.

PDT can target either tumor cells or tumor vasculature to cause damage.[24] In the former mechanism, PDT-induced $^1O_2$ acts on tumor cell membrane or mitochondria to cause necrosis or apoptosis.[25] In the second mechanism, PDT causes vascular collapse and embolization, terminating the supply of oxygen and nutrients to the tumor cells.[26] In the current study, $ZnF_{16}Pc$ was delivered by RFRTs to both tumor vasculature and U87MG tumor cells through RGD–integrin interactions (**Figure 4.3b**). Hence, both mechanisms may have played a role in the tumor destruction. It should be pointed out, however, that U87MG is chosen in the current study for its high expression of integrin $\alpha_v\beta_3$, not because of its origin. There is no indication that PDT can be used for the treatment of brain tumors, to which the delivery of either the drug or light is very challenging. For proof-of-concept, the current study was performed with subcutaneous tumors. To better assess the efficacy of P-RFRT-based PDT, it is important to investigate the modality in orthotopic tumor models with better clinical relevance (*e.g.*, orthotopic prostate tumor models).[27]

As aforementioned, a most critical issue of PDT is skin toxicity.[28] We, however, found negligible skin accumulation with P-RFRTs; instead, many of them were accumulated in the liver. In the context of PDT, however, uptake by the liver is a minor concern given its deep location and, hence, limited accessibility by light. Indeed, histology studies confirmed that the treatment caused little impact to the liver, as well as to other major organs (**Figure 4.4b**). In the

current study, we injected $ZnF_{16}Pc$ at 1.5 mg/kg and irradiated tumors at a fluence rate of 0.3 W/cm^2 for 15 min. Similar conditions were used in the previous studies.[10] Given that no adverse effects were observed, it is possible to increase the dose to improve the treatment. It is also possible to improve the efficacy by adjusting the fluence and fluence rate.

We reported very recently that drug molecules like doxorubicin can be loaded onto RFRTs with high efficiency.[5] It is envisioned that both types of therapeutics can be docked onto RFRTs and delivered to diseased areas simultaneously. PDT can then work in combination with chemotherapy to achieve synergistic therapeutic effects. Moreover, it is an interesting finding that, for $ZnF_{16}Pc$-loaded RFRTs, the nanocage structure can be broken down upon exposure to photoirradiation. This suggests a means to control the cargo unloading. That is, for dually loaded FRTs, PDT can be used as a mechanism to facilitate the release of the other drug to the surroundings. The FRT nanocages can be fabricated for delivery to a different target. Currently, RGD4C was used in the design as a tumor-targeting ligand and was imparted onto the nanocage surface through genetic modification. It is anticipated that other targeting ligands can also be introduced, through either genetic modification or chemical conjugation, onto FRT nanocages, and the new derivatives can transport drugs to different targets. Also, different types of metal-containing PSs, such as Pd-bacteriopheophorbide and motexafin lutetium, are expected to be loaded similarly. These possibilities and optimizations will be also exploited in our future investigations.

4.4 Conclusions[g]

Overall, we demonstrated in this work that RFRT nanoparticles are safe and efficient carriers for $ZnF_{16}Pc$. The resulting conjugates can home to tumors through RGD–integrin interactions and, with light irradiation, induce phototoxicity to tumors while leaving normal tissues unaffected. Boasting an extremely high PS loading rate and an ultrasmall particle size, this technology is expected to find widespread use in PDT and holds great potential in clinical translation.

[g] Zipeng Zhen, Wei Tang, Cunlan Guo, Hongmin Chen, Xin Lin, Gang Liu, Baowei Fei, Xiaoyuan Chen, Binqian Xu, and Jin Xie**ACS Nano* **2013**, *7*, 6988–6996. Reprinted here with permission of publisher.

Materials and Methods

Preparation and Purification of RFRTs: Production and purification of RFRTs have been reported previously. We constructed the DNA plasmid of R-Fn by introducing the RGD4C peptide sequence to the N-terminus of Fn with restrictions sites, NcoI and XhoI, at the 5′- and 3′-ends, respectively. Primers were designed as follows: (+) 5′ ATA TAC CAT GGG CTG CGA CTG CCG CGG AGA CTG CTT CTG CGG AGG CGG AGG CAC CAC CGC GTC T 3′; (−) 5′ CCA GAC TCG AGT TAG CTC TCA TCA 3′. The double digested PCR product was ligated into NcoI/XhoI digested plasmid pRSF with T4 DNA ligase, and the ligation mixture was used to transform competent cells of *E. coli* XL1-Blue by standard procedures. The resulting pRSF/RFRT plasmids were screened by appropriate restriction digests, verified by DNA sequencing, and then used to transform the expression strain*E. coli* BL21(DE3). For expression, a 1 L LB-kanamycin (50 μg/mL) culture of *E. coli*BL21(DE3)/RFRT was grown at 37 °C until an OD600 of 0.8 was reached. For induction, 1 mM IPTG was added to the culture and the culture was heated at 37 °C for 4 h. After sonication, the cell lysate was centrifuged at 10 400 rpm (12 930*g*) for 30 min to remove the cell debris. The supernatant was heated at 60 °C for 10 min and centrifuged at 13 000 rpm for 30 min to remove the precipitates. 2-Mercaptoethanol (10 mM) was added to stabilize the product. The raw product was purified by HPLC using a Superose 6 size exclusion column. The concentration of RFRTs was determined by Bradford protein assay. The purified FRTs/RFRTs were stored at −80 °C. For ZW800 labeling, RFRTs were incubated with ZW800-NHS[6] for 30 min and purified through a NAP-5 column to remove uncoupled dye molecules. A starting ratio of 2:1 (ZW800-NHS to RFRTs) was used. The coupling efficiency was assessed spectroscopically by comparing with a predetermined standard curve (by monitoring absorbance at 780 nm). It was determined that the final conjugates have on average one ZW800 per particle.

Loading $ZnF_{16}Pc$ into FRTs/RFRTs: The $ZnF_{16}Pc$ loading was achieved without breaking down the nanocages. Briefly, 10 μL of $ZnF_{16}Pc$ (5 mg/mL) in DMSO was dropwise added into 490 μL of RFRTs in PBS (0.5 mg/mL), and the mixture was gently shaken for ∼45 min at room temperature. The raw products were then purified using a NAP-5 column to remove the unloaded $ZnF_{16}Pc$. The $ZnF_{16}Pc$ content was determined spectroscopically by comparing with a standard absorption curve of $ZnF_{16}Pc$. The protein concentration was determined by Bradford protein assay. The loading rate was expressed in weight percent (wt %).

***In Vitro* Assays:** U87MG cells were cultured in DMEM medium containing 10% nonessential amino acids, 10% fetal bovine serum, 0.1 mg/mL streptomycin sulfate, and 100 U/mL penicillin (MediaTech, USA) at 37 °C in a humidified atmosphere with 5% CO_2. For cell uptake studies, 10^5 U87MG cells were seeded onto each well of a four-chamber slide (Lab-teck) one day prior to the studies. ZW800-labeled P-RFRTs were added to the solution to reach a final concentration of 50 μg $ZnF_{16}Pc$/mL. In the control group, 30× free c(RGDyK) was used to coincubate with P-RFRTs. At different time points, incubation was stopped. The cells were washed with PBS five times and fixed with 75% ethanol overnight at 4 °C. The slides were mounted with DAPI containing mounting medium (Vector Inc.) and imaged under an Olympus X71 fluorescence microscope. For PDT studies, the cells were exposed to a 671 nm laser at 0.1 W/cm^2 for 200 s. The cell viability was determined by MTT assays using a gradient of P-RFRTs ($ZnF_{16}Pc$ concentrations of 3, 6.25, 12.5, 25, and 50 μg/mL). In control groups, either no irradiation was

applied or free $ZnF_{16}Pc$ at the same dose was used. Live/dead assays were performed by following a protocol provided by the vendor.

Animal Models: Animal models were established by subcutaneous injection of 10^6 human glioblastoma U87MG onto the hind legs of 5–6 week athymic nude mice (Harlan). Animal studies were performed according to a protocol approved by the Institutional Animal Care and Use Committee (IACUC) of University of Georgia.

***In Vivo* Imaging:** The imaging studies were performed when tumors reached a size between 350 and 500 mm^3. We intravenously (i.v.) injected ZW800-labeled P-RFRTs (5 mg RFRT/mL) into mice ($n = 3$). For the control group, 30× c(RGDyK) was administrated 30 min prior to the R-RFRT injection ($n = 3$). Fluorescence images were acquired on a Maestro II imaging system using an orange filter (640 to 820 nm) at 1, 4, and 24 h time points. The images were unmixed using the Maestro software. The average signal (10^6 photons/cm^2/s) for each region of interest (ROI) was measured. Tumor-to-normal tissue ratio (T/N) was determined and was expressed as mean ± SD. All mice were euthanized after the 24 h imaging. Tumors as well as major organs were collected and subjected to *ex vivo* imaging. After imaging, the tissues were snap-frozen in O.C.T. (Tissue-Tek) and stored in a −80 °C freezer.

Therapy Studies: For PDT studies, 20 mice bearing U87MG tumors were randomly divided into four groups. The treatment scheme is as follows: (1) P-RFRTs (1.5 mg $ZnF_{16}Pc$/kg), with irradiation; (2) P-RFRTs (1.5 mg $ZnF_{16}Pc$/kg), without irradiation; (3) free $ZnF_{16}Pc$ (1.5 mg $ZnF_{16}Pc$/kg), with irradiation; (4) PBS, no irradiation. The photoirradiation was applied 24 h after the injection of P-RFRTs (671 nm laser, 0.3 W/cm^2 for 15 min). The tumor sizes and body weights were inspected every 3 days. The tumor weight was estimated using the formula, tumor volume = length × $(\text{width})^2/2$, assuming a tumor density of 1 mg/mL. After therapy, major organs as well as tumors were collected and sectioned to 8 μm slices for caspase 3 and H&E staining.

Immunofluorescence Staining: The cryogenic slides were fixed with cold acetone for 30 min, washed by running water for 5 min, and blocked by 10% goat serum for 1 h. Anti-integrin β_3 or anti-caspase 3 antibodies were incubated with the slides at 4 °C overnight. Cy5.5-labeled secondary antibody was then added and incubated for 1 h at 37 °C. After gently rinsing with PBS, the slides were mounted and ready for microscopic imaging.

H&E Staining: H&E staining was performed according to a protocol provided by the vendor (BBC Biochemical). Briefly, 8 μm cryogenic slides were prepared and fixed with 10% formalin for about 30 min at room temperature. After washing with running water for 5 min, the slides were treated with gradient concentrations of alcohol (100, 95, and 70%), each for 20 s. The hematoxylin staining was performed for about 3 min and washed with water for 1 min. The eosin staining was performed for about 1 min. The slides were washed, treated with xylene, and mounted with Canada balsam. The images were acquired on a Nikon Eclipse 90i microscope.

References

(1) Bessler, N. M.; Vam Study Writing, C. *Retina (Philadelphia, Pa.)* **2004**, *24*, 512.
(2) Gross, S.; Gilead, A.; Scherz, A.; Neeman, M.; Salomon, Y. *Nature Medicine* **2003**, *9*, 1327.
(3) Castano, A. P.; Mroz, P.; Hamblin, M. R. *Nature Reviews. Cancer* **2006**, *6*, 535.
(4) Dolmans, D. E.; Fukumura, D.; Jain, R. K. *Nature Reviews. Cancer* **2003**, *3*, 380.
(5) Zhen, Z.; Tang, W.; Chen, H.; Lin, X.; Todd, T.; Wang, G.; Cowger, T.; Chen, X.; Xie, J. *ACS Nano* **2013**, *7*, 4830.
(6) Choi, H. S.; Nasr, K.; Alyabyev, S.; Feith, D.; Lee, J. H.; Kim, S. H.; Ashitate, Y.; Hyun, H.; Patonay, G.; Strekowski, L.; Henary, M.; Frangioni, J. V. *Angewandte Chemie-International Edition* **2011**, *50*, 6258.
(7) Lin, X.; Xie, J.; Niu, G.; Zhang, F.; Gao, H.; Yang, M.; Quan, Q.; Aronova, M. A.; Zhang, G.; Lee, S.; Leaprnan, R.; Chen, X. *Nano Letters* **2011**, *11*, 814.
(8) Tan, M.; Lu, Z.-R. *Theranostics* **2011**, *1*, 83.
(9) Zhang, Y.; Yang, Y.; Cai, W. *Theranostics* **2011**, *1*, 135.
(10) Boyle, R. W.; Rousseau, J.; Kudrevich, S. V.; Obochi, M. O. K.; vanLier, J. E. *British Journal of Cancer* **1996**, *73*, 49.
(11) Garcia, A. M.; Alarcon, E.; Munoz, M.; Scaiano, J. C.; Maria Edwards, A.; Lissi, E. *Photochemical & Photobiological Sciences* **2011**, *10*, 507.
(12) Oda, K.; Ogura, S.; Okura, I. *Journal of Photochemistry and Photobiology B-Biology* **2000**, *59*, 20.
(13) Berg, K.; Selbo, P. K.; Weyergang, A.; Dietze, A.; Prasmickaite, L.; Bonsted, A.; Engesaeter, B. O.; Angell-Petersen, E.; Warloe, T.; Frandsen, N.; Hogset, A. *Journal of Microscopy* **2005**, *218*, 133.
(14) Dhami, S.; Phillips, D. *Journal of Photochemistry and Photobiology A-Chemistry* **1996**, *100*, 77.
(15) Conte, C.; Ungaro, F.; Maglio, G.; Tirino, P.; Siracusano, G.; Sciortino, M. T.; Leone, N.; Palma, G.; Barbieri, A.; Arra, C.; Mazzaglia, A.; Quaglia, F. *Journal of Controlled Release* **2013**, *167*, 40.
(16) Konan, Y. N.; Cerny, R.; Favet, J.; Berton, M.; Gurny, R.; Allemann, E. *European Journal of Pharmaceutics and Biopharmaceutics* **2003**, *55*, 115.
(17) van Nostrum, C. F. *Advanced Drug Delivery Reviews* **2004**, *56*, 9.
(18) Ali, M. F. M. *Lasers in Medical Science* **2011**, *26*, 267.
(19) Allemann, E.; Brasseur, N.; Benrezzak, O.; Rousseau, J.; Kudrevich, S. V.; Boyle, R. W.; Leroux, J. C.; Gurny, R.; Vanlier, J. E. *Journal of Pharmacy and Pharmacology* **1995**, *47*, 382.
(20) Chatterjee, D. K.; Fong, L. S.; Zhang, Y. *Advanced Drug Delivery Reviews* **2008**, *60*, 1627.
(21) Bechet, D.; Couleaud, P.; Frochot, C.; Viriot, M.-L.; Guillemin, F.; Barberi-Heyob, M. *Trends in Biotechnology* **2008**, *26*, 612.
(22) Takahashi, T.; Kuyucak, S. *Biophysical Journal* **2003**, *84*, 2256.
(23) Yan, F.; Zhang, Y.; Yuan, H.-k.; Gregas, M. K.; Vo-Dinh, T. *Chemical Communications* **2008**, 4579.
(24) Agostinis, P.; Berg, K.; Cengel, K. A.; Foster, T. H.; Girotti, A. W.; Gollnick, S. O.; Hahn, S. M.; Hamblin, M. R.; Juzeniene, A.; Kessel, D.; Korbelik, M.; Moan, J.; Mroz, P.; Nowis, D.; Piette, J.; Wilson, B. C.; Golab, J. *CA-a Cancer Journal for Clinicians* **2011**, *61*, 250.

(25) Fabris, C.; Valduga, G.; Miotto, G.; Borsetto, L.; Jori, G.; Garbisa, S.; Reddi, E. *Cancer Research* **2001**, *61*, 7495.
(26) Nishiyama, N.; Morimoto, Y.; Jang, W.-D.; Kataoka, K. *Advanced Drug Delivery Reviews* **2009**, *61*, 327.
(27) Kosharskyy, B.; Solban, N.; Chang, S. K.; Rizvi, I.; Chang, Y.; Hasan, T. *Cancer Research* **2006**, *66*, 10953.
(28) Baas, P.; Vanmansom, I.; Vantinteren, H.; Stewart, F. A.; Vanzandwijk, N. *Lasers in Surgery and Medicine* **1995**, *16*, 359.

CHAPTER 5

TUMOR VASCULATURE TARGETED PHOTODYNAMIC THERAPY FOR ENHANCED DELIVERY OF NANOPARTICLES[h]

[a] Wei Tang[†], Zipeng Zhen[†], Yen-Jun Chuang, Trever Todd, Weizhong Zhang, Xin Lin, Gang Niu, Gang Liu, Lianchun Wang, Zhengwei Pan, Xiaoyuan Chen, Jin Xie* ([†] Equal contribution) *ACS Nano* **2014**, *8*, 6004–6013. Reprinted here with permission of publisher.

5.1 Introduction

Nanoparticle-based drugs are emerging as an important class of therapeutics. At least nine nanoparticle drugs have received regulatory approval for the treatment and diagnosis of various indications.[1,2] These include Doxil and Abraxane, both of which have entered mainstream clinical cancer management. Unlike conventional small-molecule chemotherapeutics, nanoparticle- or macromolecule-based drugs can selectively egress at leaky tumor vasculatures and remain in the tumor interstitium for an extended period of time. This mechanism, referred to as the enhanced permeability and retention or EPR effect, has served as a foundation for modern nanomedicine.[3,4] Compared to the extensive and intensive research in this area, however, the translation of nanomedicine into the clinic has been slow, if not disappointing. This has led to recent retrospections, concerning that the EPR effect may have been overestimated.[4] Despite relative leakiness compared to normal vessels, the endothelial lining can remain a barrier to the delivery of nanoparticles to tumors. This hindrance varies among tumors of different origins, stages, and organs, and may affect the treatment efficacy significantly. One indication is the frequently reduced treatment efficacy of nanoparticle drugs in the clinic compared to animal studies. One primary reason is that many pre-clinical investigations are conducted in subcutaneous tumor models, where tumors develop within a short period of time and in a position of rich vascular network.[2] These tumors tend to have high levels of EPR that is not often observed in human patients.[2,4] This situation underscores the significance of an EPR enhancement technology that can enhance tumor endothelium leakiness.[4] Prior work in this respect has focused on chemical-based vascular mediators such as nitroglycerin, ACE inhibitor, and PGE1 agonist. With these, a 2~3 fold increase of EPR effect in tumors can be achieved.[5]

This approach, however, may potentially cause side effects to normal vasculatures and organs due to the systematic nature.

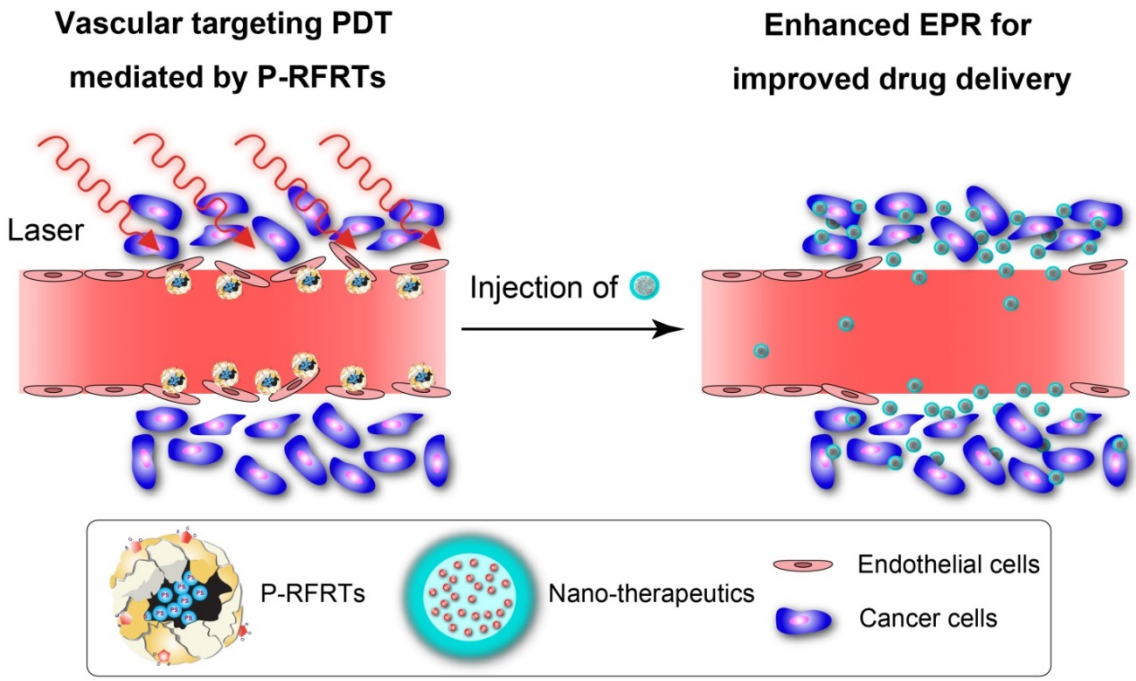

Scheme 5.1 Working mechanism of P-RFRT-mediated PDT for enhanced delivery of nanoparticles to tumors. P-RFRTs are first injected and home to tumor endothelium through RGD-integrin interactions. With irradiation at an appropriate irradiance, the procedure generates $^1O_2$ that acts on the endothelium. This leads to enlarged or newly formed endothelial gaps. Due to the increased leakiness, nanoparticles injected subsequently will extravasate and accumulate more efficiently at tumors.

We herein report a photodynamic therapy (PDT)-based method that can selectively increase vessel leakiness in tumors, linked to enhanced EPR effect. PDT is a clinically approved therapeutic procedure which consists of three components: photosensitizers, light and oxygen.[6,7] Photosensitizers, while not toxic individually, can be activated by light of a specific wavelength. This causes energy transfer to near-by oxygen molecules that produces cytotoxic $^1O_2$. A common target in conventional PDT is the tumor vasculature.[6,8] In the clinic, vasculature PDT is achieved

by controlling the time interval between photosensitizer injection and illumination, the so called drug-light interval. Lacking selectivity, this toxicity acts on both endothelial and luminal targets (*e.g.* red blood cells/platelets), causing massive destruction that include vessel collapse and thrombus formation.[6] Our hypothesis is that with selective delivery and appropriate irradiation, PDT can be managed to increasing vessel permeability but not inducing occlusion. Particles injected subsequently can benefit from the permeabilized endothelium for enhanced accumulation in tumors (**Scheme 5.1**).

To achieve this goal, we used RGD modified ferritin (RFRT) as photosensitize carriers. Ferritin is a non-toxic protein nanocage found in most living organisms, including human beings. In the nature, the main function of ferritin is to load Fe. When grown artificially (by *E. Coli*) with no iron feeding, however, ferritins afford a central cavity which, as shown in our recent studies, can encapsulate metals or metal-containing compounds with high efficiency.[9-11] In particular, $ZnF_{16}Pc$, a potent PS (λ_{max}: 671 nm; Φ_{Δ}: 0.85 in tetrahydrofuran[12]), can be encapsulated into RFRTs by up to *60 wt%*.[11] Due to multiple RGD ligands (24-mer) on the surface, RFRTs have strong binding affinity toward integrin $\alpha_v\beta_3$[13] that is overexpressed on neoplastic endothelial cells.[14,15] Our studies showed that after systemic administration, $ZnF_{16}Pc$-loaded RFRTs (P-RFRTs) can home to the endothelium of neoplastic vessels *via* RGD-integrin interactions.[11] This, in conjugation with photoirradiation at a low irradiance, can permeabilize vasculature in tumors (**Scheme 5.1**). The notion was confirmed in 4T1, U87MG, MDA-MB-435S, and PC-3 tumor xenograft models using albumins, quantum dots, and iron oxide nanoparticles (IONPs). The treatment can increase tumor accumulation of nanoparticles by as much as 20.08-fold, while causing no adverse effects to normal tissues. Using Doxil as a representative nanoparticle drug, we also studied the impact of the procedure on cancer

treatment. While exerting little cytotoxic power itself, P-RFRT-mediated PDT can improve the treatment efficacy of Doxil by 75.3%, which was attributed to the enhanced EPR effect. All these observations suggest P-RFRT-mediated PDT as a safe, selective, and effective means for enhanced nanoparticle delivery.

5.2 Results and Discussion

5.2.1 Tumor targeting with P-RFRTs

The preparation of RFRTs and how to load $ZnF_{16}Pc$ onto RFRTs have been reported previously.[11] A formulation with $ZnF_{16}Pc$ loading rate of ~41.2 wt% was used in the current studies. Despite the heavy loading, the size of the resulting $ZnF_{16}Pc$-loaded RFRTs, or P-RFRTs, is relatively small (~ 18.6 nm).[11] It has also been observed in previous studies that P-RFRTs are stable in physiological environments and are not toxic in the dark.[11]

We first studied tumor targeting efficiency of P-RFRTs in bilateral 4T1 (murine breast cancer) tumor xenograft models (n = 5). To facilitate the tracking, we labeled P-RFRTs with IRDye800 (ex/em: 780/800 nm, Licor). These labeled P-RFRTs (0.75 mg $ZnF_{16}Pc$/kg) were intravenously (i.v.) injected, and their migration was studied by fluorescence imaging on a Maestro II scanner. Accumulation of signals in both left and right tumors were observed (**Figure 5.1a** & **S5.1**). At 24 h, the average tumor-to-normal (T/N) tissue ratio was 94.51 (97.52 ± 10.60 and 91.50 ± 13.00 for left and right tumors, respectively; **Figure 5.1a & 5.1b**), indicating high tumor selectivity. It was observed that in addition to tumors, P-RFRTs also accumulated in the liver, spleen, and intestines. This distribution pattern is typical for nanoparticles of the similar sizes. There was also a certainly level of kidney accumulation. This was attributed to the moderate expression of integrin $\alpha_v\beta_3$ in the kidneys.[16] The accumulation of P-RFRTs in these

organs, however, causes little side effects[11] due to the relatively deep positions. Immunofluorescence staining on tumor sections revealed overall good correlation between the P-RFRTs distribution and positive integrin β_3 staining, suggesting that the targeting was mainly mediated by RGD-integrin interactions (**Figure 5.1c**). Notably, 4T1 cells express a relatively low level of integrin $\alpha_v\beta_3$ on the surface. Many of the P-RFRTs, therefore, were positioned on tumor vessels instead of tumor cells at 24 h (**Figure 5.1c**).

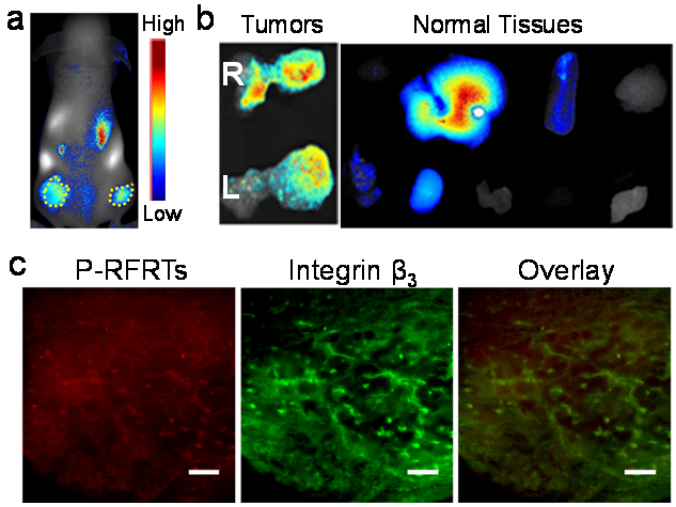

Figure 5.1 Tumor Targeting of P-RFRTs. (**a**) *In vivo* imaging studies. P-RFRTs were labeled with IRDye800 and were i.v. administered into bilateral 4T1 tumor models. Fluorescence imaging performed at 24 h showed selective accumulation of P-RFRTs in both tumors (circled by yellow dashed lines). (**b**) *Ex vivo* imaging with tumors as well as normal tissues. The normal tissues were arranged in the following order: The first row, heart, liver, spleen and skin; the second row, intestine, kidney, muscle and brain. (**c**) Immunofluorescence staining with tumor samples. Tumor vessels were stained by anti-integrin β_3 antibodies. Overall good correlation was found between P-RFRTs and positive integrin β_3 staining, suggesting that the tumor targeting was mainly mediated by RGD-integrin interactions. Scale bars, 100 μm.

5.2.2 Evaluating the EPR enhancement effect with albumins

Using human serum albumins (HSA) as drug mimics, we then studied the impact of P-RFRT-mediated PDT on the EPR effect. With a molecular weight of ~65,000 and a diameter of ~ 7 nm,

HSA is a good representative of macromolecules or small nanoparticles.[17] The study was comprised of two steps. In the first step, P-RFRTs (0.75 mg $ZnF_{16}Pc$/kg) were i.v. administered (n = 3), followed by photoirradiation by a 671 nm laser at 24 h. The laser was given in the form of a 1-cm beam that covers the right-side tumor of an animal. The left-side tumors were not irradiated and served as controls. A irradiance of 14 mW/cm^2 (for 30 min) was applied, which was much lower than the power used in conventional PDT (50-300 mW/cm^2).[18] In the second step, IRDye800-labeled HSA (1 mg/kg) was i.v. injected 5 min after the end of the laser irradiation. The animals were then subjected to fluorescence imaging, and the accumulation of probes in the left- and right-tumors was compared.

At all the time points examined, there was significantly higher uptake of probes in the right-side tumors (**Figure 5.2a**). By region-of-interest (ROI) analysis, we quantified and compared the relative increase of tumor uptake (RIU), which is the ratio of fluorescence readings between the right and left tumors. At 1, 4 and 24 h, RIU was 1.88 ± 0.29, 2.23 ± 0.34, and 2.96 ± 0.27, respectively. After the 24 h imaging, the animals were euthanized and the tumors were harvested. The *ex vivo* imaging with tumors revealed a similar level of difference in uptake between the irradiated and un-irradiated tumors (**Figure 5.2a**). The enhanced tumor uptake by PDT was further assessed by microscopy studies (**Figure 5.2b**). Interestingly, in addition to overall increased uptake, there is also a change in the distribution pattern of the albumins: In un-irradiated tumors, the albumins were found only in the tumors' peripheries; in irradiated tumors, on the other hand, albumins penetrated much deeper into the masses.

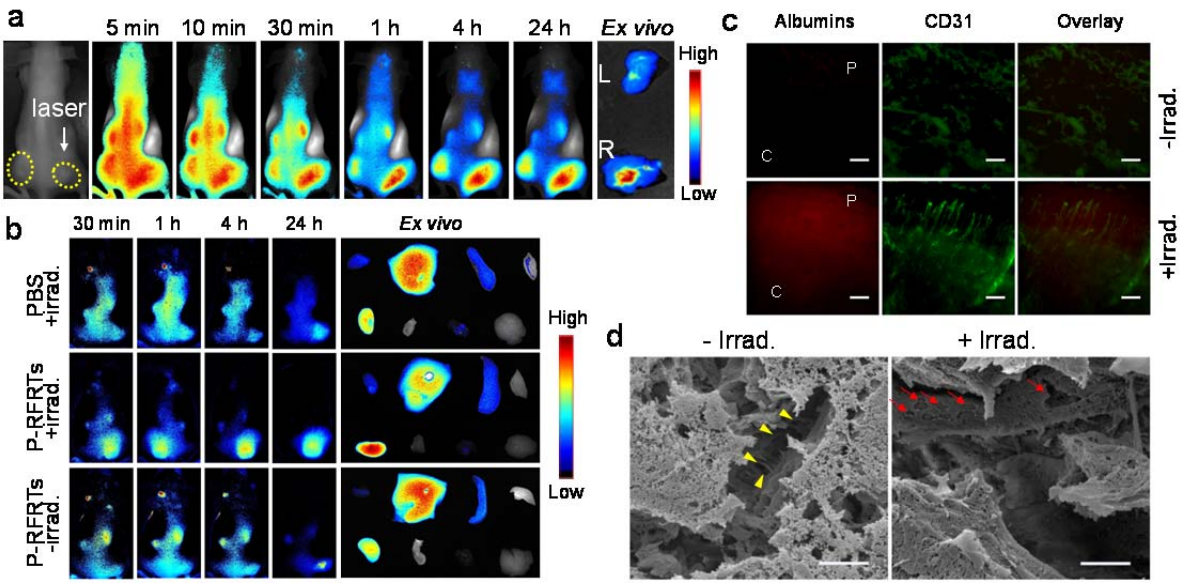

Figure 5.2 Study the EPR Enhancement Effect with Albumins. (**a**) PDT-induced EPR enhancement. The study was performed in bilateral 4T1 tumor models. P-RFRTs were i.v. injected first. A 671 nm laser was applied to the right-side tumors 24 h after injection of P-RFRTs. IRDye800-labeled HSA was injected 5 min after the end of the irradiation. Significantly enhanced tumor accumulation (by 2.96 ± 0.27 fold at 24 h, $P<0.05$) was observed in irradiated tumors over un-irradiated ones. *Ex vivo* imaging with dissected tumors showed a similar level of increase in albumin uptake. (**b**) EPR enhancement effect, investigated in 4T1 tumor models which bear one tumor each. Animals were divided into three groups (n = 3), and were treated with P-RFRTs plus irradiation, PBS plus irradiation, and P-RFRTs only, respectively. Compared to the two control groups, animals receiving the P-RFRTs and irradiation combination showed significantly increased tumor uptake of HSA. On the other hand, the distribution of albumins in normal tissues was comparable among the three groups. For *ex vivo* imaging, the tissues were arranged in the following order: The first row, heart, liver, spleen and skin; the second row, kidney, intestine, muscle and brain. (**c**) Immunofluorecence staining. Enhanced tumor accumulation was observed in the group that had undergone PDT (P-RFRTs + irradiation) before the HSA injection. It is also noted that albumins penetrated much deeper into the tumors after the PDT modulation. 'p' and 'c' indicates the peripheral and central regions of a tumor, respectively. Scale bars, 100 μm. (**d**) SEM study on tumor sections. Compared to the un-irradiated tumors, more and larger fenestrae were found on the endothelial walls of the irradiated tumors (highlighted by red arrows). In addition, compared to the un-irradiated tumors, where vessels were enriched with bridge- and tunnel-like structures (pointed by yellow arrows), the PDT treated tumors showed a much smoother wall surface. Scale bars, 2.5 μm.

To confirm the enhancement effect, we also conducted similar studies in 4T1 tumor models which bear one tumor each. We treated the tumors by the same injection and irradiation procedures (14 mW/cm^2 for 30 min at 24 h after P-RFRT injection), followed by albumin

administration (IRDye800 labeled, 1 mg/kg). In the two control groups, animals received P-RFRTs but no irradiation, or irradiation only, before albumin injections. Compared to the controls, increased tumor accumulation was observed in the PDT-treated animals (**Figure 5.2c**). At 24 h, an increased uptake of 2.41 ± 0.39 fold was observed between the irradiated and un-irradiated groups. This amplitude of increase is comparable to that observed in bilateral tumor models. As a matter of fact, comparable RIU values between the two sets of studies were observed at all time points (**Figure S5.2**). The harvested tumors and normal tissues were then subjected to *ex vivo* imaging (**Figure 5.2c**). There was no significant difference in albumin accumulation in normal tissues among the three groups. This suggests that the PDT treatment is highly selective. Aside from increasing tumor uptake, it has little impact on the delivery of albumins to other organs.

To elucidate the mechanism behind the uptake increase, in a separate study, we sacrificed animals 5 min after the end of irradiation (without injection of albumins), and harvested the tumors for scanning electron microscopy (SEM) analysis. Compared to the un-irradiated tumors, we observed many more large fenestrae on the endothelial walls of the irradiated ones (**Figure 5.2d**, highlighted by red arrows). This is attributed to PDT-induced contraction and rounding of tumor endothelial cells that enlarged endothelial gaps or formed new ones.[19] The yielded vessels are thus more permeable, which is believed to be the primary cause behind the enhanced tumor uptake. Interestingly, changes were also found on the luminal microstructures after the PDT: Without irradiation, the lumen of vessels was enriched with branched lining cells, which formed extensive bridges and tunnels (**Figure 5.2d**, highlighted by yellow arrows). These features are commonplace in poorly developed tumor vessels, as observed by others.[20] In contrast, tumors that had undergone irradiation displayed much smoother vessel surface (**Figure 5.2d**), indicating

a possible plumbing function of the PDT procedure. This hypothesis is corroborated by immunofluorescence microscopy on tumors before as well as 5 min and 24 h after the PDT (**Figure S5.3**). Un-treated tumors featured irregular and convoluted vessels, which correlate with the SEM observations. After the PDT treatment, however, the blood vessels become more regular and ordered, probably more so at 5 min (**Figure S5.3**). It indicates a possible vessel normalization effect by the PDT, although the impact is temporal. Both the vessel dredging and vessel normalization are attributed to PDT, but the exact mechanism is unknown at this stage. It could be that the $^1O_2$ acted on the branched lining cells, forcing their contraction into the endothelium or even being uprooted from it. These lead to a less degree of complexity of the microstructures. Nonetheless, bridged and tunneled microstructures in blood vessels can pose great geometric resistance to the blood flow, and in turn, lead to elevated interstitial fluid pressure (IFP).[21] Commonly observed in solid tumors, elevated IFP is a major barrier to deliver drugs to the masses, especially to the central regions. It is more an issue for delivery of macromolecules/nanoparticles which, due to relatively large size, depend heavily on convection rather than diffusion for extravasation.[22,23] A modulation that can clear and normalize the vessels is therefore of great value in improving the delivery. The hypothesis seems to be supported by microscopic imaging studies, which found in PDT-treated tumors not only increased overall accumulation, but also improved dispersion of albumins (**Figure 5.2b**).

The tumor samples were also subjected to TUNEL assays, which evaluate the toxicity caused by PDT. Interestingly, few cell deaths were detected in the PDT treated tumors (**Figure S5.4**). This suggests that despite the vascular effects the PDT induced, its toxicity to the surroundings is minimal. This is attributable to the low fluence and fluence-rate used, and also, to the accurate endothelium targeting. In combination, the $^1O_2$ generated acts as a gentle, local

cleaning of the vessels, thereby avoiding the extensive vessel occlusion and destruction that is often observed in conventional PDT.

5.2.3 Fluence dependence of the EPR enhancement

The impact of PDT is often dependent on fluence and irradiance. It is postulated, therefore, that the EPR effect is also fluence dependent. To examine, we repeated the preceding study with bilateral 4T1 tumor models but varied the irradiance (the illumination time was fixed at 30 min). RIU values from different irradiation conditions were then assessed and compared. At 3 mW/cm^2, there was almost no enhancement effect, showing an RIU value of 1.03 ± 0.24 at 24 h (**Figure 5.3a**). Increasing the irradiance to 8 mW/cm^2 led to enhanced tumor uptake (1.43 ± 0.38 at 24 h) but the amplitude was smaller than that at 14 mW/cm^2 (2.96 ± 0.27). Further increasing irradiance beyond 14 mM/cm^2 to 22 mW/cm^2 did not enhance the tumor uptake accordingly, showing a RIU value of 1.89 ± 0.36 at 24 h (**Figure 5.3a**). The difference in tumor uptake was better illustrated by immunofluorescence staining. Compared to the control and other illumination conditions, the 14 mW/cm^2 group manifested the most prominent probe accumulation and dispersion (**Figure 5.3b**). These results show that increased irradiance and fluence is not always beneficial to the EPR enhancement. While too low an irradiation dose can be insufficient to induce vessel permeabilization, a too high irradiation dose can be overkill; possibly causing partial or complete occlusion of the vessel that adversely affects the nanoparticle delivery.

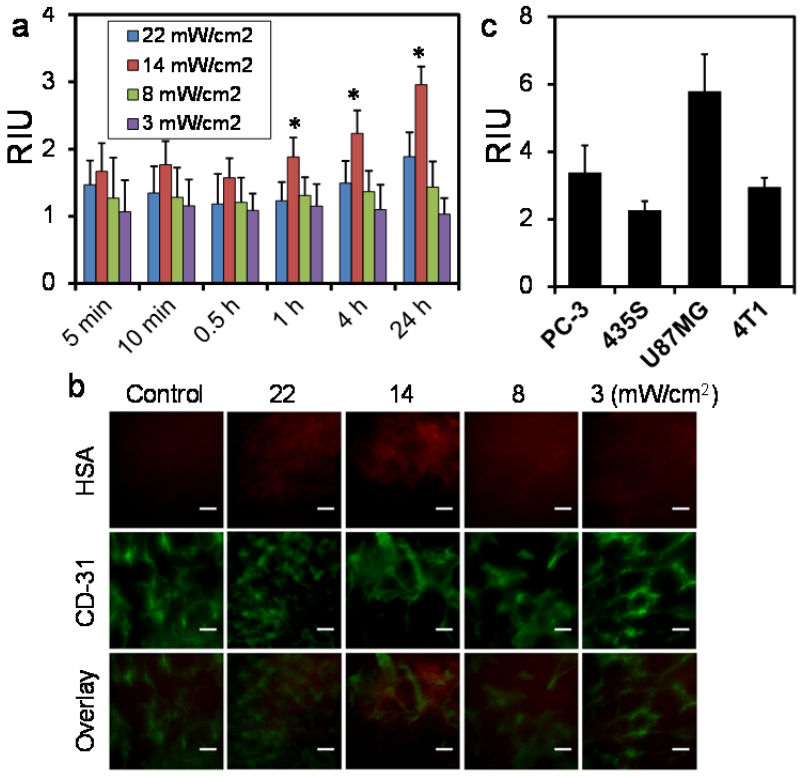

Figure 5.3 The EPR Enhancement is Irradiance Dependent. (**a**) Histogram comparison of relatively increased tumor uptake under irradiation at different irradiances. The data were derived from ROI analyses on the *in vivo* imaging results. The highest RIU values were observed at 14 mW/cm^2 for all time points. * Indicates $P < 0.05$. (**b**) Immunofluorescence staining results. Many more albumins (IRDye800, red) were found outside blood vessels (marked by CD31 staining, green) after the PDT, suggesting an enhanced EPR effect. The most prominent accumulation and dispersion were observed at 14 mW/cm^2. Scale bars, 100 μm. (**c**) EPR enhancement effect in different tumors (n = 3). The results were based on comparison of 24 h tumor accumulation between irradiated and un-irradiated tumors. Similar or even superior EPR enhancement effect was observed in PC-3, MDA-MB-435S, and U87MG tumor models.

5.2.4 EPR enhancement in different tumor models

Using the same injection and irradiation plans, we also evaluated the EPR enhancement effect in other tumor models. These include PC-3 (humane prostate cancer), MDA-MB-435S (human melanoma), and U87MG (human glioblastoma) tumor-bearing mice. In every model, we observed enhanced accumulation of albumins in tumors after the PDT treatment (**Figure 5.3d** & **S5.5-S5.7**). Specifically, 24 h RIU values were 3.39 ± 0.80, 2.27 ± 0.27, and 5.79 ± 1.10,

respectively, for PC-3, MDA-MB-435S, and U87MG tumors. Similarly, the PDT treatment caused little change in distribution of albumins in normal tissues (**Figure S5.8**). Notably, integrin $\alpha_v\beta_3$ is expressed moderately or abundantly on the surface of PC-3 (integrin $\alpha_v\beta_3^{+}$), MDA-MB-435S (integrin $\alpha_v\beta_3^{++}$), and U87MG (integrin $\alpha_v\beta_3^{+++}$) cells. Hence, some or a large amount of injected P-RFRTs homed to cancer cells in these models. The fact that a comparable or even superior enhancement effect was observed in these models suggests that the PDT effects on cancer cells do not affect the EPR enhancement, at least not adversely.

5.2.5 EPR enhancement for QDs and IONPs

We next examined whether the method applies to particles with a larger size. This was first investigated with quantum dots (QDs, from Invitrogen, ex/em: 405-665/705 nm), which have a diameter of ~50 nm (Figure S5.10). The study was performed on bilateral 4T1 tumor models. Similarly, QDs were injected after P-RFRT mediated PDT (30 pmol/mouse, n = 3). The contralateral tumor receiving no photo-irradiation served as the control. After 24 h, we sacrificed the animals and dissected the tumors for comparison by *ex vivo* imaging (**Figure 5.4a** & **S5.11**). ROI analyses on *ex vivo* imaging with dissected tumors revealed a RIU of 20.08 ± 1.28 between irradiated and un-irradiated tumors. This significant increase in the EPR enhancement over that found with albumins could be due to a number of factors, which include the difference in particle dimensions. Due to the larger size of QDs, the endothelial lining represents a more difficult barrier for them than for albumins. Therefore, the PDT treatment, which lowers the threshold, works more effectively on QDs to improve their extravasation at the tumors. The difference may have been further augmented by the fact that large nanoparticles are less mobile. That is, compared to albumins, QDs have a higher tendency to stay at the tumor interstitial space after the extravasation. This was supported by immunofluorescence staining, which found a large

amount of QDs accumulated just outside the blood vessels (**Figure 5.4a**). In contrast, albumins were disseminated much deeper from the vessels (**Figure 5.2b**).

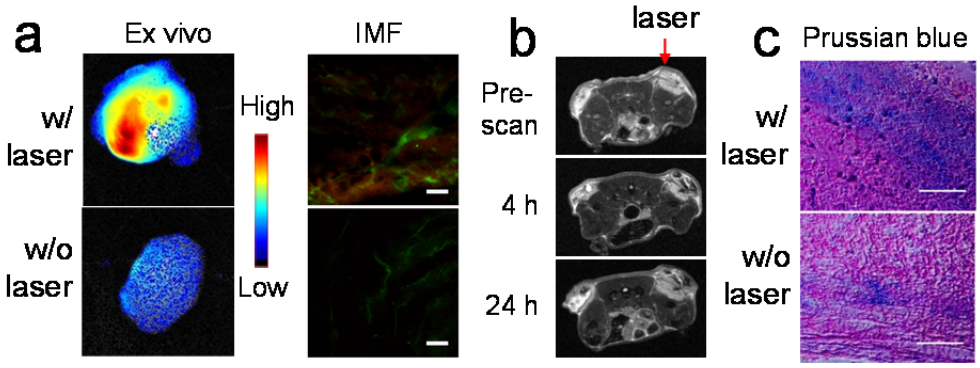

Figure 5.4 EPR Enhancement with Nanoparticles. (**a**) EPR enhancement effect with QDs. The study was performed in bilateral 4T1 tumor models. QDs were injected 5 min after the end of P-RFRT-mediated PDT, which applied only to the left-side tumors. *Ex vivo* imaging was performed on dissected tumors 24 h after the QD injection. Compared to un-irradiated tumors, irradiated tumors showed a 20.8-fold increase in tumor uptake (by ROI analysis). This was further confirmed by immunofluorescence (IMF) staining. Green, CD31, marking blood vessels. Red, QDs. Scale bars, 100 µm. (**b**) EPR enhancement effect with IONPs. The study was performed in bilateral 4T1 tumor models. IONPs were injected 5 min after the end of P-RFRT-mediated PDT, which only applied to the right-side tumors. MR images were taken before and 4 and 24 h after the injection of IONPs. More significant signal drop was observed in the right-side, irradiated tumors. (**c**) Prussian blue staining on tumor samples from b. Correlated with the *in vivo* observations, more iron deposits were found in irradiated tumors. Scale bars, 100 µm.

The PDT-based method also applies to iron oxide nanoparticles (IONPs). In a separate study, ~40 nm IONPs (core size ~15 nm, Ocean Nanotech) as model nanoparticles were injected into bilateral 4T1 tumor models after the PDT (n = 3). A commonly used MRI contrast probe, IONPs shorten T_2 relaxation times of near-by protons, causing regional signal drop on T_2-weighted MR maps. Compared to the un-irradiated side, many more signal voids were observed in the irradiated tumors, indicating an enhanced tumor accumulation (**Figure 5.4b**). The result was further validated by Prussian blue staining, which found more iron deposits in tumors that had undergone irradiation (**Figure 5.4c**).

5.2.6 EPR enhancement for improving tumor therapy with Doxil

With the encouraging imaging results, we then moved forward to therapy studies. This was evaluated in 4T1 xenograft tumor models (bearing one tumor each). Doxil, a liposome-based doxorubicin drug, was used as a nanoparticle therapeutic. Specifically, animals were injected with P-RFRTs first (0.75 mg/kg), followed by irradiation at 24 h (14 mW/cm^2 for 30 min). Right after the irradiation, Doxil (10 mg/kg) was i.v. administered (n = 5). Several control groups were also studied. These include animals receiving P-RFRTs and Doxil but no irradiation, P-RFRTs and irradiation but no Doxil, Doxil and irradiation, Doxil only, and PBS only (n = 5).

The group that received PDT only (P-RFRTs+Irrad.) showed a similar tumor growth rate to animals receiving only PBS (**Figure 5.5a**). This indicates that PDT alone caused few therapeutic effects. The data correlates well with the observations from TUNEL assays (**Figure S5.4**), which found little toxicity of PDT at this low irradiance. Animals treated with P-RFRTs + Doxil, Doxil + irradiation, and Doxil only showed comparable but mediocre tumor suppression. On day 12, tumor growth inhibition (TGI) rates were computed to be 39.4%, 56.7%, and 49.0% for these three groups, respectively (**Figure 5.5a**). In contrast, significantly improved tumor growth inhibition was observed in animals receiving both PDT and Doxil (P-RFRTs+Irrad.+Doxil). The combination almost completely arrested tumor growth in the first week, including two animals showing tumor shrinkage. On day 12, a TGI of 85.9% was observed. This represents an increased treatment efficacy by 75.3% compared to Doxil alone (**Figure 5.5a**). Given that the PDT individually has no direct therapy contribution, the improvement must have been due to the enhanced EPR caused by the PDT.

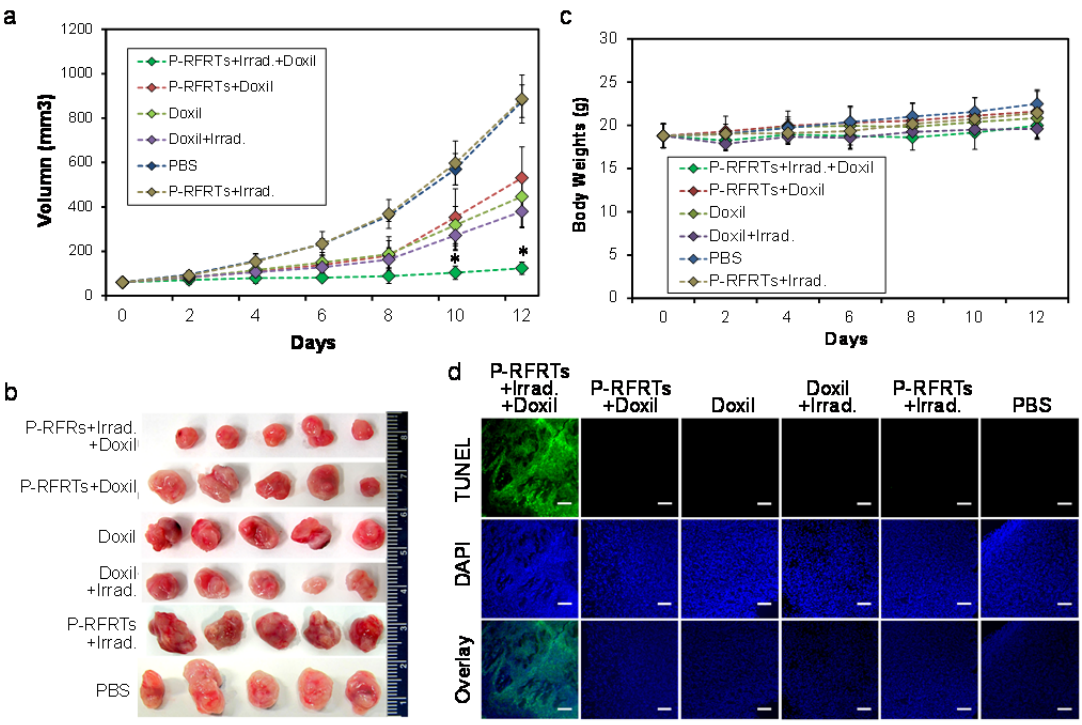

Figure 5.5 ERP Enhancement for Improved Tumor Therapy. (**a**) Therapy results. The study was performed in 4T1 tumor models (n = 5). Doxil was injected 5 min after the end of P-RFRT-mediated PDT. Control groups include animals receiving P-RFRTs and Doxil but no irradiation, Doxil only, irradiation only, P-RFRTs and irradiation but no Doxil, and PBS only. Compared to the control groups, animals receiving the PDT and Doxil combination showed much more significant tumor growth suppression, manifesting a TGI of 85.9% on day 12. * $P < 0.05$. (**b**) Photographs of dissected tumors from a. (**c**) Body weight growth curves. Compared to other groups receiving Doxil, the combination therapy caused no additional weight loss. (**d**) TUNEL assays on tumor sections. A high level of cell death was only observed in animals treated with the combination therapy. Green, TUNEL. Blue, DAPI. Scale bars, 100 μm.

After the therapy studies, we sacrificed the animals. The tumors were dissected and compared both visually (**Figure 5.5b**) and by weight (**Figure S5.9**). The results corroborate well with the measurements in **Figure 5.1a**. We also performed TUNEL assays on the tumor tissues taken from 24 h after treatment (**Figure 5.5c**). A significantly higher level of cell death was observed in the group receiving PDT and Doxil combination. Otherwise, there was no sign of additional toxicity induced by the PDT (**Figure S5.10**). These include no additional heart toxicity, which is commonly associated with Doxil-based treatments (**Figure S5.11**). Also, there

was no significant difference of body weights between the treatment group and other groups receiving Doxil (**Figure 5.5d**). All these observations suggest that the PDT modulation is highly selective and of minimal contralateral damage.

5.3 Conclusions

Nanotherapeutics, whether taking an active or passive targeting approach, relies heavily on the EPR effect to achieve tumor accumulation. Even if engineered to be long-circulating and tumor selective, without efficient extravasation at the tumor sites, nanoparticle drugs will end up accumulating in normal organs, and cause serious side-effects. P-RFRT-mediated PDT represents a novel and safe means that can augment the EPR effect without affecting normal tissues. The technology employs the inherent selective nature of PDT, site-specific delivery capacity of RFRTs, and an optimized irradiance. In combination, the method induces selective and controlled PDT stimuli to the tumor endothelium, leading to increased vessel leakiness while not blocking the blood flow. The approach has proven to be effective in different tumor models to facilitate delivery of nanoparticles to tumors. In particular, it was observed in 4T1 tumor bearing mice that the EPR enhancement effect can translate to enhanced treatment efficacy of Doxil. Future investigations, however, are needed to assess the methodology in tumors of different origins and stages, and to optimize the modulation to gain maximum therapeutic benefits and potentially reduced systematic toxicity.

PDT-induced vessel permeabilization has been observed previously.[24,25] The effect, however, is usually accompanied and often overwhelmed by other vascular effects like vessel collapse and occlusion.[25] Recently, Snyder et al. observed that HPPH-based PDT at low fluence rates can be employed to improve delivery of nanoparticles to tumors.[23] More recently, Wang et

al. reported that low dose PDT with verterpofin can lead to increased tumor uptake of Liporubicin.[26] These observations corroborate with ours on that the irradiation dose is important to EPR enhancement, and should be carefully gauged for the optimal effect. In the previous investigations, vascular targeting was achieved by controlling time interval between photosensitizer injection and illumination, the so-called drug-light interval. Illuminating at an early time point confines the damage mostly within the vasculatures, and that at a late time point mostly on cancer cells.[12] This passive targeting approach has been commonly used in the clinic for therapy purposes. It however, is often associated with side effects that may limit its uses for EPR enhancement. Most commonly used photosensitizers, such as verterpofin, HPPH, Photofrin, chlorin e6, and 5-aminolaevulinic acid, show low tumor-to-normal-tissue (T/N) ratios (around or less than 2).[13-15] In theory, PDT damage can be controlled by photoirraidation that is only given to areas of interest. In reality, however, collateral damage to surrounding normal tissues is often observed.[27] Also, poor T/N selectivity leads to photosensitivity due to high accumulation of photosensitizers in the skin and eyes. For instance, Photofrin treated patients are required to stay out of sunlight for at least 4 weeks,[17] and Foscan injected patients may experience photosensitivity to even interior lighting for at least 1 week post-treatment.[17] These side-effects can significantly affect the life quality of patients, and are not acceptable when PDT is used an adjuvant modality whose main purpose is to enhance chemotherapy. For this application, P-RFRT-mediated PDT is a better approach given the high photosensitizer payload, great tumor selectivity, and minimal skin toxicity.[11]

As mentioned before, the surface of ferritins can be easily modified. In addition to RGD, other types of vasculature targeting motifs, for instance F3 peptide[28] and sialyl Lewis^{X},[29] can be introduced onto the ferritin surface. Moreover, a very recent study by Sano et al. showed that

with proper photoirradiation, IR700-conjugated panitumumab can kill perivascular cancer cells, and in turn, enhance the tumor EPR effect.[30] It will be interesting to develop ferritin derivatives presenting different targeting motifs on the surface and evaluate them for either therapy or EPR enhancement purposes.

The technology also benefits the delivery of macromolecules to tumors, as demonstrated in the case of albumins. Macromolecule therapeutics, in particular monoclonal antibody-based drugs, have achieved rapid advances in the past decade and are emerging as a new category of therapeutics, with 13 antibodies already receiving regulatory approval.[31] This trend is further fueled by the recent progress on developing antibody-drug conjugates (ADCs), which utilizes antibodies as vehicles to transport cytotoxic agents to tumors in a site-specific manner.[32] It is highly expected that our technology as an adjuvant can find wide applications in the delivery of these drugs as well.

Materials and Methods

Cell culture. 4T1 (murine breast cancer), U87MG (human glioblastoma), PC-3 (human prostate cancer) and MDA-MB-435S (human melanoma) cell lines were purchased from ATCC. 4T1 and PC-3 cells were grown in RMPI 1640 medium supplemented with 10% fetal bovine serum (FBS) and 1% penicillin and streptomycin (MediaTech, USA). U87MG cells were grown in DMEM medium containing 10% FBS, 1% non-essential amino acids, and 1% penicillin and streptomycin. These three cell lines were incubated humidly under 37 °C and 5% CO_2. MDA-MB-435S cells were grown in the same medium as 4T1 and PC-3 but were incubated without CO_2.

Ferritin purification and $ZnF_{16}Pc$ loading. The protocols for producing RFRTs and loading $ZnF_{16}Pc$ onto them have been published reported.[11] For IRDye800 labeling, P-RFRTs were incubated with IRDye800 for 30 min and purified through a NAP-5 column to remove uncoupled dye molecules. A starting ratio of 2:1 (IRDye800 to RFRTs) was used. The coupling efficiency was assessed spectroscopically by comparing with a predetermined standard curve (by monitoring absorbance at 780 nm). It was determined that the final conjugates have on average one IRDye800 per particle.

Animal models. Animal models were established by subcutaneous injection of ~10^6 cancer cells (4T1, PC-3, MDA-MB-435S and U87MG) to either one side or both sides of the hindlimbs of 5-6 week athymic nude mice.[33] For 4T1 tumor models, the *in vivo* studies were conducted 1 week after the inoculation when the tumors reached a size of ~100 mm^3. For PC-3, MDA-MB-435S and U87MG tumor models, the *in vivo* studies were conducted 3 weeks after the inoculation when the tumors reaches a size of ~100 mm^3. All the animal studies were according to a protocol approved by the Institutional Animal Care and Use Committee (IACUC) of University of Georgia.

Tumor targeting with P-RFRTs. For tumor targeting studies, IRDye800 labeled P-RFRTs (0.75 mg $ZnF_{16}Pc$/kg) were i.v. injected to bilateral 4T1 tumor models (n = 5). Whole body fluorescence images were acquired on a Maestro II imaging system (PerkinElmer) using NIR emission filter (750-940 nm) up to 24 h post the injection. After the 24 h imaging, the animals were euthanized. The tumors as well as major organs were harvested for *ex vivo* imaging and histology studies.

EPR enhancement studies by fluorescence imaging. For EPR enhancement studies, the animals were i.v. injected with P-RFRTs (0.75 mg $ZnF_{16}Pc$/kg) first (n = 3). For bilateral tumor models, the right-side tumors were irradiated by a 671 nm laser (~1-cm diameter beam) for 30 min. The left-side tumors were shielded by aluminum foil and served as the control. For single-tumor models, two control groups (n = 3) received P-RFRTs but not irradiation and PBS only. The irradiances were measured by a laser power meter (FieldMax II, Coherent), and were varied (3, 8, 14, and 22 mW/cm^2). IRDye800 labeled HSA (0.5 mg/kg) was administered 5 min after the end of the 30 min irradiation. The animals were then subjected to fluorescence imaging on Maestro II using an NIR emission filter (750-940 nm). After 24 h imaging, the animals were sacrificed. The tumors as well as major organs were harvested for *ex vivo* imaging and histology studies. Uptake in a given organ was quantified by region of interest (ROI) analyses on both *in vivo* and *ex vivo* imaging results using the software provided by the vendor. The studies with

QDs (Invitrogen, ex/em:405-665/705 nm) were conducted in bilateral 4T1 tumor models (injected at 30 pmol per mouse). The procedures were similar to those with HSA except that different emission filter (640-820 nm) was selected.

EPR enhancement studies with IONPs. The studies were conducted in bilateral 4T1 tumor models. The animals were i.v. injected with P-RFRTs (0.75 mg $ZnF_{16}Pc$/kg) first (n = 3). The right-side tumors were irradiated 24 h later by a 671 nm laser (14 mW/cm^2, over a ~1-cm diameter beam) for 30 min. The left-side tumors were shielded by aluminum foil and served as the control. 5 min after the end of the irradiation, IONPs (Ocean Nanotech) at a dose of 10 mg Fe/kg were i.v. injected. T2-weighted FSE images were acquired on a 7 T Varian small animal MRI system before and 4 h and 24 h after the particle injection. The following parameters were used for the scans: TR = 2.5 s; TE = 48 ms; ETL = 8; FOV 40^2 mm^2; matrix size = 256^2; 13 axial slices with 1 mm slice thickness. After the 24 h scan, the mice were sacrificed. The tumors were collected and snap-frozen for Prussian blue staining.

***In vivo* therapy studies.** The therapy studies were performed in 4T1 tumor models (one tumor each animal). Briefly, 30 4-6 week female nude mice were subcutaneously injected with ~10^6 4T1 cells to the right hindlimb. The 30 mice were randomly divided to 6 groups, 5 mice each group. The study started 5 days after the inoculation (average tumor size of 50.68 ± 18.79 mm^3). For treatment group, the animals were i.v. injected with P-RFRTs first (0.75 mg $ZnF_{16}Pc$/kg). The tumors were irradiated 24 h later by a 671 nm laser (14 mW/cm^2, over a ~1-cm diameter beam) for 30 min. Doxil were i.v. injected 5 min after the end of the irradiation at a dose of 10 mg/kg. The five control groups are: 1) receiving P-RFRTs and Doxil, but no irradiation; 2) Doxil only; 3) PBS and irradiation, no P-RFRTs and Doxil; 4) PBS only; and 5) P-RFRTs and irradiation, no Doxil. The tumors sizes and body weights were measured every other day. Tumor sizes were measured by a caliper, and computed following the formulation: size (mm^3) = length (mm) × width (mm)^2/2.

Immunofluorescence staining. The cryogenic slides were fixed with cold acetone for 30 min, washed by running water for 5 min, and blocked by 10% goat serum for 1 h. Anti-integrin β_3 (ab75872, Abcam) or phycoerythrin-labeled anti-CD31 (ab25644, Abcam) antibodies were incubated with the slides at 4 °C overnight. Cy5.5-labeled secondary antibodies (ab6564, Abcam) were then added and incubated with the slides at 37 °C for 1 h. After gently rinsing with PBS, the slides were mounted and ready for microscopic imaging. TUENL assays were performed by following a protocol provided by the vendor (FITC-labeled POD, GenScript).

Scanning Electron Microscopy. Tumor blocks were cut into 10 μm slices. Those slices were mounted on coverslips, and fixed by 0.5% paraformaldehyde at 4°C for 48 hours. For dehydration, ethanol of gradient concentrations (25%, 50%, 75%, 90% and 100%) was applied to the slices at room temperature, 30 min for each step. These slides were then sputter-coated with a gold/palladium mix after critical point dried in a SAM-DRI–790 CPD,[34] and then analyzed using a field emission gun SEM (FEI INSPECT F FEG-SEM).

Hematoxylin and eosin staining. H&E staining was performed according to a protocol provided by the vendor (BBC Biochemical). Briefly, 8 μm cryogenic slides were prepared and fixed with 10% formalin for about 30 min at room temperature. After washing with running water for 5 min, the slides were treated with gradient concentrations of alcohol (100, 95, and 70%), each for

20 s. The hematoxylin staining was performed for about 3 min and washed with water for 1 min. The eosin staining was performed for about 1 min. The slides were washed, treated with xylene, and mounted with Canada balsam. The images were acquired on a Nikon Eclipse 90i microscope.

Statistical methods. Quantitative data were expressed as mean ± SD. Means were compared using Student's t-test. P values < 0.05 were considered statistically significant.

Supporting Information

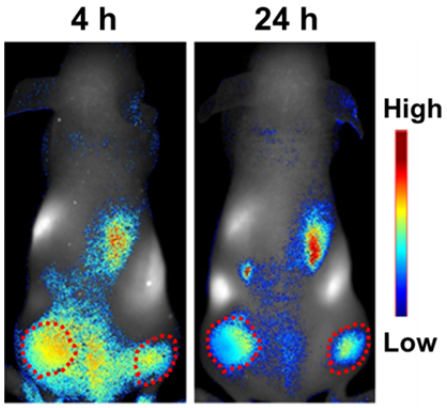

Figure S5.1 Tumor targeting study with P-RFRTs in bilateral 4T1 tumor models. The tumors were circled by red dashed lines.

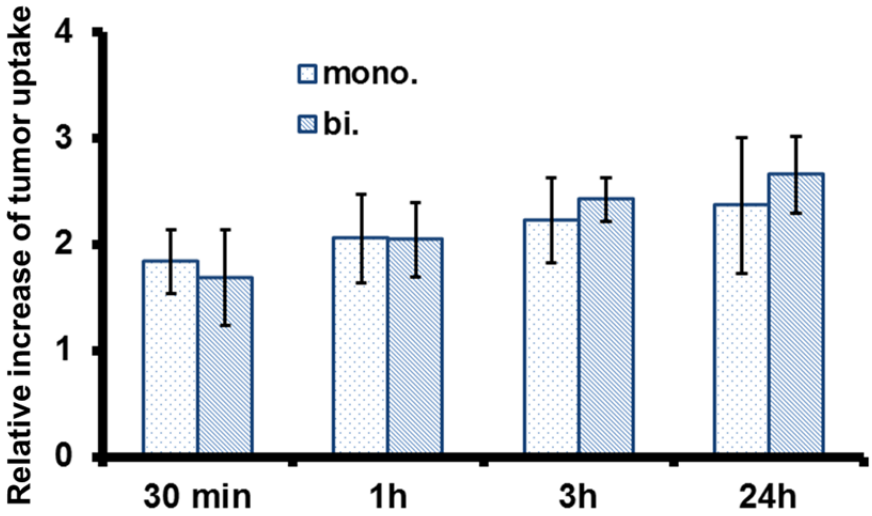

Figure S5.2 Comparison of relative increase of tumor uptake. The results came from studies performed on 4T1 tumor models bearing either one (mono) or two (bi) tumors.

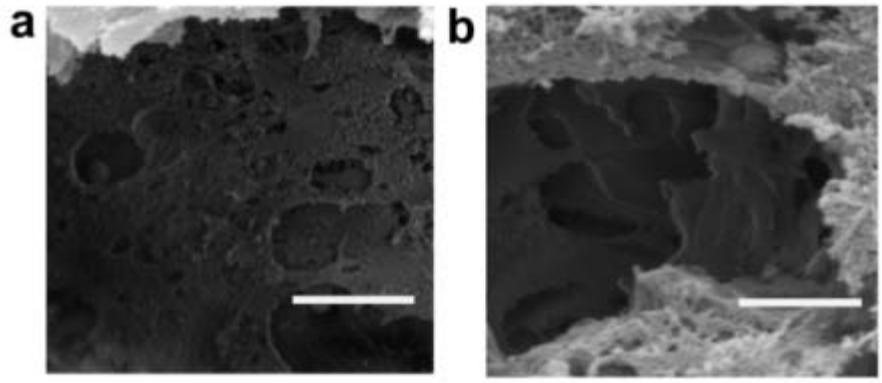

Figure S5.3 Selected SEM images of tumor tissues with (a) and without (b) PDT treatment. Scale bar, 1 μm.

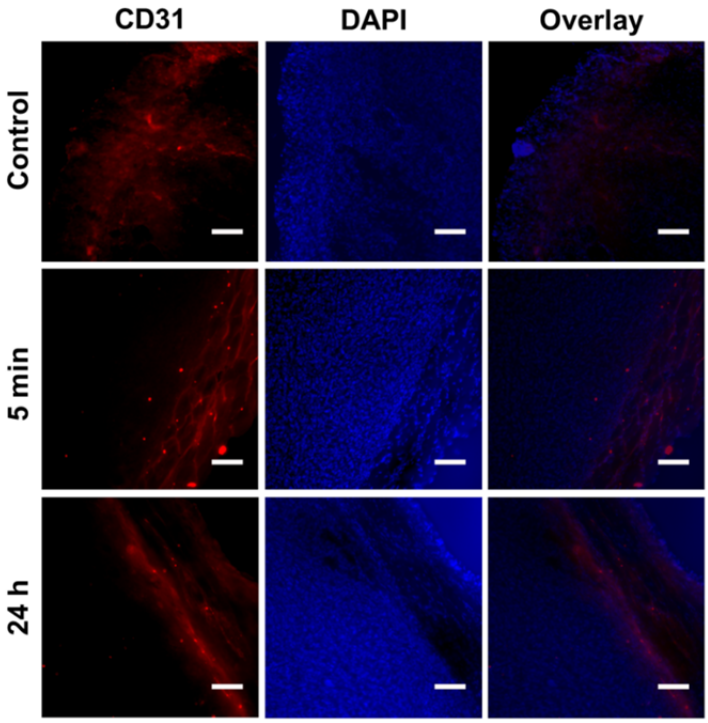

Figure S5.4 CD31 staining on 4T1 tumor samples taken before (the first row) as well as 5 min and 24 h after P-RFRT-mediated PDT. Tumor vessels were convoluted and irregular before the PDT. After the treatment, however, the vessel became more regular and ordered, more so at 5 min. Red, CD31. Blue, DAPI. Scale bars, 100 μm.

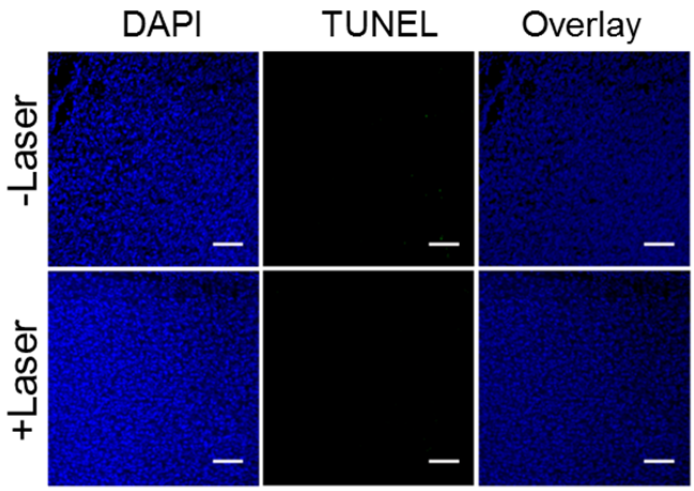

Figure S5.5 TUNEL assays on samples from irradiated (PDT-treated) and non-irradiated (non-PDT treated) tumors. There was no detection of significantly increased cell death after PDT. Blue, DAPI. Green, TUNEL. Scale bars, 100 μm.

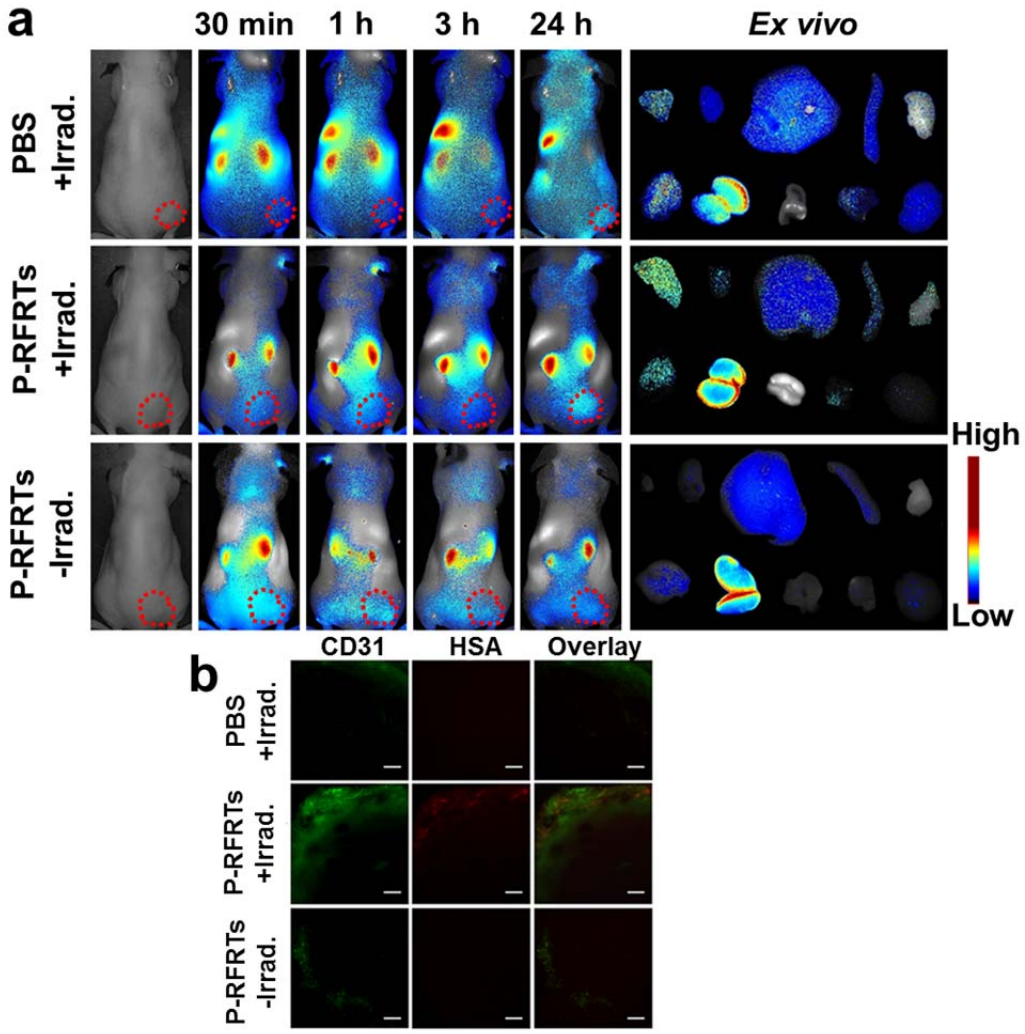

Figure S5.6 (a) *In vivo* and *ex vivo* imaging on PC-3 tumor models. P-RFRTs were i.v. injected first. Photoirradiation was applied to the tumors 24 h later. 5 min after the end of the irradiation, IRDye800 labeled HSA was administered. Control groups received P-RFRTs but no irradiation (the third row) or irradiation only (the first row) before the HSA injection. Fluorescence imaging was performed at 30 min, 1 h, 3 h, and 24 h to evaluate the uptake of the probes by tumors (circled by red dashed lines). After the 24 h imaging, the animals were sacrificed. Tumors as well as major organs were subjected to *ex vivo* imaging to further assess the impact of the PDT on biodistribution of albumins. For each group, the tissues were arranged in the following order: The first row, tumor, heart, liver, spleen and skin; the second row, lung, kidneys, intestine, muscle and brain. (b) Histology studies on tumor tissues. More albumins were observed in PDT treated tumors (the second row). Green, CD31. Red, HSA. Scale bars, 100 μm.

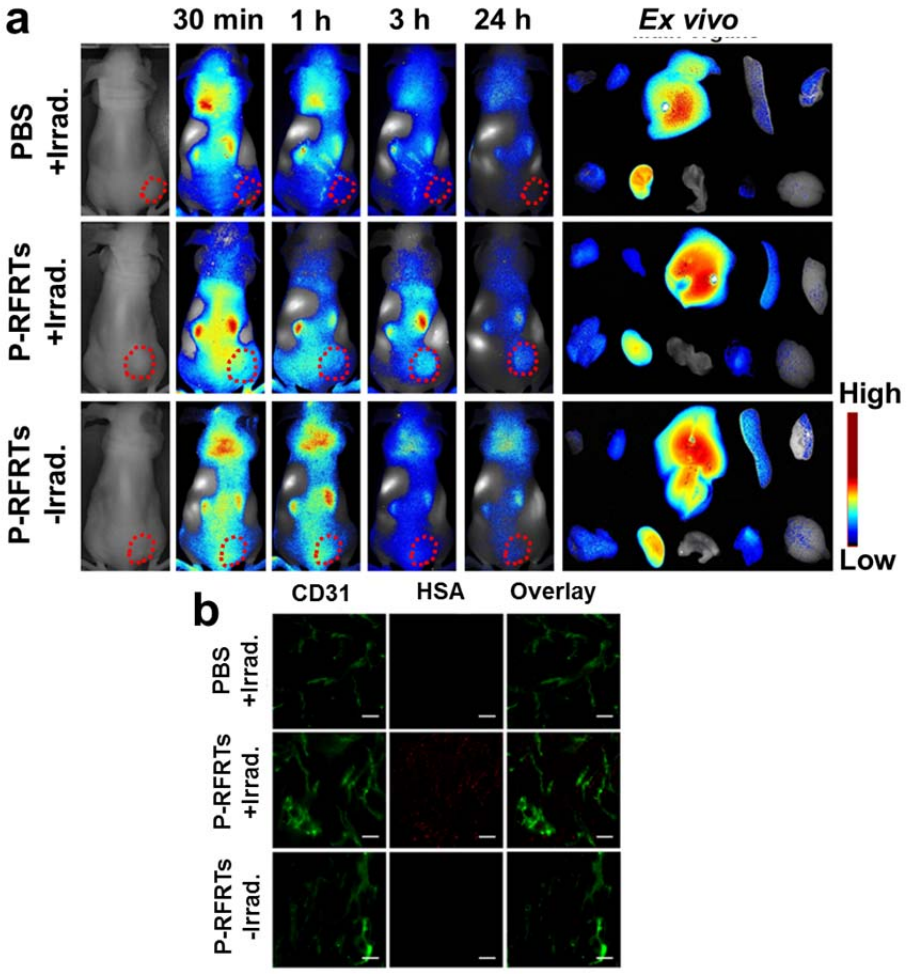

Figure S5.7 (a) *In vivo* and *ex vivo* imaging on MDA-MB-435S tumor models. P-RFRTs were i.v. injected first. Photoirradiation was applied to the tumors 24 h later. 5 min after the end of the irradiation, IRDye800 labeled HSA was administered. Control groups received P-RFRTs but no irradiation (the third row) or irradiation only (the first row) before the HSA injection. Fluorescence imaging was performed at 30 min, 1 h, 3 h, and 24 h to evaluate the uptake of the probes by tumors (circled by red dashed lines). After the 24 h imaging, the animals were sacrificed. Tumors as well as major organs were subjected to *ex vivo* imaging to further assess the impact of the PDT on biodistribution of albumins. For each group, the tissues were arranged in the following order: The first row, tumor, heart, liver, spleen and skin; the second row, lung, kidneys, intestine, muscle and brain. (b) Histology studies on tumor tissues. More albumins were observed in PDT treated tumors (the second row). Green, CD31. Red, HSA. Scale bars, 100 μm.

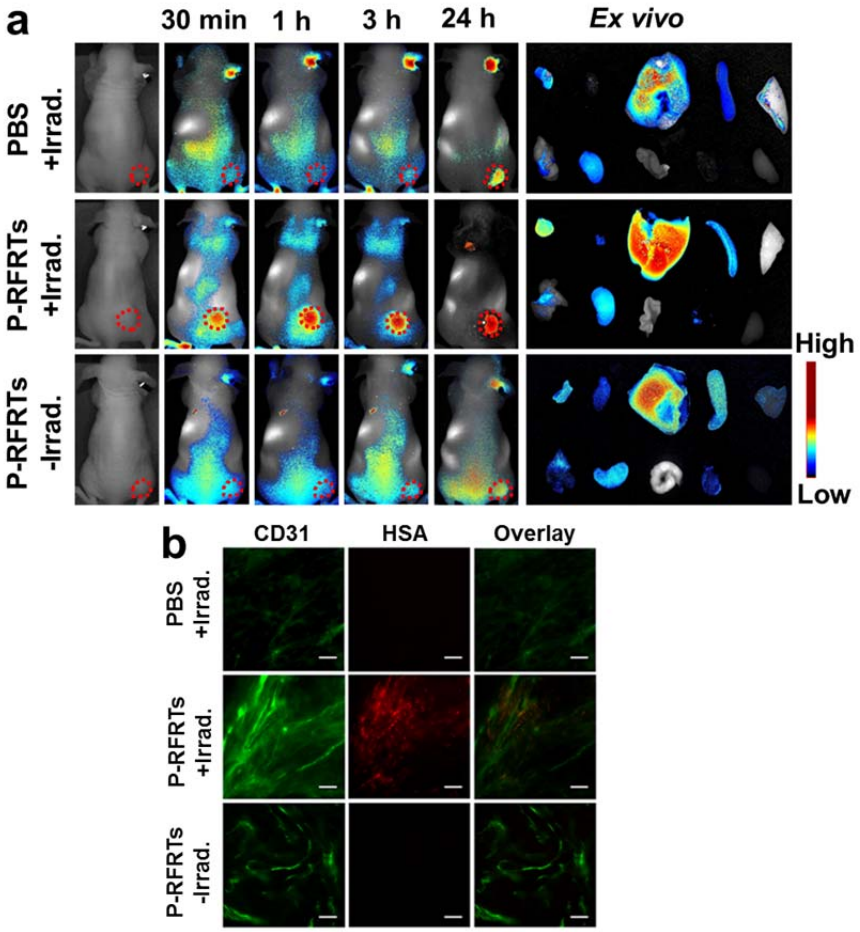

Figure S5.8 (a) *In vivo* and *ex vivo* imaging on U87MG tumor models. P-RFRTs were i.v. injected first. Photoirradiation was applied to the tumors 24 h later. 5 min after the end of the irradiation, IRDye800 labeled HSA was administered. Control groups received P-RFRTs but no irradiation (the third row) or irradiation only (the first row) before the HSA injection. Fluorescence imaging was performed at 30 min, 1 h, 3 h, and 24 h to evaluate the uptake of the probes by tumors (circled by red dashed lines). After the 24 h imaging, the animals were sacrificed. Tumors as well as major organs were subjected to *ex vivo* imaging to further assess the impact of the PDT on biodistribution of albumins. For each group, the tissues were arranged in the following order: The first row, tumor, heart, liver, spleen and skin; the second row, lung, kidneys, intestine, muscle and brain. (b) Histology studies on tumor tissues. More albumins were observed in PDT treated tumors (the second row). Green, CD31. Red, HSA. Scale bars, 100 μm.

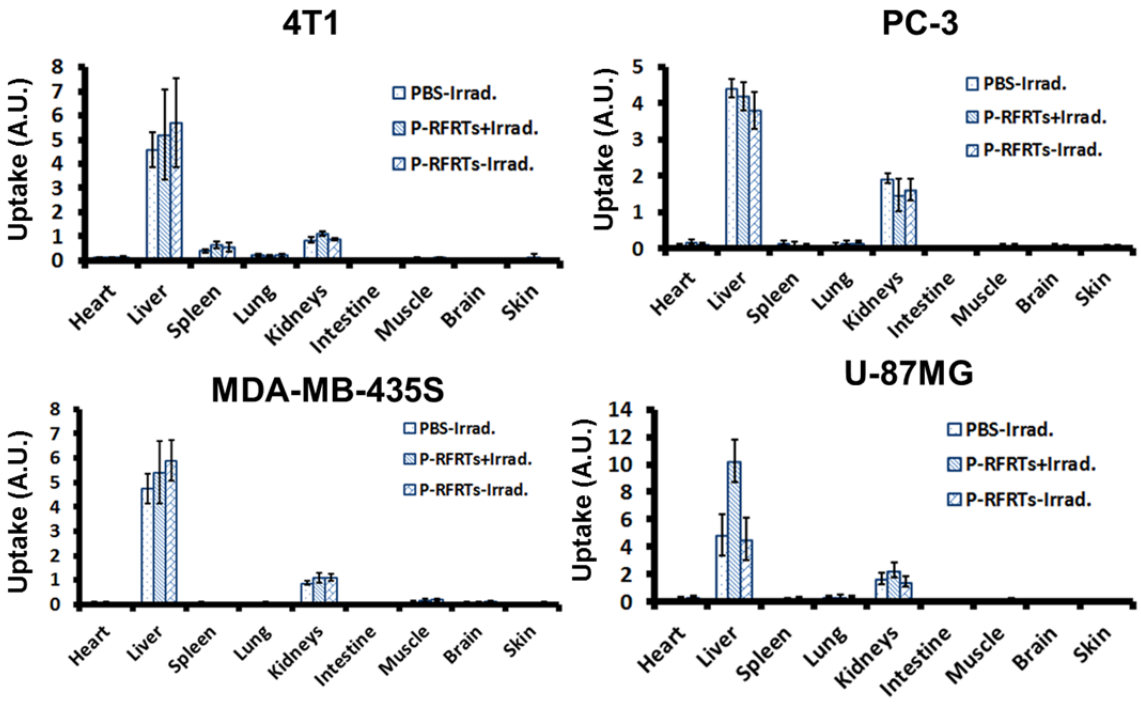

Figure S5.9 Histogram comparison of accumulation of albumins in normal tissues. The results were based on ROI analyses on *ex vivo* imaging data (from Figure 2c and Figure S5.5-S5.7).

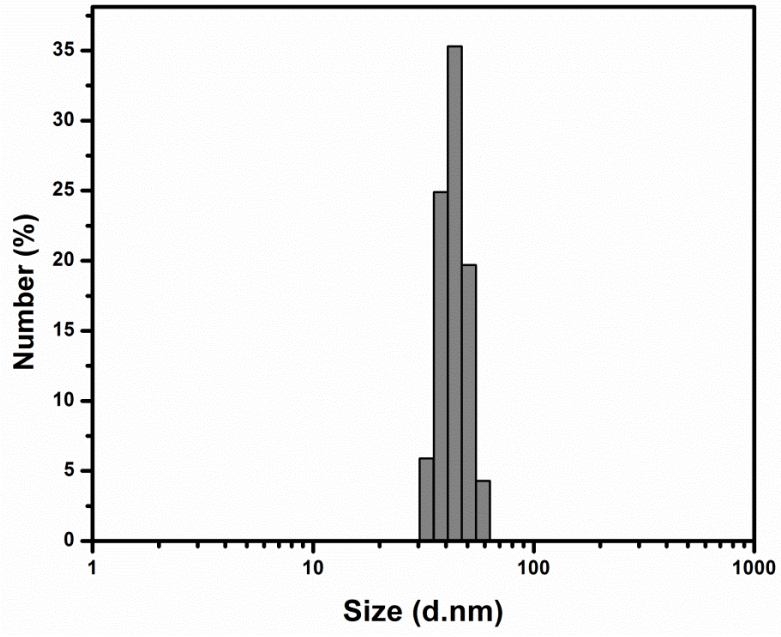

Figure S5.10 Hydrodynamic size of QDs, measured by DLS. The average size is 43.23±6.27 nm.

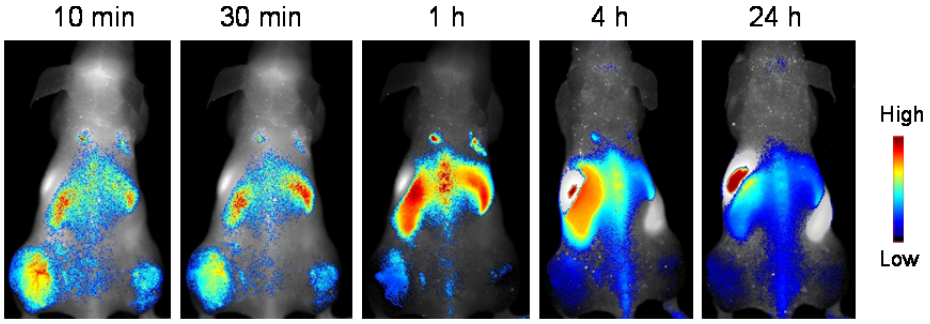

Figure S5.11 *In vivo* images taken at different time points after QD injection. P-RFRTs were injected first and irradiation was only applied to the left-side tumors. QDs were injected after the end of irradiation.

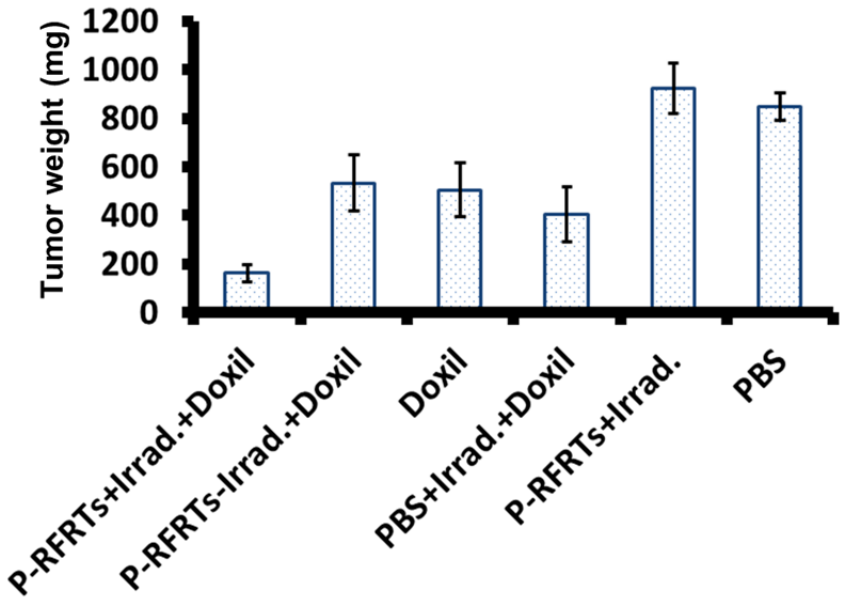

Figure S5.12 Histogram comparison of tumor weights among different therapy groups.

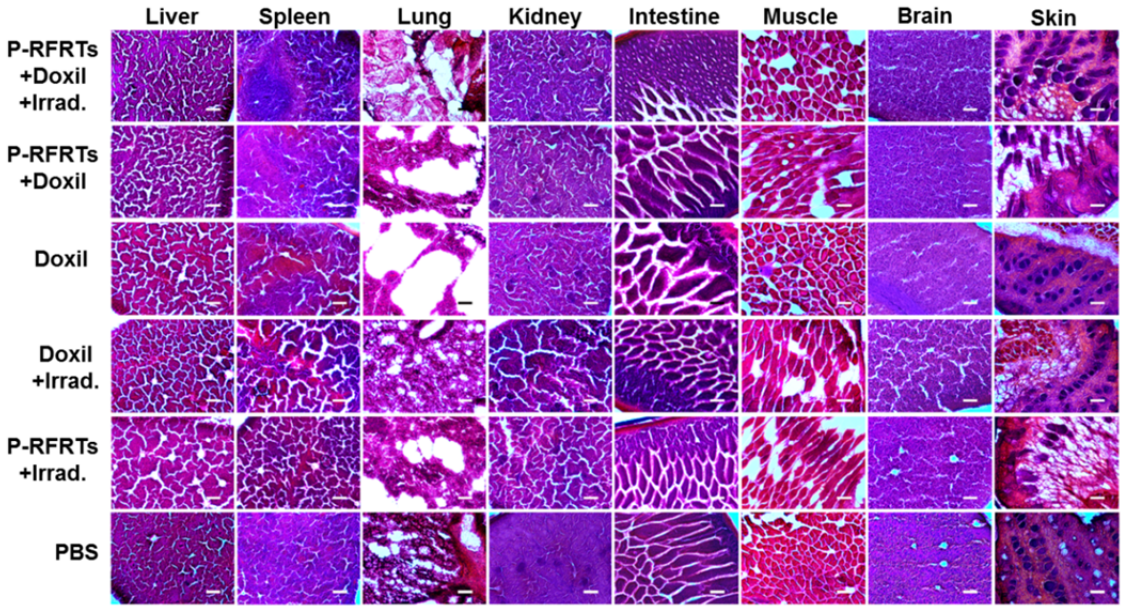

Figure S5.13 H&E staining on normal tissues from different therapy groups. No significant difference was observed between the group receiving the combination therapy (the first row) and the others receiving Doxil. Scale bars, 100 μm.

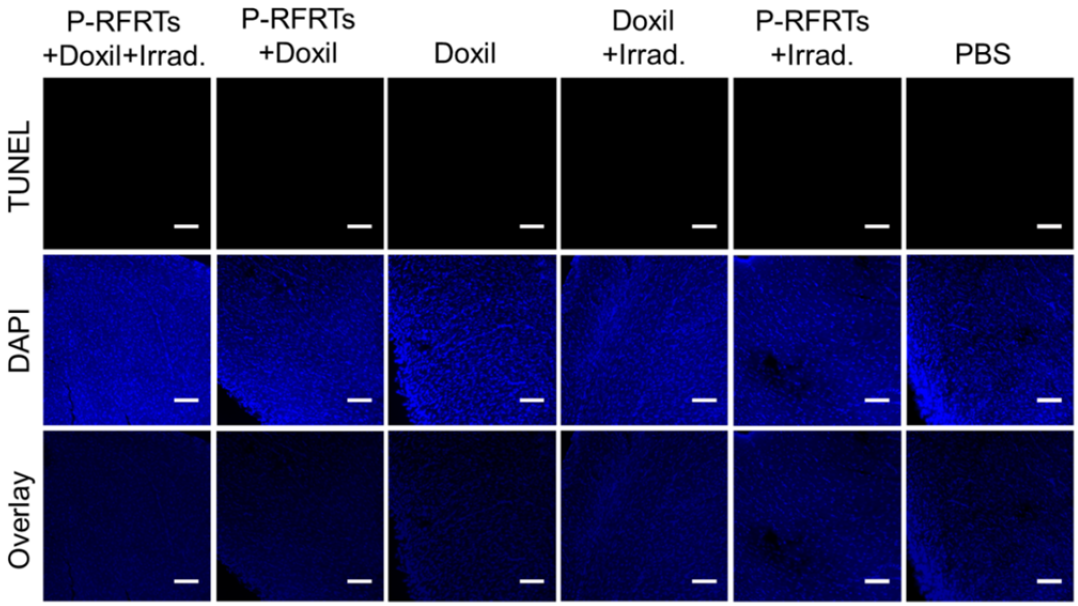

Figure S5.14 TUNEL assays with heart tissue samples from different therapy groups. Blue, DAPI. Green, TUNEL. Scale bars, 100 μm.

References

(1) Wang, A. Z.; Langer, R.; Farokhzad, O. C. *Annual Review of Medicine* **2012**, *63*, 185.

(2) Taurin, S.; Nehoff, H.; Greish, K. *Journal of Controlled Release* **2012**, *164*, 265.

(3) Maeda, H. *P Proceedings of the Japan Academy, B, Physical and Biological Sciences* **2012**, *88*, 53.

(4) Prabhakar, U.; Maeda, H.; Jain, R. K.; Sevick-Muraca, E. M.; Zamboni, W.; Farokhzad, O. C.; Barry, S. T.; Gabizon, A.; Grodzinski, P.; Blakey, D. C. *Cancer Research* **2013**, *73*, 2412.

(5) Maeda, H.; Nakamura, H.; Fang, J. *Advanced Drug Delivery Reviews* **2013**, *65*, 71.

(6) Dolmans, D. E. J. G. J.; Fukumura, D.; Jain, R. K. *Nature Review. Cancer* **2003**, *3*, 380.

(7) Fisher, A. M.; Murphree, A. L.; Gomer, C. J. *Lasers in Surgery and Medicine* **1995**, *17*, 2.

(8) Nishiyama, N.; Morimoto, Y.; Jang, W. D.; Kataoka, K. *Advanced Drug Delivery Reviews* **2009**, *61*, 327.

(9) Zhen, Z. P.; Tang, W.; Chen, H. M.; Lin, X.; Todd, T.; Wang, G.; Cowger, T.; Chen, X. Y.; Xie, J. *ACS Nano* **2013**, *7*, 4830.

(10) Todd, T. J.; Zhen, Z. P.; Xie, J. *Nanomedicine* **2013**, *8*, 1555.

(11) Zhen, Z. P.; Tang, W.; Guo, C. L.; Chen, H. M.; Lin, X.; Liu, G.; Fei, B. W.; Chen, X. Y.; Xu, B. Q.; Xie, J. *ACS Nano* **2013**, *7*, 6988.

(12) Garcia, A. M.; Alarcon, E.; Munoz, M.; Scaiano, J. C.; Edwards, A. M.; Lissi, E. *Photochemical & Photobiological Sciences* **2011**, *10*, 507.

(13) Lin, X.; Xie, J.; Niu, G.; Zhang, F.; Gao, H.; Yang, M.; Quan, Q.; Aronova, M. A.; Zhang, G.; Lee, S.; Leapman, R.; Chen, X. *Nano Letters* **2011**, *11*, 814.

(14) Tan, M.; Lu, Z. R. *Theranostics* **2011**, *1*, 83.

(15) Zhang, Y.; Yang, Y.; Cai, W. *Theranostics* **2011**, *1*, 135.

(16) Li, Z. B.; Cai, W.; Cao, Q.; Chen, K.; Wu, Z.; He, L.; Chen, X. *Journal of Nuclear Medicine* **2007**, *48*, 1162.

(17) Kong, G.; Braun, R. D.; Dewhirst, M. W. *Cancer Research* **2000**, *60*, 4440.

(18) Dougherty, T. J.; Gomer, C. J.; Henderson, B. W.; Jori, G.; Kessel, D.; Korbelik, M.; Moan, J.; Peng, Q. *Journal of the National Cancer Institute* **1998**, *90*, 889.

(19) Kanthou, C.; Tozer, G. M. *Blood* **2002**, *99*, 2060.

(20) Hashizume, H.; Baluk, P.; Morikawa, S.; McLean, J. W.; Thurston, G.; Roberge, S.; Jain, R. K.; McDonald, D. M. *The American Journal of Pathology* **2000**, *156*, 1363.

(21) Less, J. R.; Posner, M. C.; Skalak, T. C.; Wolmark, N.; Jain, R. K. *Microcirculation-Lon* **1997**, *4*, 25.

(22) Heldin, C. H.; Rubin, K.; Pietras, K.; Ostman, A. *Nature Review. Cancer* **2004**, *4*, 806.

(23) Snyder, J. W.; Greco, W. R.; Bellnier, D. A.; Vaughan, L.; Henderson, B. W. *Cancer Research* **2003**, *63*, 8126.

(24) Debefve, E.; Mithieux, F.; Perentes, J. Y.; Wang, Y. B.; Cheng, C.; Schaefer, S. C.; Ruffieux, C.; Ballini, J. P.; Gonzalez, M.; van den Bergh, H.; Ris, H. B.; Lehr, H. A.; Krueger, T. *Lasers in Surgery and Medicine* **2011**, *43*, 696.

(25) Chen, B.; Pogue, B. W.; Luna, J. M.; Hardman, R. L.; Hoopes, P. J.; Hasan, T. *Clinical Cancer Research* **2006**, *12*, 917.

(26) Wang, Y. B.; Gonzalez, M.; Cheng, C.; Haouala, A.; Krueger, T.; Peters, S.; Decosterd, L. A.; van den Bergh, H.; Perentes, J. Y.; Ris, H. B.; Letovanec, I.; Debefve, E. *Lasers in Surgery and Medicine* **2012**, *44*, 318.

(27) Allison, R. R.; Downie, G. H.; Cuenca, R.; Hu, X. H.; Childs, C. J. H.; Sibata, C. H. *Photodiagnosis and Photodynamic Therapy* **2004**, *1*, 27.
(28) Winer, I.; Wang, S. Y.; Lee, Y. E. K.; Fan, W. Z.; Gong, Y. S.; Burgos-Ojeda, D.; Spahlinger, G.; Kopelman, R.; Buckanovich, R. J. *Cancer Research* **2010**, *70*, 8674.
(29) Farr, T. D.; Lai, C. H.; Grunstein, D.; Orts-Gil, G.; Wang, C. C.; Boehm-Sturm, P.; Seeberger, P. H.; Harms, C. *Nano Letters* **2014**, *14*, 2130.
(30) Sano, K.; Nakajima, T.; Choyke, P. L.; Kobayashi, H. *ACS Nano* **2013**, *7*, 717.
(31) Sliwkowski, M. X.; Mellman, I. *Science* **2013**, *341*, 1192.
(32) Kovtun, Y. V.; Goldmacher, V. S. *Cancer Letters* **2007**, *255*, 232.
(33) Edwards, B. K.; Brown, M. L.; Wingo, P. A.; Howe, H. L.; Ward, E.; Ries, L. A.; Schrag, D.; Jamison, P. M.; Jemal, A.; Wu, X. C.; Friedman, C.; Harlan, L.; Warren, J.; Anderson, R. N.; Pickle, L. W. *Journal of the National Cancer Institute* **2005**, *97*, 1407.
(34) Moore-Scott, B. A.; Gordon, J.; Blackburn, C. C.; Condie, B. G.; Manley, N. R. *Genesis* **2003**, *35*, 164.

CHAPTER 6

RED BLOOD CELL-FACILITATED PHOTODYNAMIC THRAPY FOR CANCER TREATMENT[i]

[i] Wei Tang, Zipeng Zhen, Mengzhe Wang, Hui Wang, Yen-Jun Chuang, Weizhong Zhang, Geofferey D Wang, Trever Todd, Taku Cowger, Hongmin Chen, Zibo Li,* Jin Xie* *Advanced Functional Materials*, **2016**, *26*, 1757-1768. Reprinted here with permission of publisher.

6.1 Introduction

Photodynamic therapy (PDT) is a relatively new treatment modality that has gained widespread attention. PDT has been used in the clinic for treatment of Barrett's esophagus, age-related macular degeneration, and esophageal cancer.[1-3] It is also under intensive investigation for cancer treatment, including cancers of head and neck, brain, skin, breast, lung, bladder and prostate.[4-9] There are three essential components for PDT: light, photosensitizers, and oxygen. Individually, none of the components is toxic, but together they initiate a photochemical reaction, producing reactive oxygen species, most importantly singlet oxygen ($^1O_2$),[4,10,11] which is cytotoxic. While PDT can kill cancer cells directly, it is a common approach to use PDT to damage tumor blood vessels, leading to vessel blockage, tissue ischemia, and eventually cancer cell death.[11,12] In addition, PDT is immunostimulatory and can induce an immune response against tumors.[13]

Over the years, there have been continuous efforts on improving the delivery efficiency of photosensitizers.[14-16] O_2, another essential component of PDT, is not artificially delivered but usually taken from the biological milieu. However, O_2 is a precious resource in tumors. Uncontrolled proliferation of cancer cells often outgrows their blood supply, leading to low oxygen levels and even hypoxia.[17,18] Tumor hypoxia renders cancer cells more resistant to radiotherapy and anticancer chemotherapy, and increases the tendency of metastasis.[19] It also poses an obstacle for PDT, whose efficacy is heavily oxygen-dependent. Previous studies have shown that the efficacy of PDT decreases when partial oxygen pressure is below 40 mmHg,[20,21] and abolished in the event of tissue ischemia.[22] These facts underscore the importance of O_2 in PDT and suggest the benefits for delivering both O_2 and photosensitizers in such a treatment. So far, however, there have been few tentatives along this direction.

Herein we report a novel, red blood cell enhanced PDT (or RBC-PDT) approach that can potentially address the need. RBC-PDT uses RBCs as photosensitizer carriers; but unlike common drug carriers, RBCs bear with them a second cargo, O_2. RBCs carry 270 million hemoglobin molecules per cell (each hemoglobin binds up to 4 O_2 molecules), and are the primary source of oxygen to our body tissues.[23] Even in hypoxic tumor regions, there are O_2 molecules released from RBCs to the surroundings,[24] but they are rapidly consumed by cancer cells adjacent to capillaries, leaving distant cells poorly oxygenated.[23] Our hypothesis is that while oxygen liberated from RBCs is not sufficient to pump up whole tumors, there exists an oxygen-rich zone close to the surface of RBCs. If photosensitizers are located within the zone or resided on the RBC surface, they may benefit from the oxygen flow from RBCs to continuously produce $^1O_2$, even in hypoxic regions. As discussed above, PDT can not only directly kill cancer cells, but also damage tumor vasculatures, leading to tissue ischemia. From this perspective, the facts that RBCs afford a long circulation half-life and minimal extravasation are extra benefits to the RBC-PDT approach, ensuring maximized photodynamic impact onto the lumen and endothelium of tumor vasculatures. It is noted that unlike chemotherapy, PDT is a focal treatment modality that is largely regulated by photo-irradiation. This means that efficient vascular PDT can be achieved when there is a high intraluminal concentration of photosensitizer at the time of irradiation, even when the photosensitizers are not internalized in cancer or endothelial cells. For instance, it was observed that for verteporfin-based PDT, a short drug-light interval (e.g. 15 min) led to efficient vasculature damage whereas a long drug-light interval (e.g. 3 h) induced direct cancer cell death due to extravasation of the photosensitizer.[25,26]

One challenge, however, is how to load a large amount of photosensitizers to the surface of RBCs. Most photosensitizers are porphyrin-like molecules, which are hydrophobic, prone to

aggregation, and do not provide conjugation-friendly functional groups.[27] This problem can be solved by using nanocapsules to encapsulate photosensitizers and tether the conjugates onto RBC surface.[16] In the present study, we used ferritin, a protein-based nanocage, for the purpose. Our recent studies showed that ferritins could load photosensitizers such as $ZnF_{16}Pc$ (maximum excitation at ~671 nm, Φ_{Δ}=0.85 in THF[28]), by 40wt% without inducing significant self-quenching or compromised colloidal stability.[16] Using biotin-neutravidin mediated coupling, we were able to conjugate ~ 5×10^5 $ZnF_{16}Pc$-loaded ferritins onto each RBC. Carrying a large amount of photosensitizers and oxygen, the resulting conjugates show efficient $^1O_2$ production even under low oxygen conditions. The merit of having a carry-on oxygen reservoir translates to enhanced PDT capacity to kill cancer cells, which is confirmed both *in vitro* and *in vivo* with hypoxia tumor models. The results suggest a great potential of RBC-PDT in cancer therapy and sheds light on a new avenue to enhance the efficacy of PDT.

6.2 Results

6.2.1 Preparation of P-FRT-RBCs

Ferritin preparation and $ZnF_{16}Pc$ loading were conducted by following our published protocols.[16,29] We used a $ZnF_{16}Pc$-loaded ferritin (P-FRT) formulation with a ferritin to $ZnF_{16}Pc$ molar ratio of 1:40 for the studies. According to our previous research, at this loading rate, there is little aggregation of the loaded ferritins and the self-quenching among the encapsulated $ZnF_{16}Pc$ molecules is minimal.[16]

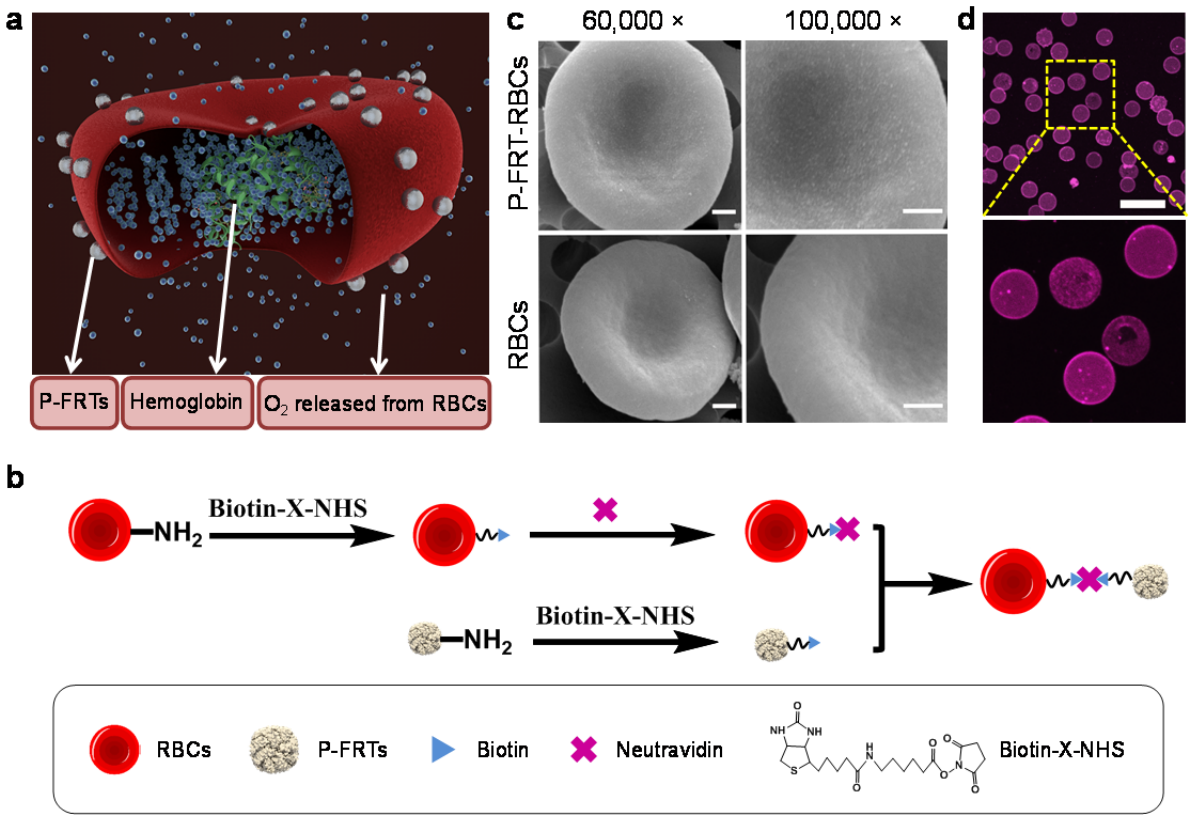

Figure 6.1 Construction of P-FRT-RBCs. (a) Schematic illustration of the formation and working mechanism of P-FRT-RBCs. (b) Schematic illustration of the synthesis of P-FRT-RBCs (not to scale). (c) SEM images of P-FRT-RBCs and RBCs. While the surface of RBCs is relatively smooth, the surface P-FRT-RBCs was adorned with small particles with sizes around 15-18 nm. Scale bars, 500 nm. (d) Confocal microscopy images of Cy5.5-labeled P-FRT-RBCs. Ex/em: 673/707 nm. Scale bar, 20 μm.

To conjugate P-FRT to RBCs, we biontinylated both ferritins and RBCs using biotin-X-NHS (Calbiochem), and then crosslinked them with neutravidin (**Figure 6.1b**, details of the procedures were described in the Methods section). The resulting, P-FRT conjugated RBCs, or P-FRT-RBCs (**Figure 6.1a**), were characterized by scanning electron microscopy (SEM, **Figure 6.1c**). P-FRT-RBCs displayed a coarse surface, adorned with a large number of nanoparticles with diameters of 15-18 nm. The size is in good agreement with photosensitizer-loaded ferritins.[16] By contrast, native RBCs presented a smooth surface (**Figure 6.1c**). The coupling efficiency of biotinylated ferritins was determined to be 24 biotin molecules per ferritin with

matrix assisted laser desorption ionization (MALDI) (**Figure S6.1**). To quantify the coupling efficiency of P-FRTs to RBCs, we labeled P-FRTs with a fluorescent dye molecule, IRDye800 (ex/em: 775/790 nm). By analyzing the 775-nm absorption and comparing it to a pre-determined standard curve, it was determined that ~ 5×10^5 P-FRTs (that is, ~ 2×10^7 $ZnF_{16}Pc$ molecules) were tethered to the surface of each RBC. The high loading was validated by fluorescence microscopy, which found intense and evenly distributed fluorescence signals on the RBC membrane (**Figure 6.1d**).

There was little $ZnF_{16}Pc$ released from P-FRT-RBCs in the serum (**Figure S6.2**), indicating minimal premature photosensitizer release. Due to the facts that the lifetime of $^1O_2$ is very short in aqueous solutions and that the P-FRT-RBCs are not soluble in organic solvents, it is not possible to measure $^1O_2$ quantum yield of them. Using SOSG assays, however, we observed comparable $^1O_2$ production between $ZnFe_{16}Pc$ and P-FRTs in our previous studies,[16] and between P-FRT-RBCs and P-RBCs in the present study (**Figure S6.3**).

6.2.2. Cytotoxicity studies with P-FRT-RBCs

The cytotoxicity of P-FRT-RBCs was evaluated with U87MG cells (human glioma) using 3-(4,5-dimethythiazon-2-yl)-2,5-diphenyl tetrazolium bromide (MTT) assays. In the absence of photo-irradiation, P-FRT-RBCs showed little cytotoxicity (**Figure S6.4**). When P-FRT-RBCs were applied in conjunction with a 671-nm laser radiation, however, the treatment led to extensive cell death (**Figure S6.5**), which is a hallmark of PDT-induced toxicity. The PDT toxicity was validated by SOSG assays, which found widespread production of $^1O_2$ (**Figure S6.6**); meanwhile, ethidium homodimer-III assay (also known as dead assay,[30] **Figure S6.6**) detected extensive positive staining, indicating severe breakage of cell membrane integrity upon the treatment. Interestingly, both MTT and ethidium homodimer-III staining results found more

effective cell killing with P-FRT-RBCs than with P-FRTs. This again was attributed to a relatively high O_2 level in P-FRT-RBC containing solutions[31] and corroborated with the $^1O_2$ production result (**Figure S6.3**).

RBCs lack nuclei and many cellular organelles and they do not undergo commonly recognized apoptosis.[32] Instead, aged RBCs manifest increased externalization of phosphatidylserine,[33] leading to their fast clearance from the circulation. Our flow cytometry analysis found no significant increase of RBC phosphatidylserine levels over their coupling with P-RBCs (**Figure S6.7**). Moreover, we observed little phosphatidylserine level enhancement when subjecting P-FRT-RBCs under continuous photo-irradiation (100 mW/cm^2, up to 1 hr, **Figure S6.8**). In other words, conjugation and PDT processes have relatively minor impact on the circulation half-lives of RBCs, which is important to the *in vivo* applications. Notably, the relatively robustness of RBCs against PDT has been observed by others as well.[34]

6.2.3 P-FRT-RBC-based PDT can efficiently produce $^1O_2$, even under low oxygen conditions

We next evaluated whether O_2 released from RBCs can benefit P-FRT-RBCs for sustained $^1O_2$ production under low oxygen conditions. This was first evaluated in solutions using SOSG as a $^1O_2$ marker. Specifically, we injected P-FRT-RBCs into a sealed cuvette that had been loaded with PBS and bubbled with Ar. We then irradiated the cuvette by a 671 nm laser (100 mW/cm^2); at selected time points, the irradiation was stopped and the amount of $^1O_2$ in the solution was assessed by measuring fluorescence increase at 525 nm.[16] For comparison, we also studied P-FRTs at the same $ZnF_{16}Pc$ concentration and irradiation doses. We observed little $^1O_2$ production with P-FRTs, likely due to the oxygen-free condition. Meanwhile, there was continuous $^1O_2$ generated in the cuvette loaded with P-FRT-RBCs (**Figure 6.2a**); this was attributed to the RBCs

in the closed system, which functioned as an O_2 reservoir. Notably, such RBC-facilitated $^1O_2$ production worked best when photosensitizers were attached to the RBC surface. In a control group, we mixed (but not conjugated) the same amounts of P-FRTs and RBCs and injected them into a cuvette; in this case, we observed increased $^1O_2$ production but the $^1O_2$ level was significant less than that with P-FRT-RBCs (**Figure 6.2a**, $P<0.05$). This may be due to the fact that an effective oxygen-rich zone only exists at the immediate surrounding of an RBC. In the case of a mixture of P-FRTs and RBCs, photosensitizers were distributed randomly in the solution and were less efficiently benefited from the O_2 released.

To further investigate the RBC-enhanced PDT under a low oxygen environment, we conducted an *in vivo* study with a murine acute hypoxia tumor model.[35] Briefly, we first implanted U87MG tumors to the hind legs of nude mice. When the tumors reached a size of 250 mm^3, a tourniquet was placed onto the tumor-bearing leg for 15 minutes to temporally suppressed the blood flow.[35] The treatment led to widespread tumor hypoxia, which was confirmed by HIF-1α staining with tumor tissues (**Figure 6.2b**). For treatment, P-FRT-RBCs (0.075 mg $ZnF_{16}Pc$/kg) were intratumorally injected into the hypoxic tumors (n = 3), followed by photo-irradiation to the tumor areas (100 mW/cm^2 for 30 min). Notably, the tourniquet remained bound to the animals during the PDT process and was removed only after the end of the irradiation. Twenty four hours after the PDT, we euthanized the animals and analyzed the tumor tissues by hematoxylin and eosin (H&E) staining (**Figure 6.2c**) as well as terminal deoxynucleotidyl transferase dUTP nick end labeling (TUNEL) assay (**Figure 6.2d**). We observed widespread cell death and severely damaged tumor architectures in the P-FRT-RBC-treated group (**Figure 6.2d**). This is in stark contrast to the P-FRT-treated animals at the same $ZnF_{16}Pc$ dose, in which case little damage to tumors was observed.

To validate that the difference in therapy was due to oxygen from RBCs, we conducted two more studies with P-FRT-RBCs. In the first study, we exposed P-FRT-RBCs to 100% O_2 (30 min) before the intratumoral injection. In the second group, P-FRT-RBCs were soaked in CO (N_2/CO, 95:5 v:v, at a pressure of 1.5 kg/cm^2, 30 min) before the injection. It is known that CO binds more strongly to hemoglobin than O_2, and the binding can temporally suspend the O_2-carrying ability of RBCs.[36] The successful CO binding was verified by the blue-shift of the characteristic absorption peaks of hemoglobin (**Figure S6.9**). Compared to normal P-FRT-RBCs, the O_2-soaked P-FRT-RBCs induced little enhancement of tumor treatment efficacy. This is not surprising because the oxygen carrying capacity of RBCs has reached the maximum under a normal oxygen partial pressure and further increasing O_2 levels barely contributes to O_2 loading (~ 160 mmHg).[37] CO-treated P-FRT-RBCs, on the other hand, almost lost their ability to induce PDT damage to tumors (**Figure 6.2d**). These results confirm that O_2 released from RBCs is a key player in P-FRT-RBC-based PDT.

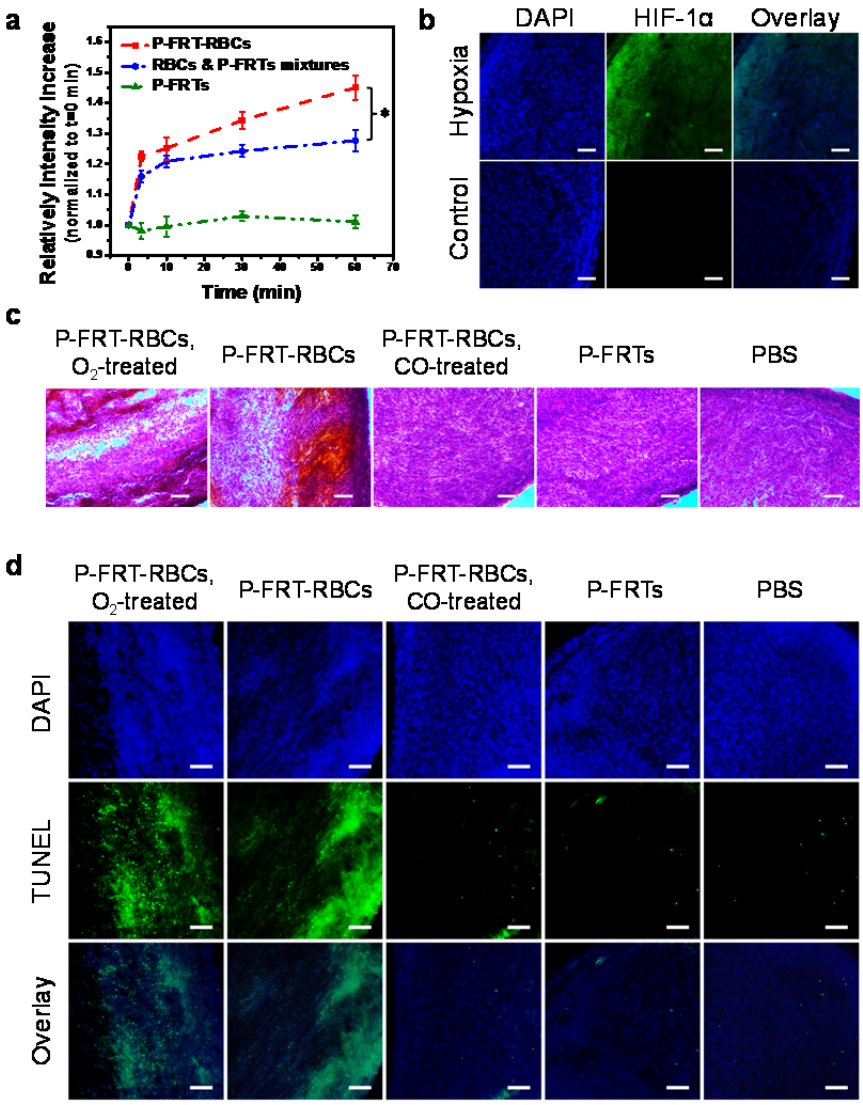

Figure 6.2 P-FRT-RBCs Showed Enhanced PDT Effect under Hypoxic Environments. (a) Comparison of $^1O_2$ generation among P-FRT-RBCs, a mixture of RBCs and free P-FRTs, and free P-FRTs, conducted in an Ar-filled cuvette. The cuvette was irradiated by a 671-nm laser (0.1 W/cm^2) for up to 60 min. SOSG was used as an indicator of $^1O_2$ production. (b) HIF-1α staining on tumor samples taken from the acute hypoxia tumor model and normal mice. Green, HIF-1α. Blue, DAPI. Scale bars, 100 μm. (c) H&E staining on hypoxic tumors treated by PDT-mediated by different formulations. While P-FRT-RBCs and O_2-treated P-FRT-RBCs induced significant damage to tumors under irradiation, CO-treated P-FRT-RBCs and P-FRTs caused minimal cancer cell death. Scale bars, 100 μm. (d) TUNEL assays on hypoxic tumors treated by PDT-mediated by different formulations. Similar to observations in (c), extensive cell death was only observed in animals treated with P-FRT-RBCs and O_2-treated P-FRT-RBCs. Green, TUNEL. Blue, DAPI. Scale bars, 100 μm.

6.2.4. Circulation half-lives and biodistribution of P-FRT-RBCs

We next intravenously (i.v.) injected P-FRT-RBCs to U87MG-bearing mice (0.75 mg $ZnF_{16}Pc$/kg) and investigated their circulation and biodistribution. In order to facilitate the tracking of P-FRT-RBCs, we labeled them with IRDye800 before the injection. As a comparison, IRDye800 labeled P-FRTs at the same $ZnF_{16}Pc$ dose were also injected. For P-FRT-RBCs injected mice, signals were distributed relatively evenly in the host at early time points and faded rather slowly (**Figure 6.3a**). The long circulation was also confirmed by florescence analysis on blood samples taken at different time points (**Figure 6.3b**).

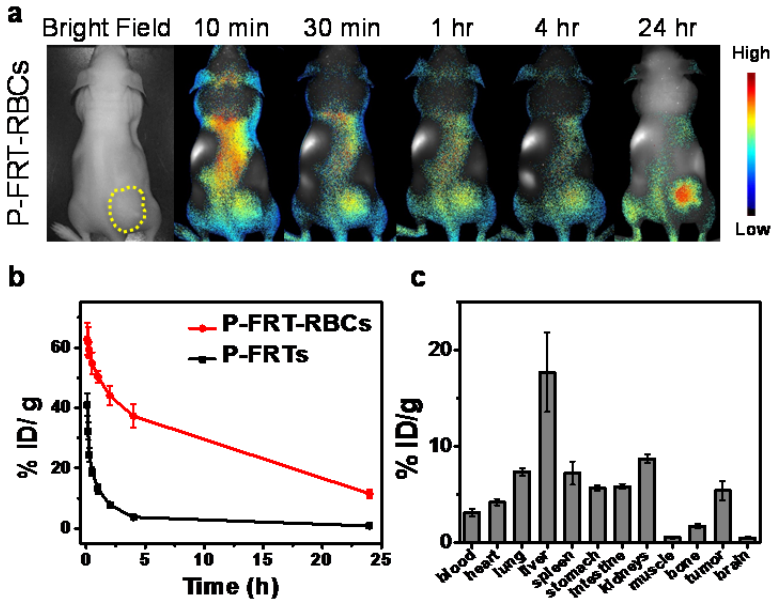

Figure 6.3 *In Vivo* Behaviors of P-FRT-RBCs. (a) Representative fluorescence images taken at different time points after P-FRT-RBC injection (labeled with IRDye800). Tumors were circled with yellow dashed lines. P-FRT-RBCs were distributed relatively evenly throughout the animals and there was slow decay of signals over time. (b) Circulation of P-FRT-RBCs, analyzed in healthy nude mice (n = 3) by measuring remaining fluorescence activities in the circulation. P-FRT-RBCs had been labeled by IRDye800 before injection. c) Bio-distribution study. P-FRT-RBCs were labeled with ^{64}Cu-PTMS and injected into U87MG tumor bearing mice. The distribution was analyzed by gamma counting with tissues taken from the animals at 24 hr.

Fast clearance of photosensitizers is common with conventional, small molecule-based PDT,[15] and leads to low intravascular photosensitizer concentrations or drop of photosensitizer

concentrations during the course of PDT (each PDT session takes 15 to 30 min)[11]. These, however, are less of concerns for P-FRT-RBCs. According to region of interest (ROI) analysis (**Figure S6.10**), the P-FRT-RBC contents in tumors were 6.9 ± 0.4, 7.5 ± 0.2, 7.2 ± 0.5, 7.0 ± 0.4, 11.4 ± 0.8% of the injection dose (ID) at 10 min, 30 min, 1 hr, 4 hr, and 24 hr, respectively. As stated above, our RBC-PDT approach targets tumor vasculatures.[11,12] The long circulation of P-FRT-RBCs and their minimal extravasation at tumor sites represent advantages in this regard.

After 24 hours of imaging, the animals were euthanized. Tumors, along with the major organs, were harvested for *ex vivo* imaging (**Figure S6.11 & S6.12**). In addition to the high IRDye800 signals in tumors, fluorescence activities were also observed in organs such as the liver, spleen, and lung, but low in the skin. Given that $ZnF_{16}Pc$ is not toxic in the dark and PDT is largely regulated by focal photo-radiation, such accumulation in internal organs poses few toxicity concerns. In addition to fluorescence imaging, we also investigated the circulation and tumor contents of P-FRT-RBCs by two other methods. One was to label P-FRT-RBCs with iron oxide nanoparticles (IONPs, details of the labeling are described in the Methods section) and monitor signal change in tumors by T_2-weighted magnetic resonance imaging (MRI, **Figure S6.13a**). Based on ROI analysis, it was derived that the signal-to-background ratio (SBR) in tumors was dropped by 10.6 ± 2.1%, 15.6 ± 3.2%, 3.3 ± 1.6%, and 4.1 ± 1.9% at 4, 24, 48 and 72 hr, respectively (**Figure S6.13b**). The results confirmed a high content of P-FRT-RBCs in tumors at early time points. The second method was to label P-FRT-RBCs with ^{64}Cu-PTSM (copper-64-pyruvaldehyde-bis(N4-methylthiosemicarbazone))[38] and assess the bio-distribution of P-FRT-RBCs by *ex vivo* gamma counting (**Figure 6.3c**, labeling details are described in Methods section). Consistent with the fluorescence results, there was a high radioactivities in the blood at early time points (7.6 ± 2.1%ID/g at 1 hr) and the signals remained strong for 24 hr (3.2

± 0.4%ID/g at 24 hr); meanwhile, high ^{64}Cu activities were also found in hypervascular tissues, including the liver, spleen, lung, and tumors (**Figure 6.3c**). It was noted that although the distribution profiles were similar between the fluorescence and gamma counting analyses, the tumor ID%/g values from gamma counting were relatively low (e.g. 5.4 ± 1.0%ID/g for the ^{64}Cu-PTSM analysis at 24 h, compared to that of 11.4 ± 0.8%ID/g for fluorescence imaging). The difference could be attributed to autofluorescence interference, and/or transmellation-induced ^{64}Cu falloff in ^{64}Cu-PTSM-based cell tracking.[38,39]

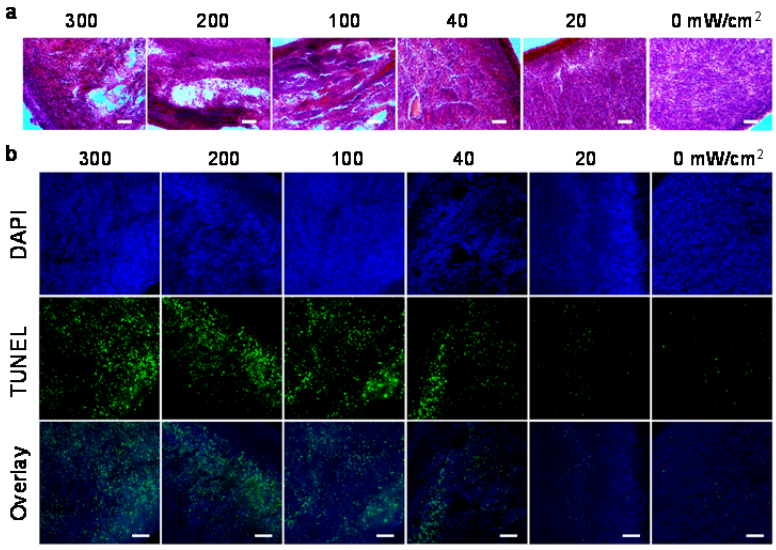

Figure 6.4 Irradiance-Dependent PDT Effect. P-FRT-RBCs were i.v. injected first (0.75 mg $ZnF_{16}Pc$/kg). A 671 nm laser was applied to tumors for 30 min at different irradiances. (a) H&E and (b) TUNEL assay results, conducted on tumor samples taken 24 hr after the PDT. There is an irradiance-dependent PDT effect that caused cancer cell death. While there was a large difference in efficacy between 100 mW/cm^2 and 40 or 20 mW/cm^2 treated animals, there was no significant improvement of efficacy when further increasing the irradiance. Scale bars, 100 μm.

6.2.5 Fluence-dependent RBC-PDT damage to tumors

One important parameter in PDT is irradiation dose, or fluence. Too low a fluence may be insufficient to induce vascular damage, while too high a fluence may cause side effects to

surrounding normal tissues. Hence, before a systematic therapy study, we investigated the impact of fluence on RBC-PDT. Specifically, we i.v. injected P-FRT-RBCs (0.75 mg $ZnF_{16}Pc$/kg) into U87MG subcutaneous tumor models and irradiated the tumors by a 671 nm laser 5 min after the injection. The irradiation time was maintained at 30 min but the fluence rate, or irradiance, was elevated from 20 to 300 mW/cm^2. All of the animals were sacrificed 24 hours after the treatment and the tumors were collected for histological analysis. H&E staining showed a clear fluence-dependent treatment efficacy (**Figure 6.4a**). While there was almost no therapy effect at 20 mW/cm^2, there were large areas of necrosis and bleeding in tumors when the irradiance was raised to 100 mW/cm^2 and above. Meanwhile, there was only marginal difference in efficacy among animals treated by 100, 200 and 300 mW/cm^2 irradiations (**Figure 6.4a & 6.4b**). Based on these observations, we chose an irradiance of 100 mW/cm^2 and irradiation time of 30 min for subsequent therapy studies. Notably, the chosen fluence and fluence rate are within the range commonly used for clinical PDT.[40]

6.2.6. Tumor therapy studies with RBC-PDT

The therapy study was conducted with U87MG tumor bearing mice (n = 5). P-FRT-RBCs were administered at a dose of 0.75 mg $ZnF_{16}Pc$/kg into the animals; photo-irradiation (671 nm, 100 mW/cm^2 for 30 min, over a 1-cm-diameter beam to cover tumors) was applied 5 min after the injection. For comparison, we also performed PDT with P-FRT-RBCs that had been soaked in O_2 or CO for 30 min before injection. Moreover, PDT with P-FRTs alone at the same $ZnF_{16}Pc$ dose was also investigated (in which case the photo-irradiation was applied at 4 hr instead of 5 min after the injection, based on imaging study results, **Figure S6.14**). For controls, animals were injected with P-FRT-RBCs or PBS but received no photo-irradiation.

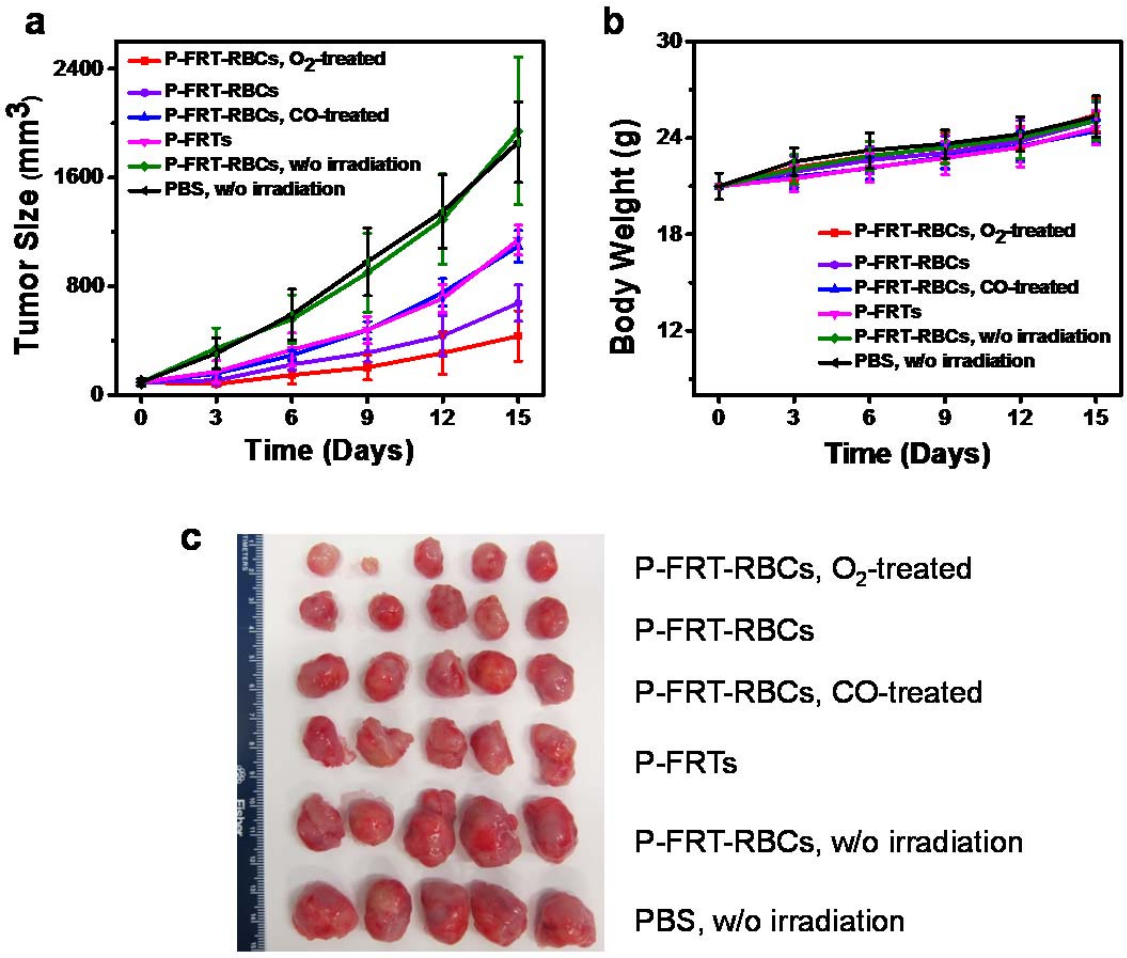

Figure 6.5 Therapy Studies on U87MG Tumor Models (n=5). (a) Tumor growth curves. Significant tumor suppression was found with animals injected with O_2-treated P-FRT-RBCs and P-FRT-RBCs, showing TGI rates of 76.7% and 63.6%, respectively, on day 15. These are much more significant than PDT-mediated by P-FRTs or CO-treated P-FRT-RBCs. (b) Body weight growth curves. No significant weight drop was found with all the treatment groups. (c) Photographs of all the dissected tumors.

P-FRT-RBC-mediated PDT induced significant tumor growth suppression (**Figure 6.5a & 6.5b**); relative to the PBS control group, a tumor growth inhibition (TGI) rate of 63.6 % ± 12.6 % was observed on day 15. The treatment efficacy was slightly improved for O_2-treated P-FRT-RBCs (TGI rate of 76.7 % ± 22.6 % on day 15). As a comparison, animals received PDT with CO-pre-soaked P-FRT-RBCs or P-FRTs alone showed significantly lower treatment efficiency (TGI values being 41.2 % ± 4.4 % and 38.7 % ± 3.7 %, respectively; $P<0.001$).

Despite the efficient cancer cell killing, there was no sign of toxicities with P-FRT-RBC mediated PDT (**Figure S6.15**), including no weight loss (**Figure 6.5b**). All of the animals were euthanized after 15 days. The inter-group difference in tumor size (**Figure 6.5c**) and weight (**Figure S6.16**) agreed well with those observed from caliper measurements. For RBC-PDT treated animals, H&E staining found no significant off-target damage to normal tissues (**Figure 6.6**). To better assess the treatment efficacy, we repeated the study with P-FRT-RBCs (no CO or O_2 pre-treatment) and P-FRTs, but this time euthanized the animals 24 hr after PDT; the tumor tissues were harvested for histology analysis. H&E and TUNEL assays found dramatic difference between the two treatment groups, with the P-FRT-RBC group showing more extensive cell killing, including to those lying deep under the skin (**Figure S6.17**).

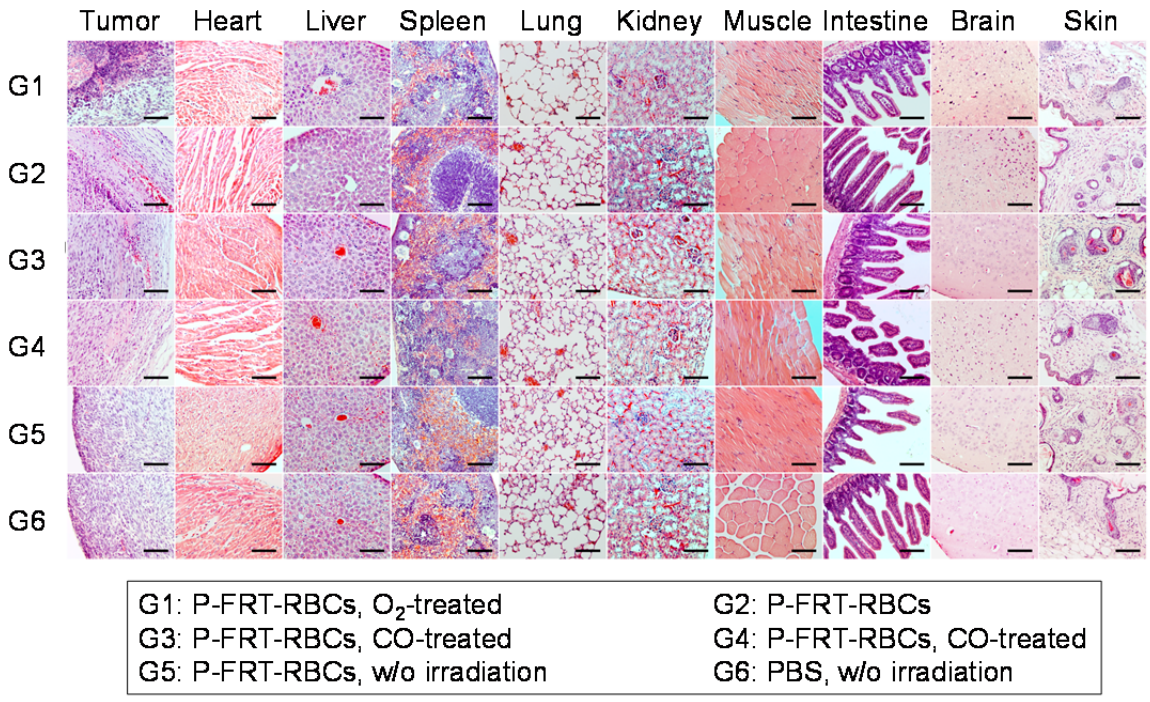

Figure 6.6 H&E Staining on Tumors and Major Organs after Therapy. The tumors from the O_2-treated P-FRT-RBCs (G1) and P-FRT-RBCs (G2) groups showed extensive cell destruction in tumors. No abnormalities were observed in major organs. Scale bars, 100 μm.

6.3. Discussion and Conclusions

Owing to good biocompatibility and long circulation, RBCs have been widely investigated as carriers for chemotherapeutics.[41-44] Using RBCs as carriers for delivery of photosensitizers, however, has seldom been explored. Very recently, the Liu group demonstrated that RBCs can be engineered to load doxorubincin, chlorine e6, and iron oxide nanoparticles for magnetic-field-guided PDT and chemotherapy.[33] However, there has been no investigation into the oxygen-providing benefits of RBCs. To the best of our knowledge, our study is the first to show that the co-delivery of oxygen and photosensitizers can lead to improved PDT efficacy.

As shown in our studies, tethering photosensitizers onto the surface of RBCs is critical for our approach. Conventionally, there are two strategies to load drugs onto or into RBCs. One is to encapsulate drug molecules into the interiors of RBCs, for instance by hypotonic dialysis.[45,46] This is inappropriate for PDT considering the short lifetime of $^1O_2$ (<0.04 microsecond).[47] The second is to conjugate drugs to RBC surface through covalent linking.[48-50] This approach is also not desirable because it is often associated with low loading efficiency, not to mention that most photosensitizers do not possess a conjugation-friendly functional group. In the current study, we first load photosensitizers into a ferritin nanocapsule and then couple the photosensitizer-loaded ferritins onto RBC membranes. Affording high $ZnF_{16}Pc$ loading efficiency, good biocompatibility, and facile surface conjugation chemistry, ferritins provides a perfect solution to the otherwise challenging task.

We have observed both *in vitro* and in hypoxic tumor models that using RBCs as photosensitizer carriers can enhance the efficacy of PDT. It was shown that the sustained O_2 supply by RBCs enabled efficient PDT even under hypoxic conditions (**Figure 6.2c & 6.2d**). It was also found that tethering photosensitizers to RBC surface was important for making the best

out of the O_2 released (**Figure 6.2a**). The merits of using RBCs as carriers were also confirmed in a PDT study where P-FRT-RBCs were systematically injected. Compared to the P-RBC and CO-treated P-FRT-RBC groups, significantly improved therapy efficacy was observed with P-FRT-RBC or O_2-treated P-FRT-RBC groups, validating the contribution of O_2 released from RBCs in the enhanced treatment. It is noted that tumor hypoxia is not equal to zero oxygen or no RBC access (in which case cancer cells would die). In tumors, O_2 molecules can diffuse shortly from blood vessels because they are quickly consumed by fast growing cancer cells adjacent to blood vessels.[51,52] Cancer cells that are ~70-100 μm from blood vessels are hypoxic and those beyond the distance become necrotic.[53] Such location-dependent oxygen levels underscore the significance of having photosensitizers very close to an oxygen source (RBCs) for efficient PDT, which is satisfied in the RBC-PDT approach. By breaking down tumor blood vessels and cutting off blood supply, RBC-PDT can induce extensive cancer necrosis, which was observed in our therapy studies (**Figure S6.17**).

According to the bio-distribution study (**Figure 6.3c**), the concentration of P-FRT-RBCs in tumors was higher at 24 h than at 4 h, indicating a possible tumor targeting mechanism (**Figure 6.3a**). This is interesting because there was no targeting ligand artificially attached to the RBC surface. A possible explanation is that RBCs are gradually opsonized by a serum protein, lactadherin, during the circulation;[54-56] possessing an RGD motif, lactadherin-attached RBCs become sticky to tumor angiogenic endothelial cells, which overexpress integrin $\alpha_v\beta_3$.[54,57,58] It was observed that artificially aged RBCs can home to the tumor endothelium and even get internalized by tumor endothelial cells.[54] Future studies are needed to understand the mechanism behind the tumor accumulation and explore the possibility to further enhance the effect.

In conclusion, we have developed a novel, RBC-facilitated PDT methodology. Using ferritins as nanocapsules, we were able to tether a large amount of $ZnF_{16}Pc$ to the surface of RBCs. RBCs, as photosensitizer carriers, extend the circulation half-lives of photosensitizers. The resulting PDT focuses on the tumor vasculatures, ensuring maximum treatment efficacy. More importantly, we found that RBCs can provide O_2 to enable sustained $^1O_2$ production even when P-FRT-RBCs were under low oxygen conditions. All together, these characteristics lead to enhanced treatment efficacy against tumors. This novel technology addresses one critical limitation of conventional PDT and is expected to find wide applications in modern oncology.

Materials and Methods

Preparation, Dye-Labelling, and Biotinylation of P-FRTs: The protocols for producing FRTs and loading $ZnF_{16}Pc$ into FRTs were published previously.[16,29] Briefly, 490 μL ferritin (0.5 mg/mL PBS) was gently mixed with 10 μL $ZnF_{16}Pc$ (5 mg/mL in DMSO) for approximately 45 min at room temperature. The mixture was then purified on a NAP-5 column to remove the unloaded $ZnF_{16}Pc$. For dye labeling, P-FRTs were incubated with IRDye800-NHS (LI-COR) or Cy5.5-NHS (Amersham) at a starting molar ratio of 1:2 for 30 min and then purified through a NAP-5 column to remove the uncoupled dye molecules. The coupling efficiency was assessed spectroscopically by comparing to a predetermined standard curve. It was determined that the final conjugates have on average one IRDye800 or Cy5.5 per P-FRT particle. To obtain biotinylated P-FRTs, the P-FRTs were mixed with 3 μL of 0.1 M biotin-X-NHS (Calbiochem) at room temperature for 1 hr and then purified through a NAP-5 column to remove uncoupled biotin molecules. The coupling efficiency was determined to be 24 biotin molecules per ferritin with matrix assisted laser desorption ionization (MALDI).

Preparation of P-FRT-RBCs: Whole blood was collected from heathy nude mice. Red blood cells (RBCs) were separated by centrifugation (1000 G, 5 min) and washed twice with cold phosphate-buffered saline (PBS, PH = 7.4). Then 100 μL of packed RBCs were resuspended in 900 μL PBS and mixed with 3 μL of 0.1 M biotin-X-NHS at 4˚C for 20 min. Subsequently, the cells were washed three times with PBS (1000 G, 5 min) to remove unbounded biotin molecules. The resulting biotinylated RBCs were mixed with 200 μL of 1 mg/mL neutravidin (Thermo Scientific) at 4˚C for 1 hr. After another wash cycle with PBS (1000 G, 5 min, 3 times), the RBCs-biotin-neutravidin were mixed with the biotinylated P-FRTs for one hour to yield P-FRT-RBCs. To quantify the molar ratio of P-FRTs to RBCs, IRDye800-labeled P-FRTs were used for the preparation of P-FRT-RBCs; the absorbance at 780 nm (maximum absorbance for IRDye800) was measured and the reading was subtracted from the absorbance of parent RBCs. The integrity of RBC cell membranes in P-FRT-RBCs were assessed by annexin V binding assay based on a protocol provided by the vendor (FITC conjugate, Life Technologies) with a Beckman Coulter CyAn flow cytometer. The $^1O_2$ quantum yield of P-FRT-RBCs was measured with a singlet oxygen sensor green reagent (SOSG, S36002, Invitrogen) as a $^1O_2$ indicator, by comparing to that of P-FRTs,

Preparation of IONP-P-FRT-RBCs: Iron oxide nanoparticle (IONPs) and P-FRT dual-labeled RBCs (IONP-P-FRT-RBCs) were prepared for the *in vivo* magnetic resonance (MR) imaging. 1 mL of IONPs with surface amine groups (Ocean Nanotech, SHA-10, 1mg Fe/mL) was mixed with 10 μL of 0.1 M biotin-X-NHS at 4˚C for 1 hr and then purified on a NAP-5 column to remove the unconjugated biotin-X-NHS. The resulting biotinylated IONPs were mixed with the biotinylated P-FRTs at a 1:1 molar ratio. Subsequently, RBCs-biotin-neutravidin were added to the mixture solution and mixed for another 1 hr to yield the IONP-P-FRT-RBCs. The final product was purified by centrifugation for three times (1000 G, 5 min).

Scanning Electron Microscopy: The P-FRT-RBCs were dropped onto a filter paper with a pore size of 1 μm. The samples were primarily fixed by 2% glutaraldehyde in PBS at 4 °C for 1 hr. After washing with PBS, the samples were incubated in 1% OsO_4 for one hour. Next, ethanol of gradient concentrations (25%, 50%, 75%, 90%, and 100%) was applied to the slices at room temperature (30 min for each concentration) to dehydrate the samples. Subsequently, the samples

were critical-point dried in a SAM-DRI-790 CPD and diffuse-coated with a gold/palladium mix with a thickness of 5 nm in a low vacuum coater (Leica EM ACE 200). Finally, the samples were analyzed using a field emission gun SEM (FEI Inspect F FEG-SEM).

Confocal Microscopy: The Cy5.5-labelled P-FRTs were conjugated to RBCs. The confocal florescence images of the resulting Cy5.5-labeled P-FRT-RBCs were imaged on a Zeiss LSM 510 META Confocal Microscope.

$ZnF_{16}Pc$ Release from the P-FRT- RBCs: Photosensitizer release was investigated on a slide-A-lyzer dialysis device (10K MWCO, Pierce), which we used in our previous studies to analyze drug release.[29] Specifically, P-FRT-RBCs in 10% human serum albumins were loaded onto the dialysis device, and the device was immersed in a 15 mL tube filled with the same solvent. The whole system was incubated at 37 °C with gentle shaking. At different time points, 0.5 mL medium was taken from the tube for analysis, and the tube was replenished with 0.5 mL of the fresh medium. The amounts of $ZnF_{16}Pc$ in the releasing media were measured on a micro reader and then compared to a standard curve. Photosensitizer release in PBS was studied similarly.

Cell Line and Animal Models: The U87MG human glioblastoma cell line was obtained from the American Type Culture Collection (ATCC) and cultured with Dulbecco's Modified Eagle Medium (DMEM) in a cell culture flask. Athymic nude mice were purchased from Harlan laboratories. The animal model was established by subcutaneously injecting approximately 5×10^6 U87MG cells into the right hind limb of each mouse. All of the experimental procedures had been conducted following a protocol approved by the University of Georgia Institutional Animal Care and Use Committee (IACUC).

MTT Assay: Approximately 1×10^4 U87-MG cells were seeded in each well of a 96-well plate. After a 24-hour incubation, P-FRT-RBCs with different $ZnF_{16}Pc$ concentrations (0, 1, 5, 10, 20, and 50 μg/mL) were added to the plate. For comparison, RBCs and P-FRTs mixture, RBCs, and P-FRTs were used in control studies. A 100 mW/cm^2 irradiation was immediately applied to each well for 200 sec. Subsequently, the medium of each well was removed; the U87MG cells were washed twice with PBS and the well was then replenished with fresh medium. After incubating for another 24 hr, MTT assay was performed to determine the cell viability. For controls, no irradiation was applied.

$^1O_2$ Production and Live & Dead Assay: A singlet oxygen sensor green reagent (SOSG, S36002, Invitrogen) was used as a $^1O_2$ indicator, and live & dead assays (Invitrogen, only dead assay was used in the study) were used to assess cytotoxicity. Specifically, approximately 1×10^5 U87MG cells were seeded in each well of a 4-well cell culture chamber and were incubated overnight. Next, 2 μL of SOSG working solution were added to incubate with the U87MG cells 30 min prior to the addition of P-FRT-RBCs or P-FRTs (both at 10 μg $ZnF_{16}Pc$/mL). A 100 mW/cm^2 irradiation was then applied to the chamber for 200 sec. Subsequently, the incubation medium was removed. The U87MG cells were washed twice with PBS and the well was then replenished with fresh medium. After 2-hour incubation, the cells were stained with EthD-III at 37 ˚C for 30 minutes and were observed under a fluorescence microscope.

PDT Effect to RBC Carriers: A solution of P-FRT-RBCs (at a concentration of 10 μg $ZnF_{16}Pc$/mL) was irradiated with a 671 nm laser (100 mW/cm^2) for different durations (0, 200

sec, 10 min, 30 min, and 60 min) in separate experiments. Subsequently, the integrity of RBC cell membranes in P-FRT-RBCs were assessed by annexin V binding assay based on the protocol provided by the vendor (FITC conjugate, Life Technologies) with a Beckman Coulter CyAn flow cytometry. RBC ghosts were also examined as positive controls.

$^1O_2$ Generation under Low Oxygen Environments: To mimic a low oxygen environment, a cuvette pre-loaded with 1 mL PBS was pumped with ultra-high pure Ar (Airgas, AR UHP300) gas for 30 min to deoxidize; the cuvette was then sealed. Next, a solution containing SOSG reagent and RBC-P-FRTs (at a final concentration of 50 μg $ZnF_{16}Pc$/mL) was injected into the cuvette. The cuvette was kept in the dark and irradiated with a 671 nm laser (100 mW/cm^2). At selected time points (200 sec, 10 min, 30 min, and 60 min), the irradiation was stopped and the amount of $^1O_2$ generated was assessed by measuring fluorescence activities at 525 nm. For controls, free P-FRT and a RBCs and P-FRTs mixture at the same photosensitizer concentrations were also tested.

Acute Hypoxia Tumor Models: We followed a published protocol with slight modifications to generate the acute hypoxia tumor model.[35] Briefly, U87MG-bearing subcutaneous models were first established. When the tumor reached about 250 mm^3, a tourniquet was placed onto the tumor-bearing leg with a clamp for 15 minutes. To confirm the successful induction of hypoxia, the mice were euthanized and the tumors were subjected to HIF-1α staining. For therapy studies, O_2-treated P-FRT-RBCs, P-FRT-RBCs, CO-treated P-FRT-RBCs, P-FRTs (all at 0.075 mg $ZnF_{16}Pc$/kg), or PBS were intratumorally injected and the tumors were irradiated by a 671 nm laser (100 mW/cm^2, 30 min). After 24 hours, the mice were euthanized, and the tumors were collected for H&E staining and TUNEL assays.

Pretreatment of P-FRT-RBCs by O_2 or CO: The protocol was modified from a published one.[59] Briefly, P-FRT-RBCs were soaked in an industrial grade O_2 or a gaseous mixture of N_2/CO (95:5 V:V) for 30 min at a pressure of 1.5 kg/cm^2. The absorbance spectra of the resulting O_2- or CO-treated P-FRT-RBCs were immediately measured by a microreader.

Circulation Half-Lives: To determine the circulation half-lives, IRDye800-labeled P-FRT-RBCs or IRDye800-labeled P-FRTs (0.75 mg $ZnF_{16}Pc$/kg) were i.v. injected into healthy nude mice. At selected time points, 10–20 μL of blood were collected from the tail vein and dissolved in heparin solution (1000 U/mL in PBS). The IRDye800 fluorescence activities in the blood were measured and subtracted by auto-fluorescence of the blood from an untreated mouse.

***In Vivo* Imaging Studies:** The imaging studies started when tumors reached a size between 200 and 500 mm^3. IRDye800 labeled P-FRT-RBCs or IRDye800 labeled P-FRTs (0.75 mg $ZnF_{16}Pc$/kg) were i.v. injected into U87MG-bearing mice (n = 3). Images were taken on a Maestro II imaging system (Perkin Elmer Inc) at 5, 10, 15, and 30 min, as well as 1, 4, and 24 hr post injection (p.i.) time points. The images were unmixed by the vendor provided software. ROIs were circled around the tumors, and the optical intensities (in total scaled counts/second) were read by the Maestro software. After the 24 hour imaging, all of the mice were euthanized. Tumors as well as major organs were harvested and subjected to *ex vivo* imaging. The images were analyzed with the Maestro software.

Magnetic resonance imaging: The studies were conducted on U87MG tumor models. The animals (n=3) were intravenously injected with IONP-P-FRT-RBCs (10 mg Fe/kg). T_2-weighted images were acquired on a 7T Varian small animal MRI system pre- and 4 hr, 24 hr, 48 hr, and 72 hr post the IONP-P-FRT-RBC injection, with the following scan parameters: TR = 2.5 s; TE = 48 ms; ETL = 8; FOV 40^2 mm^2 ; matrix size = 256^2; 11 axial slices with 1 mm slice thickness. To quantify the signal drop, we calculated the signal-to-backgroud ratio (SBR) by finely analyzing regions of interest of the MR images and calculated the values of $(SBR_{pre} - SBR_{post})/SBR_{pre}$ to represent to signal changes.[60] Signal intensity (SI) of tumor and muscle were measured before and after injection of IONP-P-FRT-RBCs. The SBR values were calculated according to $SBR = SI_{tumor} / SI_{muscle}$.

^{64}Cu-PTSM labeling and bio-distribution studies: 10 μL PTSM (1mg/mL in DMSO) was added to 10 μL 0.1 M NaOAc and the pH adjusted to 6. One mCi solution of ^{64}Cu-$CuCl_2$ was then added and vortexed for 10 min. The resulting mixture was added to Sep-Pak C18 column (Waters, MA) and eluted with ethanol. Solvent was removed by rotary evaporation and the residue was reconstituted in 500 μL 1X PBS to form ^{64}Cu-PTSM. The freshly prepared RBCs (100 μL) were then incubated with ^{64}Cu-PTSM for 30 min at 4˚C and washed 3 times with 1X PBS. ^{64}Cu labeled RBCs were re-suspended in 300 μL 1X PBS and mixed with 3 μL of 0.1 M biotin-X-NHS for 20 min. Then the mixture was washed 3 times with 1X PBS to remove the unbounded biotin. Subsequently, the biotinylated ^{64}Cu-RBCs were mixed with 200 μL of 1 mg/mL neutravidin (Thermo Scientific) at 4˚C for 1 hour. The cells were washed 3 times with 1X PBS to remove the unbounded neutravidin molecules. Finally, the ^{64}Cu-RBCs-biotin-neutravidin were mixed with the 500 μL biotinylate P-FRTs for 1 hour to yield P-FRT-RBCs. The conjugates were washed with 1X PBS for 3 times to remove effluxed ^{64}Cu before injection.

Biodistribution Studies: ^{64}Cu-RBCs-biotin-neutravidin P-FRTs (1.1–1.3 MBq) was injected intravenously into the animals. Blood samples were collated by remove up to 1 cm of the mice tail under isoflurane anesthesia at 1, 4 and 24 hour after injection. At 24 hours post-injection, the mice were sacrificed and the organs and blood were collected. All the blood samples and organs were weighed and radioactivities were counted by a gamma counter 2480 WIZARD2 Automatic Gamma Counter (PerkinElmer, Waltham, MA). Decay-corrected uptake was expressed as the percentage of injected dose per gram (%ID/g) to represent the accumulation of ^{64}Cu-RBCs-biotin-neutravidin P-FRTs in major organs. Values are expressed as the means ± SD for a group of three animals.

Fluence-Dependent *In Vivo* PDT: P-FRT-RBCs (0.75 mg $ZnF_{16}Pc$/kg) were i.v. injected into U87MG bearing mice. After 5 min, the tumors were irradiated by a 671 nm laser at different fluence rates (300, 200, 100, 40, 20, 0 mW/cm^2) for 30 min. 24 hrs after the irradiation, the mice were euthanized and tumors were collected for H&E staining and TUNEL assay.

Therapy Studies: The therapy studies were performed on U87MG tumor models. Thirty 4- to 6-week-old female nude mice were subcutaneously injected with 5×10^6 U87-MG cells on the right hind limbs. The 30 mice were randomly divided into 6 groups, 5 mice per group. The study started when the tumor size reached around 100 mm^3 (average tumor size of 93.92 ± 27.22 mm^3). For the treatment group, the mice were first i.v. injected with O_2-treated P-FRT-RBCs (0.75 mg $ZnF_{16}Pc$/kg). After 5 minutes, the tumors were irradiated by a 671 nm laser (100 mW/cm^2, over a 1 cm diameter beam) for 30 min. The five control groups received: (1) P-FRT-

RBCs and irradiation; (2) CO-pretreated P-FRT-RBCs and irradiation; (3) P-FRTs and irradiation; (4) P-FRT-RBCs only; and (5) PBS only. All groups of animals were irradiated 5 min after the injections, except for the P-FRTs group, which were irradiated 4 hours after the irradiation. Every three days, photographs of the mice were taken, and the tumor sizes and body weights were measured. Tumor sizes were measured by a caliper and computed following the formula: size (mm^3) = length (mm) × width $(mm)^2/2$. After therapy, the tumors as well as the major organs were collected and subjected to paraffin-embedded H&E staining. Photographs of the tumors were taken and the weights of tumors were measured. To better understand the treatment, we repeated the treatment with P-FRT-RBCs and free P-FRTs in a separate study but euthanized the animals 24 hour after irradiation. The tumors were dissected for H&E staining and TUNEL assays.

Hematoxylin and Eosin Staining: H&E staining for cryogenic and paraffin-embedded sections were both performed by following a protocol provided by the vendor (Oklahoma Medical Research Foundation). For cryogenic sections, 8 μm slides were prepared and fixed with 10% formalin for about 30 min at room temperature. After washing with running water for 5 min, the slides were treated with gradient concentrations of alcohol (100, 95, and 70%), each for 20 seconds. For paraffin-embedded tumor and organ sections in the therapy studies, 6 μm slides were prepared and treated with gradient xylene and/or alcohol (100% xylene, 100% xylene, 100% xylene, 50:50 xylene/100% EtOH, 100% EtOH, 100% EtOH, 95% EtOH, and 95% EtOH), each for 3 min. After washing with running water for 5 min, the slides were ready for the staining. The hematoxylin staining was performed for about 5 min, and the slides were washed with water for 1 min. The eosin staining was performed for about 1 min. The slides were then washed, treated with xylene, and mounted with Canada balsam. The images were acquired on a Nikon Eclipse 90i microscope.

Immunofluorescence Staining: The cryogenic slides were fixed with cold acetone for 10 min, washed by running water for 5 min, and blocked by 10% goat serum for 1 h. FITC-labeled anti-HIF-1-alpha antibody (ab187786, Abcam) was incubated with the slides at 4 °C overnight. After gently rinsing with PBS, the slides were mounted and ready for microscopic imaging. TUENL assays were performed by following a protocol provided by the vendor (FITC-labeled POD, GenScript).

Statistical Methods: Quantitative data were expressed as mean ± SD. Means were compared using Student's *t* test. *P* values < 0.05 were considered statistically significant.

Supporting Information

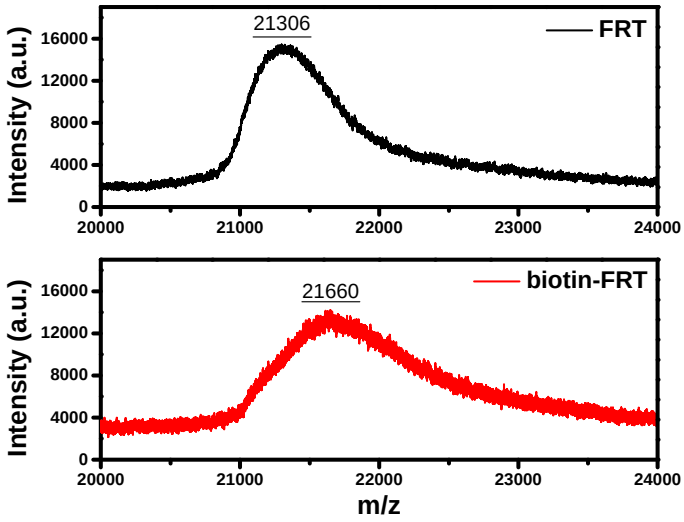

Figure S6.1 MALDI analysis with ferritin and ferritins conjugated with biotin-X-NHS. Based on the shift in mass, it was estimated that on average one biotin was coupled to one ferritin subunit.

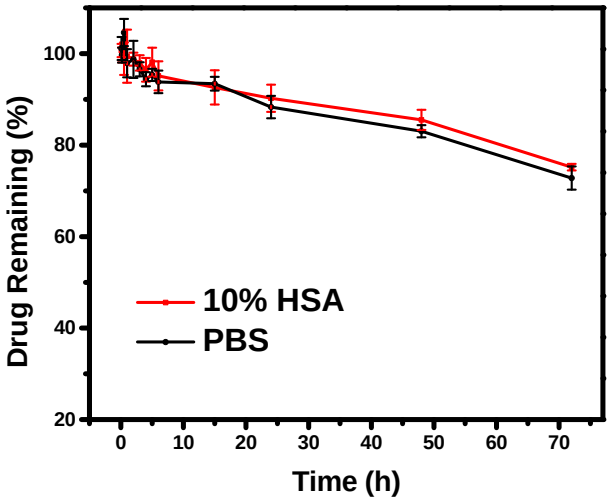

Figure S6.2 Release of $ZnF_{16}Pc$ from P-FRT-RBCs in 10% human serum albumin or PBS over time (n=3). $ZnF_{16}Pc$ shows a slow release from P-FRT-RBCs under both conditions. Even after 72 h, over 80% of $ZnF_{16}Pc$ remained bound to the conjugates.

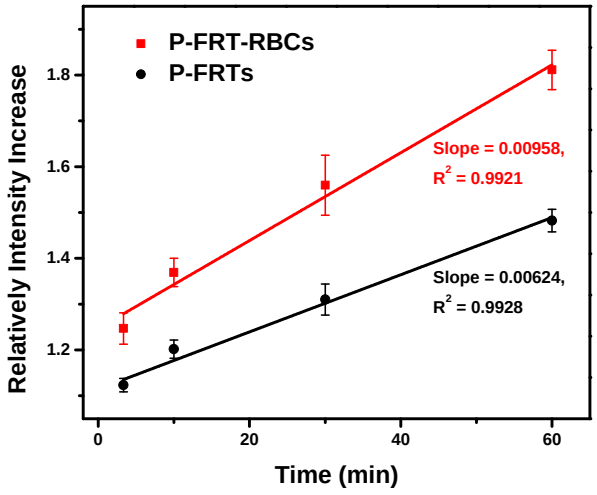

Figure S6.3 Comparison of $^1O_2$ generation between P-FRT-RBCs and free P-FRTs, conducted in the air. Relative to P-FRTs, $^1O_2$ production efficiency was increased by 154% with P-FRT-RBCs.

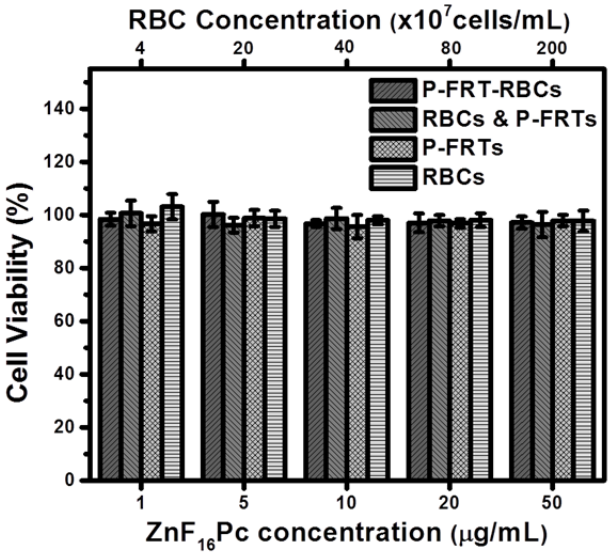

Figure S6.4 MTT assay results. U87MG cells were incubated with P-FRT-RBCs, free P-FRTs, RBCs, and a RBC and P-FRT mixture at different $ZnF_{16}Pc$ concentrations. When there was no irradiation, no cytotoxicity was observed. Results were from 24 hrs.

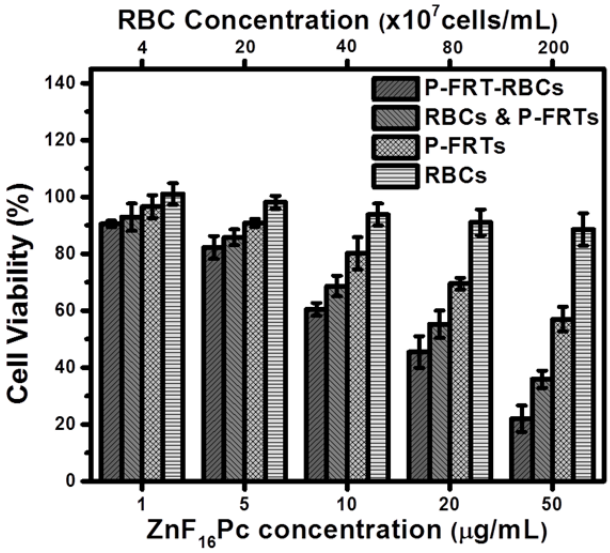

Figure S6.5 U87MG cells were incubated with P-FRT-RBCs, free P-FRTs, RBCs, and a mixture of RBC and P-FRT at different $ZnF_{16}Pc$ concentrations. The cells were irradiated by a 671 nm laser at 100 mW/cm^2 for 200 sec. An increased number of dead cells were observed when the $ZnF_{16}Pc$ concentration was elevated. At all concentrations, P-FRT-RBCs most efficiently induced cell death. The analysis was performed 24 hrs after the end of the irradiation.

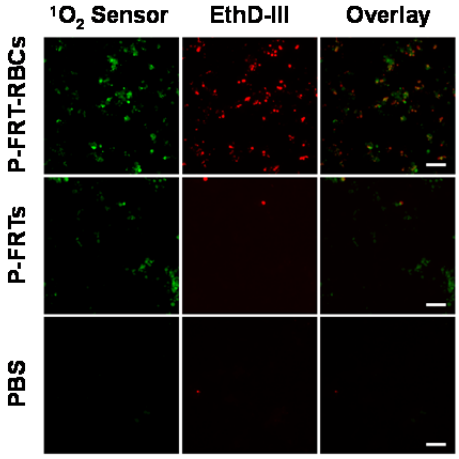

Figure S6.6 Singlet oxygen production and cell viability. U87MG cells were incubated with P-FRT-RBCs, P-FRTs (all at the same concentration of 10 μg $ZnF_{16}Pc$/mL), or PBS and then irradiated by an NIR laser (100 mW/cm^2 for 200 sec). Singlet oxygen sensor green (SOSG) reagent (Invitrogen) was added to the incubation medium before the irradiation, while EthD-III assay (Invitrogen) was applied 2 hrs after the PDT treatment. Compared to P-FRT treated cells, there was much more $^1O_2$ generated by P-FRT-RBCs; the increased $^1O_2$ level was associated with more extensive cell death. Green, $^1O_2$ sensor. Red, EthD-III. Scale bars, 100 μm.

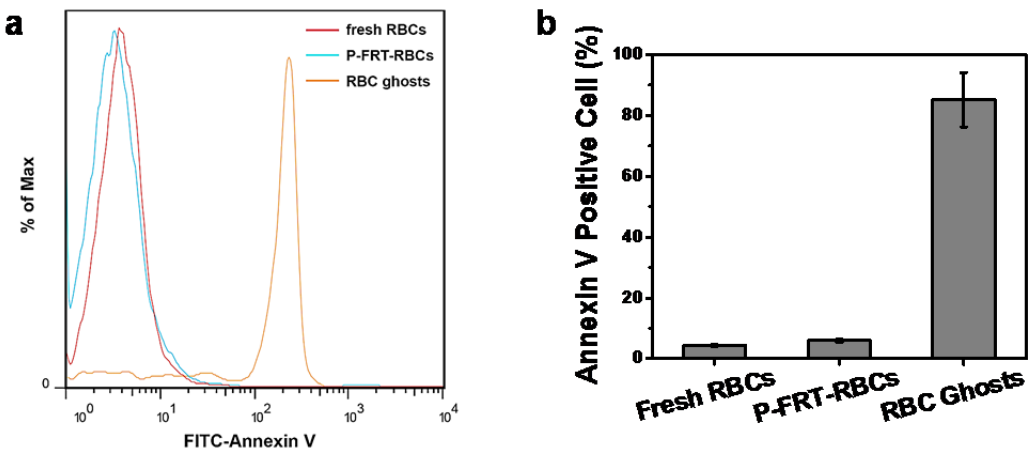

Figure S6.7 Flow cytometry analysis results. Fresh RBCs, P-FRT-RBCs or RBC ghosts were stained with FITC-annexin V that specifically binds to phosphatidylserine (PS) located at the outer leaflet of the plasma membrane. (a) Statistics of annexin V positive cells. There was no significant increase of PS presentation over the coupling, suggesting a minimal damage of photosensitizer loading to the RBCs. (b) Histograms of annexin V positive RBCs based on the results from a.

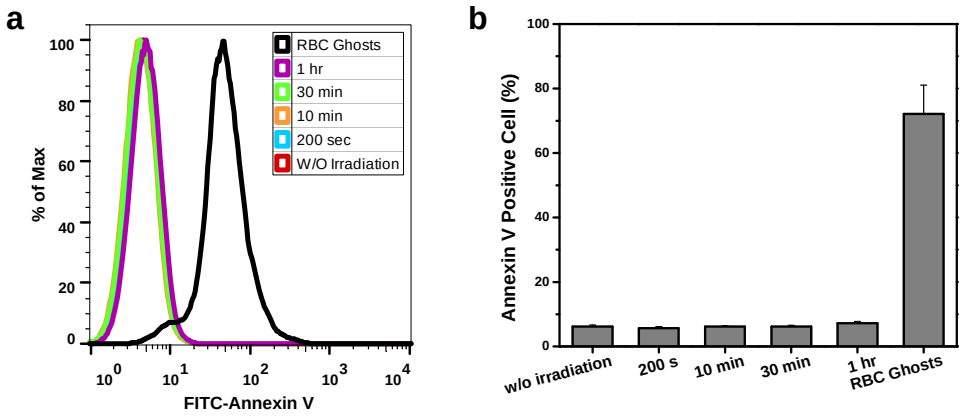

Figure S6.8 Flow cytometry analysis on the impact of PDT on PS level of RBCs. P-FRT-RBCs (10 μg $ZnF_{16}Pc$/mL) were irradiated with a 671-nm laser (100 mW/cm^2) for different amounts of time (0, 200 sec, 10 min, 30 min, and 1 hr) and were then stained with FITC-annexin V. RBC ghosts were also stained with FITC-annexin V as a positive control. (a) Statistics of annexin V positive cells. There was no significant increase of PS presentation over the irradiation. (b) Histograms showing annexin V positive RBCs based on the results from a.

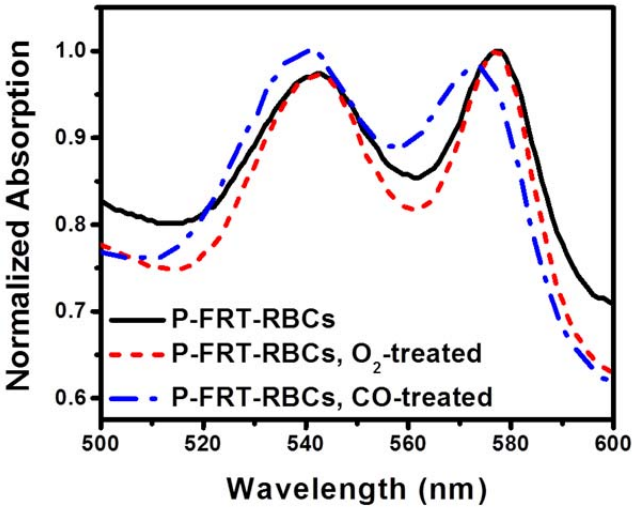

Figure S6.9 Normalized absorption spectra of P-FRT-RBCs, O_2-treated P-FRT-RBCs, and CO-treated P-FRT-RBCs. There was a blue-shift of the characteristic absorbance peaks of hemoglobin for CO-treated P-FRT-RBCs. No significant difference was found between normal and O_2-treated P-FRT-RBCs.

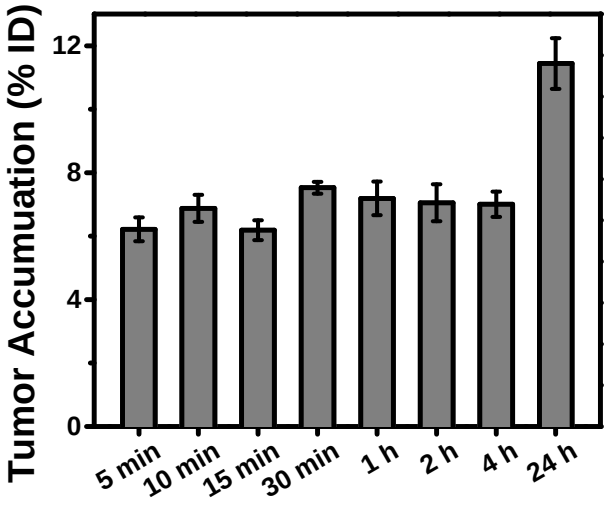

Figure S6.10 Column histograms of fluorescence activities in tumor sites at different time points, based on ROI results from Figure 6.3(a).

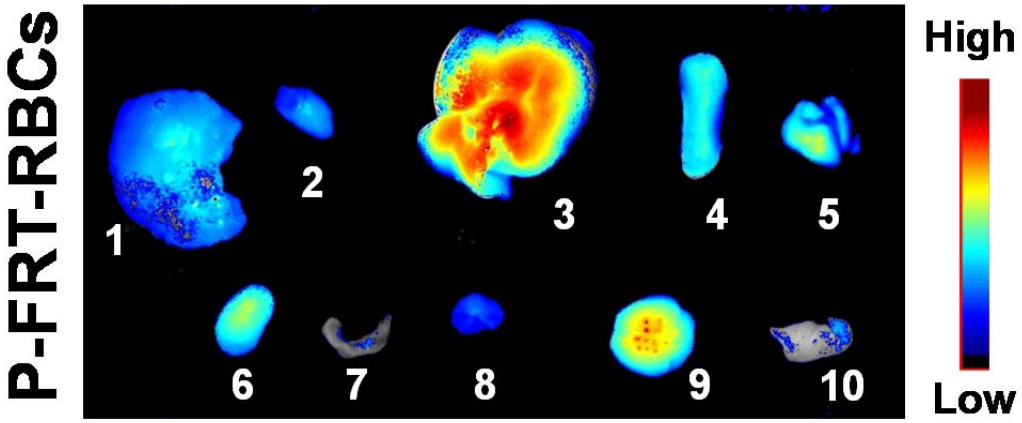

Figure S6.11 *Ex vivo* images of dissected tumors and major orange. The tissues were taken 24 hr after P-FRT-RBC. The organs were displayed in the following order: 1, tumor; 2, heart; 3, liver; 4, spleen; 5, lung; 6, kidney; 7, intestine; 8, muscle; 9, brain; 10, skin.

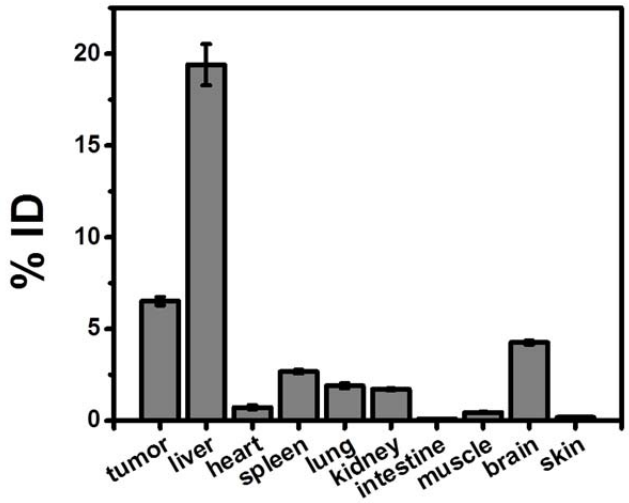

Figure S6.12 Column histograms of fluorescence activities in different organs, obtained on the basis of the *ex vivo* images in Figure S6.11.

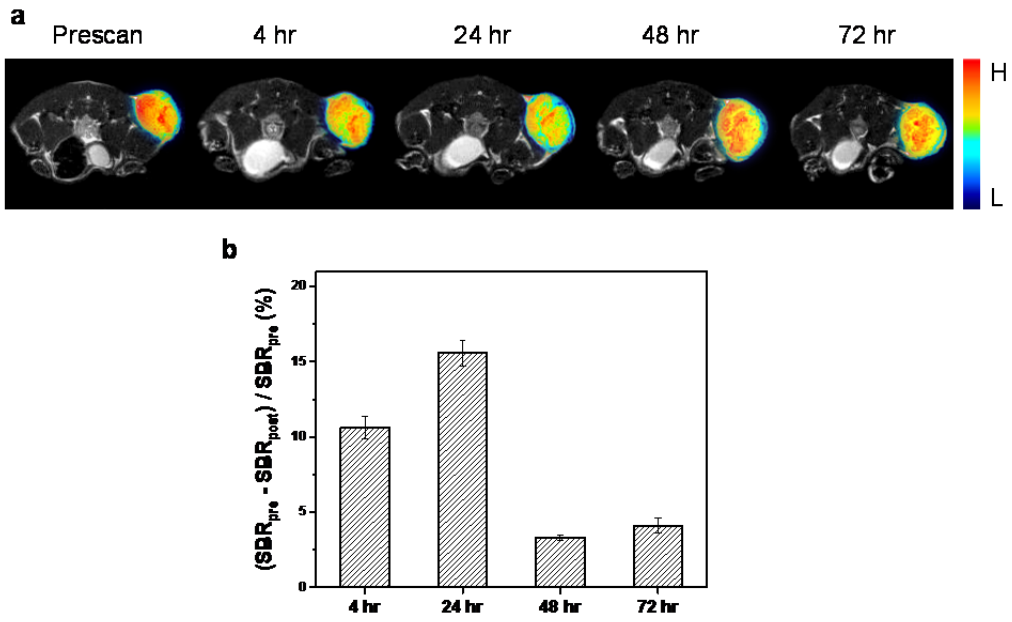

Figure S6.13 (a) T_2-weighted MR images, taken at different time points after injection of P-FRT-RBCs. P-FRT-RBCs were labeled with iron oxide nanoparticles and the conjugates were intravenously injected at 10 mg Fe/kg into U87MG tumor bearing mice. Images were acquired before as well as 4, 24, 48, and 72 hr after the injection. Significant signal drops were observed in tumors at 4 hr and 24 hr. (b) Column histograms of relative signal drop at different time points, based on imaging results from a.

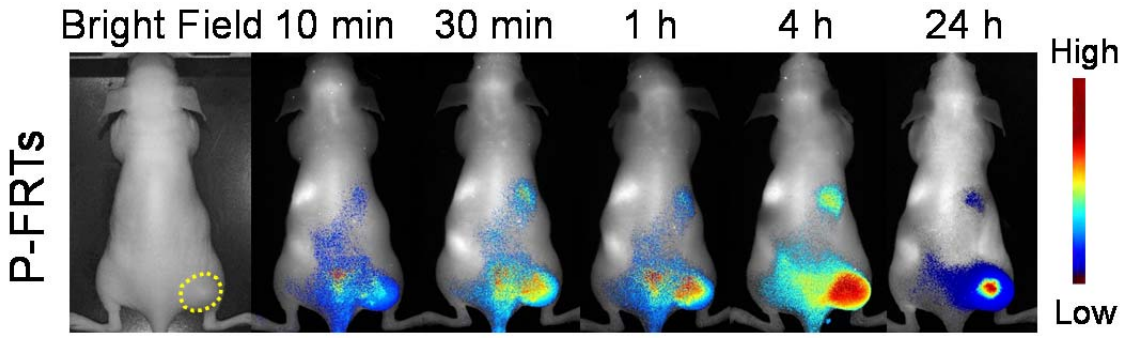

Figure S6.14 *In vivo* behaviors of P-FRTs. Fluorescence images taken at different time points after P-FRT injection (labeled with IRDye800). Tumors were circled with yellow dashed lines. P-FRTs accumulated at the tumor site over time through the enhanced permeability and retention (EPR) effect.

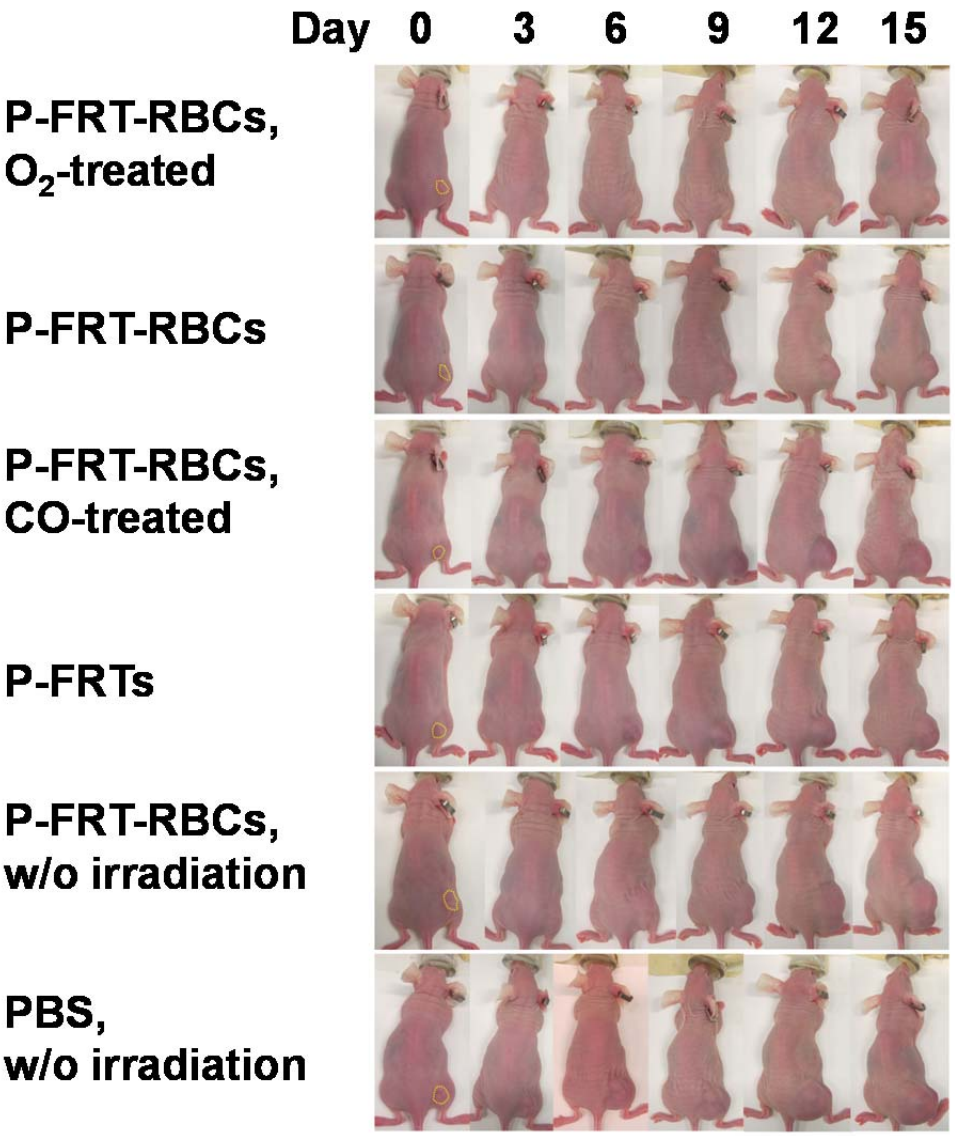

Figure S6.15 Photographs of representative mice for all treatment groups. Tumors from day 0 were circled with yellow dash lines.

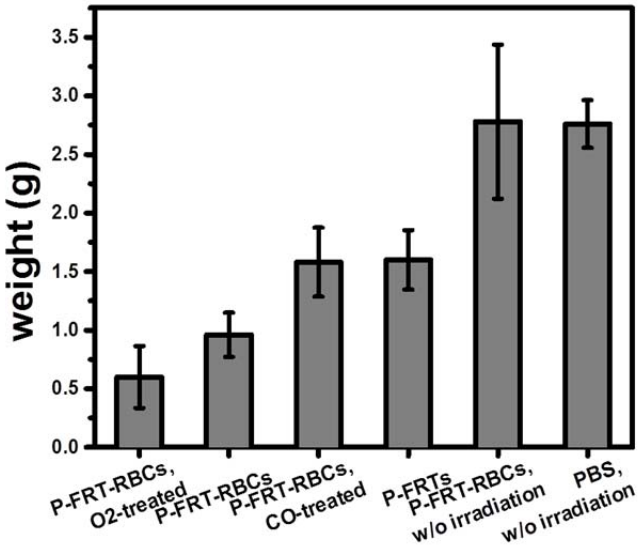

Figure S6.16 Histogram of weights of the dissected tumors for all therapy groups.

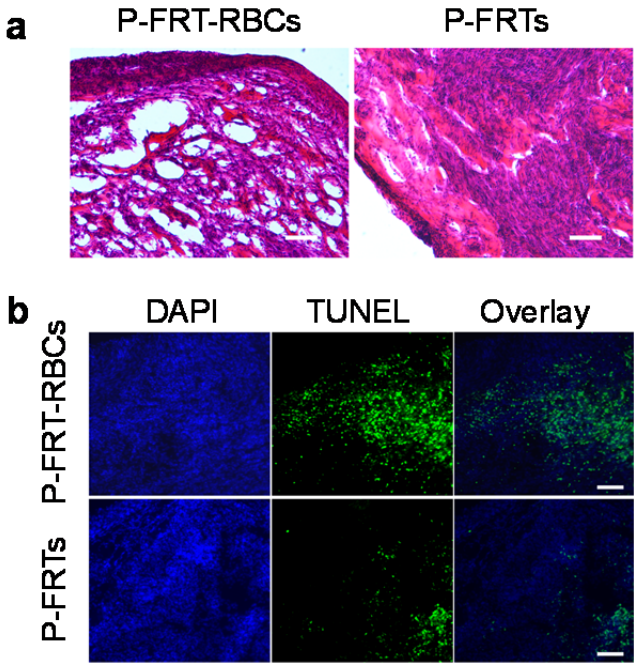

Figure S6.17 Histological analysis on tumor sections from P-FRT-RBC and P-FRT-treated animals. The samples were taken 24 hrs after the irradiation. (a) H&E staining and (b) TUNEL assays. Green, TUNEL. Blue, DAPI. Scale bars, 100 μm.

References

(1) Bessler, N. M.; Vam Study Writing, C. *Retina* **2004**, *24*, 512.
(2) Qumseya, B. J.; David, W.; Wolfsen, H. C. *Clinical Endoscopy* **2013**, *46*, 30.
(3) Weiss, A. A.; Wiesinger, H. A.; Owen, D. *Journal Canadien de Gastroenterologie* **2006**, *20*, 261.
(4) Dolmans, D. E.; Fukumura, D.; Jain, R. K. *Nature Reviews. Cancer* **2003**, *3*, 380.
(5) Eljamel, M. S.; Goodman, C.; Moseley, H. *Lasers in Medical Science* **2008**, *23*, 361.
(6) Fisher, A. M.; Murphree, A. L.; Gomer, C. J. *Lasers in Surgery and Medicine* **1995**, *17*, 2.
(7) Huang, Z. *Technology in Cancer Research & Treatment* **2005**, *4*, 283.
(8) Moore, C. M.; Pendse, D.; Emberton, M. *Nature Clinical Practice. Urology* **2009**, *6*, 18.
(9) Nishiyama, N.; Morimoto, Y.; Jang, W. D.; Kataoka, K. *Advanced Drug Delivery Reviews* **2009**, *61*, 327.
(10) Agostinis, P.; Berg, K.; Cengel, K. A.; Foster, T. H.; Girotti, A. W.; Gollnick, S. O.; Hahn, S. M.; Hamblin, M. R.; Juzeniene, A.; Kessel, D.; Korbelik, M.; Moan, J.; Mroz, P.; Nowis, D.; Piette, J.; Wilson, B. C.; Golab, J. *CA: a Cancer Journal for Clinicians* **2011**, *61*, 250.
(11) Dougherty, T. J.; Gomer, C. J.; Henderson, B. W.; Jori, G.; Kessel, D.; Korbelik, M.; Moan, J.; Peng, Q. *Journal of the National Cancer Institute* **1998**, *90*, 889.
(12) Fingar, V. H.; Wieman, T. J.; Doak, K. W. *Cancer Research* **1990**, *50*, 2599.
(13) Castano, A. P.; Mroz, P.; Hamblin, M. R. *Nature Reviews. Cancer* **2006**, *6*, 535.
(14) Jin, C. S.; Zheng, G. *Lasers in Surgery and Medicine* **2011**, *43*, 734.
(15) Konan, Y. N.; Gurny, R.; Allemann, E. *Journal of Photochemistry and Photobiology. B, Biology* **2002**, *66*, 89.
(16) Zhen, Z.; Tang, W.; Guo, C.; Chen, H.; Lin, X.; Liu, G.; Fei, B.; Chen, X.; Xu, B.; Xie, J. *ACS Nano* **2013**, *7*, 6988.
(17) Brown, J. M.; Wilson, W. R. *Nature Reviews. Cancer* **2004**, *4*, 437.
(18) Minchinton, A. I.; Tannock, I. F. *Nature Reviews. Cancer* **2006**, *6*, 583.
(19) Harris, A. L. *Nature Reviews. Cancer* **2002**, *2*, 38.
(20) Henderson, B. W.; Fingar, V. H. *Cancer Research* **1987**, *47*, 3110.
(21) Lee See, K.; Forbes, I. J.; Betts, W. H. *Photochemistry and Photobiology* **1984**, *39*, 631.
(22) Gomer, C. J.; Razum, N. J. *Photochemistry and Photobiology* **1984**, *40*, 435.
(23) Jensen, F. B. *The Journal of Experimental Biology* **2009**, *212*, 3387.
(24) Di Gregorio, E.; Ferrauto, G.; Gianolio, E.; Lanzardo, S.; Carrera, C.; Fedeli, F.; Aime, S. *ACS Nano* **2015**, *9*, 8239.
(25) Chen, B.; Pogue, B. W.; Goodwin, I. A.; O'Hara, J. A.; Wilmot, C. M.; Hutchins, J. E.; Hoopes, P. J.; Hasan, T. *Radiation Research* **2003**, *160*, 452.
(26) Chen, B.; Pogue, B. W.; Hoopes, P. J.; Hasan, T. *International Journal of Radiation Oncology, Biology, Physics* **2005**, *61*, 1216.
(27) Bonnett, R. *Chemical Society Reviews* **1995**, *24*, 19.
(28) Garcia, A. M.; Alarcon, E.; Munoz, M.; Scaiano, J. C.; Edwards, A. M.; Lissi, E. *Photochemical & photobiological Sciences* **2011**, *10*, 507.
(29) Zhen, Z.; Tang, W.; Chen, H.; Lin, X.; Todd, T.; Wang, G.; Cowger, T.; Chen, X.; Xie, J. *ACS Nano* **2013**, *7*, 4830.

(30) Tang, W.; Zhen, Z.; Yang, C.; Wang, L.; Cowger, T.; Chen, H.; Todd, T.; Hekmatyar, K.; Zhao, Q.; Hou, Y.; Xie, J. *Small* **2014**, *10*, 1245.
(31) Baim, D. S.; Grossman, W. *Grossman's Cardiac Catheterization, Angiography, and Intervention*; Lippincott Williams & Wilkins, 2006.
(32) Berg, C. P.; Engels, I. H.; Rothbart, A.; Lauber, K.; Renz, A.; Schlosser, S. F.; Schulze-Osthoff, K.; Wesselborg, S. *Cell Death and Differentiation* **2001**, *8*, 1197.
(33) Wang, C.; Sun, X.; Cheng, L.; Yin, S.; Yang, G.; Li, Y.; Liu, Z. *Advanced Materials* **2014**, *26*, 4794.
(34) Yin, H.; Zhang, G.; Chen, H.; Wang, W.; Kong, D.; Li, Y. *Artificial Organs* **2014**, *38*, 510.
(35) Jin, C. S.; Lovell, J. F.; Chen, J.; Zheng, G. *ACS Nano* **2013**, *7*, 2541.
(36) Blumenthal, I. *Journal of the Royal Society of Medicine* **2001**, *94*, 270.
(37) Wagner, M. H.; Berry, R. B. *Journal of Clinical Sleep Medicine* **2007**, *3*, 313.
(38) Li, Z.-B.; Chen, K.; Wu, Z.; Wang, H.; Niu, G.; Chen, X. *Molecular Imaging Biology* **2009**, *11*, 415.
(39) Boros, E.; Rybak-Akimova, E.; Holland, J. P.; Rietz, T.; Rotile, N.; Blasi, F.; Day, H.; Latifi, R.; Caravan, P. *Molecular Pharmaceutics* **2014**, *11*, 617.
(40) Liu, Y.; Hou, G.; Zhang, X.; Liu, J. J.; Zhang, S.; Zhang, J. *Journal of Breast Cancer* **2014**, *17*, 161.
(41) Ihler, G. M.; Glew, R. H.; Schnure, F. W. *Proceedings of the National Academy of Sciences of the United States of America* **1973**, *70*, 2663.
(42) Magnani, M.; Rossi, L.; Fraternale, A.; Bianchi, M.;s Antonelli, A.; Crinelli, R.; Chiarantini, L. *Gene Therapy* **2002**, *9*, 749.
(43) Murciano, J. C.; Medinilla, S.; Eslin, D.; Atochina, E.; Cines, D. B.; Muzykantov, V. R. *Nature Biotechnology* **2003**, *21*, 891.
(44) Muzykantov, V. R.; Murciano, J. C.; Taylor, R. P.; Atochina, E. N.; Herraez, A. *Analytical Biochemistry* **1996**, *241*, 109.
(45) Hamidi, M.; Zarrin, A.; Foroozesh, M.; Mohammadi-Samani, S. *Journal of Controlled Release* **2007**, *118*, 145.
(46) Rossi, L.; Serafini, S.; Pierige, F.; Antonelli, A.; Cerasi, A.; Fraternale, A.; Chiarantini, L.; Magnani, M. *Expert Opinion on Drug Delivery* **2005**, *2*, 311.
(47) Moan, J.; Berg, K. *Photochemistry and Photobiology* **1991**, *53*, 549.
(48) Hall, S. S.; Mitragotri, S.; Daugherty, P. S. *Biotechnology Progress* **2007**, *23*, 749.
(49) Krantz, A. *Blood Cells, Molecules & Diseases* **1997**, *23*, 58.
(50) Muzykantov, V. R.; Taylor, R. P. *Analytical Biochemistry* **1994**, *223*, 142.
(51) Thomlinson, R. H.; Gray, L. H. *British Journal of Cancer* **1955**, *9*, 539.
(52) Kizaka-Kondoh, S.; Inoue, M.; Harada, H.; Hiraoka, M. *Cancer Science* **2003**, *94*, 1021.
(53) Yeom, C. J.; Goto, Y.; Zhu, Y.; Hiraoka, M.; Harada, H. *International Journal of Molecular Sciences* **2012**, *13*, 13949.
(54) Fens, M. H.; Mastrobattista, E.; de Graaff, A. M.; Flesch, F. M.; Ultee, A.; Rasmussen, J. T.; Molema, G.; Storm, G.; Schiffelers, R. M. *Blood* **2008**, *111*, 4542.
(55) Grimsley, C.; Ravichandran, K. S. *Trends in Cell Biology* **2003**, *13*, 648.
(56) Stubbs, J. D.; Lekutis, C.; Singer, K. L.; Bui, A.; Yuzuki, D.; Srinivasan, U.; Parry, G. *Proceedings of the National Academy of Sciences of the United States of America* **1990**, *87*, 8417.

(57) Andersen, M. H.; Graversen, H.; Fedosov, S. N.; Petersen, T. E.; Rasmussen, J. T. *Biochemistry* **2000**, *39*, 6200.
(58) Hanayama, R.; Tanaka, M.; Miwa, K.; Shinohara, A.; Iwamatsu, A.; Nagata, S. *Nature* **2002**, *417*, 182.
(59) Zwart, A.; Buursma, A.; van Kampen, E. J.; Zijlstra, W. G. *Clinical Chemistry* **1984**, *30*, 373.
(60) Huang, J.; Bu, L.; Xie, J.; Chen, K.; Cheng, Z.; Li, X.; Chen, X. *ACS Nano* **2010**, *4*, 7151.

CHAPTER 7

CANCER-ASSOCIATED FIBROBLAST TARGETING PHOTO-IMMUNOTHERAPY TO ENHANCE CYTOTOXIC T CELL INFILTRATION AND TUMOR CONTROL[j]

[j] Wei Tang[†], Zipeng Zhen[†], Shiyi Zhou, Weizhong Zhang, Jin Xie.* To be submitted to *ACS Nano*.

7.1 Introduction

Carcinoma-associated fibroblasts (CAFs) refer to a subset of fibroblasts that are perpetually active in tumors[1]. CAFs are found in many types of cancer (e.g. breast, colorectal, and ovarian cancer[1]) and often account for a major portion of the tumor stroma cell population. For instance, in breast carcinomas, ~80% of stromal fibroblasts are CAFs[2]. It is increasingly clear that CAFs play important roles in cancer cell survival, proliferation, and metastasis[3,4]. These include causing accelerated extracellular matrix (ECM) turnover by excessive deposition of ECM components (e.g. type I, type III, and type V collagen and fibronectin) and secretion of ECM-degrading proteases (e.g. MMP2, -3, and -9[3,5]); promoting cancer cell proliferation and epithelial cell transformation by secreting high levels of growth factors such as HGF, EGF, and IGF[3]; and inducing an immunosuppressive tumor microenvironment by releasing cytokines such as VEGF, IL-6, IL-10, and TGF-β_1[6-9]. Related to these, recent studies found that CAFs are also involved in inducing an immune-privileged environment that prevents T cells from physically contacting with cancer cells[10]. This is achieved by producing a dense layer of ECM surrounding tumor nests which physically traps T cells[11]. Also, it was found that CXCL12 secreted by CAFs play an important role in mediating T cell exclusion, although the exact mechanism is still unkonwn[10]. T cell exclusion prevents cancer cells from immune attack despite the existence of cancer-specific T cells in patients[12,13]. As such, the phenomenon may represent a major challenge for cancer treatments, including the emerging immunotherapies such as the adoptive T cell therapy and anti-PD-1/anti-PD-L1 therapy[10].

Due to the wide distribution and participation in tumor growth, CAFs have attracted much attention as a cancer therapy target. In particular, fibroblast-activation protein (FAP), which is overexpressed on CAFs in over 90% of epithelial cancers[1] and a significant portion of

melanomas[14], was proposed as a universal tumor target antigen. To this end, anti-FAP antibody F19 and its humanized version sibrotuzumab were developed and evaluated in the clinic[15,16]. FAP-targeting vaccines[17,18], antibody-drug conjugates[19], and chimeric antigen receptor (CAR) T cells[20], have also been produced and investigated in preclinical studies. However, despite the initial thought that the expression of FAP is negligible in normal tissues, recent studies found FAP^+ cells in placenta[21], uterus[21], embryo[22], and bone marrow[23]. A systematic therapy against FAP^+ cells may lead to severe cachexia[20,24], muscle loss[24], bone toxicities[20], and even death[20]. Such wide distribution of FAP^+ cells and the associated off-target toxicities cast doubts on the use of a systemic anti-FAP therapy and largely impeded the developments of the related technologies.

To address the issue, we herein develop a novel, photoimmunotherapy (PIT) approach for localized and highly selective eradication of CAFs. Briefly, we employ apoferritin, a protein cage, to load $ZnF_{16}Pc$, a photosensitizer; and we conjugate to the surface of the protein cage an anti-FAP single chain variable fragment (scFv). Upon systemic injection into 4T1-bearing balb/c mice, the nanoconjugates, $ZnF_{16}Pc$@FRT-scFv, home to tumors via scFv-FAP interaction. Subsequent photoirradiation led to efficient killing of CAFs in tumors, and due to the localized nature of therapy, causing minimal toxicity to normal tissues. We found that while the PIT did not directly kill the majority of cancer cells, the treatment led to efficient tumor suppression and significantly extended survival. Further investigations revealed that the tumor control was mainly attributed to an activated intratumoral immune response, manifested as not only an increased frequency of $CD8^+$ T cells in tumors but also enhanced infiltration. The latter was attributed to a destructed ECM and a reduced production of CXCL12, both factors were linked to the eradication of CAFs in tumors. Such a PIT approach is different from conventional PDT, which

works by directly killing cancer cells and/or damaging tumor-related microvessels to induce tissue ischemia[25]. To the best our knowledge, the present study is the first to investigate CAF-targeted PDT and its impact on cancer cell growth and tumor microenvironment.

7.2 Results

7.2.1 Preparation and Characterization of $ZnF_{16}Pc$ loaded Ferritin (Z@FRTs)

Mouse ferritin (FRT) was prepared by following a published protocol and was purified by size-exclusion chromatography (SEC)[26]. For photosensitizer loading, $ZnF_{16}Pc$ in DMSO was added to a FRT solution in PBS and the mixture was incubated at room temperature for 45 min with agitation. The products were purified on a NAP-5 column. The $ZnF_{16}Pc$ loading rate was characterized using Uv-vis spectroscopy by comparing to a pre-established standard curve. A formulation with a 41.2 wt% $ZnF_{16}Pc$ loading rate was used for subsequent studies.

Transmission electron microscopy (TEM) analysis confirmed the cage-like structure of $ZnF_{16}Pc$-loaded FRTs, or Z@FRTs, which afforded an external diameter of ~12 nm (**Figure 7.1a**). This data corroborates with the dynamic light scattering (DLS) results, finding a hydrodynamic size of 12.25 ± 1.51 nm for Z@FRTs (**Figure 7.1a**). These results are also comparable to those with unloaded FRTs **(Figure 7.1a)**, suggesting minimal impact of $ZnF_{16}Pc$ loading on particle size and colloidal stability. Notably, free $ZnF_{16}Pc$ has poor water solubility and is quickly precipitated out in aqueous solutions (**Figure 7.1c**); as a comparison, Z@FRTs are very stable in PBS (pH 7.4) and the solution can be kept for one week without showing visible precipitation (**Figure 7.1c**). Also noted is that when pH of Z@FRT solution was decreased to 2.0, $ZnF_{16}Pc$ precipitation started to form at the bottom of the vessel (**Figure 7.1c**). This is

attributed to the breakdown of the nanocage structure and the release of payloads from the FRT cages.[27]

The capacity of $^1O_2$ generation was studied by singlet oxygen sensor green (SOSG) assay[28]. Under 671-nm laser irradiation (0.1W/cm^2), Z@FRTs were able to efficiently produce $^1O_2$, manifested in an increase of 525-nm SOSG fluorescence (**Figure S7.1**). The $^1O_2$ generation was comparable with $ZnF_{16}Pc$-only (dispersed in PBS containing 1% Tween, **Figure S7.1**) at the same concentrations, suggesting minimal self-quenching among $ZnF_{16}Pc$ molecules despite the high loading.

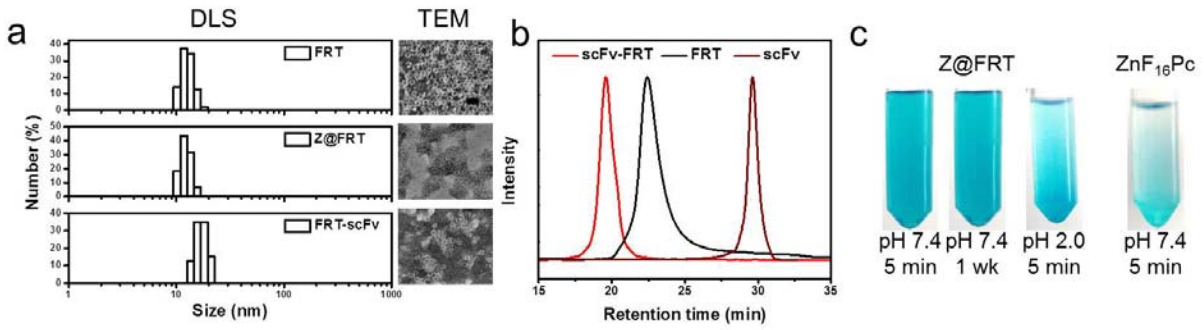

Figure 7.1 Characterization of Z@FRT-scFv. (a) DLS and TEM analysis of FRTs, Z@FRTs, and scFv-Z@FRTs. Scale bar, 20 nm. (b) SEC analyses of FRTs, scFvs, and scFv-FRTs. The retention times were 22.42, 29.63, and 19.59 min, respectively. (c) Photographs of Z@FRTs and free $ZnF_{16}Pc$ in PBS under different conditions.

7.2.2 Preparation and Characterization of anti-FAP scFv

The sequence of the anti-FAP scFv was published previously by Brocks B.[29] and was shown in **Figure S7.2**. Basically, the variable regions of light chain and heavy chain were coupled together via a 4X GGGGS linker according to the order, NH_2-Light chain-linker-Heavy chain-COOH. The 3D tertiary structure of the protein was displayed in **Figure 7.2a**. The scFv sequence was inserted into plasmid pOPE101 and expressed by *E.Coli*. The raw product was purified on a Ni-

NTA cartridge. Sodium dodecyl sulfate-polyacrylamide gel electrophoresis (SDS-PAGE) analysis confirmed that the protein size was ~26KDa (**Figure S7.3**).

We also investigated the expression of FAP with tumors taken from different murine tumor models. These include primary tumors dissected from subcutaneous 4T1, U-87MG, and PC-3 models, and lung, liver, and kidney metastases from mouse models[30]. In all cases, we observed positive staining with IRDye800 labeled anti-FAP scFv, and efficient blocking if unlabeled scFv was co-applied (**Figure S7.4**). Meanwhile, we observed negative staining with normal tissues taken from the heart, liver, kidney, muscle, and brain (**Figure S7.5**). These results corroborated with the previous observation that FAP expression is low in these tissues[31], suggesting good selectivity of the anti-FAP scFv.

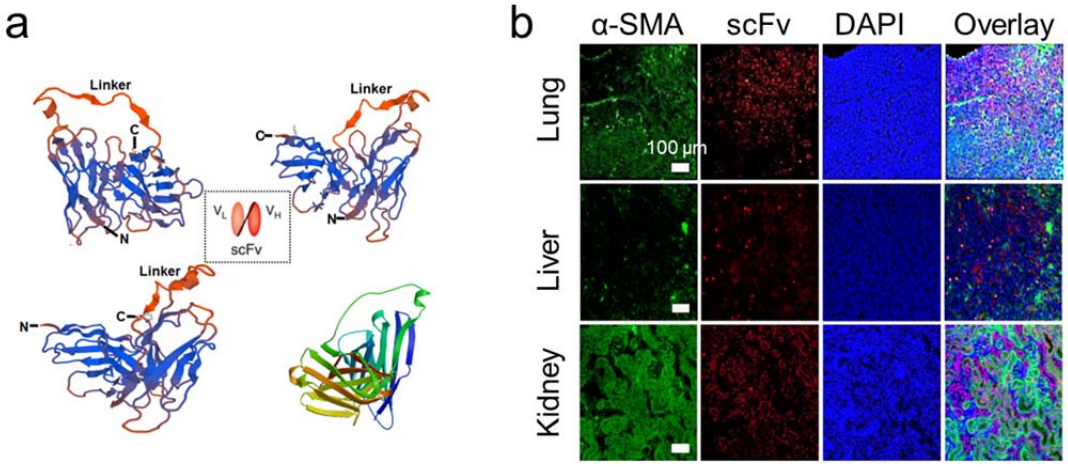

Figure 7.2 Binding Against FAP$^+$ Cells. (a) Tertiary structure of anti-FAP scFvs. (b) IMF staining with IRDye800 labeled anti-FAP scFvs against tumor tissues. Green, FITC; red, IRDye800; blue, DAPI. Scale bars, 100 μm.

7.2.3 Z@FRT-scFv preparation and *in vivo* targeting

Next, we conjugated the anti-FAP scFv to the surface of Z@FRTs using bis(sulfosuccinimidyl)suberate (or BS^3, a crosslinker) through a two-step conjugation approach[32]. The conjugation led to an increase of hydrodynamic size (to 14.58 ± 2.01 nm according to DLS, **Figure 7.1a**) and a shortened retention time on SEC (**Figure 7.1b**, Z@FRT-scFvs 19.59 min, FRTs 22.42 min).

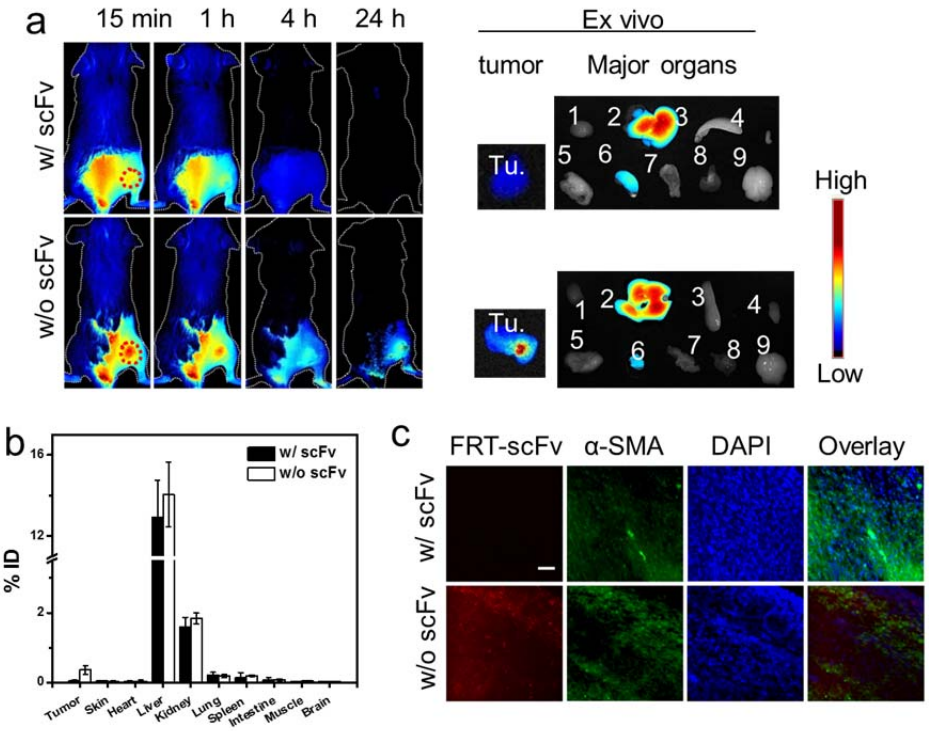

Figure 7.3 scFv-Z@FRTs Targeting Toward CAFs in a 4T1 Tumor Model. (a) *In vivo* and *ex vivo* fluorescence imaging results. IRDye800 labeled scFv-Z@FRTs were i.v. injected. Images were acquired at 15 min, 1 h, 4 h, and 24 h post injection. In a control group, free scFvs (30 ×) were administrated as a blocking agent. Tumors and major organs were harvested after 24 h imaging from the euthanized animals and displayed on a black sheet of paper for ex vivo imaging. (b) Biodistribution of scFv-Z@FRTs, based on *ex vivo* results from (a). (c) IMF staining with tumor tissues. Red, IRDye800 (scFv-Z@FRTs); green, α-SMA; blue, DAPI. Scale bar, 50 μm.

Next, we intravenously (i.v.) injected Z@FRT-scFvs to balb/c mice bearing subcutaneously implanted 4T1 tumors (n = 3). In order to facilitate the tracking of nanoparticles, Z@FRT-scFvs were labeled with IRDye800 before injection. The nanoparticles were initially distributed throughout the animal body, but were gradually accumulated in the tumor area (p.i., **Figure 7.3a**; hair of the lower body was shaven before imaging). As a comparison, when free scFv (30 ×) was injected prior to the injection of Z@FRT-scFvs, the tumor accumulation at 24 p.i. was significantly diminished (**Figure 7.3a**). Such selective tumor uptake was better displayed by *ex vivo* imaging with tumors dissected after the 24 h imaging (**Figure 7.3b**). Compared to the blocking group, tumor uptake in the Z@FRT-scFv group was 10.3 ± 2.9 times higher (**Figure 7.3b**). The targeting was also confirmed by immunofluorescence microcopy with anti-alpha smooth muscle actin (α-SMA) staining[3], finding overall good overlap between Z@FRT-scFv distribution and positive α-SMA staining (**Figure 7.3c**). Meanwhile, the distribution of Z@FRT-scFv in normal tissues was comparable between the Z@FRT-scFv and blocking groups (**Figure 7.3c**).

7.2.4 CAF-targeted PIT leads to tumor suppression and improved survival

Therapy studies were conducted with the same 4T1 tumor model (n = 5). Briefly, Z@FRT-scFvs (1.5 mg $ZnF_{16}Pc$/kg) was i.v. administered, followed by photoirradiation (671 nm, 300 mW/cm^2 for 15 min) to tumor areas at 24 hr (1PIT group). In a separate group, a second PIT procedure was applied three days after the first PIT (2PIT). For controls, animals were injected with PBS and received no photoirradiation. The PIT treatment led to efficient tumor suppression (**Figure 7.4a**). The 2PIT group, in particular, showed almost complete growth arrest in the first two weeks (88.60% tumor growth inhibition rate, or TGI, on Day 12), with 100 % of the animals showing a reduced tumor size. The efficient treatment led to significantly improved animal

survival. Specifically, the average survival was only 20% within 16 days for the control group, but was extended to 40% 20 days and 60% 30 days, respectively, for the 1PIT and 2PIT groups (**Figure 7.4b**). Meanwhile, there was no animal body weight drop during the course of the treatment (**Figure 7.4c**). H&E staining also found no pathological abnormalities in the main organs (**Figure 7.4d**), suggesting minimal collateral damage by the CAF-targeted PIT.

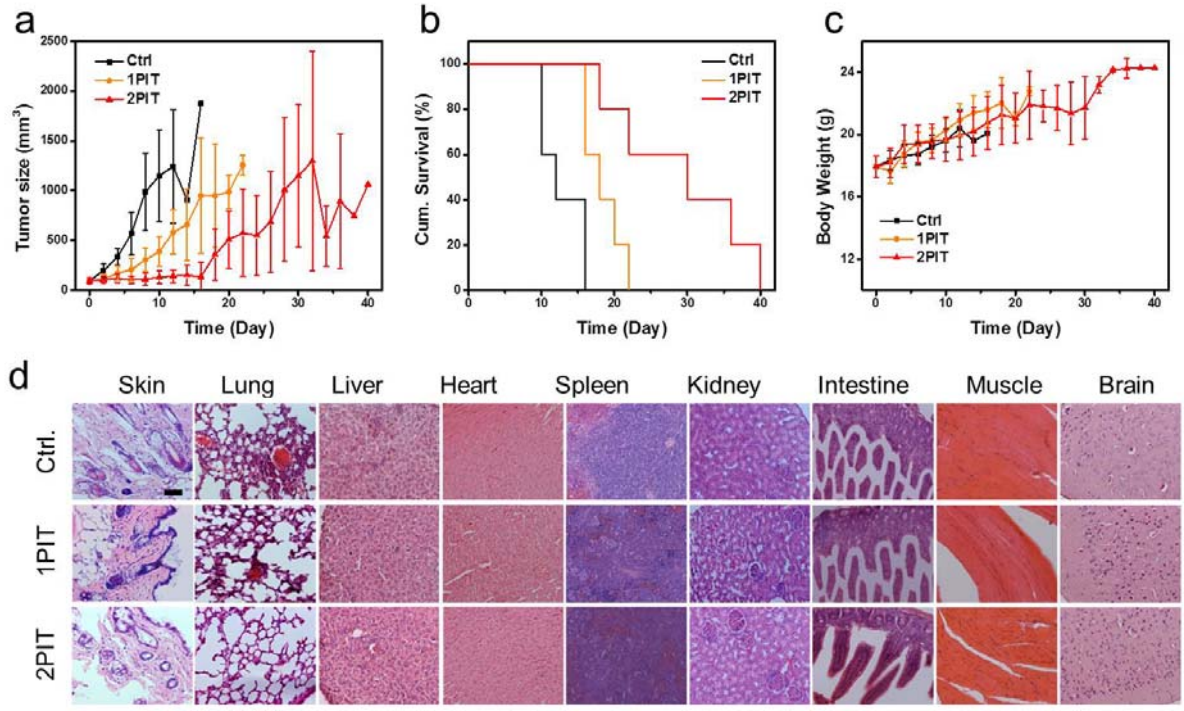

Figure 7.4 Impact of FAP-Targeted PIT on Tumor Growth and Survival. (a) Tumor growth curves (n=10). (b) Kaplan-Meier plot of animal survival. (c) Animal body weight changes. No obvious decrease of body weights was observed. (d) H&E staining of tissues taken from major organs after therapy. Scale bar: 50 μm.

7.2.5 Impact of CAF-targeted PIT to cancer cells

To further investigate the therapeutic effects, in a separate study, we euthanized mice on Day 3 after PIT treatments and analyzed the tissue and blood samples. Compared to the control group, anti-FAP PIT efficiently killed CAFs in tumors, manifested by a significantly reduced level of

anti-α-SMA positive staining (**Figure 7.5a & 7.5b**). In particular, only a background level of anti-α-SMA positive staining was observed after two PIT treatments, suggesting efficient eradication of CAFs (**Figure 7.5a**). The efficient CAF killing in the 2PIT group was also confirmed by significantly reduced serum levels of EGF and IL-6 (**Figure 7.5c**), to which CAFs are a major source of secretion[33]. Notably, in the 1PIT group, IL-6 level was increased at early time points (**Figure 7.5c**). This is likely due to the fact that IL-6 is also secreted by T cells and macrophages in response to tissue damage[34].

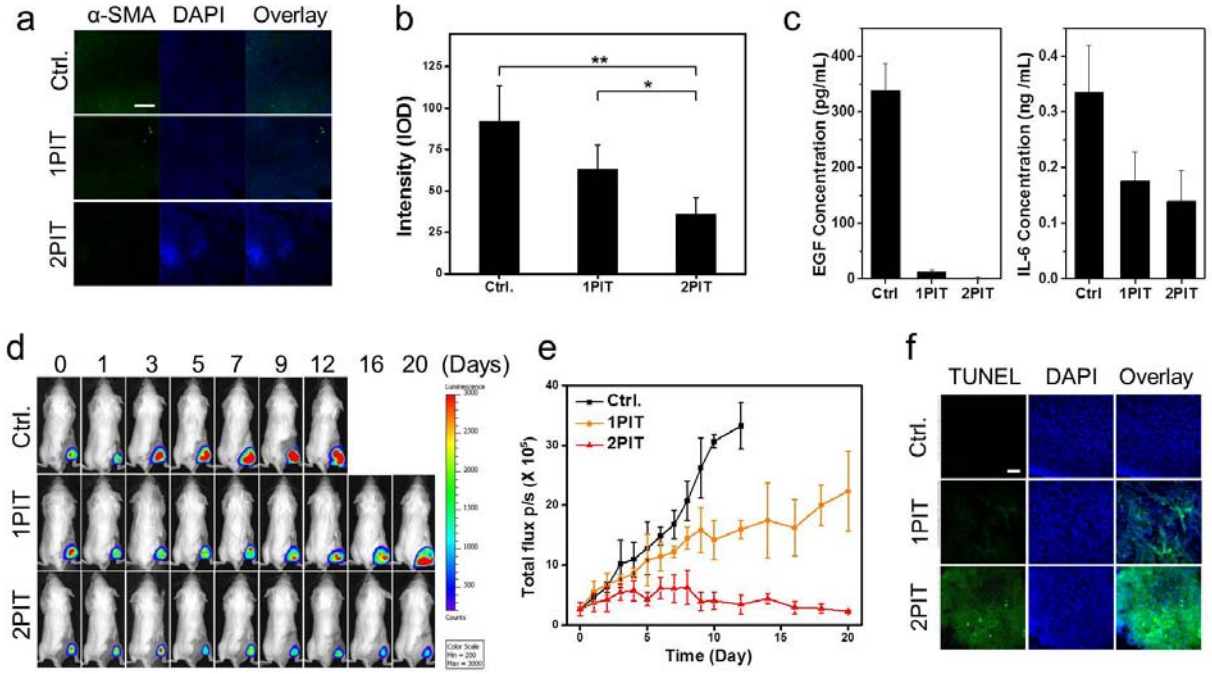

Figure 7.5 Impact of FAP-Targeted PIT on Cancer Cells and CAFs in Tumors. (a) α-SMA staining with tumor tissues. Green, α-SMA; blue, DAPI. Scale bar, 100 μm. * $P < 0.05$. ** $P < 0.01$. (b) Statistic analysis from (a). (c) Changes of plasma EGF and plasma IL-6 concentration after PIT. (d) BLI to track tumor growth after PIT. (e) Cancer cell number changes, based on ROI analysis on (d). (f) TUNEL assays on tumor tissues, taking 7 days after PIT treatment. Green, FITC; blue, DAPI; scale bar, 50 μm.

While efficiently killing CAFs, the direct impact of PIT on cancer cell viability is relatively small. This is shown in a repeating therapy study with 4T1-luc inoculated animals, where we used bioluminescence imaging (BLI) to monitor cancer cell growth. In both 1PIT and 2PIT groups, there was a low level of cancer cell death relative to the control on Day 1 and Day 2, which were determined by the total flux of photons ($x10^5$ p/s) from bioluminescence detected. We detected total flux of 5.53 ± 1.81 and 3.69 ± 1.39 respectively for 1PIT and 2PIT, compared with that of 4.64 ± 0.68 from control on Day 1; 6.80 ± 1.78 and 4.29 ± 2.07 respectively, compared with 6.35 ± 0.84 on Day 2. This suggests that the PIT selectively kills CAFs, but leaves behind most cancer cells. However, much more significant difference in viable cancer cells started to appear after Day 4. In particular, there was a significant drop of BLI signals in the 2PIT since Day 5 (**Figure 7.5d & 7.5e**). Such results corroborated with TUNEL staining with tumor tissues, finding extensive apoptotic cells in both treatment groups, and more so in the 2PIT group (**Figure 7.5f**). Since PIT is more prominent to induce cell necrosis, the results suggest a different direct cause of cancer cell death.

Next, we used immunofluorescence staining to examine the amount of $CD8^+$ T cells in tumors (**Figure 7.6a**). By analyzing multiple slices, we found that the frequency of $CD8^+$ T cells in tumors was increased by 6.13 times in the 1PIT group and 19 times in the 2PIT group (**Figure S7.6**). These corroborate with flow cytometry results (**Figure 7.6b**), which found an increase of $CD8^+$ T cell numbers in both tumors and plasma after the PIT treatment. These suggest a stimulated immunity after PIT.

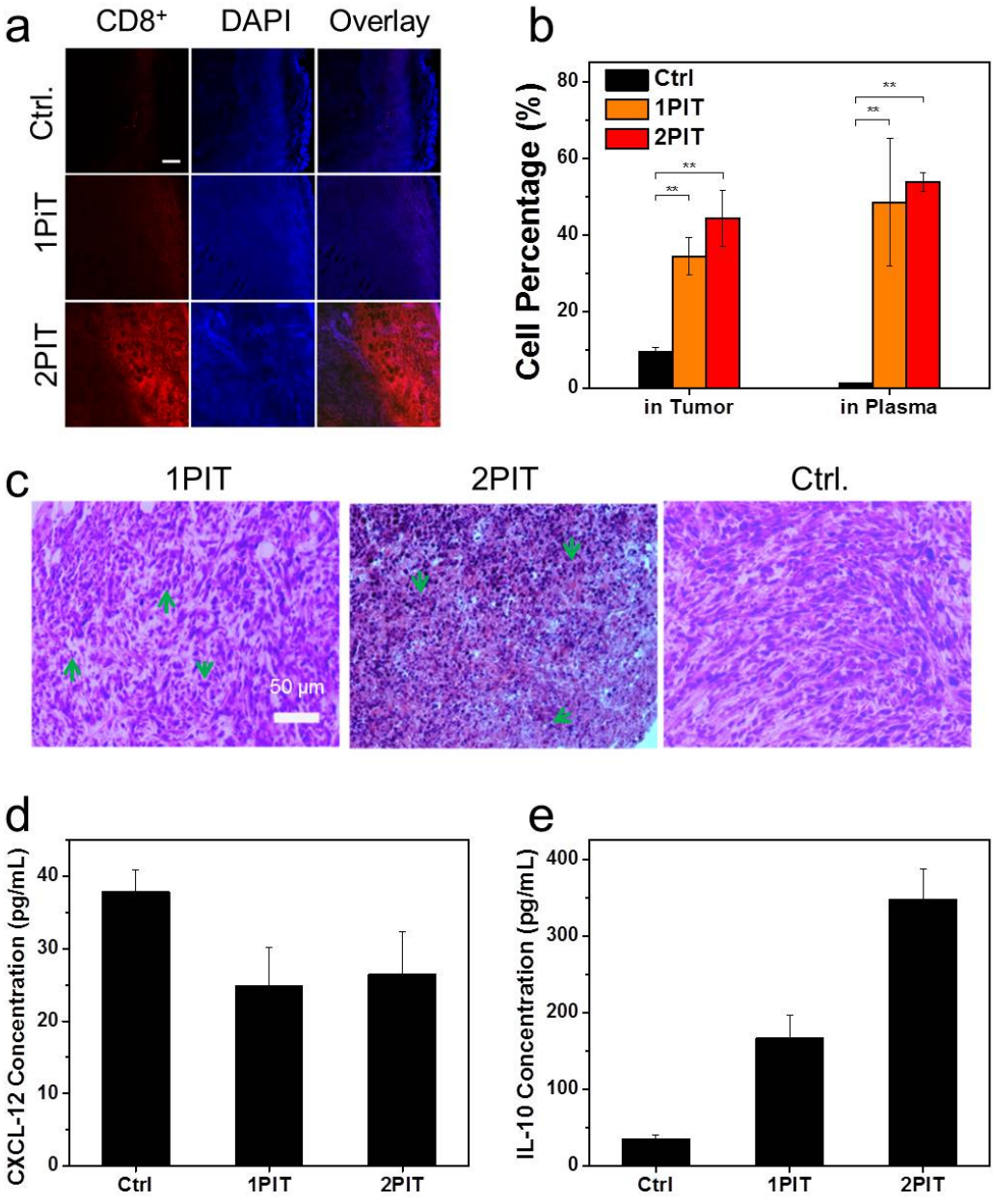

Figure 7.6 Anti-Tumor Immunity Induced by FAP-Targeted PIT. (a) CD8+ T-cell staining with tumor tissues taken 3 days after 1PIT or 2PIT. Red, CD8+ T cells. Blue, DAPI. Scale bar, 50 μm. (b) $CD8^+$ T cell number frequency changes, based on flow cytometry analysis on extracts from tumors and plasma samples. ** $P < 0.01$. (c) H&E staining of tumors after PIT. Green arrows, neutrophils. Scale bar, 50 μm. (d) and (e), changes of plasma concentration of CXCL12 and IL-10, respectively.

However, the enrichment of $CD8^+$ cells in tumors does not warranty efficient cancer cell killing. As discussed at the beginning, in many tumors, CAFs help create a T-cell exclusion environment. Indeed, we observed in the control group a significant accumulation of $CD8^+$ T cell at the peripheral of tumors but few of them at the central of tumors (**Figure 7.6a**). As a comparison, after PIT, there was significantly improved enhanced infiltration of T cells (**Figure 7.6 a & S7.6**). H&E staining also found a significantly increased number of neutrophils at the central of tumors (**Figure 7.6c**). Such improved infiltration was attributed to a destructed ECM and a reduced level of CXCL12, which was observed by ELISA (**Figure 7.6d**). Meanwhile, IL-10, which was capable of activating and expanding $CD8^+$ T cells residing in tumor[35], was also found to be upregulated after PIT (**Figure 7.6e**). Such PIT-induced CD8+ T cell accumulation and infiltration corroborates with the extensive cell death observed with TUNEL assay and is believed to be the main mechanism behind the efficient tumor control.

7.3 Discussion

The wide participation of CAFs in cancer development and the fact that FAP is selectively expressed in CAFs had promised FAP as a universal tumor targeting antigen[3]. Previously, anti-FAP monoclonal antibody F19 and sibrotuzumab were developed and tested in the clinic. While showing overall good tumor targeting[15], the antibody treatment showed no clinical efficacy[15,16], which is probably due to the fact that blocking FAP alone is insufficient to impact CAF functions[36]. Recently, Rosenberg et al. produced T cells that were genetically engineered with FAP-reactive CAR T cells[20]. However, severe cachexia and lethal bone toxicities were observed with the T-cell immunotherapy[20], which were attributed to expression of FAP on multipotent bone marrow stromal cells (BMSCs)[20]. Also, Fearon et al. reported that experimental ablation of

FAP^+ cells in mice led to a loss of muscle mass and decreased B-lymphopoiesis and erythropoiesis[24], further cautioning the use of a systemic therapy against FAP+ cells. Unlike the previous studies, the present approach combines FAP-targeted photosensitizer delivery and localized photoirradiation; the resulting PIT leads to selective CAF eradication while causing minimal systemic toxicity. Such an approach is novel and may be applied in combination with conventional chemotherapy to achieve even more effective and sustained tumor control.

CAFs produce many of the main components of ECM such as type I, type III, and type V collagen and fibronectin[3,4], and the expression level is found to be inversely correlated with tumor uptake of therapeutic molecules[37-39]. Moreover, CAFs express a high level of α-SMA and as such acquire contractile properties[3]; this leads to an increased interstitial fluid pressure (IFP)[40] which poses an obstacle for delivery of therapeutics to tumors[9]. It is highly plausible that killing CAFs may also enhance the efficiency of drug delivery. In fact, we and others have exploited PIT to target tumor vasculature[41,42] or perivascular cancer cells[43], and as such enhance tumor uptake of therapeutics. The approaches, however, have such limitations as a narrow window of effective irradiation dose[41,42], lack of a unique cancer cell biomarker, and inefficient penetration of the PIT agents themselves. CAF-targeting PIT holds clear advantages in this context.

A more exciting opportunity comes from the capacity of CAF-targeting PIT to modulate tumor microenvironment (TME) to favor anti-cancer immunity. It has long been observed that cancer-specific T cells can exist in a cancer patient while not efficiently control cancer growth[44]. One major mechanism behind this is T cell exclusion, mediated by CAFs through depositing a thick ECM layer and secreting CXCL12 to the TME[10]. There has been recent developments in immunotherapy that aims to augment the numbers and functions of cytotoxic T cells, including anti-CTLA-4 therapy[45], anti-PD-1/PD-L1 therapy[46], and CAR T-cell therapy[47]. These

approaches, however, can still be limited by the immune privilege induced by CAFs that exclude T cells from the vicinity of cancer cells[10]. In the present study, we showed after CAF-targeting PIT, both the frequency and infiltration of $CD8^+$ T cells were significantly improved, linking to extensive cancer cell death (**Figure 7.5f**). These were attributed to both a destructed ECM and also reduced secretion of immunosuppressive cytokines such as IL-6 and CXCL12. These results are intriguing, suggesting the potential of CAF-targeted PIT as a means to modulate TME and as a result enhancing T cell infiltration and sensitizing cancer cells to immunotherapy. It will be interesting in the future to combine the approach with other immunotherapies to augment the treatment efficacy.

From the perspective of PIT development, the current study also represents a major advance. Conventional PDT often uses non-targeting photosensitizer molecules and the damage is often inflicted on both cancer cells and tumor microvessels[25]. More recently, PIT, often achieved with antibody-photosensitizer conjugates, was developed[48-51] and investigated in both pre-clinical and clinical studies. Meanwhile, photosensitizer-delivery technologies using artificial nanocarriers such as polyester and polyacrylamide based nanoparticles, liposomes, silica particles, and magnetic nanoparticles, have been developed[52-54]. These approaches, however, are still focused on targeting cancer cells or endothelial cells. In the present study, we employed anti-FAP scFv as a targeting ligand to selectively kill CAFs in tumors. Moreover, we use ferritin, a natural protein cage, as photosensitizer carrier, which affords multiple advantages such as excellent biocompatibility, high photosensitizer loading capacity, and a compact size (~12 nm). These attempts are novel to PIT and the methods hold great potential in clinical translation.

7.4 Conclusions

Overall, we have developed a novel PIT technology which exploits apoferritin as a photosensitizer carrier and anti-FAP scFv as a targeting ligand. Such FAP-targeted PIT effectively and selectively eliminates CAFs in tumors but does not induce systemic toxicity due to localized photoirradiation. This is followed by ECM destruction and CXCL12 secretion reduction, both contributing to a significantly enhanced CD8+ T cell infiltration, eventually leading to efficient tumor control. Our strategy sets a different path for CAF-targeted cancer therapy, whose development has been impeded by systemic toxicity. Our observation that eliminating CAFs in tumors can modulate TME and promote T cell infiltration is novel, suggesting the great potential of the current approach to work in conjugation with chemotherapy and immunotherapy for optimal tumor management.

Materials and Methods

Expression and Purification of FRTs and scFvs: The FRT purification was followed our published protocol.[27] The anti-FAP scFv sequence reported by Brocks B et al[55]. NcoI and HindIII restriction sites were introduced to the heavy chain, flanking the normal start and stop codons. MluI and NotI were introduced to the light chain. The resulting sequence was inserted to a pOPE101 plasmid and transformed into *E.coli* JM109 with ampicillin-resistance. A PelB signal peptide was added to the N-terminus of scFv, directing the translated scFv to bacteria periplasm, where the scFv finished its folding into active architecture. To produce anti-FAP scFvs, a 1 L LB-ampicillin (25 μg/mL) culture of *E. Coli* JM109 was grown at 37 ºC until an OD600 of 0.8 was reached. IPTG (final concentration: 0.5 mM) was added to induce the production of proteins and the bacteria were incubated at 37 °C for 4 hours. The bacteria were harvested by centrifugation at 4,000 g. After sonication, the cell lysate was centrifuged at 12,930g for 30 min to remove cell debris and the supernatant was filtered through a 0.2 μm filter. A Ni-NTA cartridge was connected to HPLC and thoroughly washed with binding buffer NPI-10. The filtered supernatant was then loaded onto the Ni-NTA cartridge at 1 mL/min. NPI-20 washing buffer (10-fold column volume, i.e. 10 mL) was applied to the cartridge subsequently. Elution buffer of NPI-250 was then applied to elute the scFvs from the column. The final collections were dialyzed against 1x PBS (pH 7.4) at 4 °C for 48 hours. The concentration of scFvs was determined by a Bradford protein assay kit. The purified scFvs were stored at -80 °C. 12% SDS-PAGE was used to confirm the products.

PSs loading and anti-FAP scFv coupling to FRTs: The protocol for $ZnF_{16}Pc$ loading was published previously[56]. Briefly, 490 μL ferritin (0.5 mg/mL in 1x PBS) was gently mixed with 10 μL $ZnF_{16}Pc$ (5 mg/mL in DMSO) for ~ 45 min at room temperature. The resulting P-FRTs were then purified on a NAP-5 column to remove the unloaded $ZnF_{16}Pc$.

The anti-FAP scFvs were coupled onto ferritins via a BS^3 crosslinker. Firstly, scFv and BS^3 were mixed at a molar ratio of 1:10 for 30 min at room temperature. A 10k 0.5 mL centrifugal filter (Amicon) was used to remove unbounded BS^3 molecules. Secondly, the resultant was mixed with FRT at a molar ratio of 20:1for 30 min at room temperature. A 100k centrifuge filter (Amicon) was applied to purify the final product of FRT-scFv.

Cell lines: The 4T1, 4T1-Luc, HTB-135, and 3T3 cell lines were obtained from American Type Culture Collection (ATCC) and cultured with RMPI 1640 medium (Corning®) or DMEM medium (Corning®) supplemented with 10% fetal bovine serum (Corning®) and 1% penicillin-streptomycin solution (100×, MediaTech, USA), and incubated humidly under 37 °C and 5% CO_2.

Animal models: Balb/c mice were purchased from Envigo laboratories. The animal model was established by subcutaneously injecting ~ 10^6 4T1 or 4T1-Luc cells to the right hind limb of each mouse. All of the experimental procedures were conducted following a protocol approved by the University of Georgia Institutional Animal Care and Use Committee.

Flow cytometry and ELISA assays: Whole blood was collected with heparin-coated centrifuge tubes and centrifuged at 5000 G, 4 °C for 5 min. The supernatant was collected and stored at -80 °C for ELISA assay. The cell pellet was re-suspended in 1 mL of sterile 0.9 % NaCl solution.

Next, 9 mL of ice-cold hemolytic buffer was added into the cell suspension. After incubating on ice for 30 min, the cell pellet was separated by centrifugation (5000 G, 4 °C for 5 min) and re-suspended in 1 mL of 1x M PBS (pH 7.4). 5 μL of anti-CD3 and CD8a antibodies (Biolegend) were added into the cell suspension. After incubating for another 30 minutes at 4 °C, the cell suspension was centrifuged (5000 G, 4 °C for 5 min) and again re-suspended in 1 mL of PBS for flow cytometry analysis.

Cell extraction from organs was conducted according to the protocol provided by the enzyme vendor (Gibco). Generally, tumors were cut into 3-4 mm small fragments with sterile scissor in an ice-cold 6-well plate. Trypsin and collagenase were added at final concentrations of 0.125% and 100 U/mL, respectively. The mixture was incubated overnight at 4 °C and then filtered with a Nylon cell strainer (40 μm pore, Corning®). The filtrate was centrifuged and resuspended in 1 mL of PBS. The single cell solution was stained by anti-CD3 and CD8a antibodies (Biolegend) as mentioned above.

ELISA analysis IL-6, IL-10, EGF and CXCL12 were conducted by strictly following the protocol from the vendor (RayBiotech). The optical density was measured at 450 nm. The concentrations of IL-6, IL-10, EGF and CXCL12 were calculated by comparing to the corresponding standard curves.

***In vivo* imaging:** The imaging was started when the tumors reached a size of ~100 mm^3. IRDye800-labeled Z@FRT-scFvs (0.75 mg $ZnF_{16}Pc$/kg, equals to 1 mg scFv-FRTs/kg) were i.v. injected into 4T1 tumor bearing mice (n=5). For the control group, 30x scFvs were administrated 2 hrs prior to the Z@FRT-scFvs injection (n=5). Whole-body fluorescence images were acquired on a Maestro II imaging system (PerkinElmer) using an NIR emission filter (750 – 940 nm) at 5, 10, 15, and 30 min, as well as 1, 4, and 24 h post injection (p.i.) time points. The fluorescence images were unmixed by the vendor provided software. Region of interests (ROIs) were circled around tumor areas, and the average optical intensities (in total scaled counts/cm^2/s) were recorded and compared. After the 24 h imaging, the animals were euthanized. Tumors as well as major organs were harvested for histology studies.

Bioluminescence imaging (BLI) of 4T1-Luc tumors was performed on an IVIS lumina II imaging system. The images were acquired 15 min after the intraperitoneal (i.p.) injection of luciferin (150 mg/kg body weight). All images were analyzed by the vendor's software (Version 4.3.1 SP1, PerkinElmer).

***In vivo* therapy:** The therapy studies were performed on 4T1 tumor models. For the 1PIT treatment group (n=10), animals were i.v. injected with P@ FRT-scFvs (1.5 mg $ZnF_{16}Pc$/kg) and the tumors were irradiated at 24 h p.i. by a 671 nm laser (300 mW/cm^2, over a ~1 cm diameter beam) for 15 min. For 2 PIT treatment group (n=10), the 1PIT treatment was repeated at an interval of three days. The control group (n=10) received PBS only without laser irradiation. Tumor sizes were measured every other day by a caliper and computed following the formula: size (mm^3) = length (mm) × width $(mm)^2/2$.

Immunofluorescence staining: The cryogenic slices in 8 μm thick were fixed with ice-cold acetone for 15 min and washed by running water for 5 min. The paraffin-embedded sample blocks for immunofluorescence staining were cut to 7 μm slices. The slices were hydrated in

gradient ethanol of 100%, 90%, 75%, 50% and 25% (each for 2 min) after deparaffinization in xylene. 1x PBS (pH 7.4) was used to wash the slices twice (each for 5 min). Then, antigen retrieval was conducted in microwave. PBS washing was performed after thoroughly cooling down. Next, 10% goat serum was applied to block both cryogenic and paraffin-embedded slides for 1 h at 37 °C. Subsequently, primary antibodies, phycoerythrin-labeled anti-CD31 antibody (ab25644), Alexa Fluor®647-labeled anti-CD8a antibody (Biolegend®), and IRDye800-labelled anti-FAP scFvs were incubated with the slides at 4 °C for overnight, respectively. After gently rinsing with PBS, the slides were mounted using mounting medium containing DAPI. Images were acquired on an Olympus IX71 or a Zeiss LSM 710 confocal microscope.

Hematoxylin and eosin staining: H&E staining was performed according to a protocol provided by the vendor (BBC Biochemical). Briefly, 5 μm paraffin-embedded slides were prepared. After being treated with 100% xylene for 3 times (each for 3 min), the slides were hydrated with a gradient concentrations of alcohol (100%, 90%, 75%, 50% and 25%), each for 2 min. The hematoxylin staining was then performed for 3 min, and the slides were washed with running water for 3 min. The eosin staining was performed for 1 min. The slides were then washed, dehydrated, treated with xylene, and mounted with Canada balsam. The images were acquired on a Nikon Eclipse 90i microscope.

Statistical methods: Quantitative data were expressed as mean ± s.e.m. Two-tailed Student's t-test and Chi-squared test were used for statistically comparing the treatment group with the control group. $P < 0.05$ was considered statistically significant.

Supporting Information

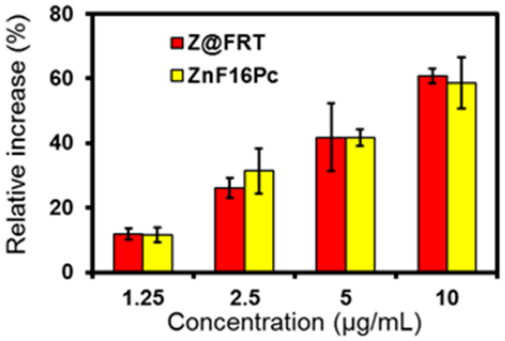

Figure S7.1 Generation of $^1O_2$ from Z@FRT in PBS and free $ZnF_{16}Pc$ PBS containing 1% Tween.

MKYLLPTAAAGLLLLAAQPAMADILMTQSPASSVVSLSGQRATISCRASK
PelB Signal Peptide
SVSTSAYSYMHWYQQKPGQPPKLLIYLASNLESGVPPRFSGSGSGTDFTL

NIHPVEEEDAATYYCQHSRELPYTFGGGTKLEIKGGGGSGGGGSGGGGS
Linker
GGGGSQVQLKQSGAELVKPGASVKLSCKTSGYTFTENIIHWVKQRSGQG

LEWIGWFHPGSGSIKYNEKKDKATLTADKSSSTVYMELSRLTSEDSAVYFC

ARHGGTGRGAMDYWGQGTSVTVSSGGGGCASHHHHHH
Linker His-Tag

Figure S7.2 Amino acid sequence of anti-FAP scFv. Light chain indicated by green letters; heavy chain indicated by red letters. A PelB signal peptide was included at N-terminus to direct translated scFv to E.coli periplasmic space. 4 x GGGGS were used to connect the light chain to the heavy chain. The cysteine residue in the sequence of GGGGCAS, was engineered for site specific conjugation. The His-tag was inserted to C-terminus for purification purpose.

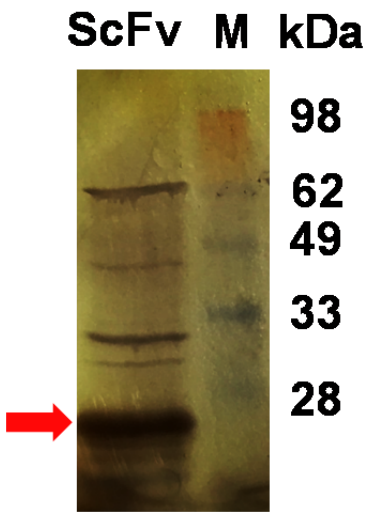

Figure S7.3 12% SDS-PAGE result of raw product of anti-FAP scFv. A band at around 26 kDa was found for scFv. M, standard protein marker; red arrow, scFv band.

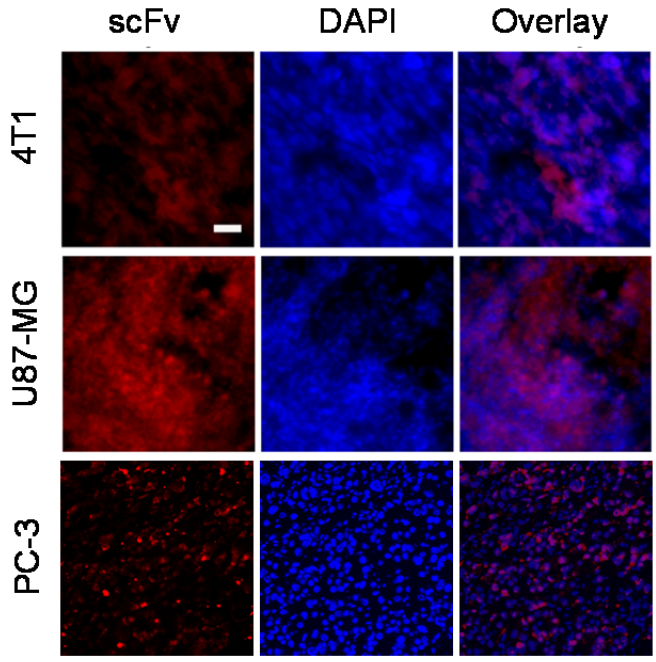

Figure S7.4 Studies of anti-FAP scFv binding affinity in s.c. 4T1, U-87MG, and PC-3 tumor tissues. Red, IRDye800; blue, DAPI; scale bar, 100 μm.

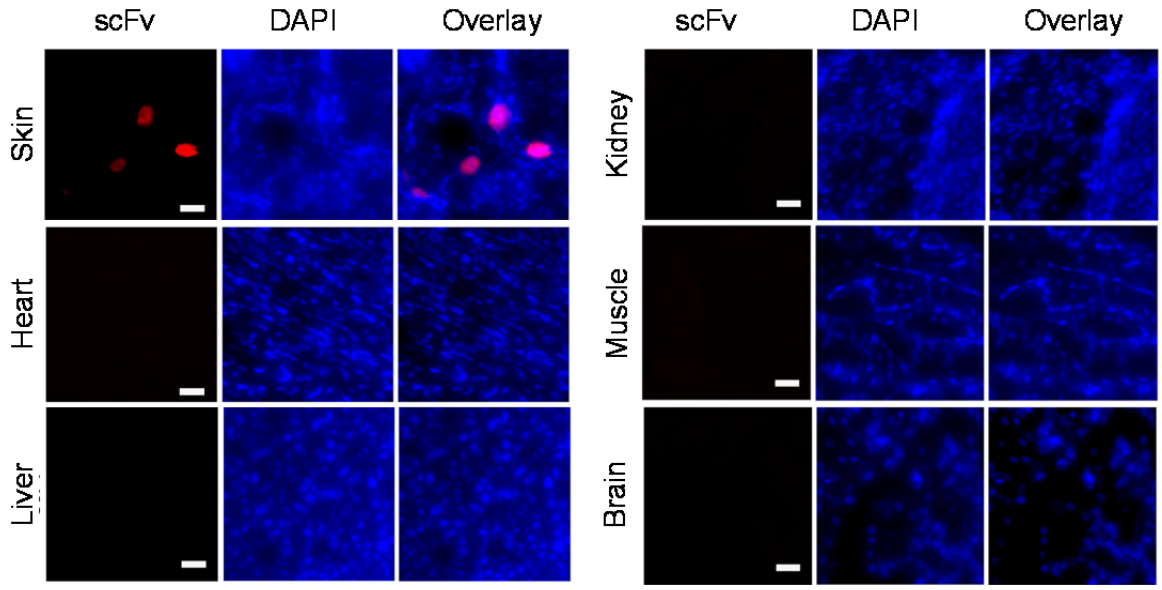

Figure S7.5 Anti-FAP scFv binding tests in healthy tissues from tumor-free Balb/c mice. Red, IRDye800; blue, DAPI; scale bar, 100μm.

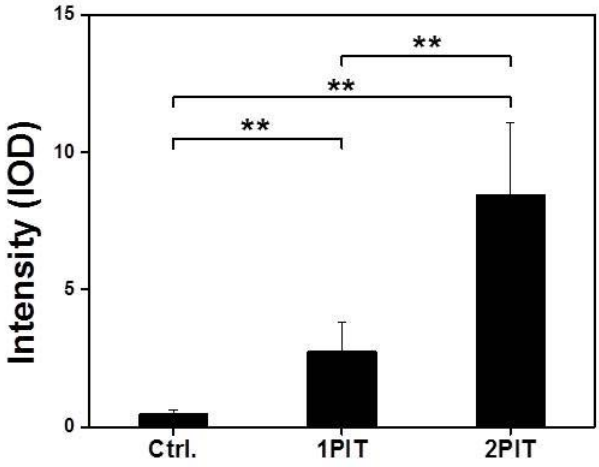

Figure S7.6 Frequency of CD8+ cells, based on analysis of fluorescence intensity of Figure 7.6a. ** $P < 0.01$.

References

(1) Garin-Chesa, P.; Old, L. J.; Rettig, W. J. *Proceedings of the National Academy of Sciences of the United States of America* **1990**, *87*, 7235.
(2) Sappino, A. P.; Skalli, O.; Jackson, B.; Schurch, W.; Gabbiani, G. *International Journal of Cancer* **1988**, *41*, 707.
(3) Kalluri, R.; Zeisberg, M. *Nature Reviews. Cancer* **2006**, *6*, 392.
(4) Tomasek, J. J.; Gabbiani, G.; Hinz, B.; Chaponnier, C.; Brown, R. A. *Nature Reviews. Molecular Cell Biology* **2002**, *3*, 349.
(5) Chang, H. Y.; Chi, J. T.; Dudoit, S.; Bondre, C.; van de Rijn, M.; Botstein, D.; Brown, P. O. *Proceedings of the National Academy of Sciences of the United States of America* **2002**, *99*, 12877.
(6) Gabrilovich, D. I.; Chen, H. L.; Girgis, K. R.; Cunningham, H. T.; Meny, G. M.; Nadaf, S.; Kavanaugh, D.; Carbone, D. P. *Nature Medicine* **1996**, *2*, 1096.
(7) Elgert, K. D.; Alleva, D. G.; Mullins, D. W. *Journal of Leukocyte Biology* **1998**, *64*, 275.
(8) Muraoka, R. S.; Dumont, N.; Ritter, C. A.; Dugger, T. C.; Brantley, D. M.; Chen, J.; Easterly, E.; Roebuck, L. R.; Ryan, S.; Gotwals, P. J.; Koteliansky, V.; Arteaga, C. L. *Journal of Clinical Investigation* **2002**, *109*, 1551.
(9) Loeffler, M.; Kruger, J. A.; Niethammer, A. G.; Reisfeld, R. A. *Journal of Clinical Investigation* **2006**, *116*, 1955.
(10) Joyce, J. A.; Fearon, D. T. *Science* **2015**, *348*, 74.
(11) Salmon, H.; Franciszkiewicz, K.; Damotte, D.; Dieu-Nosjean, M. C.; Validire, P.; Trautmann, A.; Mami-Chouaib, F.; Donnadieu, E. *Journal of Clinical Investigation* **2012**, *122*, 899.
(12) Salmon, H.; Franciszkiewicz, K.; Damotte, D.; Dieu-Nosjean, M. C.; Validire, P.; Trautmann, A.; Mami-Chouaib, F.; Donnadieu, E. *Journal of Clinical Investigation* **2012**, *122*, 899.
(13) Mukai, S.; Kjaergaard, J.; Shu, S.; Plautz, G. E. *Cancer Research* **1999**, *59*, 5245.
(14) Huber, M. A.; Kraut, N.; Park, J. E.; Schubert, R. D.; Rettig, W. J.; Peter, R. U.; Garin-Chesa, P. *The Journal of Investigative Dermatology* **2003**, *120*, 182.
(15) Welt, S.; Divgi, C. R.; Scott, A. M.; Garin-Chesa, P.; Finn, R. D.; Graham, M.; Carswell, E. A.; Cohen, A.; Larson, S. M.; Old, L. J.; et al. *Journal of Clinical Oncology* **1994**, *12*, 1193.
(16) Hofheinz, R. D.; al-Batran, S. E.; Hartmann, F.; Hartung, G.; Jager, D.; Renner, C.; Tanswell, P.; Kunz, U.; Amelsberg, A.; Kuthan, H.; Stehle, G. *Onkologie* **2003**, *26*, 44.
(17) Wen, Y.; Wang, C. T.; Ma, T. T.; Li, Z. Y.; Zhou, L. N.; Mu, B.; Leng, F.; Shi, H. S.; Li, Y. O.; Wei, Y. Q. *Cancer Science* **2010**, *101*, 2325.
(18) Liao, D.; Luo, Y.; Markowitz, D.; Xiang, R.; Reisfeld, R. A. *PloS One* **2009**, *4*, e7965.
(19) Ostermann, E.; Garin-Chesa, P.; Heider, K. H.; Kalat, M.; Lamche, H.; Puri, C.; Kerjaschki, D.; Rettig, W. J.; Adolf, G. R. *Clinical Cancer Research* **2008**, *14*, 4584.
(20) Tran, E.; Chinnasamy, D.; Yu, Z.; Morgan, R. A.; Lee, C. C.; Restifo, N. P.; Rosenberg, S. A. *The Journal of Experimental Medicine* **2013**, *210*, 1125.
(21) Dolznig, H.; Schweifer, N.; Puri, C.; Kraut, N.; Rettig, W. J.; Kerjaschki, D.; Garin-Chesa, P. *Cancer Immunity* **2005**, *5*, 10.
(22) Niedermeyer, J.; Garin-Chesa, P.; Kriz, M.; Hilberg, F.; Mueller, E.; Bamberger, U.; Rettig, W. J.; Schnapp, A. *The International Journal of Developmental Biology* **2001**, *45*, 445.

(23) Kraman, M.; Bambrough, P. J.; Arnold, J. N.; Roberts, E. W.; Magiera, L.; Jones, J. O.; Gopinathan, A.; Tuveson, D. A.; Fearon, D. T. *Science* **2010**, *330*, 827.
(24) Roberts, E. W.; Deonarine, A.; Jones, J. O.; Denton, A. E.; Feig, C.; Lyons, S. K.; Espeli, M.; Kraman, M.; McKenna, B.; Wells, R. J.; Zhao, Q.; Caballero, O. L.; Larder, R.; Coll, A. P.; O'Rahilly, S.; Brindle, K. M.; Teichmann, S. A.; Tuveson, D. A.; Fearon, D. T. *The Journal of Experimental Medicine* **2013**, *210*, 1137.
(25) Agostinis, P.; Berg, K.; Cengel, K. A.; Foster, T. H.; Girotti, A. W.; Gollnick, S. O.; Hahn, S. M.; Hamblin, M. R.; Juzeniene, A.; Kessel, D.; Korbelik, M.; Moan, J.; Mroz, P.; Nowis, D.; Piette, J.; Wilson, B. C.; Golab, J. *CA: A Cancer Journal for Clinicians* **2011**, *61*, 250.
(26) Zhen, Z. P.; Tang, W.; Guo, C. L.; Chen, H. M.; Lin, X.; Liu, G.; Fei, B. W.; Chen, X. Y.; Xu, B. Q.; Xie, J. *ACS Nano* **2013**, *7*, 6988.
(27) Lin, X.; Xie, J.; Niu, G.; Zhang, F.; Gao, H.; Yang, M.; Quan, Q.; Aronova, M. A.; Zhang, G.; Lee, S.; Leapman, R.; Chen, X. *Nano Letters* **2011**, *11*, 814.
(28) Rota, C.; Chignell, C. F.; Mason, R. P. *Free Radical Biology & Medicine* **1999**, *27*, 873.
(29) Brocks, B.; Garin-Chesa, P.; Behrle, E.; Park, J. E.; Rettig, W. J.; Pfizenmaier, K.; Moosmayer, D. *Molecular Medicine* **2001**, *7*, 461.
(30) Sun, H.; Liu, D. *Cancer Gene Therapy* **2016**, *23*, 54.
(31) Niedermeyer, J.; Scanlan, M. J.; Garin-Chesa, P.; Daiber, C.; Fiebig, H. H.; Old, L. J.; Rettig, W. J.; Schnapp, A. *International Journal of Cancer* **1997**, *71*, 383.
(32) van Meeteren, L. A.; Thorikay, M.; Bergqvist, S.; Pardali, E.; Stampino, C. G.; Hu-Lowe, D.; Goumans, M. J.; ten Dijke, P. *The Journal of Biological Chemistry* **2012**, *287*, 18551.
(33) Bhowmick, N. A.; Neilson, E. G.; Moses, H. L. *Nature* **2004**, *432*, 332.
(34) Kopf, M.; Baumann, H.; Freer, G.; Freudenberg, M.; Lamers, M.; Kishimoto, T.; Zinkernagel, R.; Bluethmann, H.; Kohler, G. *Nature* **1994**, *368*, 339.
(35) Emmerich, J.; Mumm, J. B.; Chan, I. H.; LaFace, D.; Truong, H.; McClanahan, T.; Gorman, D. M.; Oft, M. *Cancer Research* **2012**, *72*, 3570.
(36) Kelly, T.; Huang, Y.; Simms, A. E.; Mazur, A. *International Review of Cell and Molecular Biology* **2012**, *297*, 83.
(37) Netti, P. A.; Berk, D. A.; Swartz, M. A.; Grodzinsky, A. J.; Jain, R. K. *Cancer Research* **2000**, *60*, 2497.
(38) Boucher, Y.; Brekken, C.; Netti, P. A.; Baxter, L. T.; Jain, R. K. *British Journal of Cancer* **1998**, *78*, 1442.
(39) Heldin, C. H.; Rubin, K.; Pietras, K.; Ostman, A. *Nature Reviews. Cancer* **2004**, *4*, 806.
(40) Gabbiani, G. *The Journal of Pathology* **2003**, *200*, 500.
(41) Snyder, J. W.; Greco, W. R.; Bellnier, D. A.; Vaughan, L.; Henderson, B. W. *Cancer Research* **2003**, *63*, 8126.
(42) Zhen, Z.; Tang, W.; Chuang, Y. J.; Todd, T.; Zhang, W.; Lin, X.; Niu, G.; Liu, G.; Wang, L.; Pan, Z.; Chen, X.; Xie, J. *ACS Nano* **2014**, *8*, 6004.
(43) Sano, K.; Nakajima, T.; Choyke, P. L.; Kobayashi, H. *ACS Nano* **2013**, *7*, 717.
(44) Gajewski, T. F.; Schreiber, H.; Fu, Y. X. *Nature Immunology* **2013**, *14*, 1014.
(45) Weber, J. S.; D'Angelo, S. P.; Minor, D.; Hodi, F. S.; Gutzmer, R.; Neyns, B.; Hoeller, C.; Khushalani, N. I.; Miller, W. H., Jr.; Lao, C. D.; Linette, G. P.; Thomas, L.; Lorigan, P.; Grossmann, K. F.; Hassel, J. C.; Maio, M.; Sznol, M.; Ascierto, P. A.; Mohr, P.; Chmielowski, B.; Bryce, A.; Svane, I. M.; Grob, J. J.; Krackhardt, A. M.; Horak, C.; Lambert, A.; Yang, A. S.; Larkin, J. *The Lancet. Oncology* **2015**, *16*, 375.

(46) Topalian, S. L.; Hodi, F. S.; Brahmer, J. R.; Gettinger, S. N.; Smith, D. C.; McDermott, D. F.; Powderly, J. D.; Carvajal, R. D.; Sosman, J. A.; Atkins, M. B.; Leming, P. D.; Spigel, D. R.; Antonia, S. J.; Horn, L.; Drake, C. G.; Pardoll, D. M.; Chen, L.; Sharfman, W. H.; Anders, R. A.; Taube, J. M.; McMiller, T. L.; Xu, H.; Korman, A. J.; Jure-Kunkel, M.; Agrawal, S.; McDonald, D.; Kollia, G. D.; Gupta, A.; Wigginton, J. M.; Sznol, M. *The New England Journal of Medicine* **2012**, *366*, 2443.
(47) Gross, G.; Eshhar, Z. *Annual Review of Pharmacology and Toxicology* **2016**, *56*, 59.
(48) Kobayashi, H.; Choyke, P. L.; Ogawa, M. *Current Opinion in Chemical Biology* **2016**, *33*, 32.
(49) Nagaya, T.; Nakamura, Y.; Sato, K.; Zhang, Y. F.; Ni, M.; Choyke, P. L.; Ho, M.; Kobayashi, H. *Oncotarget* **2016**.
(50) Sato, K.; Nagaya, T.; Mitsunaga, M.; Choyke, P. L.; Kobayashi, H. *Cancer Letters* **2015**, *365*, 112.
(51) Mitsunaga, M.; Ogawa, M.; Kosaka, N.; Rosenblum, L. T.; Choyke, P. L.; Kobayashi, H. *Nature Medicine* **2011**, *17*, 1685.
(52) Lucky, S. S.; Soo, K. C.; Zhang, Y. *Chemical Reviews* **2015**, *115*, 1990.
(53) Chatterjee, D. K.; Fong, L. S.; Zhang, Y. *Advanced Drug Delivery Reviews* **2008**, *60*, 1627.
(54) Calixto, G. M.; Bernegossi, J.; de Freitas, L. M.; Fontana, C. R.; Chorilli, M. *Molecules* **2016**, *21*, 342.
(55) Brocks, B.; Garin-Chesa, P.; Behrle, E.; Park, J. E.; Rettig, W. J.; Pfizenmaier, K.; Moosmayer, D. *Molecular Medicine* **2001**, *7*, 461.
(56) Zhen, Z.; Tang, W.; Chen, H.; Lin, X.; Todd, T.; Wang, G.; Cowger, T.; Chen, X.; Xie, J. *ACS Nano* **2013**, *7*, 4830.

CHAPTER 8

CONCLUSIONS

Ferritin (FRT) is a major iron storage protein found in humans and most living organisms. Each FRT is composed of 24 subunits, which self-assemble to form a cage-like nanostructure. The surface of FRT nanocage can be easily modified for tumor targeting and/or imaging. The interior of FRT can be loaded with different therapeutics. For example, we have used RGD-modified FRTs (RFRTs) to selectively deliver doxorubicin to tumors. The doxorubicin-loaded RFRTs showed improved tumor uptake, enhanced treatment efficacy, and reduced cardiotoxicity compared to free doxorubicin.

The FRT nanocages can also be loaded with photosensitizers to facilitate photodynamic therapy (PDT). By choosing different targeting ligands, PDT can target different components in a tumor. For instance, folic acid-conjugated and $ZnF_{16}Pc$-loaded FRTs can efficiently kill cancer cells in tumors. $ZnF_{16}Pc$-loaded RFRTs, on the other hand, target tumor endothelium, and the impact is highly dependent on irradiation doses: at high irradiation doses, the enabled PDT causes vasculature collapse and blockage, leading to tissue ischemia; at low irradiation doses, PDT causes temporally enhanced vasculature permeability, which is beneficial to delivery of nanoparticles to tumors. More recently, we conjugated an anti-fibroblast activation protein (anti-FAP) scFv to $ZnF_{16}Pc$-loaded FRTs and investigated the enabled PDT. The treatment efficiently killed cancer associated fibroblasts (CAFs) but left most cancer cells unharmed. Yet, efficient tumor growth suppression and extended survival was observed, which was mainly attributed to

activated intra-tumoral immune responses, manifested as not only an increased frequency of $CD8^+$ T cells in tumors but also enhanced infiltration.

We've also developed a technology called red blood cell-facilitate PDT (RBC-PDT). So far, most PDT-related research has focused on delivery of photosensitizers. O_2, another essential component of PDT, is not artificially delivered but taken from the biological milieu. However, cancer cells demand a large amount of O_2 to sustain their growth and that often leads to tumor hypoxia. In the RBC-PDT, we tether a large amount of photosensitizer-loaded FRTs to erythrocytes, which are natural O_2 transporters. Because photosensitizers are located within an O_2 rich zone on RBC membrane, they can efficiently produce $^1O_2$ even when the overall oxygen level is low, for instance, in hypoxic tumor areas. This leads to efficient tumor therapy and represents a novel PDT approach.

In summary, FRT-based drug delivery is a safe and efficient technology that holds great potential in clinical translation.